VILNIUS UNIVERSITY
CENTER FOR PHYSICAL SCIENCES AND TECHNOLOGY

Vincentas Mindaugas Mačiulis

Application of Metallic and Metal Oxides Nanostructures for Proteins Biosensing by Ellipsometry and Quartz Crystal Microbalance

DOCTORAL DISSERTATION

Natural Sciences,
Chemistry (N003)

VILNIUS 2023

The dissertation was prepared between 2019 and 2023 at the Center for Physical Sciences and Technology. The research was supported by Research Council of Lithuania, through a scholarship for academic accomplishments.

This doctoral dissertation will be defended in a public meeting of the Dissertation Defence Panel:

Chairman – Prof. Dr. Rimantas Ramanauskas (Center for Physical Sciences and Technology, Natural Sciences, Chemistry, N 003).
Members:
Assoc. Prof. Dr. Rima Budvytytė (Vilnius University, Natural Sciences, Biochemistry, N 004),
Assoc. Prof. Dr. Deivis Plaušinaitis (Vilnius University, Natural Sciences, Chemistry, N 003),
Prof. Dr. Tautgirdas Ruzgas (Malmö University, Natural Sciences, Biochemistry, N 004),
Prof. Dr. Vida Vičkačkaitė (Vilnius University, Natural Sciences, Chemistry, N 003).

The dissertation shall be defended at a public meeting of the Dissertation Defence Panel at 10 am on 6th of October 2023 in meeting room D401 in the Center for Physical Sciences and Technology.
Address: Sauletekio al., 3, D401 Vilnius, Lithuania
Tel. +370 264 9211 ; e-mail: office@ftmc.lt

The text of this dissertation can be accessed at the libraries of Libraries of Vilnius University and Center for Physical Sciences and Technology, as well as on the website of Vilnius University:
www.vu.lt/lt/naujienos/ivykiu-kalendorius

VILNIAUS UNIVERSITETAS
FIZINIŲ IR TECHNOLOGIJOS MOKSLŲ CENTRAS

Vincentas Mindaugas Mačiulis

Metalų ir metalų oksidų nanostruktūrų taikymas baltymų nustatymui taikant elipsometriją ir kvarco kristalo mikrogravimetriją

DAKTARO DISERTACIJA

Gamtos mokslai,
Chemija (N 003)

VILNIUS 2023

ACKNOWLEDGMENT

I would like to thank my supervisor Ieva and all of the colleagues and co-authors for their support and valuable lessons.

I also cannot go on without thanking my significant otter Karolina, without whom I would probably be lesser version of myself than I am today.

And to all friends who encouraged me to apply for a PhD.

Once again thank you all!

LIST OF INCLUDED PUBLICATIONS

Paper 1 **Vincentas Maciulis**, Uldis Malinovskis, Donats Erts, Arunas Ramanavicius, Almira Ramanaviciene, Saulius Balevicius, Silvija Juciute, Ieva Plikusiene, Porous aluminium oxide coating for the development of spectroscopic ellipsometry based biosensor: Evaluation of human serum albumin adsorption, *Coatings*, (2020), 10(11), 1018, https://doi.org/10.3390/coatings10111018

Paper 2 Ieva Plikusiene, **Vincentas Maciulis**, Octavio Graniel, Mikhael Bechelany, Saulius Balevicius, Vilius Vertelis, Zigmas Balevicius, Anton Popov, Arunas Ramanavicius, Almira Ramanaviciene, Total internal reflection ellipsometry for kinetics-based assessment of bovine serum albumin immobilization on ZnO nanowires, *Journal of Materials Chemistry C*, 9(4), (2021), 1345-1352, https://doi.org/10.1039/D0TC05193D

Paper 3 Ieva Plikusiene, **Vincentas Maciulis**, Silvija Juciute, Ruta Maciuleviciene, Saulius Balevicius, Arunas Ramanavicius, Almira Ramanaviciene, Investigation and Comparison of Specific Antibodies' Affinity Interaction with SARS-CoV-2 Wild-Type, B. 1.1. 7, and B. 1.351 Spike Protein by Total Internal Reflection Ellipsometry, *Biosensors*, 12(5), (2022), 351, https://doi.org/10.3390/bios12050351

Paper 4 Ieva Plikusiene, **Vincentas Maciulis**, Silvija Juciute, Arunas Ramanavicius, Zigmas Balevicius, Rimantas Slibinskas, Indre Kucinskaite-Kodze, Martynas Simanavicius, Saulius Balevicius, Almira Ramanaviciene, Investigation of SARS-CoV-2 nucleocapsid protein interaction with a specific antibody by combined spectroscopic ellipsometry and quartz crystal microbalance with dissipation, *Journal of Colloid and Interface Science*, 626, (2022), 113-122, https://doi.org/10.1016/j.jcis.2022.06.119

Paper 5 **Vincentas Maciulis**, Almira Ramanaviciene, Ieva Plikusiene, Recent Advances in Synthesis and Application of Metal Oxide Nanostructures in Chemical Sensors and Biosensors, *Nanomaterials*, 12(24), (2022), 4413, https://doi.org/10.3390/nano12244413

AUTHOR'S CONTRIBUTION TO INCLUDED PUBLICATIONS

Paper 1   Carried out the measurement of human serum albumin adsorption to porous aluminium oxide, recorded spectroscopic ellipsometry spectra, prepared the initial draft and contributed to the preparation of the manuscript, published the paper as a first co-author.

Paper 2   Executed the preparation and functionalization of ZnO nanowire substrates, recorded bovine serum albumin covalent immobilization to the substrate using spectroscopic ellipsometry, contributed to the preparation of the manuscript.

Paper 3   Performed the preparation of gold substrates and recorded the covalent immobilization of SARS-CoV-2 spike proteins and their interaction with specific antibodies using spectroscopic ellipsometry, contributed to the initial data analysis, contributed to the preparation of the manuscript.

Paper 4   Implemented the measurement of covalent immobilization of SARS-CoV-2 nucleocapsid protein and its' interaction with specific antibodies using spectroscopic ellipsometry combined with quartz crystal microbalance with dissipation, analysed acquired data, contributed to the preparation of the manuscript.

Paper 5   Outlined the theme and assessed publications fit for a literature review manuscript, prepared the initial draft of the review, contributed to the preparation of the manuscript, published the paper as a first co-author.

TABLE OF CONTENTS

LIST OF ABBREVIATIONS

pAAO	Porous Anodic Aluminium oxide
ZnO	Zinc Oxide
IEP	Isoelectric point
NWs	Nanowires
MOCVD	Metal-organic chemical vapour deposition
SPR	Surface plasmon resonance
QCM-D	Quartz crystal microbalance with dissipation
TIRE	Total internal reflection ellipsometry
BSA	Bovine serum albumin
HSA	Human serum albumin
SAM	Self-assembled monolayer
11-MUA	11-mercaptoundecanoic acid
APTES	3-aminopropyltriethoxysilane
SCoV2-N	SARS-CoV-2 virus nucleocapsid protein
SCoV2-S	SARS-CoV-2 virus spike protein
SCoV2-αS	SARS-CoV-2 Alpha variant spike protein
SCoV2-βS	SARS-CoV-2 Beta variant spike protein
Ab	Antibody
RNP	Ribonucleoprotein complex
RBD	Receptor binding domain
ACE2	Angiotensin converting enzyme 2
EMA	Effective media approximation

INTRODUCTION

Nanostructured materials have several benefits, including a high surface area, improved mechanical and other physical characteristics, and adjustable electrical properties, which can be useful in the development of different sensors [1–5]. Nanometric thickness layers are a common form of nanostructure utilised for different chemical and biological sensors. Such sensors are usually based on optical, or acoustic signal detection. Recently, there has been a lot of interest in the application and development of biosensors in which the response is obtained by spectroscopic ellipsometry, quartz crystal microbalance or their combination [6–8]. These very sensitive and non-destructive surface sensitive methods enabled to create a new generation of biosensing systems, which were successfully used for various proteins studies. The future goals in this area are application of advanced materials and structures for the improvement of the sensors as well as the investigation of various proteins [9].

The study of protein adsorption/desorption to/from various nanoporous materials is an important task because such materials can be applied to protein separation, purification, and the development of biosensors that can be used to determine various analytes that are important in biology, biochemistry, medical diagnostics, pharmacy, or the food industry [10]. Because of the beneficial physical and chemical features of protein-modified nanoporous surfaces, nanoporous coatings are especially useful in the creation of such biosensors [11]. Nanoporous anodic aluminium oxide (pAAO) presents distinct advantages for the development of various biosensors due to its highly ordered structure, desirable pore geometry, outstanding optical and electrical properties, high mechanical and thermal stability, chemical resistance, the large amount of hydroxyl groups present on its porous surface, large surface-to-volume ratio, and biocompatibility [12–15]. Coupling specific molecules to the pAAO pore wall surfaces, broadens the application of pAAO structure, from synthesis of new nanomaterials to manufacture of devices for sensing and recognition. Various biosensing platforms based on pAAO coatings have been used in optical and electrochemical biosensors during the last decade [16,17].

ZnO along with nanostructures made from this metal oxide are gaining popularity for use in transparent electronics, photocatalysis, solar cells, sensors, and optical biosensors [18–22]. ZnO nanowires (ZnO-NWs) are typical 1D ZnO nanostructures that have been used in the construction of nanosized electrodes because of their large surface area, direct electron pathway in the c-axis direction, biocompatibility, and chemical stability. The

surface of ZnO-NWs is useful for functionalization because it allows for the efficient immobilisation of biomolecules with sufficient loading capacity, high biological activity, and good stability [23–25].

These nanomaterials can be combined to create complementary composite structures, where an inclusion of a material enhances the properties of the whole structure. For example, gold film deposition on pAAO or ZnO-NWs, combines the advantages of both materials. Gold film provides a stable and inert surface, allowing the use of well-known functionalization procedures, while a deposited nanostructure underneath provide a high surface area and signal enhancement [26].

Bovine serum albumin (BSA) and human serum albumin (HSA) are proteins that are utilised as "blocking agents" in many bioanalytical systems to reduce non-specific interactions and improve the selectivity and sensitivity of bioanalytical systems [27,28]. As a result, it is critical to analyse how strongly these proteins interact with surfaces used in the design of bioanalytical systems, as well as how durable these protein monolayers are.

SARS-CoV-2 nucleocapsid (SCoV2-N) is a structural protein of the SARS-CoV-2 virus. SCoV2-N research is significant because of its function in genomic RNA packing and viral replication of SARS-CoV-2 [29]. Antibodies against the SCoV2-N have been found in infected individuals, and a high concentration of these antibodies is associated with an increased risk of potentially life - threatening conditions [30]. Research on SCoV2-N and specific anti-SCoV2-N is essential for the industry involved in production of antibody-antigen tests, medication and vaccines.

SARS-CoV-2 spike (SCoV2-S) is a structural protein that binds to host cells via the ACE2 receptor, promoting SARS-CoV-2 infection [31]. The human immune system can develop antibodies that neutralise SCoV2-S and prevent it from binding to ACE2 [32]. However, mutations of the SARS-CoV-2 virus, result in changes of the SCoV2-S creating spike variants like; SCoV2-αS and SCoV2-βS and others. These variations usually are amino acid substitutions that can reduce the efficacy of vaccinations, treatment medications, and diagnostic instruments [33].

The aim of the study is to investigate possibilities to apply modified nanometric Au films and coatings of porous Al_2O_3 and ZnO nanowires for the design of biosensing systems, based on advanced optical and acoustic research methods, spectroscopic ellipsometry (SE) and quartz crystal microbalance with dissipation (QCM-D).

The objectives of the study:

1. To study the optical properties of a porous pAAO coating and to analyse the HSA adsorption/desorption process from this coating using the SE method.

2. To investigate the optical properties and capabilities of ZnO-NWs surface structures for the TIRE mode signal enhancement during biosensing and real-time measurement of covalent BSA binding.

3. To perform the investigation and comparison of affinity interaction with SARS-CoV-2 S, -αS and -βS protein mutations by Total Internal Reflection Ellipsometry method. To study the association (k_a), dissociation (k_d), stable immune complex formation (k_r) rate constants and steric factors (P_s) for the immune complexes formation between covalently immobilized SARS-CoV-2 spike proteins of different mutations and polyclonal human antibody (pAb-SCoV2-S) produced after vaccination.

4. To use the hybrid SE/QCM-D technique for investigation of (i) the covalent immobilization of SARS-CoV-2 nucleocapsid protein on the 11-mercaptoundecanoic acid (11-MUA) self-assembled monolayer (SAM) and (ii) the interaction with specific antibodies followed by an immune complex formation process.

SCIENTIFIC NOVELTY

The novelty of the research presented in this dissertation is based on the application of nanometre-scale metal and metal oxide structures (porous AAO coating and ZnO-NWs), which can be used for the development of high-sensitivity biosensing systems based on SE and hybrid SE/QCM-D techniques. In addition, the dissertation was prepared during the COVID 19 pandemic, and structural proteins and specific antibodies were studied for the first time using these optical and acoustic methods.

Investigation of the adsorption of human serum albumin (HSA) on the pAAO coating using SE showed that: (i) the protein concentration within the nanopores was approximately 200 to 600 times higher than that in buffer solution, depending on the exposure time; (ii) the initial phase of the accumulation process is slow (3.23 mg·cm^{-3}·min^{-1}) compared to the protein decrease rate (21.2 mg·cm^{-3}·min^{-1}) by washing the pAAO layer; (iii) conventional washing with PBS solution and deionized water does not completely remove the HSA molecules from the pAAO pores, so the HSA concentration in the nanopores is still almost 100 times higher than that in the PBS solution after 16 hours of washing. These results indicate a new possibility that HSA can be successfully used for the blocking of the

remaining free surface, which is applied for the reduction in non-specific binding after immobilization of biorecognition molecules on the pAAO surface.

During the investigation of the ZnO-NWs as a potential substrate for biosensing, it was found that the time of signal saturation in PBS buffer could be related to the different density of ZnO-NWs regions on the substrate. The shorter time of stabilization is related to the lower density of ZnO-NWs, while a longer time is related to the higher density of these nanostructures. This property of the ZnO-NWs shows the new possibilities to use the ZnO-NWs for the development of selective biosensors.

The study of the interaction kinetics between the covalently immobilized SARS-CoV-2 S protein variants and the real samples of specific polyclonal antibodies from diluted volunteer blood serum using the highly sensitive TIRE method allows us to obtain the affinity constants of pAb-SCoV2-S and S protein immune complex formation. This demonstrates for the first time that these antibodies, which are developed by the humoral response of the immune system after vaccination, are able to bind to all three types of S protein with high affinity.

For the first time, the hybrid SE/QCM-D method was used to study immune complex formation between covalently immobilized SARS-CoV-2 nucleocapsid protein and specific antibodies. The obtained results showed that the flexibility of anti-SCoV2-N is an important factor for bivalent interaction with small nucleocapsid proteins that are widely separated at the solid-liquid interface.

STATEMENTS FOR DEFENSE:

- An electrochemically synthesized porous pAAO coating with a thickness of hundreds of nm, in which the pores with a radius of ≈ 40 nm are arranged at a distance of ≈ 110 nm in a regular hexagonal structure, can accumulate HSA proteins at a concentration ≈ 100 times higher than that in the PBS solution, changing the effective refractive index of the coating by ≈ 7.5% and enabling optical biosensing of HSA proteins.
- The ≈ 40 nm wide and ≈ 350 nm long ZnO wires fabricated by electrodeposition on a ZnO coated ITO/glass substrate are able to accumulate BSA molecules, inducing changes of ellipsometric parameter Δ about 2.24 times higher compared to the flat-type ZnO sensor. For this reason, the application of ZnO-NWs can increase the sensitivity of the optical BSA biosensor.
- The equilibrium constants and steric factors obtained by TIRE for three types of pAb-SCoV2-S complexes formed with the SCoV2-S, α-, and β-antibodies produced by Vaxzevria vaccination showed that they readily formed an immune complex compared with the nucleocapsid, demonstrating the ability of these antibodies to protect the population from the α- and β-mutation of SARS-CoV-2.
- The SE/QCM-D measurement showed that the monolayer of covalently immobilized SCoV2-N is more rigid in comparison with monolayer of anti-SCoV2-N after the interaction with SCoV2-N formed a soft, flexible, and viscous layer with ≈ 4 times higher energy dissipation. The flexibility of the antibody Fab arms allows them to establish a bivalent interaction between proteins in formed SCoV2-N/anti-SCoV2-N complex.

LITERATURE REVIEW

1.1. Nanostructures of metals and metal oxides

Structures and layers of metals and metal oxides having dimensions in the nanometre range (1 - 100 nm) in at least one relevant direction are named nanostructured materials [34]. The properties of nanostructured materials differ from their bulk counterparts. The differences in nanostructures properties compared to bulk materials are resulted due to the significant effects of quantum confinement on optical, electrical, and thermal properties [35–37]. When the size of a particle is reduced to the nanometre scale, a larger fraction of the atoms are located at the surface of the structure than in structures with larger volume [38]. These surface atoms behave differently than atoms located inside or in ideal crystal structures, possessing high surface energy and activity (becoming unstable and easily combining with other atoms) [9]. An additional advantage of using nanostructured materials is the increase in effective surface area that could be used for attachment of various biologically active substances used for biosensing [5,39].

Nanostructures can be divided into a few classes. Structures that are less than 100 nm in all relevant directions are named zero-dimensional (0D) nanostructures; these include nanoclusters, nanospheres, and quantum dots [40–42]. One-dimensional (1D) nanostructures are structures with a size of > 100 nm in one dimension, including nanowires, nanorods, and nanobelts [43–45]. Two-dimensional (2D) nanostructures are coatings, walls, and layers with limited thickness (< 100 nm) that have a high surface-to-volume ratio [1,46]. Three-dimensional (3D) nanostructures are not bound to the nanoscale, but these structures consist of 0D, 1D, and 2D nanostructures that are in close contact with each other and have a large effective surface area compared to bulk materials [47,48]. Classes of nanostructures and methods of synthesis are illustrated in Figure 1.
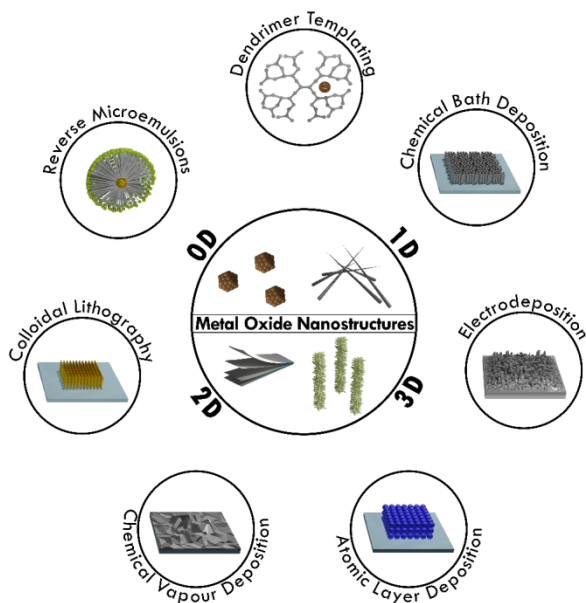
Figure 1. Classes of metal oxide nanostructures and methods of synthesis.

Metal oxide nanomaterials are an important class of materials due to their optical, magnetic, and electronic properties and a variety of formable nanostructures that can be applied for biosensing [49,50]. Further reading on the topic of synthesis and application of nanostructures in biosensing is published in a review (Paper 5) [51].

The investigation of protein adsorption/desorption to/from various nanostructured materials is an important task due to the ability to use such materials for proteins separation, purification, and in the development of biosensors, which can be applicable for the determination of various analytes that are important in biology, biochemistry, medical diagnostics, pharmaceutical, or food industry.

1.1.1. Porous anodic aluminium oxide

Nanoporous coatings are especially important in the development of such biosensors due to the valuable physical and chemical properties of protein-modified nanoporous surfaces [11]; for example, nanoporous anodic aluminium oxide (pAAO) presents exclusive features for the development of various biosensors due to its highly ordered structure, desirable pore geometry, outstanding optical and electrical properties, high mechanical and thermal stability, chemical resistance, the large amount of hydroxyl groups

present on its porous surface, large surface-to-volume ratio, and biocompatibility [12,14,15,52]. An additional advantage of pAAO coating is based on the electrochemical anodization procedure, which enables the formation of uniform nanochannels within the Al_2O_3 matrix [52]. During the last decade, various biosensing platforms based on pAAO coatings were applied in optical and electrochemical biosensors [14,15,53].

Porous anodic aluminium oxide (pAAO) is an oxide with a self-organised arrangement of pores formed by anodizing aluminium in acid electrolytes and belongs to 3D class of nanostructures. The pores have a cylindrical shape and are arranged hexagonally with constant diameter and ideally with constant spacing between pores [54]. The dimensions of the pAAO templates can be tailored to the specific application by adjusting the acid electrolyte composition, concentration, temperature, and anodization voltage [55]. The composition of the acid electrolyte also affects the optical properties of pAAO (colour, photoluminescence), as it traps anionic species, that contaminate the pAAO layer during the anodization process [56]. The thickness of the pAAO layer depends on the anodization time, with a longer time period resulting in a thicker pAAO layer. Figure 2 demonstrates a SEM micrograph of pAAO from side, top and tilted view.
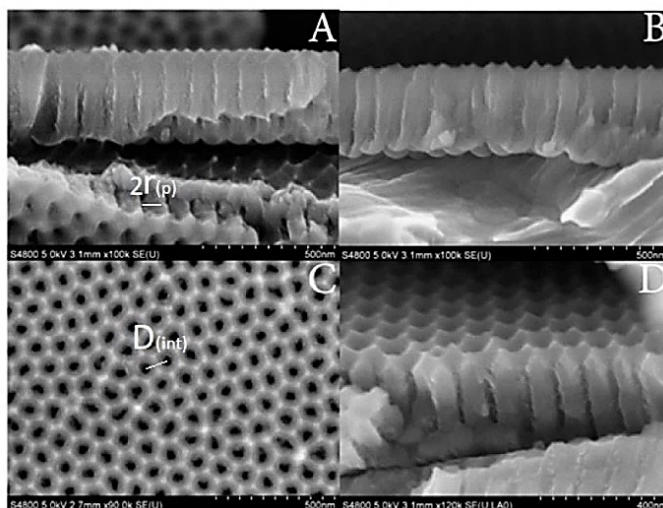
Figure 2. SEM micrographs of porous anodic aluminium oxide (pAAO); (**A, B**) - cross sections; (**C**) - top view; (**D**) - tilted view [4].

Due to the high thermal stability of alumina and the homogeneous pore distribution in pAAO, this material has been widely used as a template for the formation of one-dimensional nanostructures [57]. Despite the overwhelming application of pAAO as a template material, pAAO has attractive properties

(photoluminescence, transmittance, reflectivity) to be used as a sensing platform for optical biosensor development [53]. pAAO films are well suited for miniaturisation and integration into current microchip technology and can be functionalized with specific functional groups that further can be used for immobilization of biologically active substances. The unique structure of pAAO can be used not only as an active biosensing surface for nucleic acid, protein and bacteria detection, but also as a container for accumulated biomaterial [4,13,58,59]. Biosensors based on pAAO are viable for medical diagnosis, for example detecting SARS-CoV2 genomic material [60]. As well as for rapid antibiotic efficacy tests, where the pAAO membrane is used to capture live bacteria [61].

1.1.2. Zinc oxide nanowires

Another class of nanostructured materials that can be formed from metal oxides and attracts attention for the application in biosensing is 1D structures. Among other metal oxides zinc oxide (ZnO) can be distinguished due to the its thermal stability, high mechanical strength, biocompatibility and non-toxicity [62]. ZnO is a semiconductor that has a high isoelectric point (IEP) of pH values between 9.0 and 9.5, wide bandgap (3.37 eV), and a high exciton binding energy (60 meV) [50]. The 1D structures as nanowires (NWs) can be easily formed from ZnO using atomic layer deposition (ALD) [63], chemical bath deposition (CBD) [50,64], electrodeposition [5,65]. Possessing unique electronic and optical properties that enable applications in photodetectors, gas sensors, and solar cells and biosensors [66–69]. In addition, the properties of ZnO-NWs can be further modified by selective introduction of impurities [70]. ZnO-NWs are commonly synthesized by metal-organic chemical deposition (MOCVD), electrodeposition, or chemical bath deposition, with the latter two methods being more cost and time efficient. Thus more suited for large-scale production processes [66,71,72]. A cross-section view of ZnO-NWs formed by electrochemical deposition is shown in Figure 3.
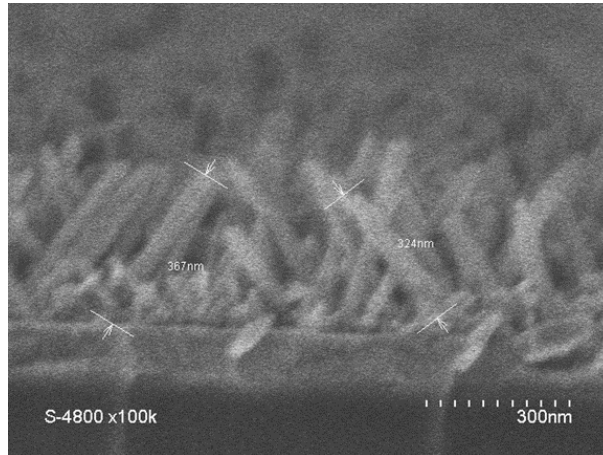
Figure 3. SEM image of ZnO-NWs deposited on ZnO/ITO/glass substrate [5].

The surface of ZnO-NWs is well suited for functionalization, providing a large effective surface area with good stability. Functionalization of ZnO-NWs can be achieved in three ways: (i) by electrostatic interaction of biological materials (enzymes, antibodies, DNA) with low IEP values [73], (ii) by silane chemistry, forming a siloxane network with specific end groups suitable for the immobilization of biomolecules [5], (iii) by decoration with Au nanoparticles and functionalization with linkers using Au-thiol interaction [74].

Thus, ZnO-NWs and similar 1D nanostructures find many applications, particularly when formed in hybrid or doped structures with other materials and are applied in the field of medical diagnostics, such as, glucose, biosensors [75,76].

1.2. Application of Au nanometric layers for biosensing

Au is one of the most widely used metals for biosensing due to its biocompatibility, optical and electronic properties, and simple modification protocols [77–79]. Thin Au films (~50 nm) that belongs to the class of 2D nanostructures can be successfully applied for generating surface electromagnetic waves for surface plasmon resonance excitation combing with special optical elements in total internal reflection mode [80–82]. The advantage of Au surface is that it can be easily modified by functional groups for specific binding of biomolecules and can be used not only in optical detection but in piezoelectric devices as well [7].

Gold sputtered quartz crystals are commonly used for piezoelectric sensors. One of which, is a mass sensitive technique of quartz crystal

microbalance with dissipation (QCM-D). A sensing method that monitors changes of surface mass density at the solid-liquid interface, thus requiring an inert and easily modifiable surface [7,83].

In biosensing, thin Au films are usually functionalized using self-assembled monolayers with thiol end groups. Allowing functionalization of surfaces with biomolecules and therefore recognition and sensing of target analytes such as viral antigens, antibodies and ligands [84–87].

1.3. Human (HSA) and bovine serum albumin (BSA) model system for biosensing

The detection of various protein biomarkers, relevant in numerous biomedical applications that range from disease diagnosis, drug discovery and treatment applications plays an important role. Among many proteins some of them as human serum albumin (HSA) and bovine serum albumin (BSA) are applied as model systems for the testing of novel biosensing platforms.

Serum albumin proteins are the most abundant water-soluble proteins in vertebrate blood plasma (35-50 mg/ml). In general, serum albumin consists of a single polypeptide chain with ~585 amino acid residues [88]. Serum albumin is responsible for 80% of the colloidal osmotic pressure in blood and acts as a transporter for many circulatory, nutritional and physiological functions [89].

BSA and, similarly though to a lesser extent, HSA are widely used as model antigens in immunology because of their known structure and availability [90]. BSA has been used as a model antigen in sensor designs based on hydrogel imprinting, gold nanorods [91], ZnO nanospheres, Al_2O_3/ZnO nanolaminates [1], and Al nanopillars [92] and became a standard protein in the development of new immunological assays [93]. Since the goal of many new designs is accuracy and reproducibility, a protein with known structure, dimensions, and properties is essential.

1.4. SARS-CoV-2 coronavirus structural proteins and antibodies

SARS-CoV-2 virions have a spherical shape with a diameter of 108 ± 8 nm. The surface of the virion is covered with spike proteins (SCoV2-S) that are flexible relative to the membrane and can tilt up to 90°. The viral outer membrane consists of the membrane protein (SCoV2-M) and the envelope protein (SCoV2-E). Inside the virion are the nucleocapsid (SCoV2-N) protein and the viral RNA genome [94]. The specific antibodies or immunoglobulins can form immune complexes with structural proteins. Figure 4 shows the 3D

models of two SARS-CoV-2 structural proteins (SCoV2-N, SCoV2-S) and antibody molecule (Ab).

SCoV2-N **SCoV2-S** **Ab**

3x4x2 nm 16x12x12 nm 15x12x4 nm
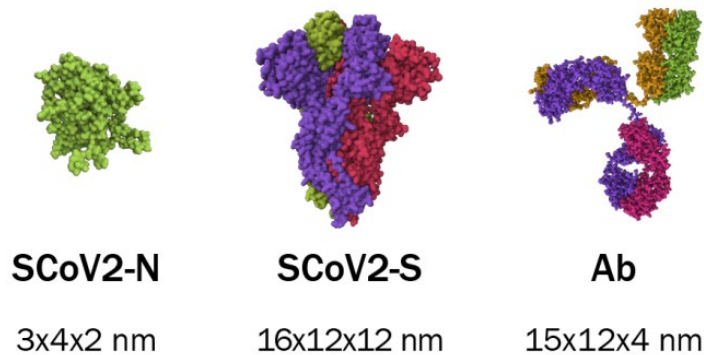
Figure 4. SARS-CoV-2 nucleocapsid (SCoV2-N), SARS-CoV-2 spike (SCoV2-S), and antibody (Ab), and their dimensions determined from [31,95,96].

1.4.1. SARS-CoV-2 nucleocapsid protein

The nucleocapsid (SCoV2-N) protein is located inside the SARS-CoV-2 virus. This is an important structural protein that is abundant in coronaviruses and is responsible for viral replication. The SCoV2-N protein is a small spherical protein with a diameter of about 3 nm and a mass of 48 kDa. It consists of two structural domains: the NTD (the RNA-binding domain) and the CTD (the dimerization domain). The SCoV2-N protein has a strong positive charge, which may explain the ability of the protein to bind to nonspecific nucleic acids [97].

The main function of the SCoV2-N is to bind to viral RNA and form a ribonucleoprotein complex (RNP). After infection, the RNPs enter the host cell, participate in replication, and process the assembly of viral particles and their eventual release [94].

1.4.2. SARS-CoV-2 spike protein

The SCoV2-S protein is an approximately 450 to 600 kDa trimer, one of the largest known in its class. It plays a critical role in viral infection by recognising host cell receptors and mediating fusion between viral and host cell membranes. Because it elicits a strong immune response, it has been a target for the development of a vaccines, testing tools and therapeutics against SARS-CoV-2 [98,99].

The S protein is divided into S1 and S2 subunits. These subunits form a heterodimer (SCoV2-S monomer), which then forms a trimer, resulting in the formation of the S protein in the viral membrane. The S1 subunit is of central interest because it possesses the receptor binding domain (RBD). During SARS-CoV-2 infection, the RBD binds to angiotensin converting enzyme 2 (ACE2), allowing fusion of viral and host membranes. The RBD site is important not only for SARS-CoV-2 virus replication, but also for neutralisation of SARS-CoV-2 virus by targeting the RBD of the SCoV2-S with neutralising antibodies [100,101].

1.4.3. SARS-CoV-2 spike protein variants of concern

As of writing this thesis The World Health Organization (WHO) designated five mutations of SARS-CoV-2 as variants of concern (VOC): Alpha, Beta, Gamma, Delta, and Omicron. The designation of VOC is based on increased transmissibility or an increase/change in disease severity. A SARS-CoV-2 variant results from mutations in coronavirus structural proteins, particularly those occurring in the S protein, due to the role of the RBD region in ACE2 recognition and binding. A change in the amino acid sequence in the RBD region can drastically affect the binding affinity of the SCoV2-S and thus the infectivity of SARS-CoV-2 [102,103].

The first genomes of the variant now referred to as the alpha variant were sequenced in United Kingdom and showed 23 mutations. Of these 23 mutations, 6 were amino acid substitutions in the S protein. This variant was associated with an increase in COVID-19 cases. There was also evidence of increased viral load and a reduction in the neutralizing abilities of some RBD antibodies [104].

Beta variants circulated in South Africa and are defined by an additional 5 S protein amino acid substitutions. Antibody binding affinity was likely affected as there have been studies in which nearly half (48%) of convalescent plasma samples failed to neutralize the beta variant [105].

Gamma variant first was documented in Brazil as a 1.7-2.4 times as transmissible as other local variants. With some of the same mutations in its spike protein, as Alpha and Beta variants, though not nearly as transmissible [106,107].

Delta variant was discovered in India during its' second wave of infections, exhibiting extremely infectious properties and immunity to neutralizing antibodies of previously infected people [108].

Omicron variant was first discovered in South Africa and Botswana. Showing an increased rate of transmissibility compared to Delta variant. The

symptoms of Omicron infection are less dangerous than those of other strains, but it is more infectious and less susceptible to vaccines. However, the rate of mortality is lower [109].

1.5. Antibodies against SARS-CoV-2 structural proteins

Due to the abundance of the SCoV2-N protein during infection and its highly immunogenic properties, high levels of immunoglobulin G (IgG) antibodies against the SCoV2-N protein are found in convalescent plasma from the 10th day of illness [110]. A high number of IgG antibodies against the SCoV2-N (anti-SCoV2-N) is a prognostic factor for the clinical course of the disease [111]. Further reading on analysis of immune complex formation of SCoV2-N and anti-SCoV2-N is published (Paper 4) [7].

Since the spread of COVID-19 by SARS-CoV-2 is based on the virus ability to bind to ACE2 receptor with SCoV2-S protein, the most direct way of blocking the interaction is antibodies against SCoV2-S (anti-SCoV2-S) [31,112]. Antibody neutralising ability can be evaluated by determining antibody affinity upon immune complex formation with SCoV2-S. More in depth investigation and analysis of anti-SCoV2-S interaction and SCoV2-S, SCoV2-αS, SCoV2-βS is published (Paper 3) [82].

2. METHODS

2.1. Porous Aluminium oxide formation

pAAO has been formed on high purity (99.999%) aluminium substrate, using a two-step anodization protocol. Aluminium substrates were cut, degreased and electrochemically polished in 0 °C perchloric acid-ethanol solution consisting of 1 part 60% $HClO_4$ and 4 parts 96% ethanol, at 15 V. Then, substrates were anodized for 2h in 0.3 M oxalic acid solution at 40 V potential and the formed AAO layer was subsequently removed using chromic-orthophosphoric acid mixture of 4% H_2CrO_4 and 11% H_3PO_4) at 70°C. Formation and removal of AAO creates uniform pattern of depressions of the aluminium surface. Then a patterned aluminium substrate was anodized again for 80s in 0.3 M oxalic acid solution. After the second anodization step, AAO pores were cleaned and widened using 5% orthophosphoric acid solution for 1 min, washed with water and dried.

2.2. Zinc oxide nanowires formation

ZnO-NWs were prepared on Indium-Tin Oxide (ITO) glass substrates. First, a seeding layer of 20 nm of ZnO was deposited on ITO/glass, using atomic layer deposition (ALD) with diethyl zinc (DEZ) and deionised water as precursors. ZnO is deposited by exposing the ITO/glass surface to DEZ and deionised water in sequential pulses, separated with a purge with argon (Ar) gas at a constant 100 °C temperature. A typical deposition cycle is 0.2s pulse of DEZ, 40s of DEZ exposure, 60s Ar purge, 2s pulse of deionised water, 40s of deionised water exposure, and 60s Ar purge.

ZnO-NWs were grown on ZnO/ITO/glass substrate using electrodeposition in a three electrode configuration; ZnO/ITO/glass acted as a working electrode, Pt plate acted as a counter electrode and Ag/AgCl acted as a reference electrode. Deposition solution consisted of 0.05mM $ZnCl_2$ and 0.1 M KCl. Electrodeposition was conducted under constant O_2 bubbling at 80 °C with a -1.0 V potential.

2.3. Surface functionalization for proteins immobilization

Surface functionalization of metals or metal oxides with linkers is a common method to enable or enhance the binding of proteins or DNA in biosensors and ligands in drug delivery [113,114]. Various materials and nanostructures have different chemical properties and surface functional groups that can be functionalized. The most common surface modification aims to add organic functional groups (amine, carboxylic acid) to enable covalent immobilization of proteins [115,116].

2.3.1. Surface functionalization using 11-MUA

Gold and other noble metals can be functionalized using linkers with groups known for strong binding affinity to noble metals, e.g., thiol groups (-SH) [117]. Thiocarboxylic acids are linkers commonly used to functionalize gold surfaces with carboxyl groups, one of the most commonly used being 11-mercaptoundecanoic acid (11-MUA). These linkers form a self-assembling monolayer (SAM), an ordered molecular arrangement consisting of a functional group at each end of a linear hydrocarbon chain, with a sulphur head group at one end and carboxylic acid group at the other. Functionalization of a metal surface with SAM increases protein binding capacity, provides a stable base for immobilization, and minimizes nonspecific binding [118].

SAM formation of 11-MUA molecules starts by rinsing the Au substrate with hexane, methanol, and treated with ultrasound under methanol for 3 minutes. Once dried, substrates are placed in a 1 mM solution of 11-MUA in methanol for 18h to allow the formation of SAM of 11-MUA molecules.

2.3.2. Surface functionalization using APTES

3-Aminopropyltriethoxysilane (APTES) is one of many organosilanes used for silane-based surface functionalization processes that enable the binding of biomolecules to surfaces. Essentially used for functionalizing oxide surfaces, APTES is a silicon based molecule with three ethoxy groups at one end and an amine functional group at the other. During the functionalization process, the APTES molecules polymerize on the oxide surface in three steps: Hydrolysis of the ethoxy group, condensation and phase separation. The result is a network of siloxane bonds near the oxide surface and amine groups further from the surface [119].

APTES deposition was performed by vapour-phase deposition. Few drops of APTES were deposited in a small vial, that was placed next to the samples in a Petri dish. The dish was covered and isolated using heat resistant tape, and placed in a 90 °C oven overnight. Afterwards, APTES modified substrates are cleaned using toluene, ethanol and distilled water, and dried in a 110 °C oven.

2.4. Covalent protein immobilization

Proteins can be immobilized on surfaces functionalized with carboxylic acid (-COOH) or amine groups (-NH_2) by crosslinking using a mixture of N-Ethyl-N'-(3-(dimethylamino)-propyl)carbodiimide hydrochloride (EDC) and N-Hydroxysuccinimide (NHS). EDC/NHS mixture is a prerequisite for protein immobilization and is usually referred as 'activation'. An example of covalent protein immobilization (SCoV2-S on 11-MUA) is illustrated in Figure 5.
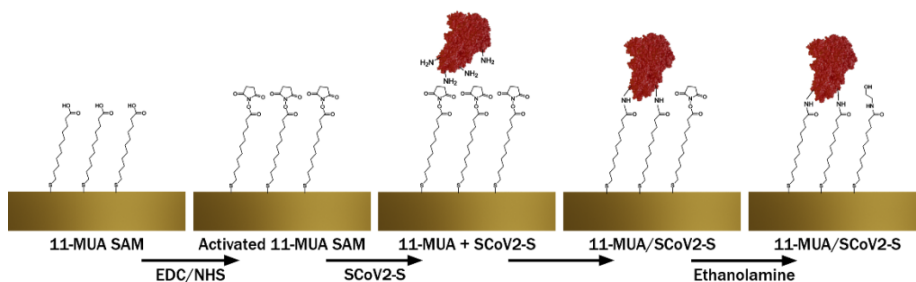
Figure 5. Schematic representation of SARS-CoV-2 S protein (SCoV2-S, SCoV2-αS, or SCoV2-βS) covalent immobilization on the gold-coated SPR sensor disc pre-modified with 11-MUA SAM [82].

Briefly, a -COOH group (from a protein or functionalized surface) reacts with EDC crosslinker, forming an unstable o-acylisourea intermediate ester. Then, NHS molecule interacts with the o-acylisourea molecule, creating a semi-stable NHS ester that reacts well to -NH$_2$ groups. Enabling -NH$_2$ groups (from proteins, or functionalized surfaces) to react and form a stable amide bond, thus immobilizing proteins to surfaces.

The methodology of protein immobilization differs based on the surface bound functional groups. If the surface is functionalized with -COOH groups, then a solution of 0.1M NHS and 0.4M EDC mixed in equal parts is injected into a chamber for 15 minutes where it will react with surface bound -COOH groups. If the surface is functionalized with -NH$_2$ groups, then the protein is activated using 0.1M NHS, 0.4M EDC mixture separately for 15 minutes.

After immobilization of proteins, a blocking step is required to deactivate remaining free NHS-ester groups. Blocking is done with a solution of a primary amine in alkaline pH e.g. 1M ethanolamine in pH 8.5 for 10 min.

2.5. Regeneration of protein layers

Regeneration of protein layers is the action of removing bound analytes from immobilized proteins or other ligands. To maintain integrity of immobilized protein, the regeneration has to be under as mild conditions as possible. A solution of 10 mM NaOH, 17.34 mM SDS was used to remove affinity bound antibodies.

2.6. Spectroscopic Ellipsometry

Ellipsometric measurements were performed using a J.A. Woollam M200X spectroscopic ellipsometer with a rotating compensator. Recorded

spectra were in the 200 - 1000 nm wavelength range. Recorded ellipsometric parameters: Δ - phase difference, Ψ - amplitude change; were used to determine optical properties of the substrates and protein molecules monolayers. Ellipsometric measurements were undertaken in few configurations: (i) standard reflection mode, (ii) total internal reflection mode, (iii) hybrid mode in combination with QCM-D.

Using the standard reflection mode, the samples were placed on a measurement table, the appropriate angle of incident light was set, and an ellipsometric spectra were recorded.

Total internal reflection ellipsometry (TIRE) mode was applied to study time-resolved proteins immobilization and affinity interaction with antibodies at the solid-liquid interface. Using TIRE, high sensitivity of spectroscopic ellipsometry is achieved in combination with the surface plasmon resonance (SPR) effect due to the ability to register two kinetic curves $\Psi(t)$ and $\Delta(t)$ simultaneously in contrary by only registering the light intensity in SPR based sensors. TIRE is able to detect biomolecules mass changes at solid-liquid interface with a better accuracy than that of SPR, which is achieved due to phase shift measurement [79]. Using TIRE, a 70° BK7 glass prism is attached to commercial SPR sensor disk by refractive index matching fluid and mounted on the measurement chamber. TIRE measurement mode is illustrated in Figure 6.
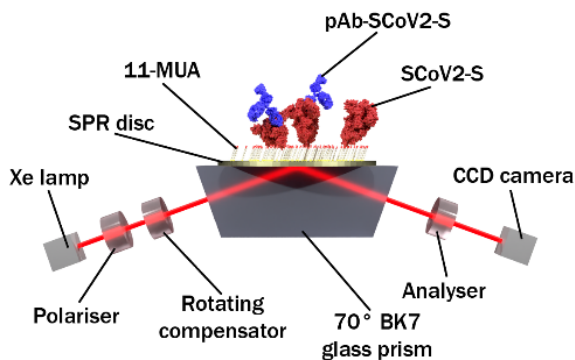
Figure 6. The principle scheme representing total internal reflection ellipsometry measurements [82].

Hybrid mode was conducted in a purpose built, temperature controlled, QCM-D spectroscopic ellipsometry module, to allow simultaneous QCM-D and SE measurements. The SE module has windows to allow the

incident/reflected light, fixing the angle of incidence to 65°. The measurements were conducted at 65° angle of incidence, at 20°C.

2.7. Quartz crystal microbalance with dissipation

QCM-D measurements were performed using Q-Sense Explorer, operating at fundamental frequency of 5 MHz with capability to record up to 6 overtones simultaneously and allowing viscoelastic modelling. All measurements were recording using proprietary software QSoft401 and analysed using proprietary software Dfind. Recorded parameters: ΔF - frequency change, and ΔD - layer dissipation; were used to calculate the amount of adsorbed biomaterial and if applicable determine the formed layer viscoelastic properties.

3. RESULTS AND DISCUSSION

The investigation of protein adsorption/desorption to/from various nanoporous materials is an important task since such materials may be used for protein separation, purification, and in the development of biosensors. The ability of large molecules such as proteins, particularly albumins to adsorb within nanopores is highly dependent on pore size and hydrophobicity/hydrophilicity. The findings of human serum albumin (HSA) adsorption/desorption to/from pAAO coating examined using SE are presenter further and provided in paper 1.

3.1. HSA adsorption to pAAO

Adsorption of HSA to pAAO was determined using the ellipsometric parameter Δ shift in the spectra and regression analysis. A shift in Δ values toward longer wavelengths indicates adsorption of HSA molecules, while a Δ shift toward shorter wavelengths indicates desorption of HSA molecules. Figure 7 shows the Δ parameter spectra from 300 nm to 370 nm wavelength, showing a distinct Δ peak.
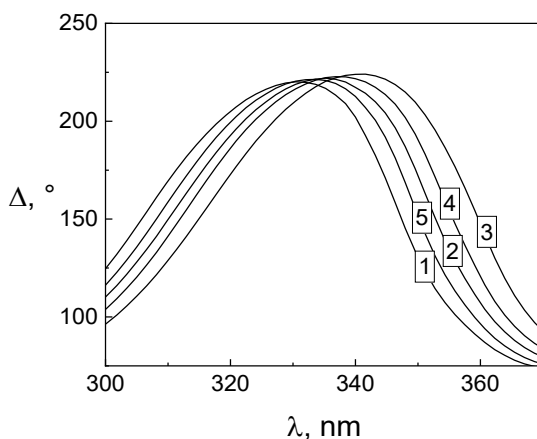
Figure 7. Ellipsometric parameter Δ *vs.* λ peak position at different time instances: (1) pAAO/air at $\lambda = 330$ nm; (2) pAAO/HSA(1 h incub.) at $\lambda = 335$ nm; (3) pAAO/HSA(2 h incub.) at $\lambda = 341$ nm; (4) pAAO/HSA(3 h incub. + 15 min wash) at $\lambda = 336$ nm; (5) pAAO after washing with deionised water at $\lambda = 333$ nm.

The curve 1 (Fig. 6, curve 1) was recorded for pAAO/air, with its peak at 330 nm. After 1 h of incubation in 1 mg/mL HSA solution, Δ shifts to 335 nm; and after 2 h of incubation, the peak shifts to 341 nm (Fig. 6, curves 2, 3).

After 3 h of incubation, washing in PBS for 15 min, resulted in a Δ shift to shorter wavelengths, with the peak observed at 336 nm, indicating desorption of HSA molecules (Fig. 6, curve 4). A 30-minute wash with deionized water showed greater desorption of HSA molecules from the pAAO surface, with the Δ peak observed at 333 nm (Fig. 6, curve 5). These results confirm that the has adsorption to pAAO is reversible. Moreover, the pAAO/HSA structure was more sensitive to deionized water, as more HSA molecules were removed, than by pH 7.4 0.01 M PBS.

To determine and quantify the adsorption of HSA molecules to the pAAO surface and pores, the changes in refractive index (n) were evaluated. Using the effective media approximation (EMA) optical model for the pAAO layer was constructed. The parameters of the pAAO structure were kept fixed (layer thickness, roughness, etc.), which were calculated by modelling the pAAO/air structure [4].

The changes in n due to adsorption/desorption of HSA were modelled using a Cauchy function and shown in Figure 8. Figure 8A shows the n of the pAAO layer, modelled with an EMA for: (1) pAAO in PBS, assuming all pores are filled with PBS; (2) pAAO after 1 h of HSA adsorption; (3) pAAO after 2 h of HSA adsorption; (4) pAAO after 3 h of HSA adsorption and 15 min of rinsing with PBS; (5) pAAO in air. Figure 8B shows n inside the nanopore channels of pAAO: (1) filled with PBS; (2) after 1 h of HSA incubation; (3) after 2 h of HSA incubation; (4) after 3h of HSA incubation and 15 min PBS wash.
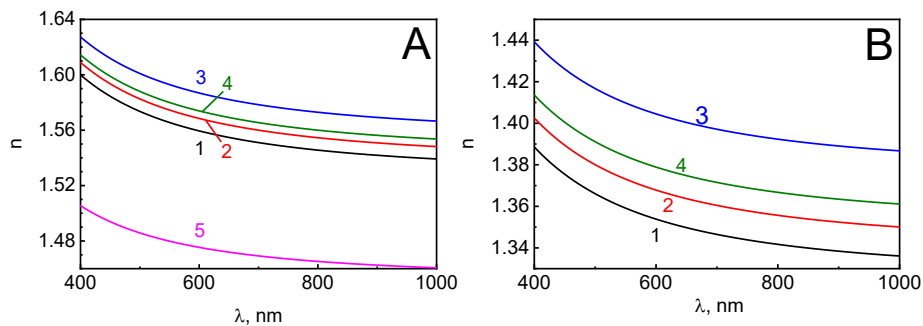
Figure 8. n dispersion of pAAO/X (A): (1) pAAO/PBS, (2) pAAO/HSA (1 h incub.), (3) pAAO/HSA (2 h incub.), (4) pAAO/HSA (3 h incub. + 15 min wash), and (5) pAAO/air; (B) n dispersion inside nanoporous layer filled with: (1) PBS, (2) HSA after one 1 h incubation, (3) HSA after 2 h incubation, and (4) HSA after 3 h incubation followed by 15 min wash.

Cauchy function is a widely used equation in ellipsometry for dielectric material n determination, that is also applicable for proteins (Eq. 1):

$$n(\lambda) = A + \frac{B}{\lambda^2} + \frac{C}{\lambda^4} \qquad (1)$$

Where A, B, C - Cauchy coefficients, λ - wavelength, $n(\lambda)$ - refractive index dependence on wavelength.

In the regression analysis, the parameters of the Cauchy function: A, B of HSA and the ratio of HSA and Al_2O_3 in the EMA-based optical model were free fitting parameters; this resulted in a dispersion of n for each evaluated structure (Fig. 8 A) and n within the nanoporous channels of pAAO (Fig.8 B).

To further illustrate the differences in n between the selected pAAO and HSA structures, the values at λ=600 nm were used for calculations and presented in Table 1.

Table 1. Values of refractive indices of pAAO layer and trapped HSA concentration calculated inside nanopores.

t_{ex}, h	0	1	2	3	0.25 washing	24 washing
n_{EMA}	1.486	1.5678	1.5865	1.5985	1.5733	1.5594
n_p	1 (void)	1.3679	1.4042	1.43	1.3788	1.3538
c_{HSA}	0	194	395	572	254	115

t_{ex} - pAAO substrate incubation time in 1 mg/mL HSA solution in PBS; n_{EMA} - pAAO effective refractive index, n_p - refractive index of HSA solution in pores; c_{HSA} - concentration of HSA in pores.

The determination of HSA concentration in nanopore channels follows a linear dependence between the n of the protein solution and the protein concentration. This was used to calculate HSA concentration (c_{HSA}) by transforming a mathematical expression for calculating the n of solutions with known concentration [120]:

$$c_{HSA} = (n_p - n_{PBS})/I_n \qquad (2)$$

Here, n_{PBS} - refractive index of PBS (1.333); I_n - refractive index increment for proteins (0.18 mL/g) [121].

The data presented in Table 1 show three important findings about the adsorption of HSA on pAAO coatings: (1) the protein concentration in the nanopore channels depends on the exposure time and is about 200 to 600 times higher than in the bulk solution; (2) HSA accumulation is a slow process (3.23 mg·cm^{-3}·min^{-1}), compared with HSA decrease (21.2 mg·cm^{-3}·min^{-1}); (3) washing with buffer solution does not provide sufficient desorption of HSA molecules.

3.2. Covalent immobilization of BSA to ZnO-NWs

The surface of ZnO-NWs is relevant for functionalization, providing an effective immobilization of biomolecules with appropriate loading capacity, high biological activity, and good stability. Because the diameters of ZnO nanostructures are near to the sizes of biological and chemical molecules, they can be effective transducers. The results in paper 2 highlight and explore the properties of ZnO-NWs for biosensing, via covalent BSA immobilization.

3.2.1. Comparison of ZnO and ZnO-NWs optical properties.

As mentioned earlier, the formation of ZnO-NWs on a substrate significantly increases the effective surface area. To analyse the contribution of the grown NWs to the optical response, compared to flat ZnO substrate, a simulation of a glass/ITO/ZnO multilayer system in TIR conditions was conducted. Simulated spectra of ellipsometric parameters of multilayer structures containing flat 350 nm ZnO layer were compared with experimentally obtained multilayer structures containing 350 nm ZnO-NWs. Detailed optical simulations ZnO/ITO/glass and the measured ZnO-NWs/ZnO/ITO/glass structures are published (Paper 2) [5]. The simulated data are shown in Figure 9A, while the experimentally obtained data are shown in Figure 9B.

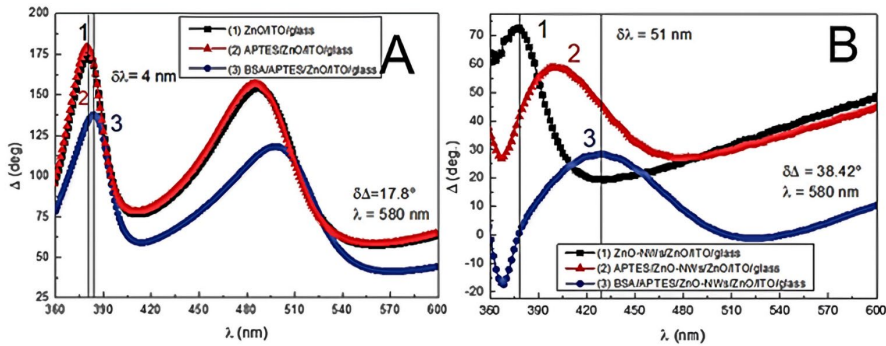Figure 9. Simulation of ellipsometric parameter *Δ* *vs* wavelength during flat ZnO modification. A) experimental curves of ellipsometric parameter *Δ* *vs* wavelength for (1) ZnO/ITO/glass, (2) APTES/ZnO/ITO/glass (3) BSA/APTES/ZnO/ITO/glass. B) experimental curves of ellipsometric parameter *Δ* *vs* wavelength for (1) ZnO-NWs/ZnO/ITO/glass, (2) APTES/ZnO-NWs/ZnO/ITO/glass and (3) BSA/APTES/ZnO-NWs/ZnO/ITO/glass.

Only the ellipsometric parameter Δ is presented in Figures 9 A and B because it has been shown to have higher sensitivity [122]. Figure 9A depicts the ellipsometric spectra obtained by simulations of the structures with a flat ZnO layer prior and after APTES and BSA modifications. Modification with APTES did not result in a significant difference in the simulated spectra, and the spectra of bare flat ZnO and APTES-modified ZnO overlapped. The simulated spectra after adding BSA show a small variation, with an observed red shift of 4 nm when the n change is $n_{BSA} - n_{ZnO} = 0.366$. As a result, the flat ZnO structure has a sensitivity of 11.9 nm per refractive index unit (RIU).

Figure 9B illustrates the experimentally acquired ellipsometric parameter Δ spectra of ZnO-NW/ZnO/ITO/glass structure under TIRE conditions before (1) after APTES modification (2) after covalent BSA bonding (3). The ellipsometric parameter $\Delta(\lambda)$ peak for unaltered ZnO-NWs/ZnO/ITO/glass substrate, is at 377 nm, with the ZnO-NW/ZnO/ITO/glass structure $n_{ZnO-NWs} = 1.355$ (at 580 nm), obtained using Bruggeman's effective media approximation (EMA). After modification with APTES, the $n_{APTES} = 1.521$ (at 580 nm), and a significant red shift was observed, as the $\Delta(\lambda)$ peak is located at 401 nm value. This results in a n difference of 0.166 per 23 nm. A further modification to the APTES/ZnO-NWs/ZnO/ITO/glass surface was covalent immobilization of BSA. A red shift of ellipsometric parameter Δ spectra was measured to be 28 nm for $n_{BSA} - n_{APTES} = 0.17$. This corresponds to a total change in n from the unmodified substrate to completed BSA covalent immobilization of $n_{BSA} - n_{ZnO-NWs} = 0.366$ and a shift of 51 nm in spectra. The calculated sensitivity of the BSA/APTES/ZnO-NWs/ZnO/ITO/glass structure was 151.8 nm per RIU. This shows the increased sensitivity of spectral shift to refractive index of structures with ZnO NWs by 13 times compared to structures with flat ZnO.

In addition to the Δ spectral sensitivity to n, the change in Δ amplitude was also determined. For flat ZnO/ITO/glass structure before and after APTES and BSA modification, the Δ amplitude change was 17.8°, which corresponds to 53° per RIU (Fig. 9A). For the structures containing ZnO-NWs (Fig. 9B), the Δ amplitude change for analogous modifications was 38.42°, corresponding to a sensitivity of 114.3° per RIU. The sensitivity of the structure was increased by 2.24 times, by using ZnO-NWs. The increase in sensitivity can be explained by two factors (i) from multiple reflections occurring in the ZnO-NW medium when the structure is in TIR mode, (ii) from a significant increase in covalently immobilized BSA molecules due to the larger surface area.

Modification of surfaces with nanowires can lead to light scattering, for this reason, reflectance intensity spectra (R) were recorded to compare the flat ZnO and ZnO-NWs samples and are displayed in Figure 10.
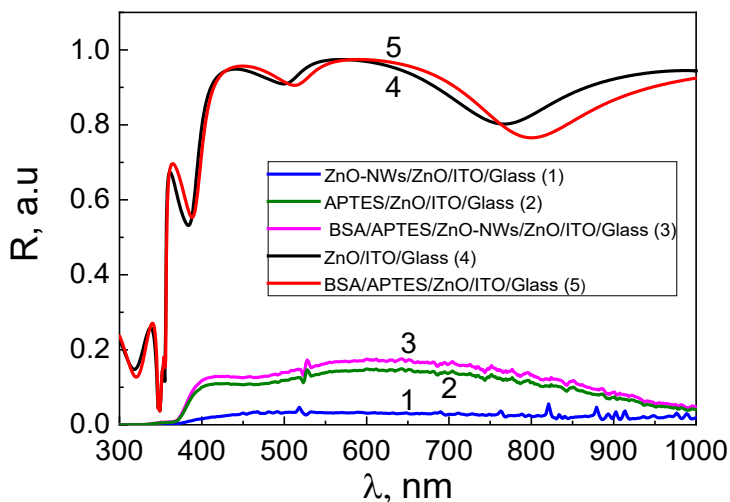
Figure 10. Reflectance intensity (R) spectra of 1 - ZnO-NWs/ZnO/ITO/glass, 2 - APTES/ZnO-NWs/ZnO/ITO/glass, 3 - BSA/APTES/ZnO-NWs/ZnO/ITO/glass, 4 - ZnO/ITO/glass, 5 - BSA/APTES/ZnO/ITO/glass.

The R spectra of the structures with flat ZnO before (Fig. 10, curve 4) and after covalent immobilization of BSA (Fig. 10, curve 5) have values from 0.8 to 1 in the wavelength range from 400 nm to 1000 nm. This indicates that almost all of the incident light is reflected from the sample surface, with no significant difference between the R spectra. The measurement of the change in reflectance difference was only 0.021 a. u. at 650 nm. The R spectra for ZnO-NWs structures before (Fig. 10, curve 1), after APTES (Fig. 10, curve 2), and after BSA modification (Fig. 10, curve 3) show low R values in the range of 0 - 0.2 due to the strong light scattering. However, this scattering effect does not affect the quality of the ellipsometric spectra, due to the relative value measurements of ellipsometric parameters. Although the R values for ZnO-NWs substrates are low, the increase during the experiment is clear (Fig. 10, curves 1, 3). For the ZnO-NWs/ZnO/ITO/glass substrate, the R value at 650 nm was 0.03 a. u., however by the end of covalent BSA immobilization the R value was 0.17 a.u., which increased by 0.14 a. u., and about 6.6 times higher when compared to flat ZnO structure.

This can be explained by a decrease in diffuse scattering due to the immobilization of BSA molecules. A surface of ZnO-NWs becomes more "smoother" when more BSA molecules are immobilized, which increases the reflectance while the overall n of the layer increases. Moreover, due to the

relative values of the Δ and Ψ parameters, stable ellipsometric measurements can be performed at low light intensity.

3.2.2. Kinetics of BSA covalent immobilization

The kinetics of covalent BSA immobilization was investigated using TIRE at wavelength of 390.8 nm, since this is the point in the spectra most sensitive to changes in the n for the ellipsometric parameter Δ. The kinetics of the ellipsometric parameter Δ for BSA immobilization is shown in Figure 11.
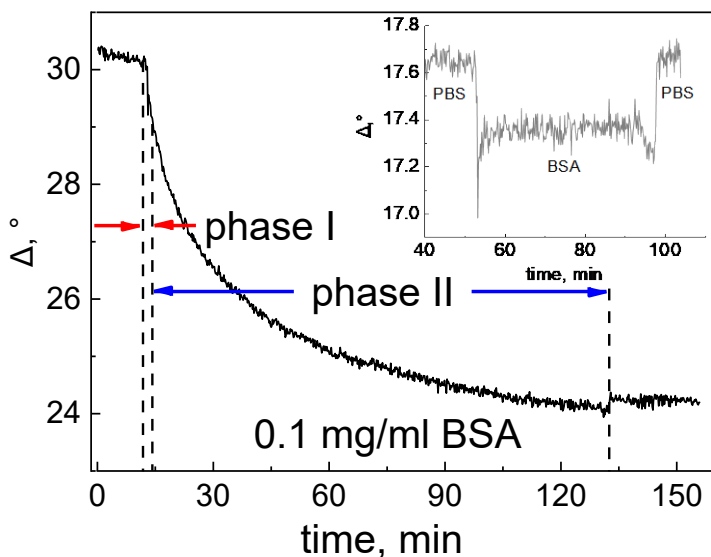
Figure 11. Kinetics of BSA covalent immobilization on the APTES/ZnO-NWs/ZnO/ITO/glass substrate; kinetics of BSA covalent immobilization on APTES/ZnO/ITO/glass substrate (inset).

After injection of a 0.1 mg/mL BSA solution immobilization kinetics was recorded for 121 minutes. The total change in the ellipsometric parameter Δ was 6.11°. The kinetics of covalent BSA immobilization on ZnO-NWs can be divided into two phases. Phase I takes place in a short time frame of about 5 s, in which the total change in Δ is 0.5°. In phase II, most of the injected BSA is immobilized on the APTES/ZnO-NWs/ZnO/ITO/glass substrate; this phase lasts more than 100 min. and the change in Δ is 5.61°. Non-specifically bound molecules were removed by washing with PBS, registering a Δ change of only 0.17°. This confirms, that the non-specific binding of BSA was negligible and the formed BSA layer is stable under the washing conditions.

Inset in Figure 11 shows the BSA immobilization on flat type ZnO. It can be seen that Δ parameter change coincides with that of the phase I for ZnO-NWs, confirming that this phase is the result of BSA immobilization at the top of ZnO-NWs.

Successful covalent immobilization of BSA molecules demonstrate the possible application of ZnO-NWs for optical biosensor development. In contrast to the simulated flat-type ZnO layer, the ZnO-NWs can accumulate considerably more BSA molecules. TIRE technique demonstrated that substrates with ZnO-NWs outperform flat-type ZnO substrates for spectral sensitivity to n shift by 13 times. Furthermore, the substrates with ZnO-NWs exhibited greater changes to ellipsometric parameters Ψ and Δ during covalent immobilization of BSA, confirming TIRE method's high sensitivity when measuring protein interactions.

3.2.3. Diffusion of BSA molecules into ZnO-NWs

As seen in Figure 11, BSA covalent immobilization has a phase II in which an irreversible, time dependent process is occurring over 100 min. time period. This prolonged duration is assumed to be due to diffusion of BSA in PBS through nanochannels that exist between ZnO-NWs. To verify and quantify the diffusion of BSA into ZnO-NWs structure, modelling of ellipsometric parameter Δ was conducted.

Figure 12 shows the normalized ellipsometric parameter Δ change vs time in TIRE mode. Δ parameter in this case is proportional to the effective refractive index of the whole measured structure of APTES/ZnO-NWs structures on ZnO/BK7 and BSA molecules in PBS. During the covalent immobilization of BSA, the diffusion of BSA molecules into nanochannels between ZnO-NWs induces the refractive index change, thus the Δ parameter change.
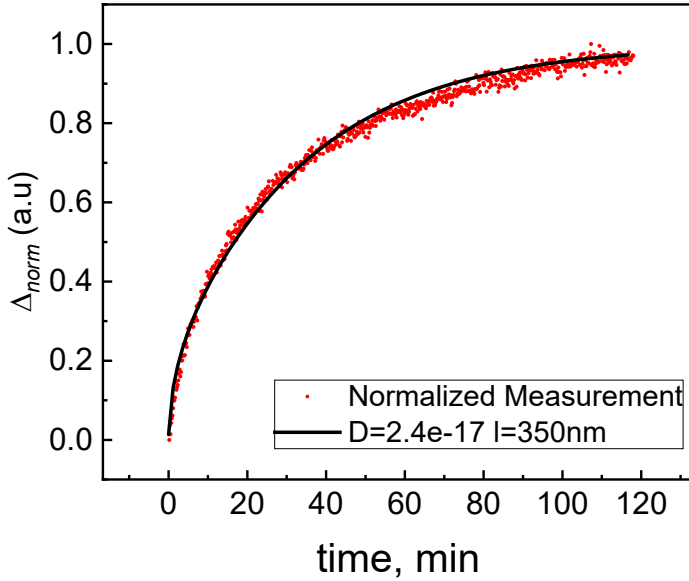
Figure 12. Dependence of the normalized signal Δ_{norm} of ellipsometric parameter vs time during BSA covalent immobilization on APTES/ZnO-NWs/ZnO/ITO/glass substrate.

Considering that the refractive index of the solution depends on the concentration of BSA molecules, we assume a direct proportionality between Δ and C.

A one-dimensional diffusion equation can be used to numerically solve the distribution of BSA molecule concentration in a channel between ZnO-NWs as a function of time:

$$D \frac{\partial^2 C(x,t)}{\partial x^2} = \frac{\partial C(x,t)}{\partial t} \qquad (3)$$

Here $C(x, t)$ is concentration of BSA molecules, x is the position along the nanowire, t is time, and D is a diffusion coefficient. The following boundary conditions for this equation are $C(0,0) = C(d,\infty) = C_0$ that is the concentration of BSA in PBS outside the nanowires matrix and $\partial C(d,t)/\partial t = 0$, where d is the length of channel filled exclusively with PBS.

The average concentration of BSA inside the channel (C_a) is:

$$C_a(t) = \frac{\int_0^d C(x,t)dx}{d} \qquad (4)$$

The numerical calculation results are presented as a black curve in Figure 12, and the D was calculated to be $2.4 \cdot 10^{-17}$ m^2/s, 6 orders of magnitude lower

38

than BSA diffusion in PBS. This suggests that the diffusion plays a significant role in BSA immobilization on APTES functionalized ZnO-NWs substrate.

3.3. Specific antibody interaction with SCoV2-S, -αS, and -βS

One of the key factors in preventing the spread of coronavirus disease 2019 (COVID-19), is the ability of the human immune system to produce neutralizing antibodies that could successfully block the SARS-CoV-2 spike (S) protein (in specific regions) and prevent its binding to the angiotensin-converting enzyme 2 (ACE2) receptor. However, the mutations in SARS-CoV-2 RBD part over time, are associated with viral survival capability, the rate of virus spread, and the severity of the disease. The results presented in paper 3 were obtained performing a highly sensitive, label-free, and real-time TIRE monitoring of the interaction kinetics between the specific polyclonal human antibody (pAb-SCoV2-S) produced after vaccination and the covalently immobilized spike proteins of the three SARS-CoV-2 variants of concern.

TIRE method was used for the investigation of real-time SCoV2-S, SCoV2-αS, and SCoV2-βS covalent immobilization on 11-MUA modified gold surface and immune complex formation with human blood serum containing polyclonal antibodies (pAb-SCoV2-S). Diluted convalescent serum samples were prepared from 1 dose Vaxzevria vaccinated volunteer blood serum. A Schematic representation of the experiment is presented in Figure 13.
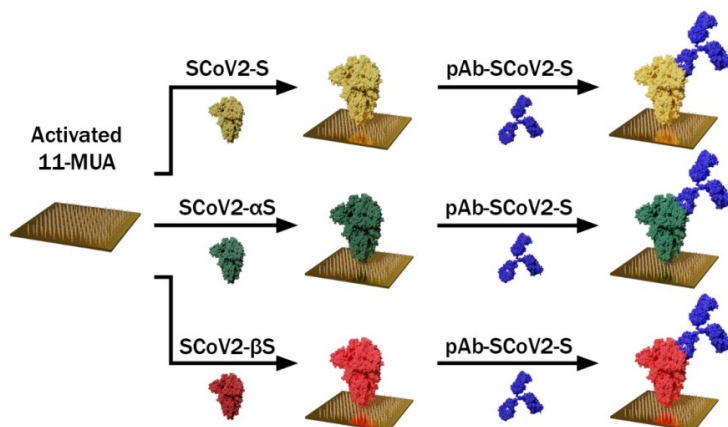
Figure 13. Schematic representation of SCoV2-S, SCoV2-αS, and SCoV2-βS covalent immobilization and interaction with pAb-SCoV2-S.

The 333 nM solutions in PBS of SCoV2-S, SCoV2-αS, and SCoV2-βS were injected into the TIRE measurement chamber for 55-60 minutes and then washed with PBS. After each step of surface modification, spectra of ellipsometric parameters Ψ, Δ vs. λ were recorded and compared. Figure 14A demonstrates the immobilization kinetics of SCoV2-S, and the interaction with diluted blood serum samples. Assessment of affinity interaction between immobilized SCoV2-S and pAb-SCoV2-S, was performed by injecting diluted blood serum samples at 1:4, 1:10, 1:20, 1:30, and 1:40 ratios (Fig. 14B). The spectral shifts of Δ and Ψ are presented in Figure 14C, D, respectively.
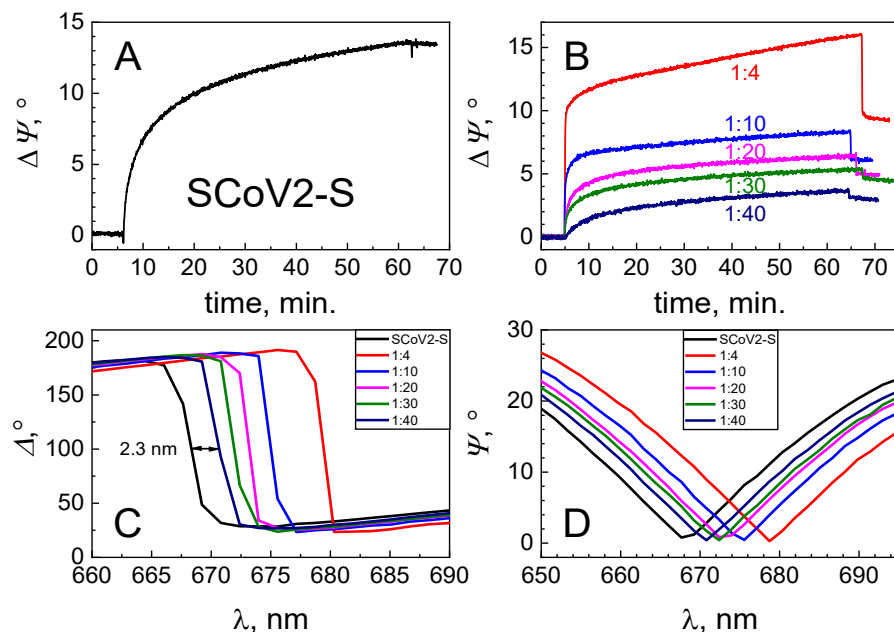
Figure 14. Time-resolved TIRE kinetics and ellipsometric parameters of SCoV2-S immobilization and interaction with specific polyclonal antibodies. (A) Kinetics of covalent SCoV2-S immobilization on 11-MUA SAM modified gold-coated SPR sensor disc; (B) kinetics of polyclonal antibody interaction with covalently immobilized SCoV2-S at different serum dilutions (1:4, 1:10, 1:20, 1:30, and 1:40); (C) Δ and (D) Ψ spectral shift after immune complex formation using the same dilutions of polyclonal antibodies.

The change in Ψ after 65 min for SCoV2-S covalent immobilization was 13.5°. For analogous covalent immobilization of SCoV2-αS and SCoV2-βS, the changes were 14.0° and 11.0°, respectively.

The spectral shift of the ellipsometric parameters Δ and Ψ, resulting from the formation of pAb-SCoV2-S/SCoV-2 immune complex, using 1:40 diluted blood serum was 2.3 nm (Fig. 14 C, D). After immune complex formation between immobilized SCoV2-S, SCoV2-αS, SCoV2-βS and pAb-SCoV2-S, the chamber was washed with PBS. The change in Ψ of 2.01° and 4.96° was registered for SCoV2-αS, SCoV2-βS interaction with pAb-SCoV2-S, respectively. The spectral shifts of Δ and Ψ due to immune complex formation were 3.1 nm (SCoV2-αS), 4.7 nm (SCoV2-βS).

To evaluate the nonspecific interaction, a control experiment was performed with the blood serum collected before COVID-19 pandemic. The blood serum solution diluted 1:40 was injected into the chamber. After 60 minutes, the interaction signal change $\Delta\Psi = 2.5°$ was recorded for nonspecific interaction. When plotting the specific interaction between pAb-SCoV2-S and SCoV2-S, the signal change for the nonspecific interaction was eliminated (Fig. 14 B). When examining the interaction between pAb-SCoV2-S and immobilised SCoV2-αS and SCoV2-βS, nonspecific interaction was also taken into consideration.

3.3.1. Thermodynamic properties of immune complex formation between SCoV2-S, SCoV2-αS, SCoV2-βS and pAb-SCoV2-S

The immune complexes formation between SCoV2-S, SCoV2-αS, SCoV2-βS and pAb-SCoV2-S were analysed using two-step irreversible binding kinetics modelling [79,116,123]. The fitting of the experimentally obtained kinetics, normalized surface concentration, allowed the calculation of association and dissociation rate constants (k_a, k_d), rate constant for the formation of a stable immune complex (k_r), equilibrium association and dissociation constants (K_A, K_D) and steric factors (P_S). The fitting results using two step irreversible binding mathematical model presented Figure 15.
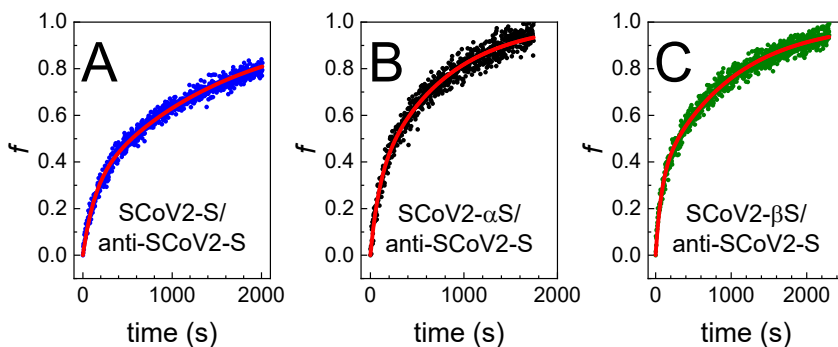
Figure 15. Normalized pAb-SCoV2-S antibody surface concentration (f) evolution in time obtained using 1:40 diluted blood serum during the formation of the immune complex with (A) SCoV2-S, (B) SCoV2-αS, (C) SCoV2-βS. Points correspond to experimentally obtained results, while lines for fitting are derived by using two-step irreversible binding immune complex formation mathematical modelling.

Fitting the kinetics of immune complex formation and the calculating the thermodynamic parameters of such an interaction may provide a deeper understanding of specific pAb-SCoV2-S antibody from human blood serum interaction with SCoV2-S, SCoV2-αS and SCoV2-βS. Thermodynamic parameters are shown in Table 2.

Table 2. Thermodynamic properties of specific antibody interaction with variants of concern.

	SCoV2-S	SCoV2-αS	SCoV2-βS
k_a (M^{-1} s^{-1}) $\cdot$ 10^6	3.19	5.01	5.92
k_d (s^{-1}) $\cdot$ 10^{-6}	10.3	19.7	3.27
K_A (M^{-1}) $\cdot$ 10^{12}	30.9	25.4	18.1
K_D (M) $\cdot$ 10^{-9}	0.322	0.393	0.547
k_r (s^{-1}) $\cdot$ 10^{-6}	5.05	14.8	13.3
P_s (%)	1.51	1.88	2.01

Association rate constant (k_a), dissociation rate constant (k_d), rate constant for the formation of a stable immune complex (k_r), equilibrium association constant (K_A), equilibrium dissociation constant (K_D), and steric factor (P_S).

The pAb-SCoV2-S antibodies to the target SCoV2-S have the lowest K_D values (0.322 $\cdot$ 10^{-9} M). The values are in the same 10^{-9} range, for SCoV2-S

and for variants SCoV2-αS and SCoV2-βS indicating that the vaccines can successfully protect against SARS-CoV-2 and its' mutations.

The steric factor P_S was calculated for all immune complexes: SCoV2-S/pAb-SCoV2-S, SCoV2-αS/pAb-SCoV2-S, and SCoV2-βS/pAb-SCoV2-S. P_S is a percentage value for the probability of a successful interaction between an antigen and a specific antibody resulting in a stable complex and can be calculated using encounter theory [124,125]. Immune complexes with SCoV2-S and its' variants have similar steric factor values; 1.51 for SCoV2-S, 1.88 (24% increase) for SCoV2-αS, and 2.01 (33% increase) for SCoV2-βS. However, when compared to the immune complex with SCoV2-N protein, the SCoV2-S protein immune complex has 100-fold lower requirements [79]. The lower requirements are mainly due to the size difference, with smaller antigens ($M_{SCoV2-N}$=49 kDa) requiring stricter alignment of antibodies for stable immune complex formation, than larger antigens ($M_{SCoV2-S}$=432 kDa).

As a consequence of amino acid substitutions in the S protein, 6 for SCoV2-αS and additional 5 for SCoV2-βS. The thermodynamic properties of pAb-SCoV2-S interaction with SCoV2-S, SCoV2-αS, and SCoV2-βS are in the same range and are comparable. This demonstrates the high sensitivity of TIRE measurements and ability to evaluate differences in SCoV2-S, SCoV2-αS, and SCoV2-βS interaction kinetics with specific antibodies.

3.4. SE/QCM-D monitored SCoV2-N and specific antibody affinity interaction analysis

Another object that was investigated in the present thesis was immune complex formation between covalently immobilized SCoV2-N protein and specific polyclonal antibodies. The hinge-mediated flexibility of the specific antibody Fab fragments during immune complex formation and conformational changes was investigated using hybrid SE/QCM-D technique and are presented in paper 4.

3.4.1 Viscoelastic properties of SCoV2-N and anti-SCoV2-N monolayers

Optical and acoustic methods were combined for the investigation of SCoV2-N covalent immobilization on sensing surface and immune complex formation with specific antibodies. The SE/QCM-D hybrid measurement setup was used. In this combined method SE provides information on the dielectric properties of the formed SCoV2-N and specific antibody monolayers and QCM-D provides information on the mechanical (viscoelastic) properties of the monolayers.

Optical and acoustic signal monitoring covered three different steps of the experiment: (i) covalent immobilization of SCoV2-N, (ii) affinity interaction of anti-SCoV2-N with immobilized SCoV2-N, (iii) nonspecific interaction of anti-BSA with immobilized SCoV2-N. A schematic representation of the formation of the SCoV2-N/anti-SCoV2-N immune complex is displayed in Figure 16.

$$[\text{SCoV2-N}]+[\text{anti-SCoV2-N}] \underset{k_d}{\overset{k_a}{\rightleftharpoons}} [\text{SCoV2-N/anti-SCoV2-N}]^* \overset{k_r}{\longrightarrow} [\text{SCoV2-N/anti-SCoV2-N}]$$
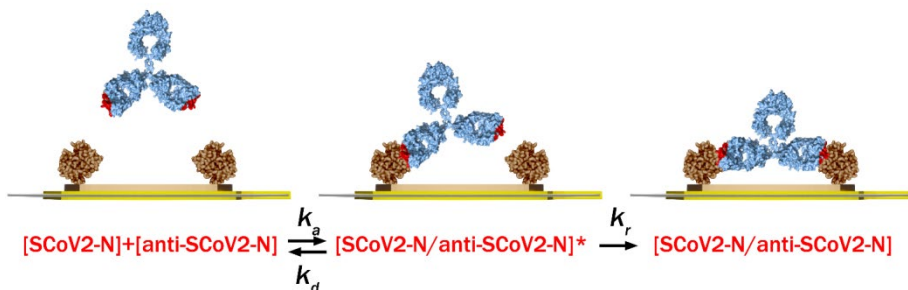
Figure 16. Schematic representation of the anti-SCoV2-N interaction with covalently immobilized SCoV2-N. The formation of the immune complex takes two steps.

Both SE and the QCM-D method are sensitive to changes in surface mass density, either during covalent immobilization or during a immune complex formation [7].

To illustrate the monolayer formation and viscoelasticity of SCoV2-N and anti-SCoV2-N layers, $\Delta D/\Delta F$ plots are obtained from QCM-D data by plotting ΔF (frequency change representing a change in the mass on the QCM-D sensor) on the x-axis and ΔD (energy dissipation representing the viscoelastic properties of the formed layer). Figure 17 shows the $\Delta D/\Delta F$ plots for the covalent immobilization of SCoV2-N and the subsequent affinity interaction with anti-SCoV2-N, illustrating the different viscoelastic properties of the protein layers.
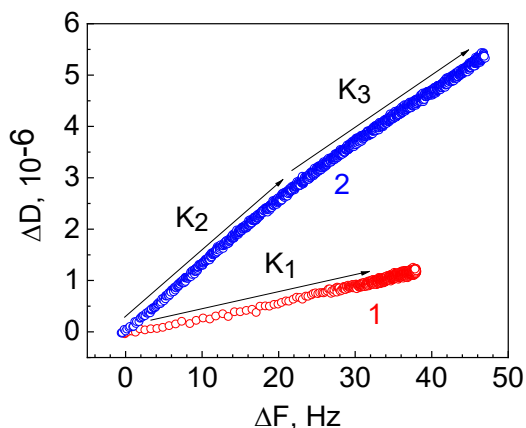
Figure 17. $\Delta D/\Delta F$ plots for: SCoV2-N covalent immobilization on 11-MUA SAM (curve 1), and affinity interaction with anti-SCoV2-N (curve 2). The arrows K_1, K_2, and K_3 indicate the slopes to curves 1 and 2.

Covalent immobilization of SCoV2-N on 11-MUA resulted in a linear increase of ΔD and ΔF (Fig. 17, curve 1). Although, time was eliminated as a parameter, it can be inferred. Point density indicates fast initial immobilization kinetics from 0 Hz to 25 Hz, followed by slower immobilization from 25 Hz to 38 Hz. The slope K_1 calculated for the covalent immobilization of SCoV2-N was equal to 0.031. A small value of K_1 indicates a rigid monolayer, so the Sauerbrey equation can be accurately applied [126].

$$\Delta m = C \cdot \frac{\Delta f_n}{n} \qquad (3)$$

Here C = 17.7 ng/Hz·cm², Δf - frequency change at the nth overtone, n - overtone number.

Similarly, the formation of the SCoV2-N/anti-SCoV2-N immune complex resulted in an increase in to ΔD (Fig. 17, curve 2), with the difference to SCoV2-N being the higher ΔD values, indicating that the formation of the immune complex creates a layer of viscoelastic anti-SCoV2-N molecules. The increase in ΔD was gradual from the beginning, with a slight change in slope at 22 Hz. Thus, the immune complex formation was characterized by two tangents - K_2 and K_3. In Figure 17, curve 2 the small variation in slope can be explained by a change in the interaction between SCoV2-N and anti-SCoV2-N, which was due to conformational changes and rearrangements during the formation of the immune complex. The slope values of K_2 and K_3 are, 0.134 and 0.121, respectively, which are close to the values obtained by other authors for an analogous interaction between cysteine peptidase and specific

antibodies [127]. Moreover, the $\Delta D/\Delta F$ plot for the formation of the SCoV2-N/anti-SCoV2-N immune complex shows its relatively slow formation rate, as the point density in the curve is distributed densely from beginning to end.

3.4.2. "Wet" and "dry" surface mass densities of SCoV2-N and anti-SCoV2-N monolayers

To evaluate the covalent immobilization of SCoV2-N and the formation of the SCoV2-N/anti-SCoV2-N immune complex by specific antibody interaction, surface mass density of the protein monolayer was calculated. Depending on the chosen measurement (SE or QCM-D), the values of surface mass density differ. SE can only measure the change in surface mass due to the change in the amount of surface-bound protein molecules and is therefore referred to as "dry surface mass". In contrast, the QCM-D is sensitive to changes of mass from protein molecules and captured aqueous solution, thus referred to as "wet surface mass".

For SE, the experimentally obtained ellipsometric parameters Ψ and Δ were modelled by designing an optical model to calculate SCoV2-N and anti-SCoV2-N n and thickness (d). The monolayer of SCoV2-N was described using the Bruggeman effective media approach (EMA), the details of which are published (Paper 4) [7]. Briefly, the SCoV2-N layer was composed of 66% PBS ($n = 1.333$) and 34% SCoV2-N ($n = 1.610$). In the regression analysis, the EMA value was a free fitting parameter, while the d was fixed at $d_{SCoV2-N}$ = 5.9 nm. Then, $d_{SCoV2-N}$ evolution in time was modelled by fixing the n values of fully formed layers, as shown in Figure 18 A. Analysis of the formation of anti-SCoV2-N layers was performed analogously using Bruggeman EMA. The anti-SCoV2-N monolayer consisted of 81% PBS and 19% anti-SCoV2-N. The thickness value $d_{anti-SCoV2-N}$ = 8.1 nm was determined by regression analysis (Fig. 18 B) and is a feasible value based on the dimensions of IgG class antibodies, when antibodies are bivalently bound to antigens about 13.7 nm apart [128].
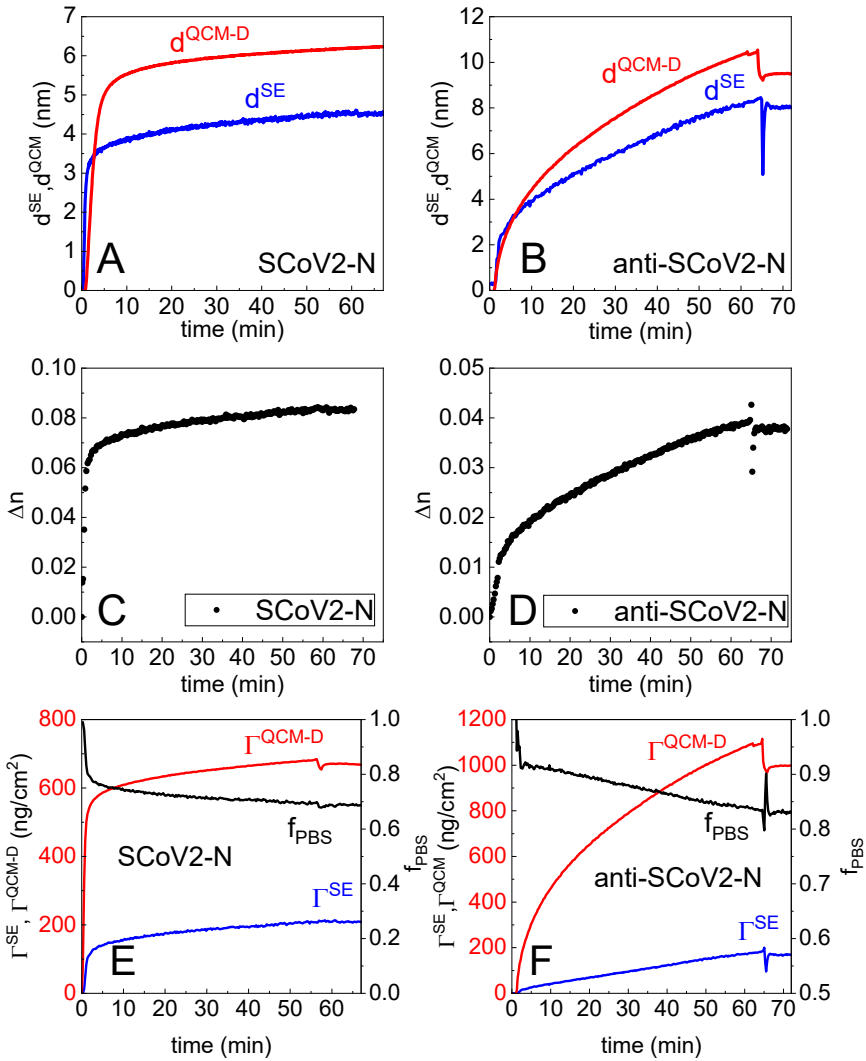
Figure 18. Evolution of the formation of SCoV2-N and anti-SCoV2-N monolayers in time dry (d^{SE}) and wet (d^{QCM-D}) monolayer thickness versus time for SCoV2-N (A) and anti-SCoV2-N (B), change of n versus time for SCoV2-N (C) and anti-SCoV2-N (D), and dry (Γ^{SE}) and wet (Γ^{QCM-D}) surface mass density for SCoV2-N (E) anti-SCoV2-N (F).

Figure 18 C, D shows the change in n for SCoV2-N and anti-SCoV2-N, respectively. After 70 min of SCoV2-N monolayer formation, the $\Delta n_{SCoV2-N} = 0.08$, and for anti-SCoV2-N $\Delta n_{anti-SCoV2-N} = 0.38$. Calculation of monolayer d and n change allowed the evaluation of the dry surface mass density of SCoV2-N and anti-SCoV2-N, shown in Figure 18 E, F. The calculated dry

mass Γ^{SE} after 70 minutes; for SCoV2-N was 200 ng/cm^2 and anti-SCoV2-N was 167 ng/cm^2.

The surface mass density of layers, that exhibit high ΔD values, can be inaccurately determined when applying the Sauerbrey equation. Thus, viscoelastic modelling is used for the calculations, when the dissipation is high. Figure 18 E, shows the Γ^{QCM-D} wet surface mass density for SCoV2-N, a rigid layer, as previously analysed (Fig. 17 curve 1). Surface mass density of SCoV2-N was calculated with Sauerbrey equation, $\Gamma^{QCM-D} = 672$ ng/cm^2. After specific antibody interaction with SCoV2-N, the anti-SCoV2-N monolayer formed a viscous layer (Fig. 17 curve 2). Therefore, the wet surface mass calculations included Voinova-Voigt viscoelastic modelling [129,130]. Wet surface mass of anti-SCoV2-N was, $\Gamma^{QCM-D} = 995$ ng/cm^2. QCM-D determined layer thicknesses of SCoV2-N and anti-SCoV2-N monolayers were 6.24 nm and 9.55 nm, presented in Figure 18 A, B respectively.

The resulting difference between wet and dry surface mass ($\Gamma^{QCM-D} > \Gamma^{SE}$) allows the calculation of hydration (f_{PBS}), it is presented in Figure 18 E, f_{PBS} illustrating the amount of PBS solution trapped in monolayers of SCoV2-N and anti-SCoV2-N. f_{PBS} was calculated using the following formula:

$$f_{PBS} = 1 - \frac{\Gamma^{SE}}{\Gamma^{QCM-D}} \qquad (4)$$

Here Γ^{SE} - dry surface mass density; Γ^{QCM-D} - wet surface mass density. The obtained hydration values of 0.7 for SCoV2-N monolayer and 0.83 anti-SCoV2-N monolayer were in good agreement with EMA% values obtained from SE modelling, where the amount of PBS solution was 66% and 81%, respectively.

To interpret hydration values beyond the amount of PBS inside protein monolayer a geometric model was created, shown in Figure 19. Assuming that SCoV2-N molecules formed a monolayer in a square shape lattice, from obtained hydration values it is possible to estimate minimal average distance between immobilized SCoV2-N antigens, referred to as lattice constant d_l. In a square lattice d_l is calculated as such:

$$d_l = r \cdot \sqrt{\frac{2\pi}{3 f_{PBS}}} \qquad (5)$$

Here, r - radius of ball-shaped SCoV2-N molecule, f_{PBS} - hydration of SCoV2-N monolayer. In the case, of this SCoV2-N monolayer where $r = 3$ nm and $f_{PBS} = 0.3$; the calculated d_l was about 7.9 nm. Another important lattice parameter of such geometric model is the diagonal distance (d_d), obtained by multiplying the lattice constant by $2^{1/2}$: $d_d = d_l \cdot 2^{1/2} = 11.2$ nm.

Thus, based on this geometric model, there are two ways for anti-SCoV2-N molecules to bind to immobilized SCoV2-N antigens. In this case, anti-SCoV2-N molecules favour binding to SCoV2-N over d_d, because of measured layer thicknesses (Fig. 18 B) suggest that flexible anti-SCoV2-N molecules are present in T shape (Fig. 16).
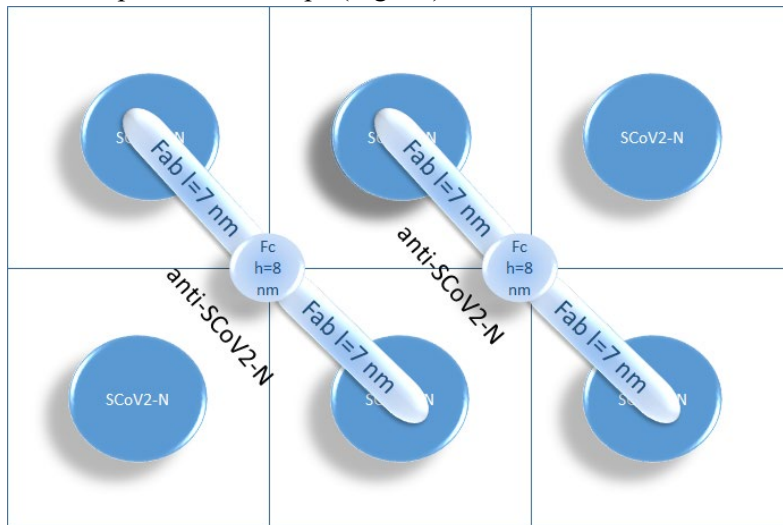
Figure 19. Schematic representation (the relative sizes of SCoV2-N and anti-SCoV2-N are not in scale) of the displacement of SCoV2-N approximated by a square lattice. The lattice constant is the average distance between SCoV2-N molecules of the real monolayer.

A single lattice unit consisted of a centred SCoV2-N antigen and half of an anti-SCoV2-N antibody. The volume of a single lattice unit was $V_l=874$ nm³ (7.9 nm x 7.9 nm x 14 nm), and the height of a single lattice unit is the sum of thicknesses of SCoV2-N (6 nm) and anti-SCoV2-N (8 nm) monolayers. Considering the known dimensions of SCoV2-N and anti-SCoV2-N, and assuming that both proteins have the same density, the volume occupied by the proteins (one SCoV2-N and half anti-SCoV2-N) in a single lattice unit was $V_{pr}=434$ nm³. Therefore, theoretical hydration of the anti-SCoV2-N/SCoV2-N immune complex is about 0.5, which is close to a sum of hydration values for SCoV2-N and anti-SCoV2-N monolayers of 0.47 (Fig. 18 E, F).

CONCLUSIONS OF THE THESIS

The relationship between 1D and 2D nanostructures such as porous anodic aluminium oxide, zinc oxide nanowires, and thin gold films lies in their significance as substrates for biosensor platforms. Each material comes with unique properties that can be used in optical biosensor devices to enhance sensitivity, specificity, stability, and overall performance in detecting target biomolecules. An intriguing prospect for each of the analysed materials is the combined usage in biosensing.

1. The determined HSA concentration in the nanopores varied with incubation time and higher trapped HSA amount was after longer incubation. Conventional washing with PBS solution does not fully wash away all the HSA molecules from pAAO pores and even after rinsing with deionised water lasting 16 h, HSA concentration inside nanopores still remains approximately 100 times higher. HSA concentration inside nanopores of pAAO was from 200 to 600 times that of the surrounding bulk solution, suggesting that HSA can be used for surface blocking. Hence, pores of pAAO operate as "traps" for HSA proteins, cumulating molecules of this material. However, HSA should be carefully used for the blocking of the remaining free surface of signal transducers based on pAAO when significant reduction in non-specific binding is expected.

2. Comparison of flat ZnO and ZnO-NWs optical properties demonstrated that the application of ZnO-NWs for biosensing enhanced optical sensitivity in TIRE mode for 13 times to changes in refractive index and 6.6 times to changes in reflective intensity. The increase in sensitivity can be attributed to multiple reflections between ZnO-NWs medium in TIRE mode, as well as increased surface area for covalent immobilization of BSA. This highlights the potential of ZnO-NWs based optical biosensor application.

3. Specific antibodies obtained from a vaccinated volunteers blood serum formed high affinity immune complexes with SCoV2-S, SCoV2-αS and SCoV2-βS. Thermodynamic properties of the immune complex formation were obtained using two-step irreversible binding kinetic model. It is evident from immune complex formation K_D values that an increase in amino acid substitutions in RBD region decreases the affinity to specific antibodies. However, antibodies developed after vaccination are able to bind with all three S proteins variants of concern with high affinity. This investigation could become of use in the development of effective immunosensors for COVID-19.

4. The SCoV2-N monolayer formed on the solid–liquid interface as a result of covalent immobilization can be described as a rigid due to low energy

dissipation registered during QCM-D measurement. In contrary, anti-SCoV2-N monolayer after the interaction with the covalently immobilized SCoV2-N formed a soft, flexible, and viscous layer with 3.9 times higher energy dissipation. The calculated hydration values of total protein layer was 0.5 and experimentally obtained value was 0.47. Moreover, it was obtained that flexibility of the antibody Fab arms allows them to reach the more distantly located SCoV2-N and to establish a bivalent interaction between proteins in formed SCoV2-N/anti-SCoV2-N complex.

REFERENCES

1. Balevicius, Z.; Paulauskas, A.; Plikusiene, I.; Mikoliunaite, L.; Bechelany, M.; Popov, A.; Ramanavicius, A.; Ramanaviciene, A. Towards the application of Al2O3/ZnO nanolaminates in immunosensors: total internal reflection spectroscopic ellipsometry based evaluation of BSA immobilization. *J. Mater. Chem. C* **2018**, *6*, 8778–8783, doi:10.1039/c8tc03091j.

2. Filipovic, L.; Selberherr, S. Application of Two-Dimensional Materials towards CMOS-Integrated Gas Sensors. *Nanomaterials* **2022**, *12*, 3651, doi:10.3390/nano12203651.

3. Tyagi, D.; Wang, H.; Huang, W.; Hu, L.; Tang, Y.; Guo, Z.; Ouyang, Z.; Zhang, H. Recent advances in two-dimensional-material-based sensing technology toward health and environmental monitoring applications. *Nanoscale* **2020**, *12*, 3535–3559, doi:10.1039/c9nr10178k.

4. Maciulis, V.; Malinovskis, U.; Erts, D.; Ramanavicius, A.; Ramanaviciene, A.; Balevicius, S.; Juciute, S.; Plikusiene, I. Porous aluminium oxide coating for the development of spectroscopic ellipsometry based biosensor: Evaluation of human serum albumin adsorption. *Coatings* **2020**, *10*, 1–10, doi:10.3390/coatings10111018.

5. Plikusiene, I.; Maciulis, V.; Graniel, O.; Bechelany, M.; Balevicius, S.; Vertelis, V.; Balevicius, Z.; Popov, A.; Ramanavicius, A.; Ramanaviciene, A. Total internal reflection ellipsometry for kinetics-based assessment of bovine serum albumin immobilization on ZnO nanowires. *J. Mater. Chem. C* **2021**, *9*, 1345–1352, doi:10.1039/d0tc05193d.

6. Plikusiene, I.; Balevicius, Z.; Ramanaviciene, A.; Talbot, J.; Mickiene, G.; Balevicius, S.; Stirke, A.; Tereshchenko, A.; Tamosaitis, L.; Zvirblis, G.; et al. Evaluation of affinity sensor response kinetics towards dimeric ligands linked with spacers of different rigidity: Immobilized recombinant granulocyte colony-stimulating factor based synthetic receptor binding with genetically engineered dimeric analyte d. *Biosens. Bioelectron.* **2020**, *156*, 112112, doi:10.1016/j.bios.2020.112112.

7. Plikusiene, I.; Maciulis, V.; Juciute, S.; Ramanavicius, A.; Balevicius, Z.; Slibinskas, R.; Kucinskaite-Kodze, I.; Simanavicius, M.; Balevicius, S.; Ramanaviciene, A. Investigation of SARS-CoV-2 nucleocapsid protein interaction with a specific antibody by combined spectroscopic ellipsometry and quartz crystal microbalance with dissipation. *J. Colloid Interface Sci.* **2022**, *626*, 113–122, doi:10.1016/j.jcis.2022.06.119.

8. Plikusienė, I.; Bužavaitė-Vertelienė, E.; Mačiulis, V.; Valavičius, A.; Ramanavičienė, A.; Balevičius, Z. Application of tamm plasmon polaritons and cavity modes for biosensing in the combined

spectroscopic ellipsometry and quartz crystal microbalance method. *Biosensors* **2021**, *11*, doi:10.3390/bios11120501.

9. Shi, D.; Guo, Z.; Bedford, N. Basic Properties of Nanomaterials. In *Nanomaterials and Devices*; Elsevier, 2015; pp. 1–23 ISBN 9781455777549.

10. Puziy, A.M.; Poddubnaya, O.I.; Derylo-Marczewska, A.; Marczewski, A.W.; Blachnio, M.; Tsyba, M.M.; Sapsay, V.I.; Klymchuk, D.O. Kinetics of protein adsorption by nanoporous carbons with different pore size. *Adsorption* **2016**, *22*, 541–552, doi:10.1007/s10450-015-9723-3.

11. Dai, Z.; Ju, H. Bioanalysis based on nanoporous materials. *TrAC - Trends Anal. Chem.* **2012**, *39*, 149–162, doi:10.1016/j.trac.2012.05.008.

12. Md Jani, A.M.; Losic, D.; Voelcker, N.H. Nanoporous anodic aluminium oxide: Advances in surface engineering and emerging applications. *Prog. Mater. Sci.* **2013**, *58*, 636–704, doi:10.1016/j.pmatsci.2013.01.002.

13. Li, S.J.; Xia, N.; Yuan, B.Q.; Du, W.M.; Sun, Z.F.; Zhou, B. Bin A novel DNA sensor using a sandwich format by electrochemical measurement of marker ion fluxes across nanoporous alumina membrane. *Electrochim. Acta* **2015**, *159*, 234–241, doi:10.1016/j.electacta.2015.02.010.

14. Rajeev, G.; Melville, E.; Cowin, A.J.; Prieto-Simon, B.; Voelcker, N.H. Porous Alumina Membrane-Based Electrochemical Biosensor for Protein Biomarker Detection in Chronic Wounds. *Front. Chem.* **2020**, *8*, 1–11, doi:10.3389/fchem.2020.00155.

15. Rajeev, G.; Prieto Simon, B.; Marsal, L.F.; Voelcker, N.H. Advances in Nanoporous Anodic Alumina-Based Biosensors to Detect Biomarkers of Clinical Significance: A Review. *Adv. Healthc. Mater.* **2018**, *7*, 1–18, doi:10.1002/adhm.201700904.

16. Krismastuti, F.S.H.; Bayat, H.; Voelcker, N.H.; Schönherr, H. Real Time Monitoring of Layer-by-Layer Polyelectrolyte Deposition and Bacterial Enzyme Detection in Nanoporous Anodized Aluminum Oxide. *Anal. Chem.* **2015**, *87*, 3856–3863, doi:10.1021/ac504626m.

17. Santos, A.; Kumeria, T.; Losic, D. Optically optimized photoluminescent and interferometric biosensors based on nanoporous anodic alumina: A comparison. *Anal. Chem.* **2013**, *85*, 7904–7911, doi:10.1021/ac401609c.

18. Fortunato, E.; Barquinha, P.; Pimentel, A.; Gonçalves, A.; Marques, A.; Pereira, L.; Martins, R. Recent advances in ZnO transparent thin film transistors. *Thin Solid Films* **2005**, *487*, 205–211, doi:10.1016/j.tsf.2005.01.066.

19. Chen, X.; Wu, Z.; Liu, D.; Gao, Z. Preparation of ZnO Photocatalyst for the Efficient and Rapid Photocatalytic Degradation of Azo Dyes. *Nanoscale Res. Lett.* 2017, *12*.

20.   Shashanka, R.; Esgin, H.; Yilmaz, V.M.; Caglar, Y. Fabrication and characterization of green synthesized ZnO nanoparticle based dye-sensitized solar cells. *J. Sci. Adv. Mater. Devices* 2020, *5*, 185–191.

21.   Kim, E.B.; Seo, H.K. Highly sensitive formaldehyde detection using well-aligned zinc oxide nanosheets synthesized by chemical bath deposition technique. *Materials (Basel).* **2019**, *12*, doi:10.3390/ma12020250.

22.   Faria, A.M.; Mazon, T. Early diagnosis of Zika infection using a ZnO nanostructures-based rapid electrochemical biosensor. *Talanta* **2019**, *203*, 153–160, doi:10.1016/j.talanta.2019.04.080.

23.   Tripathy, N.; Kim, D.H. Metal oxide modified ZnO nanomaterials for biosensor applications. *Nano Converg.* 2018, *5*.

24.   Clark, L.C.; Lyons, C. Electrode systems for continuous monitoring in cardiovascular surgery. *Ann. N. Y. Acad. Sci.* **1962**, *102*, 29–45, doi:10.1111/j.1749-6632.1962.tb13623.x.

25.   Monk, D.; Walt, D. Optical fiber-based biosensors. *Anal. Bioanal. Chem.* **2004**, *379*, doi:10.1007/s00216-004-2650-x.

26.   Endo, T.; Kerman, K.; Nagatani, N.; Hiepa, H.M.; Kim, D.K.; Yonezawa, Y.; Nakano, K.; Tamiya, E. Multiple label-free detection of antigen-antibody reaction using localized surface plasmon resonance-based core-shell structured nanoparticle layer nanochip. *Anal. Chem.* **2006**, *78*, 6465–6475, doi:10.1021/ac0608321.

27.   Alarcon, E.I.; Bueno-Alejo, C.J.; Noel, C.W.; Stamplecoskie, K.G.; Pacioni, N.L.; Poblete, H.; Scaiano, J.C. Human serum albumin as protecting agent of silver nanoparticles: Role of the protein conformation and amine groups in the nanoparticle stabilization. *J. Nanoparticle Res.* **2013**, *15*, doi:10.1007/s11051-012-1374-7.

28.   Vogt, R. V.; Phillips, D.L.; Omar Henderson, L.; Whitfield, W.; Spierto, F.W. Quantitative differences among various proteins as blocking agents for ELISA microtiter plates. *J. Immunol. Methods* **1987**, *101*, 43–50, doi:10.1016/0022-1759(87)90214-6.

29.   Cong, Y.; Ulasli, M.; Schepers, H.; Mauthe, M.; V'kovski, P.; Kriegenburg, F.; Thiel, V.; de Haan, C.A.M.; Reggiori, F. Nucleocapsid Protein Recruitment to Replication-Transcription Complexes Plays a Crucial Role in Coronaviral Life Cycle. *J. Virol.* **2020**, *94*, 1–21, doi:10.1128/jvi.01925-19.

30.   Leung, D.T.M.; Tam, F.C.H.; Chun, H.M.; Chan, P.K.S.; Cheung, J.L.K.; Niu, H.; Tam, J.S.L.; Pak, L.L. Antibody response of patients with Severe Acute Respiratory Syndrome (SARS) targets the viral nucleocapsid. *J. Infect. Dis.* **2004**, *190*, 379–386, doi:10.1086/422040.

31.   Walls, A.C.; Park, Y.J.; Tortorici, M.A.; Wall, A.; McGuire, A.T.; Veesler, D. Structure, Function, and Antigenicity of the SARS-CoV-2 Spike Glycoprotein. *Cell* **2020**, *181*, 281-292.e6, doi:10.1016/j.cell.2020.02.058.

32.   Wang, C.; Li, W.; Drabek, D.; Okba, N.M.A.; van Haperen, R.;

Osterhaus, A.D.M.E.; van Kuppeveld, F.J.M.; Haagmans, B.L.; Grosveld, F.; Bosch, B.J. A human monoclonal antibody blocking SARS-CoV-2 infection. *Nat. Commun.* **2020**, *11*, 1–6, doi:10.1038/s41467-020-16256-y.

33. Tao, K.; Tzou, P.L.; Nouhin, J.; Gupta, R.K.; de Oliveira, T.; Kosakovsky Pond, S.L.; Fera, D.; Shafer, R.W. The biological and clinical significance of emerging SARS-CoV-2 variants. *Nat. Rev. Genet.* **2021**, *22*, 757–773, doi:10.1038/s41576-021-00408-x.

34. Pokropivny, V. V.; Skorokhod, V. V. Classification of nanostructures by dimensionality and concept of surface forms engineering in nanomaterial science. *Mater. Sci. Eng. C* **2007**, *27*, 990–993, doi:10.1016/j.msec.2006.09.023.

35. Alivisatos, A.P. Semiconductor clusters, nanocrystals, and quantum dots. *Science (80-.).* **1996**, *271*, 933–937, doi:10.1126/science.271.5251.933.

36. Martel, R.; Schmidt, T.; Shea, H.R.; Hertel, T.; Avouris, P. Single- and multi-wall carbon nanotube field-effect transistors. **1998**, *73*, 2447–2449.

37. Berber, S.; Kwon, Y.-K.; Tománek, D. Unusually High Thermal Conductivity of Carbon Nanotubes. *Phys. Rev. Lett.* **2000**, *84*, 4613–4616, doi:10.1103/PhysRevLett.84.4613.

38. Oberdörster, G.; Oberdörster, E.; Oberdörster, J. Nanotoxicology: An emerging discipline evolving from studies of ultrafine particles. *Environ. Health Perspect.* **2005**, *113*, 823–839, doi:10.1289/ehp.7339.

39. Duffin, R.; Tran, L.; Brown, D.; Stone, V.; Donaldson, K. Proinflammogenic effects of low-toxicity and metal nanoparticles in vivo and in vitro: Highlighting the role of particle surface area and surface reactivity. *Inhal. Toxicol.* **2007**, *19*, 849–856, doi:10.1080/08958370701479323.

40. Rosenberg, D.J.; Alayoglu, S.; Kostecki, R.; Ahmed, M. Synthesis of microporous silica nanoparticles to study water phase transitions by vibrational spectroscopy. *Nanoscale Adv.* **2019**, *1*, 4878–4887, doi:10.1039/c9na00544g.

41. Yadav, M.; Dhanda, M.; Arora, R.; Jagdish, R.; Singh, G.; Lata, S. Titania (TiO2)/silica (SiO2) nanospheres or NSs amalgamated on a pencil graphite electrode to sense l-ascorbic acid electrochemically and augmented NSs for antimicrobial behaviour. *New J. Chem.* **2022**, *46*, 12783–12796, doi:10.1039/d2nj01892f.

42. García de Arquer, F.P.; Talapin, D. V.; Klimov, V.I.; Arakawa, Y.; Bayer, M.; Sargent, E.H. Semiconductor quantum dots: Technological progress and future challenges. *Science* **2021**, *373*, doi:10.1126/science.aaz8541.

43. Mikhael, B.; Elise, B.; Xavier, M.; Sebastian, S.; Johann, M.; Laetitia, P. New silicon architectures by gold-assisted chemical etching. *ACS Appl. Mater. Interfaces* **2011**, *3*, 3866–3873, doi:10.1021/am200948p.

44. Chua, W.H.; Yaacob, M.H.; Tan, C.Y.; Ong, B.H. Chemical bath deposition of h-MoO3 on optical fibre as room-temperature ammonia gas sensor. *Ceram. Int.* **2021**, *47*, 32828–32836, doi:10.1016/j.ceramint.2021.08.179.

45. Zhang, J.B.; Li, X.N.; Bai, S.L.; Luo, R.X.; Chen, A.F.; Lin, Y. High-yield synthesis of SnO 2 nanobelts by water-assisted chemical vapor deposition for sensor applications. *Mater. Res. Bull.* **2012**, *47*, 3277–3282, doi:10.1016/j.materresbull.2012.07.023.

46. Hao, W.; Marichy, C.; Journet, C. Atomic layer deposition of stable 2D materials. *2D Mater.* **2019**, *6*, doi:10.1088/2053-1583/aad94f.

47. Dondapati, J.S.; Govindhan, M.; Chen, A. Direct growth of three-dimensional nanoflower-like structures from flat metal surfaces. *Chem. Commun.* **2022**, *1*, 11127–11130, doi:10.1039/d2cc04358k.

48. Karam, C.; Habchi, R.; Tingry, S.; Miele, P.; Bechelany, M. Design of multilayers of urchin-like zno nanowires coated with tio2 nanostructures for dye-sensitized solar cells. *ACS Appl. Nano Mater.* **2018**, *1*, 3705–3714, doi:10.1021/acsanm.8b00849.

49. Khaleel, A.A. Nanostructured Pure ψ-Fe2O3 via Forced Precipitation in an Organic Solvent. *Chem. - A Eur. J.* **2004**, *10*, 925–932, doi:10.1002/chem.200305135.

50. Husham, M.; Hamidon, M.N.; Paiman, S.; Abuelsamen, A.A.; Farhat, O.F.; Al-Dulaimi, A.A. Synthesis of ZnO nanorods by microwave-assisted chemical-bath deposition for highly sensitive self-powered UV detection application. *Sensors Actuators, A Phys.* **2017**, *263*, 166–173, doi:10.1016/j.sna.2017.05.041.

51. Maciulis, V.; Ramanaviciene, A.; Plikusiene, I. Recent Advances in Synthesis and Application of Metal Oxide Nanostructures in Chemical Sensors and Biosensors. *Nanomaterials* **2022**, *12*, doi:10.3390/nano12244413.

52. Reta, N.; Saint, C.P.; Michelmore, A.; Prieto-Simon, B.; Voelcker, N.H. Nanostructured Electrochemical Biosensors for Label-Free Detection of Water- and Food-Borne Pathogens. *ACS Appl. Mater. Interfaces* **2018**, *10*, 6055–6072, doi:10.1021/acsami.7b13943.

53. Santos, A.; Kumeria, T.; Losic, D. Nanoporous anodic aluminum oxide for chemical sensing and biosensors. *TrAC - Trends Anal. Chem.* **2013**, *44*, 25–38, doi:10.1016/j.trac.2012.11.007.

54. Vajtai, R. *Springer handbook of nanomaterials*; 2013; ISBN 9783642205958.

55. Nielsch, K.; Choi, J.; Schwirn, K.; Wehrspohn, R.B.; Gösele, U. Self-ordering Regimes of Porous Alumina: The 10% Porosity Rule. *Nano Lett.* **2002**, *2*, 677–680, doi:10.1021/nl025537k.

56. Eftekhari, A.; Alkire, Ri.C.; Gogotsi, Y.; Simon, P. *Nanostructured Materials in Electrochemistry*; WILEY-VCH, 2008; Vol. 4; ISBN 978-3-527-31876-6.

57. Zhang, X.Y.; Wen, G.H.; Chan, Y.F.; Zheng, R.K.; Zhang, X.X.;

Wang, N. Fabrication and magnetic properties of ultrathin Fe nanowire arrays. *Appl. Phys. Lett.* **2003**, *83*, 3341–3343, doi:10.1063/1.1621459.

58. Santos, A.; MacÍas, G.; Ferré-Borrull, J.; Pallarès, J.; Marsal, L.F. Photoluminescent enzymatic sensor based on nanoporous anodic alumina. *ACS Appl. Mater. Interfaces* **2012**, *4*, 3584–3588, doi:10.1021/am300648j.

59. Zhou, C.X.; Mo, R.J.; Chen, Z.M.; Wang, J.; Shen, G.Z.; Li, Y.P.; Quan, Q.G.; Liu, Y.; Li, C.Y. Quantitative Label-Free Listeria Analysis Based on Aptamer Modified Nanoporous Sensor. *ACS Sensors* **2016**, *1*, 965–969, doi:10.1021/acssensors.6b00333.

60. Makela, M.; Lin, Z.; Lin, P.T. Surface Functionalized Anodic Aluminum Oxide Membrane for Opto-Nanofluidic SARS-CoV-2 Genomic Target Detection. *IEEE Sens. J.* **2021**, *21*, 22645–22650, doi:10.1109/JSEN.2021.3109022.

61. Tsou, P.H.; Sreenivasappa, H.; Hong, S.; Yasuike, M.; Miyamoto, H.; Nakano, K.; Misawa, T.; Kameoka, J. Rapid antibiotic efficacy screening with aluminum oxide nanoporous membrane filter-chip and optical detection system. *Biosens. Bioelectron.* **2010**, *26*, 289–294, doi:10.1016/j.bios.2010.06.034.

62. Tereshchenko, A.; Bechelany, M.; Viter, R.; Khranovskyy, V.; Smyntyna, V.; Starodub, N.; Yakimova, R. Optical biosensors based on ZnO nanostructures: Advantages and perspectives. A review. *Sensors Actuators, B Chem.* **2016**, *229*, 664–677, doi:10.1016/j.snb.2016.01.099.

63. Chaaya, A.A.; Bechelany, M.; Balme, S.; Miele, P. ZnO 1D nanostructures designed by combining atomic layer deposition and electrospinning for UV sensor applications. *J. Mater. Chem. A* **2014**, *2*, 20650–20658, doi:10.1039/c4ta05239k.

64. Greene, L.E.; Law, M.; Tan, D.H.; Montano, M.; Goldberger, J.; Somorjai, G.; Yang, P. General route to vertical ZnO nanowire arrays using textured ZnO seeds. *Nano Lett.* **2005**, *5*, 1231–1236, doi:10.1021/nl050788p.

65. Makhlouf, H.; Karam, C.; Lamouchi, A.; Tingry, S.; Miele, P.; Habchi, R.; Chtourou, R.; Bechelany, M. Analysis of ultraviolet photo-response of ZnO nanostructures prepared by electrodeposition and atomic layer deposition. *Appl. Surf. Sci.* **2018**, *444*, 253–259, doi:10.1016/j.apsusc.2018.02.289.

66. Greene, L.E.; Yuhas, B.D.; Law, M.; Zitoun, D.; Yang, P. Solution-grown zinc oxide nanowires. *Inorg. Chem.* **2006**, *45*, 7535–7543, doi:10.1021/ic0601900.

67. Law, M.; Greene, L.E.; Johnson, J.C.; Saykally, R.; Yang, P. Nanowire dye-sensitized solar cells. *Nat. Mater.* **2005**, *4*, 455–459, doi:10.1038/nmat1387.

68. Lupan, O.; Cretu, V.; Postica, V.; Ahmadi, M.; Cuenya, B.R.; Chow, L.; Tiginyanu, I.; Viana, B.; Pauporté, T.; Adelung, R. Silver-doped

zinc oxide single nanowire multifunctional nanosensor with a significant enhancement in response. *Sensors Actuators, B Chem.* **2016**, *223*, 893–903, doi:10.1016/j.snb.2015.10.002.

69. Pan, Y.-W.; Peng, S.-J.; Ma, Y.-L.; CaO, P.-J.; Hu, F. Flat-Type Gas Sensors Based on ZnO Nanorod Arrays. *J. Nanosci. Nanotechnol.* **2020**, *20*, 7800–7807, doi:10.1166/jnn.2020.18890.

70. Yuhas, B.D.; Zitoun, D.O.; Pauzauskie, P.J.; He, R.; Yang, P. Transition-metal doped zinc oxide nanowires. *Angew. Chemie - Int. Ed.* **2006**, *45*, 420–423, doi:10.1002/anie.200503172.

71. Wu, Y.; Li, G.; Hong, Y.; Zhao, X.; Reyes, P.I.; Lu, Y. Rapid and dynamic detection of antimicrobial treatment response using spectral amplitude modulation in MZO nanostructure-modified quartz crystal microbalance. *J. Microbiol. Methods* **2020**, *178*, 106071, doi:10.1016/j.mimet.2020.106071.

72. Elias, J.; Utke, I.; Yoon, S.; Bechelany, M.; Weidenkaff, A.; Michler, J.; Philippe, L. Electrochemical growth of ZnO nanowires on atomic layer deposition coated polystyrene sphere templates. *Electrochim. Acta* **2013**, *110*, 387–392, doi:10.1016/j.electacta.2013.04.168.

73. Wang, J.X.; Sun, X.W.; Wei, A.; Lei, Y.; Cai, X.P.; Li, C.M.; Dong, Z.L. Zinc oxide nanocomb biosensor for glucose detection. *Appl. Phys. Lett.* **2006**, *88*, 98–101, doi:10.1063/1.2210078.

74. Danielson, E.; Dhamodharan, V.; Porkovich, A.; Kumar, P.; Jian, N.; Ziadi, Z.; Grammatikopoulos, P.; Sontakke, V.A.; Yokobayashi, Y.; Sowwan, M. Gas-Phase Synthesis for Label-Free Biosensors: Zinc-Oxide Nanowires Functionalized with Gold Nanoparticles. *Sci. Rep.* **2019**, *9*, 1–10, doi:10.1038/s41598-019-53960-2.

75. Zhou, F.; Jing, W.; Wu, Q.; Gao, W.; Jiang, Z.; Shi, J.; Cui, Q. Effects of the surface morphologies of ZnO nanotube arrays on the performance of amperometric glucose sensors. *Mater. Sci. Semicond. Process.* **2016**, *56*, 137–144, doi:10.1016/j.mssp.2016.08.009.

76. Zhang, J.; Xiao, X.; He, Q.; Huang, L.; Li, S.; Wang, F. A Nonenzymatic Glucose Sensor Based on a Copper Nanoparticle-Zinc Oxide Nanorod Array. *Anal. Lett.* **2014**, *47*, 1147–1161, doi:10.1080/00032719.2013.865198.

77. Hill, R.T. Plasmonic biosensors. *WIREs Nanomedicine and Nanobiotechnology* **2015**, *7*, 152–168, doi:10.1002/wnan.1314.

78. Sakalauskiene, L.; Popov, A.; Kausaite-Minkstimiene, A.; Ramanavicius, A.; Ramanaviciene, A. The Impact of Glucose Oxidase Immobilization on Dendritic Gold Nanostructures on the Performance of Glucose Biosensors. *Biosensors* **2022**, *12*, 320, doi:10.3390/bios12050320.

79. Plikusiene, I.; Maciulis, V.; Ramanaviciene, A.; Balevicius, Z.; Buzavaite-Verteliene, E.; Ciplys, E.; Slibinskas, R.; Simanavicius, M.; Zvirbliene, A.; Ramanavicius, A. Evaluation of kinetics and thermodynamics of interaction between immobilized SARS-CoV-2

nucleoprotein and specific antibodies by total internal reflection ellipsometry. *J. Colloid Interface Sci.* **2021**, *594*, 195–203, doi:10.1016/j.jcis.2021.02.100.

80. Homola, J.; Yee, S.S.; Gauglitz, G. Surface plasmon resonance sensors: review. *Sensors Actuators, B Chem.* **1999**, *54*, 3–15, doi:10.1016/S0925-4005(98)00321-9.

81. Buzavaite-Verteliene, E.; Plikusiene, I.; Tolenis, T.; Valavicius, A.; Anulyte, J.; Ramanavicius, A.; Balevicius, Z. Hybrid Tamm-surface plasmon polariton mode for highly sensitive detection of protein interactions. *Opt. Express* **2020**, *28*, 29033, doi:10.1364/oe.401802.

82. Plikusiene, I.; Maciulis, V.; Juciute, S.; Maciuleviciene, R.; Balevicius, S.; Ramanavicius, A.; Ramanaviciene, A. Investigation and Comparison of Specific Antibodies' Affinity Interaction with SARS-CoV-2 Wild-Type, B.1.1.7, and B.1.351 Spike Protein by Total Internal Reflection Ellipsometry. *Biosensors* **2022**, *12*, 351, doi:10.3390/bios12050351.

83. Bianco, M.; Aloisi, A.; Arima, V.; Capello, M.; Ferri-Borgogno, S.; Novelli, F.; Leporatti, S.; Rinaldi, R. Quartz crystal microbalance with dissipation (QCM-D) as tool to exploit antigen-antibody interactions in pancreatic ductal adenocarcinoma detection. *Biosens. Bioelectron.* **2013**, *42*, 646–652, doi:10.1016/j.bios.2012.10.012.

84. Baleviciute, I.; Balevicius, Z.; Makaraviciute, A.; Ramanaviciene, A.; Ramanavicius, A. Study of antibody/antigen binding kinetics by total internal reflection ellipsometry. *Biosens. Bioelectron.* **2013**, *39*, 170–176, doi:10.1016/j.bios.2012.07.017.

85. Balevicius, Z.; Ramanaviciene, A.; Baleviciute, I.; Makaraviciute, A.; Mikoliunaite, L.; Ramanavicius, A. Evaluation of intact- and fragmented-antibody based immunosensors by total internal reflection ellipsometry. *Sensors Actuators, B Chem.* **2011**, *160*, 555–562, doi:10.1016/j.snb.2011.08.029.

86. Plikusiene, I.; Maciulis, V.; Ramanaviciene, A.; Balevicius, Z.; Buzavaite-Verteliene, E.; Ciplys, E.; Slibinskas, R.; Simanavicius, M.; Zvirbliene, A.; Ramanavicius, A. Evaluation of kinetics and thermodynamics of interaction between immobilized SARS-CoV-2 nucleoprotein and specific antibodies by total internal reflection ellipsometry. *J. Colloid Interface Sci.* **2021**, *594*, 195–203, doi:10.1016/j.jcis.2021.02.100.

87. Plikusiene, I.; Balevicius, Z.; Ramanaviciene, A.; Talbot, J.; Mickiene, G.; Balevicius, S.; Stirke, A.; Tereshchenko, A.; Tamosaitis, L.; Zvirblis, G.; et al. Evaluation of affinity sensor response kinetics towards dimeric ligands linked with spacers of different rigidity: Immobilized recombinant granulocyte colony-stimulating factor based synthetic receptor binding with genetically engineered dimeric analyte d. *Biosens. Bioelectron.* **2020**, *156*, 112112, doi:10.1016/j.bios.2020.112112.

88. Jahanban-Esfahlan, A.; Panahi-Azar, V.; Sajedi, S. Interaction of glutathione with bovine serum albumin: Spectroscopy and molecular docking. *Food Chem.* **2016**, *202*, 426–431, doi:10.1016/j.foodchem.2016.02.026.

89. Sułkowska, A. Interaction of drugs with bovine and human serum albumin. *J. Mol. Struct.* **2002**, *614*, 227–232, doi:10.1016/S0022-2860(02)00256-9.

90. Aleksic, M.; Pease, C.K.; Basketter, D.A.; Panico, M.; Morris, H.R.; Dell, A. Investigating protein haptenation mechanisms of skin sensitisers using human serum albumin as a model protein. *Toxicol. Vitr.* **2007**, *21*, 723–733, doi:10.1016/j.tiv.2007.01.008.

91. Zhu, W.; Xuan, C.; Liu, G.; Chen, Z.; Wang, W. A label-free fluorescent biosensor for determination of bovine serum albumin and calf thymus DNA based on gold nanorods coated with acridine orange-loaded mesoporous silica. *Sensors Actuators, B Chem.* **2015**, *220*, 302–308, doi:10.1016/j.snb.2015.05.100.

92. Jiao, F.; Li, F.; Shen, J.; Guan, C.; Khan, S.A.; Wang, J.; Yang, Z.; Zhu, J. Wafer-scale flexible plasmonic metasurface with passivated aluminum nanopillars for high-sensitivity immunosensors. *Sensors Actuators, B Chem.* **2021**, *344*, 130170, doi:10.1016/j.snb.2021.130170.

93. Jahanban-Esfahlan, A.; Ostadrahimi, A.; Jahanban-Esfahlan, R.; Roufegarinejad, L.; Tabibiazar, M.; Amarowicz, R. Recent developments in the detection of bovine serum albumin. *Int. J. Biol. Macromol.* **2019**, *138*, 602–617, doi:10.1016/j.ijbiomac.2019.07.096.

94. Hardenbrook, N.J.; Zhang, P. A structural view of the SARS-CoV-2 virus and its assembly. *Curr. Opin. Virol.* **2022**, *52*, 123–134, doi:10.1016/j.coviro.2021.11.011.

95. Dinesh, D.C.; Chalupska, D.; Silhan, J.; Koutna, E.; Nencka, R.; Veverka, V.; Boura, E. Structural basis of RNA recognition by the SARS-CoV-2 nucleocapsid phosphoprotein. *PLoS Pathog.* **2020**, *16*, 1–16, doi:10.1371/journal.ppat.1009100.

96. Harris, L.J.; Larson, S.B.; Hasel, K.W.; McPherson, A. Refined structure of an intact IgG2a monoclonal antibody. *Biochemistry* **1997**, *36*, 1581–1597, doi:10.1021/bi962514+.

97. Zeng, W.; Liu, G.; Ma, H.; Zhao, D.; Yang, Y.; Liu, M.; Mohammed, A.; Zhao, C.; Yang, Y.; Xie, J.; et al. Biochemical characterization of SARS-CoV-2 nucleocapsid protein. *Biochem. Biophys. Res. Commun.* **2020**, *527*, 618–623, doi:10.1016/j.bbrc.2020.04.136.

98. Du, S.; Cao, Y.; Zhu, Q.; Yu, P.; Qi, F.; Wang, G.; Du, X.; Bao, L.; Deng, W.; Zhu, H.; et al. Structurally Resolved SARS-CoV-2 Antibody Shows High Efficacy in Severely Infected Hamsters and Provides a Potent Cocktail Pairing Strategy. *Cell* **2020**, *183*, 1013-1023.e13, doi:10.1016/j.cell.2020.09.035.

99. Zost, S.J.; Gilchuk, P.; Case, J.B.; Binshtein, E.; Chen, R.E.; Nkolola,

J.P.; Schäfer, A.; Reidy, J.X.; Trivette, A.; Nargi, R.S.; et al. Potently neutralizing and protective human antibodies against SARS-CoV-2. *Nature* **2020**, *584*, 443–449, doi:10.1038/s41586-020-2548-6.

100. Cai, Y.; Zhang, J.; Xiao, T.; Peng, H.; Sterling, S.M.; Walsh, R.M.; Rawson, S.; Rits-Volloch, S.; Chen, B. Distinct conformational states of SARS-CoV-2 spike protein. *Science (80-.).* **2020**, *369*, 1586–1592, doi:10.1126/science.abd4251.

101. Zhu, X.; Mannar, D.; Srivastava, S.S.; Berezuk, A.M.; Demers, J.P.; Saville, J.W.; Leopold, K.; Li, W.; Dimitrov, D.S.; Tuttle, K.S.; et al. Cryo-electron microscopy structures of the N501Y SARS-CoV-2 spike protein in complex with ACE2 and 2 potent neutralizing antibodies. *PLoS Biol.* **2021**, *19*, 1–17, doi:10.1371/journal.pbio.3001237.

102. Kemp, S.A.; Collier, D.A.; Datir, R.P.; Ferreira, I.A.T.M.; Gayed, S.; Jahun, A.; Hosmillo, M.; Rees-Spear, C.; Mlcochova, P.; Lumb, I.U.; et al. SARS-CoV-2 evolution during treatment of chronic infection. *Nature* **2021**, *592*, 277–282, doi:10.1038/s41586-021-03291-y.

103. Magazine, N.; Zhang, T.; Wu, Y.; McGee, M.C.; Veggiani, G.; Huang, W. Mutations and Evolution of the SARS-CoV-2 Spike Protein. *Viruses* **2022**, *14*, 1–11, doi:10.3390/v14030640.

104. Kidd, M.; Richter, A.; Best, A.; Cumley, N.; Mirza, J.; Percival, B.; Mayhew, M.; Megram, O.; Ashford, F.; White, T.; et al. S-Variant SARS-CoV-2 Lineage B1.1.7 Is Associated With Significantly Higher Viral Load in Samples Tested by TaqPath Polymerase Chain Reaction. *J. Infect. Dis.* **2021**, *223*, 1666–1670, doi:10.1093/infdis/jiab082.

105. Wibmer, C.K.; Ayres, F.; Hermanus, T.; Madzivhandila, M.; Kgagudi, P.; Oosthuysen, B.; Lambson, B.E.; de Oliveira, T.; Vermeulen, M.; van der Berg, K.; et al. SARS-CoV-2 501Y.V2 escapes neutralization by South African COVID-19 donor plasma. *Nat. Med.* **2021**, *27*, 622–625, doi:10.1038/s41591-021-01285-x.

106. Banho, C.A.; Sacchetto, L.; Campos, G.R.F.; Bittar, C.; Possebon, F.S.; Ullmann, L.S.; Marques, B. de C.; da Silva, G.C.D.; Moraes, M.M.; Parra, M.C.P.; et al. Impact of SARS-CoV-2 Gamma lineage introduction and COVID-19 vaccination on the epidemiological landscape of a Brazilian city. *Commun. Med.* **2022**, *2*, 1–11, doi:10.1038/s43856-022-00108-5.

107. Duong, D. Alpha, Beta, Delta, Gamma: What's important to know about SARS-CoV-2 variants of concern? *CMAJ* **2021**, *193*, E1059–E1060, doi:10.1503/cmaj.1095949.

108. Dhawan, M.; Sharma, A.; Priyanka; Thakur, N.; Rajkhowa, T.K.; Choudhary, O.P. Delta variant (B.1.617.2) of SARS-CoV-2: Mutations, impact, challenges and possible solutions. *Hum. Vaccines Immunother.* **2022**, *18*, doi:10.1080/21645515.2022.2068883.

109. Chatterjee, S.; Bhattacharya, M.; Nag, S.; Dhama, K.; Chakraborty, C. A Detailed Overview of SARS-CoV-2 Omicron: Its Sub-Variants,

Mutations and Pathophysiology, Clinical Characteristics, Immunological Landscape, Immune Escape, and Therapies. *Viruses* **2023**, *15*, 1–27, doi:10.3390/v15010167.

110. To, K.K.W.; Tsang, O.T.Y.; Leung, W.S.; Tam, A.R.; Wu, T.C.; Lung, D.C.; Yip, C.C.Y.; Cai, J.P.; Chan, J.M.C.; Chik, T.S.H.; et al. Temporal profiles of viral load in posterior oropharyngeal saliva samples and serum antibody responses during infection by SARS-CoV-2: an observational cohort study. *Lancet Infect. Dis.* **2020**, *20*, 565–574, doi:10.1016/S1473-3099(20)30196-1.

111. Batra, M.; Tian, R.; Zhang, C.; Clarence, E.; Sacher, C.S.; Miranda, J.N.; De La Fuente, J.R.O.; Mathew, M.; Green, D.; Patel, S.; et al. Role of IgG against N-protein of SARS-CoV2 in COVID19 clinical outcomes. *Sci. Rep.* **2021**, *11*, 1–9, doi:10.1038/s41598-021-83108-0.

112. Li, Q.; Wu, J.; Nie, J.; Zhang, L.; Hao, H.; Liu, S.; Zhao, C.; Zhang, Q.; Liu, H.; Nie, L.; et al. The Impact of Mutations in SARS-CoV-2 Spike on Viral Infectivity and Antigenicity. *Cell* **2020**, *182*, 1284-1294.e9, doi:10.1016/j.cell.2020.07.012.

113. Banihashem, S.; Nezhati, M.N.; Panahia, H.A. Synthesis of chitosan-grafted-poly(N-vinylcaprolactam) coated on the thiolated gold nanoparticles surface for controlled release of cisplatin. *Carbohydr. Polym.* **2020**, *227*, 115333, doi:10.1016/j.carbpol.2019.115333.

114. Le, N.C.H.; Gubala, V.; Gandhiraman, R.P.; Coyle, C.; Daniels, S.; Williams, D.E. Total internal reflection ellipsometry as a label-free assessment method for optimization of the reactive surface of bioassay devices based on a functionalized cycloolefin polymer. *Anal. Bioanal. Chem.* **2010**, *398*, 1927–1936, doi:10.1007/s00216-010-4099-4.

115. Kim, W.J.; Kim, S.; Lee, B.S.; Kim, A.; Ah, C.S.; Huh, C.; Sung, G.Y.; Yun, W.S. Enhanced protein immobilization efficiency on a TiO2 surface modified with a hydroxyl functional group. *Langmuir* **2009**, *25*, 11692–11697, doi:10.1021/la901615e.

116. Balevicius, Z.; Baleviciute, I.; Tumenas, S.; Tamosaitis, L.; Stirke, A.; Makaraviciute, A.; Ramanaviciene, A.; Ramanavicius, A. In situ study of ligand-receptor interaction by total internal reflection ellipsometry. *Thin Solid Films* **2014**, *571*, 744–748, doi:10.1016/j.tsf.2013.10.090.

117. Sanità, G.; Carrese, B.; Lamberti, A. Nanoparticle Surface Functionalization: How to Improve Biocompatibility and Cellular Internalization. *Front. Mol. Biosci.* **2020**, *7*, doi:10.3389/fmolb.2020.587012.

118. Zhao, X.; Lu, M. *Nanophotonics in Biomedical Engineering*; Zhao, X., Lu, M., Eds.; Springer Singapore: Singapore, 2021; ISBN 978-981-15-6136-8.

119. Sypabekova, M.; Hagemann, A.; Rho, D.; Kim, S. Review: 3-Aminopropyltriethoxysilane (APTES) Deposition Methods on Oxide Surfaces in Solution and Vapor Phases for Biosensing Applications. *Biosensors* **2023**, *13*, doi:10.3390/bios13010036.

120. Ball, V.; Ramsden, J.J. Buffer dependence of refractive index increments of protein solutions. *Biopolymers* **1998**, *46*, 489–492, doi:10.1002/(sici)1097-0282(199812)46:7<489::aid-bip6>3.0.co;2-e.

121. Vörös, J. The density and refractive index of adsorbing protein layers. *Biophys. J.* **2004**, *87*, 553–561, doi:10.1529/biophysj.103.030072.

122. Arwin, H.; Poksinski, M.; Johansen, K. Total internal reflection ellipsometry: Principles and applications. *Appl. Opt.* **2004**, *43*, 3028–3036, doi:10.1364/AO.43.003028.

123. Balevicius, Z.; Talbot, J.; Tamosaitis, L.; Plikusiene, I.; Stirke, A.; Mickiene, G.; Balevicius, S.; Paulauskas, A.; Ramanavicius, A. Modelling of immunosensor response: the evaluation of binding kinetics between an immobilized receptor and structurally-different genetically engineered ligands. *Sensors Actuators, B Chem.* **2019**, *297*, 126770, doi:10.1016/j.snb.2019.126770.

124. Berdnikov, V.M.; Doktorov, A.B. Steric factor in diffusion-controlled chemical reactions. *Chem. Phys.* **1982**, *69*, 205–212, doi:10.1016/0301-0104(82)88147-0.

125. Doktorov, A.B. Encounter Theory of Chemical Reactions in Solution: Approximate Methods of Calculating Rate Constants. In *Chemical Kinetics*; WORLD SCIENTIFIC (EUROPE), 2019; pp. 35–64 ISBN 978-1-78634-700-8.

126. Sauerbrey, G. Verwendung von Schwingquarzen zur Wägung dünner Schichten und zur Mikrowägung. *Zeitschrift für Phys.* **1959**, *155*, 206–222, doi:10.1007/BF01337937.

127. Afonso, A.S.; Zanetti, B.F.; Santiago, A.C.; Henrique-Silva, F.; Mattoso, L.H.C.; Faria, R.C. QCM immunoassay for recombinant cysteine peptidase: A potential protein biomarker for diagnosis of citrus canker. *Talanta* **2013**, *104*, 193–197, doi:10.1016/j.talanta.2012.11.003.

128. Tan, Y.H.; Liu, M.; Nolting, B.; Go, J.G.; Gervay-Hague, J.; Liu, G. A Nanoengineering Approach for Investigation and Regulation of Protein Immobilization. *ACS Nano* **2008**, *2*, 2374–2384, doi:10.1021/nn800508f.

129. Voinova, M. V.; Jonson, M.; Kasemo, B. "Missing mass" effect in biosensor's QCM applications. *Biosens. Bioelectron.* **2002**, *17*, 835–841, doi:10.1016/S0956-5663(02)00050-7.

130. Voinova, M. V.; Jonson, M.; Kasemo, B. Dynamics of viscous amphiphilic films supported by elastic solid substrates. *J. Phys. Condens. Matter* **1997**, *9*, 7799–7808, doi:10.1088/0953-8984/9/37/011.

131. Masuda, H.; Fukuda, K. Ordered Metal Nanohole Arrays Made by a Two-Step Replication of Honeycomb Structures of Anodic Alumina. *Science (80-.).* **1995**, *268*, 1466–1468.

SANTRAUKA LIETUVIŲ KALBA

SANTRUMPOS

pAAO	Porėtas anodinis aliuminio oksidas
ZnO-NWs	Cinko oksido nanovielos
QCM-D	Kvarco kristalo mikrogravimetrija su disipacija
HSA	Žmogaus serumo albuminas
BSA	Jaučio serumo albuminas
SCoV2-S	SARS-CoV-2 viruso spyglio baltymas
SCoV2-αS	SARS-CoV-2 viruso α varianto, spyglio baltymas
SCoV2-βS	SARS-CoV-2 viruso β varianto, spyglio baltymas
SCoV2-N	SARS-CoV-2 viruso nukleokapsidės baltymas
RBD	Receptorių jungimosi domenas
ACE2	Angiotenziną konvertuojantis fermentas 2
Anti-SCoV2-N	Antikūnai prieš SCoV2-N baltymą
pAb-SCoV2-S	Polikloniniai antikūnai prieš SCoV2-S baltymą
11-MUA	11-merkaptoundekano rūgštis
SAM	Savitvarkis monosluoksnis
APTES	3-aminopropiletoksisilanas
EDC	N-etil-N'-(3-(dimetilamino)-propil)karbodiimido hidrochloridas
NHS	N-hidroksisukcinimidas
SE	Spektrinė elipsometrija

ĮVADAS

Kuriant įvairius biologinius ar cheminius jutiklius, dažnai naudojamos nanostruktūrinės medžiagos dėl palankių mechaninių ir elektrinių savybių bei didelio paviršiaus ploto [1–5]. Nanometriniai sluoksniai dažniausiai taikomi jutikliams, kuriuose naudojamas optinis ar akustinis signalas. Pastaruoju metu susidomėta biojutikliais, kuriuose naudojama spektrinė elipsometrija, kvarco kristalo mikrogravimetrija su disipacija ar jų deriniu [6–8]. Šie metodai yra paklausus, nes leidžia sudaryti nedestruktyvias ir labai jautrias biojutiklių sistemas. Tolimesni žingsniai šioje srityje apima pažangių medžiagų ir struktūrų naudojimą jutikliams tobulinti ir įvairiems baltymams tirti [9].

Baltymų adsorbcijos/desorbcijos į/iš įvairių nanostrūrizuotų medžiagų tyrimai yra svarbūs siekiant pritaikyti tokias medžiagas baltymų gryninimui ar biojutiklių kurimui [10,11]. Anodinis aliuminio oksidas (pAAO) ir ZnO nanovielos (ZnO-NWs) dėl savo unikalių fizinių ir cheminių savybių yra dažnai naudojamos biojutikliuose [12]. pAAO pasižymi biologiniu suderinamumu, tvarkingu nanoporų išsidėstymu ir geometrija, o ZnO-NWs turi didelį paviršiaus plotą ir funkcionalizuojamą paviršių biologinių molekulių imobilizavimui [15,23]. Abejos struktūros naudojamos optinių ir elektrocheminių biologinių jutiklių kūrime [13,14,20–22].

Galvijų serumo albuminas (BSA) ir žmogaus serumo albuminas (HSA) yra baltymai, kurie dažnai naudojami kaip „blokuojančios medžiagos" bioanalitinėse sistemose, siekiant sumažinti nespecifinę sąveiką, pagerinti selektyvumą ir jautrumą [27,28]. Dėl to yra labai svarbu išanalizuoti, kaip stipriai šie baltymai sąveikauja su bioanalitinėse sistemose naudojamais paviršiais ir kiek patvarūs yra šie baltymų monosluoksniai.

SARS-CoV-2 nukleokapsidė (SCoV2-N) yra struktūrinis baltymas, randamas SARS-CoV-2 viruso viduje. SCoV2-N baltymas atlieka funkciją RNR pakavime ir SARS-CoV-2 viruso replikacijoje [29]. Antikūnai prieš SCoV2-N yra aptinkami užsikrėtusių asmenų kraujyje, o didelė šių antikūnų koncentracija yra susieta su padidėjusia komplikacijų nuo COVID-19 infekcijos rizika [30]. SCoV2-N ir anti-SCoV2-N tyrimas yra svarbūs vaistų, vakcinų ar greitųjų testų pramonei [7].

SARS-CoV-2 spyglio (SCoV2-S) yra struktūrinis baltymas, kurio pagrindinė funkcija yra jungtis prie šeimininko ląstelės per ACE2 receptorių ir dalyvauti ląstelės ir viruso susijungime [31]. Žmogaus imuninė sistema geba sukurti antikūnus, kurie neutralizuoja SCoV2-S ir neleidžia jam prisijungti prie ACE2 [32]. Tačiau SARS-CoV-2 viruso mutacijos sukelia pokyčius SCoV2-S struktūroje, susidarant SCoV2-αS, SCoV2-βS spyglių variantams. Pokyčiai tarp spyglio baltymų, dažniausiai, yra aminorūgščių pakeitimas, kuris daro neigiamą įtaką skiepų, vaistų ir diagnostinių instrumentų veiksmingumui [33].

Tyrimo tikslas ištirti galimybes pritaikyti nanometrinius Au sluoksnius, porėto aliuminio oksidą ir cinko oksido nanovielų paviršius kuriant biologinių jutiklių sistemas, spektrinės elipsometrijos (SE) ir kvarco kristalo mikrogravimetrijos su disipacija (QCM-D) matavimo metodams.

Tyrimo uždaviniai:

1. Pritaikant spektrinės elipsometrijos metodą ištirti porėto aliuminio oksido dangos optines savybes ir išanalizuoti HSA baltymų adsorbcijos ir desorbcijos procesus šiai dangai.

2.   Ištirti cinko oksido nanovielų dangos optines savybes, galimybes stiprinti signalą visiško vidaus atspindžio elipsometrijos režime ir pritaikomumą biologiniams jutikliams stebint kovalentinę BSA baltymų imobilizaciją realiu laiku.

3.   Ištirti SARS-CoV-2 S, -αS ir -βS baltymų sąveiką su specifiniais antikūnais esančiais žmogaus kraujo serume naudojant visiško vidaus atspindžio elipsometrijos metodą, palyginti asociacijos (k_a), disociacijos (k_d), stabilaus imuninio komplekso susiformavimo (k_r), greičio konstantas ir erdvinio išsidėstymo faktorius (P_s) susiformavusiems imuniniams kompleksams.

4.   Pritaikyti hibridinę SE/QCM-D metodiką siekiant ištirti (i) kovalentinę SARS-CoV-2 nukleokapsidės baltymų imobilizaciją ant 11-MUA savitvarkio sluoksnio ir (ii) sąveiką tarp specifinių antikūnų besiformuojant imuniniam kompleksui.

Šioje disertacijoje pateiktų tyrimų naujumas yra paremtas plonų metalų sluoksnių ir metalų oksidų struktūrų pritaikymui didelio jautrio biologinių jutiklių sistemoms. Šios sistemos - paremtos spektrinės elipsometrijos, kvarco kristalo mikrogravimetrijos su disipacija metodais arba jų jungtine matavimo metodika. Šalia to, ši disertacija buvo rengiama COVID 19 pandemijos metu taigi SARS-CoV-2 viruso struktūrinių baltymų sąveika su specifiniais antikūnais buvo tiriami, šiais metodais optiniais ir akustiniais metodais, pirmą kartą.

Žmogaus serumo albumino adsorbcijos tyrimas ant pAAO dangos parodė jog HSA baltymai gali būti naudojami paviršiaus blokavimui siekiant sumažinti nespecifinę sąveiką tarp atpažinimo elemento ir analitės pAAO dangos paviršiuje.

Tyrimo metu siekiant nustatyti ZnO-NWs pritaikomumą biologiniams jutikliams nustatyta, jog ZnO-NWs danga pasižymi dideliu nanovielų tankiu, tai rodo ilga BSA kovalentinės imobilizacijos kinetika ir ilgas bazinės linijos nusistovėjimo laikas. Suformuotas ZnO-NWs dangos paviršius buvo apie 13 kartų jautresnis lūžio rodiklio pokyčiams nei plokščias ZnO paviršius ir 6,6 karto jautresnis atsispindėjusios šviesos intensyvumo pokyčiams. Tai rodo jog ZnO-NWs paviršius pasižymi savybėmis, kurios gali būti naudingos optiniams biologiniams jutikliams.

Sąveikos tyrimai tarp kovalentiškai imobilizuotų SARS-CoV-2 S baltymo mutacijų ir specifinių antikūnų iš realių mėginių taikant TIRE metodą leidžia nustatyti imuninio komplekso SCoV2-S/pAb-SCoV2-S afiniškumo konstantas. Tai parodo, pirmą kartą, kad šie antikūnai suformuoti imūninės

sistemos po vakcinacijos gali jungtis su -S, -αS, -βS baltymais, dideliu afiniškumu.

Pirmą kartą, hibridinis SE/QCM-D metodas buvo pritaikytas tiriant imuninio komplekso susiformavimą tarp kovalentiškai imobilizuoto SCoV2-N ir anti-SCoV2-N. Rezultatai parodė jog anti-SCoV2-N lankstumas yra svarbus veiksnys esant dvivalentei sąveikai su mažų dimensijų SCoV2-N baltymais.

Ginamieji teiginiai:

• Elektrochemiškai suformuota anodinė aliuminio oksido danga, kurios storis 300 nm, porų diametras 40 nm, o atstumas tarp porų 110 nm, gali kaupti HSA baltymus iki 100 kartų didesnes koncentracijas nei aplinkoje, keičiant bendrą lūžio rodiklį per 7.5% taip leidžiant kiekybiškai nustatyti HSA baltymus.

• Elektrochemiškai suformuotas 40 nm storio ir 350 nm ilgio ZnO-NWs paviršius ant ITO/stiklo, gali būti naudojamas BSA baltymų imobilizacijai, lyginant su plokščio ZnO struktūros paviršiumi elipsometrinis parametras $\mathit{\Delta}$ buvo jautresnis 2,15 karto, taigi ZnO-NWs gali pagerinti optinio BSA biologinio jutiklio jautrį.

• pAb-SCoV2-S ir SCoV2-S/-αS/-βS sąveikos pusiausvyros konstantos ir erdvinio išsidėstymo faktoriai, apskaičiuoti iš VVAE matavimų, rodo jog antikūnai susidarę žmogaus organizme po 1 „Vaxzevria" dozės gali sėkmingai suformuoti imuninį kompleksą su kovalentiškai imobilizuotais skirtingų mutacijų S baltymais.

• SE/QCM-D matavimo metu nustatyta, jog kovalentiškai imobilizuotų SCoV2-N monosluoksnis yra neelastiškas lyginant su anti-SCoV2-N monosluoksniu, kuris pasižymi viskoelastinėmis savybėmis su 4 kartus didesnėmis disipacijos vertėmis. Antikūnai pasižymi lankstumu, o tai leidžia jiems prisijungti prie SCoV2-N baltymo naudojant abi Fab dalis.

LITERATŪROS APŽVALGA

Šis darbas yra skirtas tirti plonų metalų sluoksnių ir metalo oksidų nanostruktūrų pritaikymą optiniams biologiniams jutikliams.

Nanostruktūros - tai struktūros, kurių vienas iš matmenų yra nanometrinėje skalėje (1 - 100 nm) [34]. Kai metalo ar metalo oksido dalelės dydis yra palaipsniui apribojamas iki nanometrinio dydžio, šios struktūros tūris mažėja ir taip atsiranda vis didesnis kiekis paviršinių atomų [38]. Paviršiniai atomai pasižymi didesne paviršiaus energija ir aktyvumu nei atomai esantys dalelės tūryje [9]. Šis apribojimas gali stipriai pakeisti metalų ir metalų oksidų

termines, elektrines ir optines savybes [35–37]. Taip pat, nanostruktūrizuoti paviršiai pasižymi padidėjusiu paviršiaus plotu, kurį galima išnaudoti imobilizuojant didelį kiekį biologiškai aktyvių medžiagų, taip pritaikant paviršių biologinių jutiklių gamybai [5,39].

Porėtas anodinis aliuminio oksidas (pAAO). Tai oksido danga, elektrochemiškai formuojama anoduojant aliuminį rūgštiniuose elektrolituose. Anodavimo metu formuojasi savitvarkės, šešiakampiais išsidėsčiusios, nanoporos. Šios poros - cilindrinės, turinčios pastovų diametrą ir išsidėstymą tarp porų [54]. Norint suformuoti tolygiai išsidėsčiusias nanoporas yra taikomas dvipakopis anodavimas, išrastas 1995 metais japonų mokslininkų Masuda ir Fukuda [131]. pAAO dangos struktūra priklauso nuo elektrolito kuriame yra atliekamas anodavimas sudėties, pH ir temperatūros, bei nuo anodavimo įtampos ir trukmės. Taip pat, anodavimo metu į besiformuojančią oksidinę dangą įsiskverbia anijonai, taigi rūgštinio elektrolito sudėtis gali paveikti pAAO dangos spalvą ar suteikti fotoliuminenscencinių sąvybių [55,56].

pAAO dangos yra dažnai pritaikomos kaip šabloninė medžiaga formuojant nanostruktūras. Tačiau pAAO dangos pasižymi tokiomis savybėmis, kaip fotoliuminescencija, optinis pralaidumas ir atspindžio geba, kurias galima pritaikyti optinių biologinių jutiklių gamybai. Unikalią pAAO struktūrą galima ne tik pritaikyti jutiklio gamybai, bet ir išnaudoti pAAO poras, kaip talpą biologinėms medžiagoms [4,13,58,59].

Cinko oksido nanovielos (angl. zinc oxide nanowires, ZnO-NWs). ZnO nanostruktūros yra termiškai stabilios, mechaniškai atsparios ir pasižymi biologiniu suderinamumu, taigi dažnai taikomos biologiniams jutikliams [62]. ZnO-NWs galima formuoti keliais metodais pavyzdžiui: atomo sluoksnio nusodinimu [63], cheminiu nusodinimu [50,64] ar elektriniu nusodinimu [5,65]. Suformuotos ZnO-NWs pasižymi unikaliomis elektroninėmis bei optinėmis savybėmis, kurių dėka ZnO-NWs yra dažnai taikomos fotodetektorių, jutiklių ir Saulės elementų kūrime [66–68]. Šalia to, ZnO-NWs savybes galima koreguoti, selektyviai legiruojant priemaišomis (metalų jonais) [70].

ZnO-NWs struktūros yra stabilios ir pasižymi dideliu paviršiaus plotu, taigi puikiai tinka funkcionalizavimui baltymais. ZnO-NWs funkcionalizavimas gali būti atliekamas trimis būdais: (i) elektrostatine sąveika su žemų izoelektrinių verčių biologinėmis molekulėmis (fermentai, antikūnai, DNR) [73]; (ii) formuojant siloksano sluoksnį su paviršinėmis funkcinėmis grupėmis [5]; (iii) nusodinant ir funkcionalizuojant Au nanodaleles paviršinėmis funkcinėmis grupėmis, naudojant organines medžiagas su -SH grupe, per Au-SH sąveiką [74].

Plonų Au sluoksnių pritaikymas biojutikliuose. Au yra vienas iš plačiausiai naudojamų metalų biojutikliuose dėl Au biosuderinamumo, optinių ir elektroninių savybių bei paprastų paviršiaus funkcionalizavimo protokolų [77–79]. Ploni Au sluoksniai (~ 50 nm) gali būti naudojami elektromagnetinių bangų generavimui ir yra plačiai pritaikomi paviršiaus plazmonų rezonanso sužadinimui [80–82].

Au dengti kvarco kristalai yra dažnai taikomi pjezoelektriniuose jutikliuose pavyzdžiui, kvarco kristalo mikrogravimetrijoje su disipacija (QCM-D). Dažnai QCM-D metodu yra matuojamas masės pokytis tirpaluose, tokiems matavimams yra reikalingas stabilus ir lengvai funkcionalizuojamas paviršius [7,83].

Žmogaus (HSA) ir jaučio (BSA) serumų albuminų modelinės sistemos. Serumo albuminai (HSA ir BSA) yra vandenyje tirpūs baltymai, kurių gausu (35 - 50 mg/mL) stuburinių gyvūnų kraujo plazmoje [88]. BSA ir HSA yra atsakingi už osmosinio slėgio palaikymą kraujyje ir veikia kaip pernešėjas daugelyje funkcijų [89].

BSA ir HSA yra naudojami, kaip modeliniai antigenai imunologijoje dėl žinomos struktūros ir prieinamumo [90]. BSA tapo standartiniu baltymu išbandant naujus pagrindus biojutikliams [91–93].

SARS-CoV-2 viruso struktūriniai baltymai ir antikūnai. SARS-CoV-2 virusas priklauso koronavirusų šeimai ir yra sferos formos su 108 ± 8 nm skersmeniu. Viruso paviršius yra padengtas lanksčiais spyglio baltymais (SCoV2-S), kurie viruso paviršiaus atžvilgiu gali pakrypti iki 90°. Viruso membrana yra sudaryta iš membraninio baltymo (SCoV2-M) ir apvalkalo baltymo (SCoV2-E). Viruso viduje yra nukleokapsidės (SCoV2-N) baltymas ir viruso RNR genomas [94].

Nukleokapsidės (SCoV2-N) baltymas yra svarbus struktūrinis baltymas esantis SARS-CoV-2 viruso viduje, atsakingas už viruso replikaciją. Tai mažos masės (48 kDa) sferinis baltymas, kurio skersmuo ~3 nm. SCoV2-N baltymas yra sudarytas iš dviejų struktūrinių domenų: NTD (RNR jungimosi domeno) ir CTD (dimerizacijos domeno), ir pasižymi stipriu teigiamu krūviu, tai parodo geba jungtis su nespecifinėmis nukleorūgštimis [97]. Pagrindinė SCoV2-N funkcija yra prisijungti prie virusinės RNR ir sudaryti kompleksą, kuris patenka į užkrečiamą ląstelę, dalyvauja replikacijoje [94].

Spyglio (SCoV2-S) baltymas yra didelės masės trimeras, maždaug 450 - 600 kDa, kuris atlieka svarbų vaidmenį viruso infekcijos metu: atpažįsta šeimininko ląstelės receptorius ir tarpininkauja susiliejimui tarp viruso bei šeimininko ląstelės. Šis baltymas sukelia stiprų imuninį atsaką, taigi jis tapo vakcinų, gydymo ir testavimo priemonių nuo SARS-CoV-2 taikinys [98,99]. SCoV2-S yra padalintas į S1 ir S2 subvienetus; S1 subvienete yra receptorių

jungimosi domenas (RBD), kuris SARS-CoV-2 infekcijos metu jungiasi prie angiotenziną konvertuojančio fermento 2 (ACE2), taip susiliejant viruso ir šeimininko membranoms. RBD dalis yra reikšminga ne tik viruso replikacijai, bet taip pat viruso neutralizavimui specifiniais antikūnais prieš RBD [100,101].

Pasaulio Sveikatos Organizacija (PSO) nurodė penkias SARS-CoV-2 mutacijas, kaip susirūpinimą keliančius variantus (VOC); alfa, beta, gama, delta ir omikron, atsižvelgiant į padidėjusį variantų užkrečiamumą ir infekcijos sunkumą. Variantai atsiranda dėl koronaviruso struktūrinių baltymų mutacijų, ypač SCoV2-S baltymo. Kadangi aminorūgščių seka RBD regione gali daryti stiprią įtaką SCoV2-S jungimuisi su ACE2 ir SARS-CoV-2 užkrečiamumui [102,103]. Alfa variantas, pirmą kartą aptiktas Jungtinėje Karalystėje, turėjo 23 mutacijas. Iš jų 6 buvo aminorūgščių keitimai SCoV2-S baltyme. Šis variantas buvo susijęs su padidėjusiu užkrečiamumu ir COVID-19 atvejų pagausėjimu [104]. Beta variantas, aptiktas Pietų Afrikos Respublikoje, turėjo 5 papildomus aminorūgščių pakeitimus SCoV2-S baltyme. Tikėtina, jog papildomi pakeitimai galimai sumažino antikūnų sąveikos stiprumą, kadangi atliktuose tyrimuose beveik pusei (48%) sveikstančių pacientų kraujo plazmos mėginių nepavyko neutralizuoti beta varianto [105].

Antikūnai prieš SARS-CoV-2 viruso struktūrinius baltymus susidaro kaip imuninis atsakas SARS-CoV-2 infekcijos arba vakcinacijos metu. Nuo 10 ligos dienos kraujo plazmoje yra daug IgG klasės antikūnų prieš SCoV2-N baltymą, kuris infekcijos metu yra labai imunogeniškas [110]. Didelis kiekis antikūnų prieš SCoV2-N (anti-SCoV2-N) gali būti laikomu COVID-19 infekcijos klinikinės eigos prognozės kriterijumi [111]. Imuninio komplekso susiformavimo tarp SCoV2-N ir anti-SCoV2-N analizės publikacija yra prisegta (4 Straipsnis) [7]. Siekiant užkirsti kelią COVID-19 plitimui organizme, antikūnai prieš SCoV2-S baltymą (anti-SCoV2-S) yra gaminami imuninio atsako metu, kad blokuotų viruso ir ACE2 receptoriaus sąveiką. Viruso neutralizavimo antikūnais gebėjimas gali būti įvertintas nustatant antikūnų afiniškumą, kai susidaro imuninis kompleksas su SCoV2-S. Išsami anti-SCoV2-S sąveikos ir SCoV2-S, SCoV2-αS ir SCOV2-βS analizė prisegta (3 Straipsnis) [82].

Porėto aliuminio oksido (pAAO) formavimas. Tyrime naudota pAAO danga yra suformuota ant labai gryno (99,999%) aliuminio pagrindo naudojant dviejų pakopų anodavimo metodą. Aliuminio pagrindai buvo supjaustyti, nuriebalinti ir elektrochemiškai poliruoti 0 °C perchlorato rūgšties-etanolio mišinyje, 1 dalis 60% $HClO_4$ ir 4 dalys 96% etanolio, esant 15 V įtampai. Aliuminio pagrindai toliau buvo anoduoti 0,3 M oksalo rūgšties tirpale 2 val. esant 40 V įtampai ir suformuota oksido danga buvo ištirpinta chromo-fosforo rūgščių mišinyje (4% H_2CrO_4 ir 11% H_3PO_4) ties 70 °C. Taip ant aliuminio paviršiaus susidaro vienodų įdubimų raštas, kuris vėliau vėl anoduojamas oksalo rūgšties tirpale (0,3M; 15V; 80s). Po antro anodavimo, pAAO nanoporos buvo išplėstos su 5% fosforo rūgšties tirpalu, nuplautos vandeniu ir išdžiovintos.

Cinko oksido nanovielų (ZnO-NWs) formavimas. ZnO-NWs buvo suformuotos ant indžio-alavo oksidu (ITO) dengtų stiklo substratų. 20 nm ZnO sluoksnis buvo padengtas ant ITO/stiklo, atominio sluoksnio nusodinimo metodu (ALD) kaip pirmtakais naudojant dietilcinką ir dejonizuotą vandenį. Toliau ZnO-NWs buvo auginamos ant ZnO/ITO/stiklo substrato, naudojant elektrocheminį nusodinimą trijų elektrodų konfigūracijoje (ZnO/ITO/stiklas darbinis, Pt pagalbinis, Ag/AgCl palyginamasis). Nusodinimo tirpalą sudarė 0,05 mM ZnCl2 ir 0,1 M KCl, elektrocheminis nusodinimas buvo vykdomas 80 °C temperatūroje, esant -1V įtampai, pastoviai leidžiant O_2 dujas į elektrolitą.

Paviršių funkcionalizavimas baltymų kovalentinei imobilizacijai. Dažniausiai taikoma paviršiaus modifikacija - organinių funkcinių grupių (-NH_2, -COOH) pridėjimas prie paviršiaus, siekiant kovalentiškai imobilizuoti baltymus [115,116].

Au gali būti funkcionalizuojamas naudojant molekules su funkcinėmis grupėmis, kurios stipriai jungiasi su Au atomais, pavyzdžiui tiolio grupės (-SH). Tiokarboksirūgštys, tokios kaip 11-merkaptoundekano rūgštis (11-MUA), yra dažnai naudojamos Au paviršiams funkcionalizuoti karboksirūgšties grupėmis. Šios molekulės aukso paviršiuje susiformuoja į savaime susidarantį monosluoksnį (SAM). Šis SAM leidžia per -COOH funkcines grupes kovalentiškai jungtis baltymams, suteikdamas stabilų pagrindą imobilizacijai ir sumažindamas nespecifinį jungimąsi [118]. 11-MUA molekulių SAM sudarymas prasideda nuo Au paviršiaus plovimo heksanu, metanoliu ir palaikant 3 min. ultragarso vonelėje, metanolyje. Išdžiūvus aukso substratai yra dedami į 1 mM 11-MUA tirpalą metanolyje ir laikomi 18 val.

Metalų oksidams funkcionalizuoti dažnai naudojami silanai. 3-aminopropiletoksisilanas (APTES) yra silano pagrindo molekulė, naudojama oksido paviršiams funkcionalizuoti, siekiant kovalentiškai imobilizuoti baltymus. APTES molekulė yra sudaryta iš 3 etoksigrupių ir 1 amino grupės. Funkcionalizacijos proceso metu APTES molekulės polimerizuojasi ant oksido paviršiaus, sudarydamos monosluoksnį. Taip susiformuoja siloksano jungčių tinklas prisijungęs metalo oksido sluoksnio su toliau nuo paviršiaus išsidėsčiusiomis amino grupėmis. APTES nusodinimas atliktas garų nusodinimo metodu. Mažas APTES kiekis buvo padėtas šalia mėginių uždaroje Petri lėkštutėje ir kaitintas orkaitėje 90 °C per naktį. Modifikuoti mėginiai buvo nuvalyti toluenu, etanoliu ir distiliuotu vandeniu, ir išdžiovinti 110 °C orkaitėje.

Kovalentinė baltymų imobilizacija. Baltymus galima pritvirtinti prie paviršių, kurie yra funkcionalizuoti karboksirūgšties (-COOH) ar amino grupėmis (-NH_2) naudojantis mišiniu iš N-etil-N'-(3-(dimetilamino)-propil)karbodiimido hidrochlorido (EDC) ir N-hidroksisukcinimido (NHS). Šis EDC/NHS mišinys paprastai vadinamas „aktyvacijos" tirpalu ir yra naudojamas baltymų imobilizacijai, cheminiais ryšiais sujungiant karboksirūgšties ir amino grupes.

Aktyvacijos metu, prie karboksirūgšties grupės prisijungia EDC molekulė ir suformuoja o-acilizokarbamido esterį, šis nestabilus esteris jungiasi su NHS molekulę ir sudaro pusiau stabilų NHS esterį, kuris reaguoja su -NH_2 grupėmis ir sudaro stabilų cheminį ryšį. Imobilizacijos metodika priklauso nuo substrato paviršiuje esančių grupių. Jei paviršiuje yra -COOH grupės 0,1M NHS ir 0,4M EDC mišinys yra įleidžiamas į matavimo celę ir laikomas 15 min t.y. aktyvuojamas paviršius. Jei paviršiuje yra -NH_2 tai aktyvavimo tirpalas yra sumaišomas su imobilizuojamu baltymu t.y. aktyvuojamas baltymas. Sekant imobilizaciją yra atliekamas blokavimas, siekiant deaktyvuoti likusias laisvas NHS-esterio grupes pavyzdžiui, naudojant 8,5 pH 1M etanolamino tirpalą. Tiriant imobilizuoto baltymo sąveiką su analitėmis ir siekiant atlikti pakartotinį eksperimentą yra atliekama regeneracija. Tai procesas, kurio metu yra šalinamos prie imobilizuoto baltymo prisijungusios molekulės ar baltymai. Siekiant išlaikyti baltymo sluoksnio vientisumą ir sumažinti denatūravimo riziką, regeneracija atliekama kuo švelnesnėmis sąlygomis. Tyrimo metu naudotas 10 mM NaOH, 17,34 mM SDS tirpalas.

Spektrinė elipsometrija. Elipsometriniai matavimai buvo atlikti su *J.A. Woollam M2000X* spektriniu elipsometru, substratų ir baltymų optinėms savybėms nustatyti. Buvo naudojamos trys matavimo konfigūracijos: standartinis režimas, visiško vidaus atspindžio režimas ir hibridinis režimas su QCM-D. Standartinio režimo metu, bandinys yra pastatomas ant matavimo

stalelio, nustatomas šviesos kritimo kampas ir pamatuojamas elipsometrinių parametrų Ψ ir Δ spektrai 200 nm - 1000 nm ruože. Matavimas visiško vidaus atspindžio elipsometrijos (*angl.* Total Internal Reflection Ellipsometry, TIRE) režime yra atliekamas tefloninėje celėje su primontuota stiklo prizme, taip atsiranda galimybė įleisti ir keisti tirpalus matavimo metu. TIRE režime dėl naudojamos prizmės yra apribojamas šviesos kritimo kampas, tačiau yra pasiekiamas didesnis jautrumas. Hibridinis matavimas (SE/QCM-D) atliktas QCM-D modulyje, skirtame atlikti matavimus kartu su spektrine elipsometrija. Modulyje yra optiniai langai skirti krentančiai ir atsispindėjusiai šviesai. Šviesos kritimo kampas fiksuotas ties 65°, o temperatūra 20 °C.

Kvarco kristalo mikrogravimetrija su disipacija (QCM-D). QCM-D matavimai atlikti naudojant Q-Sense Explorer, veikianti ties 5 MHz pagrindiniu dažniu ir galinčiu įrašyti iki 6 obertonų vienu metu. Matavimai įrašyti naudojantis QSoft401 programinę įrangą ir duomenys analizuoti naudojantis Dfind programine įranga, leidžiančia viskoelastinį modeliavimą. Registruojami parametrai: ΔF - dažnio pokytis, ΔD - energijos išsklaidymas. Šie parametrai naudojami adsorbuotos medžiagos kiekiui apskaičiuoti ir, jei reikia, nustatyti susidariusio sluoksnio viskoelastines savybes.

REZULTATŲ APTARIMAS

HSA adsorbcija į pAAO. 1-jame straipsnyje nagrinėjama žmogaus serumo albumino (HSA) adsorbcija ir desorbcija į pAAO. Šis tyrimas svarbus siekiant pAAO pritaikymo baltymų atskyrimui, gryninimui ar biojutiklio kūrimui. Tyrime spektrinės elipsometrijos metodu charakterizuota pAAO danga ir patikrinta didelių molekulių, tokių kaip HSA, geba adsorbuotis nanoporose.

Tyrimo metu iš elipsometrinio parametro Δ poslinkio, buvo galima matyti, jog HSA adsorbcija į pAAO buvo grįžtama (Fig. 7, 27 p.). Δ parametro spektras slinkosi link ilgesnių bangų ilgio HSA adsorbcijos metu ir trumpesnių bangų ilgių link HSA desorbcijos metu. Siekiant nustatyti ir kiekybiškai įvertinti HSA molekulių adsorbciją į pAAO paviršių ir poras, įvertinant lūžio rodiklio (*n*) pokyčius, buvo naudojamas efektyvus terpės aproksimacijos modelis [4]. Pirmiausia, buvo įvertinta pAAO/oro struktūra: sluoksnių *n*, sluoksnių storiai (*d*), procentinė oro dalis ir paviršiaus šiurkštumas. Toliau, *n* pokyčiai atsirandantys nuo HSA adsorbcijos ar desorbcijos buvo modeliuojami naudojant Košį funkciją. Gautos *n* atskiros dispersijos visai pAAO struktūrai ir pAAO nanoporoms (Fig. 8, 28 p.). Nustatyta HSA koncentracija nanoporose naudojant matematinę išraišką, kuri atitinka tiesinę priklausomybę tarp baltymo tirpalo *n* verčių ir baltymų koncentracijos [121]. Duomenys pateikti (Tab. 1, 29 p.) parodo, kad baltymų

koncentracija nanoporose yra daug didesnė nei tirpale (200 - 600 kartų) ir priklauso nuo adsorbcijos laiko. Tyrimas taip pat parodė, kad HSA adsorbcija yra lėta (3.23 mg·cm^{-3}·min^{-1}), palyginus su HSA desorbcija (21.2 mg·cm^{-3}·min^{-1}) ir plovimas buferiu ar dejonizuotu vandeniu yra nepakankamas pilnai HSA desorbcijai.

Kovalentinė BSA imobilizacija ant ZnO nanovielų. 2-jame straipsnyje pagrindinis dėmesys yra skiriamas ZnO-NWs panaudojimui biologinio jutiklio pritaikymui, kovalentiškai imobilizuojant jaučio serumo albumino molekules (BSA).

Tam, kad būtų išanalizuotas suformuotų ZnO-NWs indelis į optinį atsaką lyginant su ZnO, buvo atliktas stiklo/ITO/ZnO daugiasluoksnės sistemos modeliavimas. Simuliuoti elipsometrinių parametrų spektrai buvo lyginami su eksperimentiškai gautomis daugiasluoksnėmis struktūromis, turinčiomis ZnO-NWs. Simuliuoti ZnO ir eksperimentiniai ZnO-NWs duomenys rodo, kad ZnO-NWs jautrumas *n* pokyčiams yra 13 kartų didesnis (Fig. 9, 30 p.). Taigi, ZnO-NWs struktūrų funkcionalizavimas APTES ir BSA sluoksniais yra akivaizdžiai matomas elipsometrinio parametro *Δ* spektrų poslinkiuose.

Taip pat registruoti atspindžio intensyvumo spektrai (*R*) lyginant plokščius ZnO ir ZnO-NWs mėginius, po APTES ir BSA modifikacijų (Fig. 10, 32 p.). Plokščiųjų ZnO struktūrų *R* spektrai prieš ir po BSA imobilizacijos neparodė reikšmingo skirtumo, abejais atvejais atspindžio intensyvumas nuo ZnO bandinių buvo stiprus. Tuo tarpu ZnO-NWs struktūros *R* vertės dėl stiprios šviesos sklaidos buvo žemos, tačiau tai nepaveikė elipsometrinių spektrų kokybės. *R* vertės padidėjo BSA kovalentinės imobilizacijos metu, tai buvo siejama su ZnO-NWs struktūrų difuzinės sklaidos sumažėjimu, kai susiformavęs BSA monosluoksnis sumažina paviršiaus šiurkštumą.

Toliau analizuota BSA kovalentinės imobilizacijos kinetika ant APTES/ZnO-NWs/ZnO/ITO/stiklo substrato, naudojant TIRE režimą ties 390 nm bangos ilgiu (Fig. 11, 33 p.). BSA kinetiką galima išskirti į dvi fazes: I fazė trunka 5s kur bendras *Δ* pokytis yra 0,5°, o II-a fazė trunka virš 100 min., kur imobilizuojasi didžioji dalis įleisto BSA ir *Δ* pokytis - 5,61°. Lyginant su plokščiu ZnO substratu, ZnO-NWs parodė didesnį jautrumą baltymų imobilizacijai ir galima teigti jog ZnO-NWs struktūros rodo galimą pritaikymą optiniams biojutikliams.

Įvertinta difuzijos įtaka BSA molekulių kovalentinei imobilizacijai į ZnO-NWs paviršių (Fig. 12, 35 p.). Apskaičiuota difuzijos koeficiento vertė - 6 kartus mažesnė nei BSA difuzija PBS tirpale.

Specifinių antikūnų sąveika su SCoV2-S, SCoV2-αS, SCoV2-βS. Žmogaus imuninė sistema gamina specifinius antikūnus prieš SARS-CoV-2 viruso spyglio baltymą, bet virusui mutuojant susidarantys pokyčiai spyglio

baltyme gali turėti įtakos viruso išlikimui, plitimui ar ligos sunkumui. 3-jame straipsnyje aprašoma sąveikos kinetika tarp polikloninių žmogaus antikūnų (pAb-SCoV2-S) gautų skiedžiant vakcinuoto savanorio kraujo serumą ir kovalentiškai imobilizuotų SCoV2-S, SCoV2-αS, SCoV2-βS (Fig. 13, 37 p.). Sąveika tirta ant 11-MUA modifikuoto aukso paviršiaus, matuojant TIRE režime.

Baltymai buvo imobilizuoti ant 11-MUA paviršiaus ir buvo stebima imobilizacijos kinetika, kur Ψ pokytis: 13,5° SCoV2-S, 14° SCoV2-αS ir 11° SCoV2-βS. Toliau buvo suleisti serumo mėginiai ir stebima giminingumo sąveikos kinetika tarp SCoV2-S, SCoV2-αS ir SCoV2-βS, ir pAb-SCoV2-S. Įvykdžius kovalentinę imobilizaciją ir susidarius imuniniam kompleksui, buvo registruoti Ψ ir Δ pokyčiai laike, ir spektre (Fig. 14, 38 p.).

Imuninių kompleksų susidarymas tarp SARS-CoV-2 spyglio baltymų variantų (SCoV2-S, SCoV2-αS, SCoV2-βS) ir specifinių antikūnų (pAb-SCoV2-S) buvo analizuojamas normalizuojant n pokytį ir taikant dviejų pakopų matematinį modelį (Fig. 15, 39 p.). Modelį pritaikius buvo galima apskaičiuoti termodinaminius parametrus, įskaitant asociacijos ir disociacijos greičio konstantas, pusiausvyros konstantas ir sterinius veiksnius (Tab. 2, 40 p.). Įvertinus apskaičiuotas imuninio komplekso formavimosi termodinaminius parametrus, matoma, jog pAb-SCoV2-S prieš SCoV2-S turi mažiausias disociacijos konstantas. Tuo tarpu SCoV2-αS ir SCoV2-βS disociacijos konstantos yra didesnės, tačiau vertės yra tos pačios eilės, o tai rodo sėkmingą apsaugą nuo SARS-CoV-2 variantų. Nustatyti imuninių kompleksų steriniai faktoriai (tikimybė susiformuoti imuniniam kompleksui, išreikšta procentine dalimi) ir nustatyta, kad SCoV2-S baltymui yra keliami 100 kartų mažesni reikalavimai nei imuniniam kompleksui su SCoV2-N.

SE/QCM-D režime tirta SCoV2-N sąveika su specifiniais antikūnais. Šiame darbe (4-jame straipsnyje) buvo tiriamas imuninio komplekso susidarymas tarp imobilizuoto SARS-CoV-2 nukleokapsidės (SCoV2-N) baltymo ir specifinių antikūnų prieš nukleokapsidę (anti-SCoV2-N) (Fig. 16, 41 p.). Analizuotas anti-SCoV2-N Fab fragmentų lankstumas imuninio komplekso formavimosi metu naudojant hibridinį SE/QCM-D režimą.

Hibridinis SE/QCM-D matavimo režimas leidžia atlikti tą patį matavimą dvejomis, viena, kitą papildančiomis metodikomis: SE metodas suteikia informaciją apie monosluoksnių dielektrines sąvybes, QCM-D metodas - apie mechanines savybes. Tyrimo metu buvo stebimos trys sąveikos: kovalentinis SCoV2-N imobilizavimas ant 11-MUA, anti-SCoV2-N giminingumo sąveika su SCoV2-N, anti-BSA nespecifinė sąveika su SCoV2-N.

QCM-D duomenys pateikti $\Delta D/\Delta F$ grafike (Fig. 17, 42 p.) leidžia pamatyti, kaip formuojasi SCoV2-N ir anti-SCoV2-N monosluoksniai, bei

matyti viskoelastinių savybių skirtumus tarp jų. Kovalentinio SCoV2-N imobilizavimo metu buvo stebimas greitas pradinis imobilizacijos greitis, po kurios sekė lėtesnė imobilizacija. Disipacijos pokytis buvo linijinis ir buvo apibrėžtas žema K_1 verte (K_1=0.031), tai rodo, jog susiformavęs SCoV2-N monosluoksnis yra kompaktiškas ir palyginus kietas, nepasižymi viskoelastinėmis savybėmis. Imuninio komplekso susiformavimą apibrėžė dvi liestinės (K_2=0,134 ir K_3=0,121), kurios rodo, kad imuninio komplekso formavimosi metu vyko konformaciniai pokyčiai ar persitvarkymai. Šalia to, anti-SCoV2-N monosluoksnis imuniniame komplekse pasižymi didelėmis disipacijos vertėmis ir taipogi viskoelastinėmis savybėmis.

Toliau buvo apskaičiuotos baltymų paviršinės masės, naudojant SE ir QCM-D metodus. Apskaičiuotos paviršinės masės skiriasi priklausomai nuo matavimo metodo ($\Gamma^{SE}<\Gamma^{QCM-D}$) (Fig. 18, 44 p.). SE metodu apskaičiuota monosluoksnio paviršinė masė yra vadinama „sausa", nes masės pokytis priklauso tik nuo baltymo (SCoV2-N ar anti-SCoV2-N) indelio. Tuo tarpu, QCM-D metodu apskaičiuota monosluoksnio masė yra vadinama „šlapia", nes kartu su baltymo molekulėmis yra įskaičiuojamas ir aplinkos tirpalo indelis. Šis paviršinių masių skirtumas leido nustatyti monosluoksnio hidrataciją: 0,7 SCoV2-N ir 0,83 anti-SCoV2-N. Siekiant interpretuoti hidratacijos vertes, apart PBS kiekio įvertinimo, buvo sukurtas geometrinis modelis (Fig. 19, 46 p.). Modelyje daroma prielaida, kad SCoV2-N molekulės sudaro kvadratinės gardelės monosluoksnį. Taigi, kiekvienos gardelės centre yra SCoV2-N molekulė, o anti-SCoV2-N yra išsidėsčiusi taip, jog yra prisijungusi prie dviejų SCoV2-N molekulių įstrižai. Naudojantis hidratacijos vertėmis apskaičiuota gardelės konstanta (d_l = 7,9 nm) ir įstrižainės atstumas (d_d = 11,2 nm). Nustačius gardelės aukštį, kaip eksperimentiškai nustatytų SCoV2-N ir anti-SCoV2-N monosluoksnių storių sumą (14 nm), gautas gardelės tūris. Įvertinus baltymų molekulių išmatavimus gauta teorinė imuninio komplekso hidratacijos vertė (0,5), kuri buvo panaši eksperimentinei (0,47).

IŠVADOS

1. HSA koncentracija pAAO nanoporosė tiesiogiai kinta nuo inkubacijos laiko, kur didesni HSA kiekiai yra aptinkami po ilgesnės inkubacijos. pAAO plovimas PBS buferiu ne visiškai desorbuoja HSA molekules iš nanoporų ir net po 16 valandų plovimo dejonizuotu vandeniu HSA koncentracija nanoporose išlieka apie 100 didesnė nei tirpale. HSA koncentracija prieš nuplovimą buvo nuo 200 iki 600 kartų didesnė nei tirpale,

o tai rodo, kad HSA gali būti naudojamas paviršiaus blokavimui. Tačiau tūrėtų būti naudojamas atsargiai, jei yra tikimasi nespecifinės sąveikos sumažėjimo.

2. Plokščių ZnO ir ZnO-NWs paviršių palyginimas parodė, jog ZnO-NWs pritaikymas biologiniams jutikliams padidino optinį jautrumą TIRE režime: 13 kartų *n* pokyčiams ir 6,6 karto *R* pokyčiams. Jautrumo padidėjimą galima priskirti daugiakartiniam atspindžiui tarp ZnO-NWs TIRE režime, taip pat padidintam paviršiaus plotui, kuris leido imobilizuoti didesnį kiekį BSA molekulių.

3. Specifiniai antikūnai, gauti iš vakcinuoto savanorio serumo, sudarė didelio afiniškumo iminius kompleksus su SCoV2-S, SCoV2-αS ir SCoV2-βS. Iminio komplekso susidarymo termodinaminiai parametrai buvo nustatyti naudojant dviejų pakopų negrįžtamo jungimosi kinetinį modelį. Iš nustatytų iminio komplekso formavimosi K_D verčių matyti, kad aminorūgščių pakeitimų padidėjimas, spyglio baltymui mutuojant, RBD dalyje sumažina afiniškumą specifiniams antikūnams. Tačiau po vakcinacijos susiformavę antikūnai, gali prisijungti prie SCoV2-S, SCoV2-αS ir SCoV2-βS baltymų su dideliu afiniškumu. Šis tyrimas galėtų būti naudingas kuriant veiksmingus COVID-19 imunojutiklius.

4. SCoV2-N monosluoksnį, susidarantį kovalentinės imobilizacijos metu ant kietos medžiagos ir skysčio ribos, galima apibūdinti kaip standų sluoksnį dėl mažų ΔD verčių. Priešingai, anti-SCoV2-N monosluoksnis po sąveikos su kovalentiškai imobilizuotu SCoV2-N sudarė minkštą, lankstų ir klampų sluoksnį su 3,9 karto didesnėmis ΔD vertėmis. Apskaičiuotos teorinės iminio komplekso sluoksnio hidratacijos vertės buvo 0,5, o eksperimentinės vertės buvo 0,47. Taip pat, buvo nustatyta, jog antikūnų Fab dalių lankstumas leidžia joms pasiekti toliau esančius SCoV2-N baltymus ir sukurti dvivalentę sąveiką tarp baltymų SCoV2-N/anti-SCoV2-N imuniniame komplekse.

CURRICULUM VITAE

PERSONAL INFORMATION

Name, Surname	Vincentas Mindaugas Mačiulis
Date of birth	1994-06-24
E-mail	vincentas.maciulis@ftmc.lt
	vincentmmaciulis@gmail.com

ACADEMIC EDUCATION

2013 – 2017	Vilnius University, Chemistry BSc
2017 – 2019	Vilnius University, Physical Sciences MSc

PROFESSIONAL EXPERIENCE

2019 – 2021	Engineer, Center for Physical Sciences and Technology Department of Functional Materials and Electronics Nanotechnology Laboratory, Vilnius, Lithuania
2021 – present	Junior Researcher, Center for Physical Sciences and Technology Department of Nanotechnology, Vilnius, Lithuania

INTERNSHIPS

2022-04 - 2022-05	European Institute of Membranes, Montpellier, France

PUBLISHED CONTRIBUTIONS TO ACADEMIC CONFERENCES

1.	Vincentas Mačiulis (poster presentation), Almira Ramanavičienė, Miglė Stančiauskaitė, Ieva Plikusienė. Metal oxide nanostructures in chemical sensors and biosensors, Open Readings 2023, Vilnius, April 18-21

2.	Vincentas Mačiulis (oral presentation, awarded for best category), Ieva Plikusienė, Silvija Juciutė, Justina Liesytė, Arūnas Ramanavičius, Zigmas Balevičius, Rimantas Slibinskas, Indrė Kučinskaitė-Kodzė, Martynas Simanavičius, Saulius Balevičius, Almira Ramanavičienė. Study of SARS-CoV-2 nucleocapsid protein and specific antibodies interaction by combined optical and acoustic methods, Chemistry & Chemical Technology 2022, Kaunas, Lithuania, October 14

3.	Vincentas Maciulis (poster presentation), Ieva Plikusiene, Zigmas Balevicius, Ernesta Buzavaite-Verteliene, Evaldas Ciplys, Martynas Simanavicius, Aurelija Zvirbliene, Rimantas Slibinskas, Arunas Ramanavicius, Almira Ramanaviciene. Evaluation of SARS-CoV-2 nucleocapsid protein and specific antibody interaction kinetics by total internal reflection ellipsometry, 7th International Conference on Bio-Sensing Technology 2022, Sitges, Spain, May 22-25

4.	Vincentas Mačiulis (poster presentation), Ieva Plikusienė, Silvija Juciutė, Justina Liesytė, Saulius Balevičius, Arūnas Ramanavičius, Vilius Vertelis, Almira Ramanavičienė, Assessment of ZnO nanowires application for the covalent proteins immobilization by total internal reflection ellipsometry, Open Readings 2022, Vilnius, March 15-18

5.	V. Maciulis (oral presentation, awarded for best in category), Evaluation of novel coronavirus SARS-CoV-2 nucleocapsid protein interaction with specific antibodies by total internal reflection ellipsometry, Fiztech 2021, Vilnius, October 20-21

6.	Vincentas Mačiulis (poster presentation), Ieva Plikusienė, Silvija Juciutė, Justina Liesytė, Almira Ramanavičienė, Arūnas Ramanavičius, Analysis of Interaction Kinetics between SARS-CoV-2 Nucleoprotein and Specific Antibody by Combined SE/QCM-D Method, Advanced Materials and Technologies, 2021, Palanga, August 23-27

7.	Vincentas Mačiulis (poster presentation), Ieva Plikusienė, Octavio Graniel, Mikhael Bechelany, Saulius Balevičius, Vilius Vertelis, Zigmas Balevičius, Anton Popov, Arūnas Ramanavičius, Almira Ramanavičienė Proteins immobilization sensing platform based on ZnO nanowires using total internal reflection ellipsometry, 31st World Congress on Biosensors 2020/2021, July 26-29

8.   V. Maciulis (poster presentation), S. Juciute, U. Malinovskis, D. Erts, A. Ramanavicius, A. Ramanaviciene, S. Balevicius, I. Plikusiene, Towards spectroscopic ellipsometry based biosensor: evaluation of human serum albumin adsorption to porous aluminium oxide, Open Readings 2021, online conference, March 16-19

9.   V. Maciulis (oral presentation), Application Al_2O_3 and ZnO nanostructures for optical albumin detection, Fiztech 2020, Vilnius, October 22-23

10.   V. Maciulis (poster presentation), I. Plikusiene, O.Graniel, M. Bechelany, S. Balevicius, V. Vertelis, Z. Balevicius, A. Popov, A. Ramanavicius, A Ramanaviciene, Towards application of ZnO nanowires in optical biosensor design, Advanced Materials and Technologies 2020, Palanga, August 24-28

11.   V. Maciulis (poster presentation), I. Plikusiene, A. Ramanaviciene, A. Popov, O. Graniel, M. Bechelany, A. Ramanavicius, Investigation of planar and nanostructured ZnO and Al_2O_3 in biosensors design, Open Readings 2020, Vilnius, March 17-20

CO-AUTHORED SCIENTIFIC PUBLICATIONS

1.   Maciulis V., Malinovskis U., Erts D., Ramanavicius A., Ramanaviciene A., Balevicius S., Juciute S., Plikusiene I. 2020. Porous Aluminium Oxide Coating for the Development of Spectroscopic Ellipsometry Based Biosensor: Evaluation of Human Serum Albumin Adsorption, *Coatings* 10(11): 1018.

2.   Plikusiene, I.; Maciulis, V.; Graniel, O.; Bechelany, M.; Balevicius, S.; Vertelis, V.; Balevicius, Z.; Popov, A.; Ramanavicius, A.; Ramanaviciene, A. Total Internal Reflection Ellipsometry for Kinetics-Based Assessment of Bovine Serum Albumin Immobilization on ZnO Nanowires. *Journal of Materials Chemistry C*, 2021, 9, 1345–1352.

3.   Plikusiene, I.; Maciulis, V.; Ramanaviciene, A.; Balevicius, Z.; Buzavaite-Verteliene, E.; Ciplys, E.; Slibinskas, R.; Simanavicius, M.; Zvirbliene, A.; Ramanavicius, A. Evaluation of Kinetics and Thermodynamics of Interaction between Immobilized SARS-CoV-2 Nucleoprotein and Specific Antibodies by Total Internal Reflection Ellipsometry. *Journal of Colloid and Interface Science*, 2021, 594, 195–203.

4.   Plikusienė, I.; Bužavaitė-Vertelienė, E.; Mačiulis, V.; Valavičius, A.; Ramanavičienė, A.; Balevičius, Z. Application of Tamm Plasmon Polaritons and Cavity Modes for Biosensing in the Combined Spectroscopic Ellipsometry and Quartz Crystal Microbalance Method. *Biosensors*, 2021, 11, 501.

5.   Plikusiene, I.; Maciulis, V.; Ramanavicius, A.; Ramanaviciene, A. Spectroscopic Ellipsometry and Quartz Crystal Microbalance with Dissipation for the Assessment of Polymer Layers and for the Application in Biosensing. *Polymers*, 2022, 14, 1056.

6.   Plikusiene, I.; Maciulis, V.; Juciute, S.; Maciuleviciene, R.; Balevicius, S.; Ramanavicius, A.; Ramanaviciene, A. Investigation and Comparison of Specific Antibodies' Affinity Interaction with SARS-CoV-2 Wild-Type, B.1.1.7, and B.1.351 Spike Protein by Total Internal Reflection Ellipsometry. *Biosensors*, 2022, 12, 351.

7.   Bužavaitė-Vertelienė, E.; Maciulis, V.; Anulytė, J.; Tolenis, T.; Baskys, A.; Plikusiene, I.; Balevičius, Z. Total Internal Reflection Ellipsometry Approach for Bloch Surface Waves Biosensing Applications. *Biosensors*, 2022, 12, 584.

8.   Plikusiene, I.; Maciulis, V.; Juciute, S.; Ramanavicius, A.; Balevicius, Z.; Slibinskas, R.; Kucinskaite-Kodze, I.; Simanavicius, M.; Balevicius, S.; Ramanaviciene, A. Investigation of SARS-CoV-2 Nucleocapsid Protein Interaction with a Specific Antibody by Combined Spectroscopic Ellipsometry and Quartz Crystal Microbalance with Dissipation. *Journal of Colloid and Interface Science*, 2022, 626, 113–122.

9.   Maciulis, V.; Ramanaviciene, A.; Plikusiene, I. Recent Advances in Synthesis and Application of Metal Oxide Nanostructures in Chemical Sensors and Biosensors. *Nanomaterials*, 2022, 12, 4413.

10.   Plikusiene, I.; Maciulis, V.; Juciute, S.; Ramanavicius, A.; Ramanaviciene, A. Study of SARS-CoV-2 Spike Protein Wild-Type and the Variants of Concern Real-Time Interactions with Monoclonal Antibodies and Convalescent Human Serum. *Biosensors*, 2023, 13, 784.

Paper 1

Porous aluminium oxide coating for the development of spectroscopic ellipsometry based biosensor: Evaluation of human serum albumin adsorption

Vincentas Maciulis, Uldis Malinovskis, Donats Erts, Arunas Ramanavicius, Almira Ramanaviciene, Saulius Balevicius, Silvija Juciute, Ieva Plikusiene

Porous Aluminium Oxide Coating for the Development of Spectroscopic Ellipsometry Based Biosensor: Evaluation of Human Serum Albumin Adsorption

Vincentas Maciulis [1], Uldis Malinovskis [2], Donats Erts [2], Arunas Ramanavicius [1,3], Almira Ramanaviciene [3], Saulius Balevicius [1], Silvija Juciute [3] and Ieva Plikusiene [1,3,*]

[1] Center for Physical Sciences and Technology, LT-10225 Vilnius, Lithuania; vincentas.maciulis@ftmc.lt (V.M.); arunas.ramanavicius@chf.vu.lt (A.R.); saulius.balevicius@ftmc.lt (S.B.)

[2] Institute of Chemical Physics, University of Latvia, LV-1586 Riga, Latvia; uldis.malinovskis@lu.lv (U.M.); donats.erts@lu.lv (D.E.)

[3] Faculty of Chemistry and Geoscience, Vilnius University, LT-03225 Vilnius, Lithuania; almira.ramanaviciene@chf.vu.lt (A.R.); silvija.juciute@chgf.stud.vu.lt (S.J.)

* Correspondence: ieva.plikusiene@chgf.vu.lt

Abstract: An electrochemically synthesised porous anodic aluminium oxide (pAAO) layer has been analysed by means of spectroscopic ellipsometry. The determined thickness of the formed pAAO layer obtained from spectroscopic ellipsometry measurements and modelling was 322.75 ± 0.12 nm. The radius of the nanopores estimated from SEM images was 39 ± 5 nm and the distance between nanopores was 107 ± 6 nm. The investigation of human serum albumin (HSA) adsorption on the pAAO coating showed that: (i) the protein concentration inside nanopores, depending on exposure time, approximately was from 200 up to 600 times higher than that determined in buffer solution; (ii) the initial phase of the adsorption process is slow (3.23 mg·cm^{-3}·min^{-1}) in comparison with the protein desorption rate (21.2 mg·cm^{-3}·min^{-1}) by means of pAAO layer washing; (iii) conventional washing with PBS solution and deionised water does not completely remove HSA molecules from pAAO pores and, therefore, the HSA concentration inside nanopores after 16 h of washing still remains almost 100 times higher than that present in PBS solution. Thus, due to such binding ability, HSA can be successfully used for the blocking of the remaining free surface, which is applied for the reduction in non-specific binding after the immobilisation of biorecognition molecules on the pAAO surface. It was determined that some desorption of HSA molecules from the pAAO layer occurred during the sensor's surface washing step; however, HSA concentration inside the nanopores still remained rather high. These results recommend the continued application of pAAO in the development of biosensors.

Keywords: spectroscopic ellipsometry; human serum albumin; porous aluminium oxide; optical biosensors

1. Introduction

The investigation of protein adsorption/desorption to/from various nanoporous materials is an important task due to the ability to use such materials for proteins separation, purification, and in the development of biosensors, which can be applicable for the determination of various analytes that are important in biology, biochemistry, medical diagnostics, pharmacy, or food industry [1]. The ability of large molecules such as proteins to adsorb within nanopores significantly depends on

hydrophobicity/hydrophility and pore sizes. As it was shown in some research works [2–5], the pore size range of such porous materials should be equal or greater than the size of adsorbed protein molecules [6].

Highly sensitive biosensors based on nanomaterial coatings that are dedicated to the determination of specific proteins attract significant attention [7]. Nanoporous coatings are especially important in the development of such biosensors due to the valuable physical and chemical properties of protein-modified nanoporous surfaces [8]; for example, nanoporous anodic aluminium oxide (pAAO) presents exclusive features for the development of various biosensors due to its highly ordered structure, desirable pore geometry, outstanding optical and electrical properties, high mechanical and thermal stability, chemical resistance, the large amount of hydroxyl groups present on its porous surface, large surface-to-volume ratio, and biocompatibility [9–12]. An additional advantage of pAAO coating is based on the electrochemical anodization procedure, which enables the formation of uniform nanochannels within the Al_2O_3 matrix [12]. During the last decade, various biosensing platforms based on pAAO coatings were applied in optical and electrochemical biosensors [7,10,13].

Bovine serum albumin (BSA) and human serum albumin (HSA) are proteins, which mostly are used in various bioanalytical systems as "blocking agents" [14,15], which reduce non-specific interactions and increase the selectivity and sensitivity of bioanalytical systems. The main problem related to this kind of modification is possible removal of adsorbed HSA during washing and regeneration of biosensors after each analyte determination step. Therefore, it is highly important to assess how strongly HSA interacts with surfaces applied in the design of bioanalytical systems and how washing procedures influence the stability of the adsorbed HSA layer. As it was shown in some research works, HSA-modified pAAO substrate was used as a sensing layer for the determination of cathepsin B [16].

The method of spectroscopic ellipsometry can be successfully applied for optical biosensing because it is a non-destructive method, measurements do not need any labelling, and light does not affect or destroy the samples [14–19]. In addition, high sensitivity can be achieved due to phase shift measurements, particularly if samples are inhomogeneous [17]. As was shown by other authors [16], HSA-modified pAAO substrate was applied as a sensing layer for the designed optical biosensors. In this case, the researchers have used Reflective Interferometric Fourier Transform Spectroscopy (RIFTS), which was suitable for the determination of low protein concentrations. However, according to [18], this method has several drawbacks. The modulation amplitude is somewhat less well fit in part due to the difficulty of obtaining a suitable background spectrum to compensate the variation of light source intensity with wavelength. Additionally, significant differences in the predicted and observed modulation depth of the reflectivity appear due to the effects of surface roughness on the reflectivity of the aluminium foil substrate. This is a result of the RIFTS method, which uses only one *s*-polarisation measurement that in the case of the porous layer, produces partial transformation of *s*-polarised light to *p*-polarisation, resulting in discrepancies of reflected light amplitude. This disadvantage can be avoided using spectroscopic ellipsometry (SE), as this method enables the determination of relative values of reflected electric field amplitudes Ψ and phase differences Δ, which makes it possible to perform simultaneous measurement of both *s* and *p* polarisation and consequently, to obtain better agreement between the experiment and modelling [19]. The SE method was successfully used for the investigation of HSA binding by porous Si [19]. Meanwhile, the possibilities to analyse the HSA adsorption/desorption to/from pAAO coating using the SE method were not demonstrated yet. Therefore, this kind of evaluation has been determined as the main aim of the present research.

2. Materials and Methods

Phosphate-buffered saline (PBS) solution was prepared using PBS tablets (0.14 M NaCl, 0.0027 M KCl, and 0.01 M phosphate buffer pH 7.4). All salts were purchased from Sigma-Aldrich (St. Louis, MO, USA). Human serum albumin (HSA) was purchased from ABCAM (Cambridge, UK). The HSA concentration in 0.01 M PBS, pH 7.4, used for all experiments, was 1 mg/mL.

The porous anodic aluminium oxide (pAAO) layer was formed on high purity (99.999%, 100 mm × 100 mm × 0.32 mm, Good Fellow, Lille, France) aluminium substrate, using a standard two step anodization protocol [20–22]. The aluminium substrate was cut into 10 mm × 18 mm size pieces, degreased, and electrochemically polished in an ice cold perchloric acid–ethanol mixture (1 part 60% $HClO_4$; 4 parts 96% C_2H_5OH) at 15 V. Then, the electrochemically polished aluminium substrate was anodized for 2 h in 0.3 M oxalic acid electrolyte at a constant 40 V anodization potential. The obtained pAAO layer was removed using a chromic–orthophosphoric acid mixture (4% H_2CrO_4; 11% H_3PO_4) at 70 °C. The removal of the pAAO coating creates a pattern of concaves on the surface of the aluminium substrate. This patterned aluminium substrate was anodized again to create a more uniform pAAO coating. pAAO with ~300 nm thickness was synthesised during the 80 s lasting second anodization step under the same conditions as was performed during the first anodization step. After the second anodization step, pores of oxide were cleaned and widened by immersion into 5% orthophosphoric acid solution for 1 min at room temperature, washed with deionised water, and then, dried in the air.

Ellipsometric measurements were performed using a J.A. Woollam M2000X spectroscopic ellipsometer (Lincoln, NE, USA) with a rotating compensator and an angle of incidence was 70°. All spectra were recorded in a 200–1000 nm wavelength range. Appropriate optical models for characterisation of optical properties of all layers were performed using Complete EASE software (version 5.08gcs) from J.A. Woollam (Lincoln, NE, USA).

In this work, two samples were analysed: pAAO and Al_2O_3. The pAAO substrate was used as a sensing surface for non-specific HSA adsorption to nanopores. Ellipsometric data of Al_2O_3 were simulated using "Complete EASE" software in order to reveal the differences in optical properties between pAAO and Al_2O_3. Before incubation of the pAAO substrate in the HSA-containing solution, the optical properties of pAAO in air were determined by spectroscopic ellipsometry. After this, the same substrate was immersed into PBS solution for 5 min, and then, incubated in the HSA-containing solution for 1, 2, and 3 h periods. Immediately after an incubation lasting 3 h, the pAAO coating was removed from the solution and "washed" with PBS for 15 min. After each pAAO immersion in HSA solution and washing step, ellipsometric parameters $\Psi(\lambda)$ and $\Delta(\lambda)$ were registered. Optical models were constructed in order to calculate the thickness of pAAO and refractive index dispersion for the effective pAAO layers and refractive index inside nanopores.

3. Results

In order to evaluate the differences of the sensing substrates as Al_2O_3 and pAAO, scanning electron microscope images and ellipsometric study (measurements and simulations) were performed. SEM images of pAAO were used for the first approximation of the thickness and porosity. Then, ellipsometric measurements of pAAO/air, pAAO/HSA$_{(1\,h\,incub.)}$, pAAO/HSA$_{(2\,h\,incub.)}$, pAAO/HSA$_{(3\,h\,incub.\,+\,15\,min\,wash)}$, and data simulation for Al_2O_3 and Al_2O_3/HSA were performed in order to compare the spectral shift for non-structured (Al_2O_3) and nanostructured (pAAO) substrates, which were used as sensing layers for HSA protein adsorption.

3.1. SEM Measurements

The morphology of pAAO was investigated using a scanning electron microscope (SEM). As can be seen from Figure 1A,B, the obtained substrate thickness (including the intermediate Al/Al_2O_3 layer) was of 339 ± 10 nm. Pore radius (r_p) and distance between pores (D_{int}) were estimated using SEM micrographs presented in Figure 1A,C, considering that pore diameter represents a larger (less intensive) spot in Figure 1C and the width of the trench visible in the cut-off of the layer (see bottom of Figure 1A). It was determined that $r_p \approx 39 \pm 5$ nm and $D_{int} \approx 107 \pm 6$ nm. The porosity (P) of the pAAO layer was evaluated using the formula for the hexagonal structure of pores displacement [23].

$$P = \frac{2\pi}{\sqrt{3}} \times \left(\frac{r_p}{D_{int}} \right)^2 \times 100\% \tag{1}$$

Using this formula, it was calculated that in this case, *P* was about 51% ± 10%.

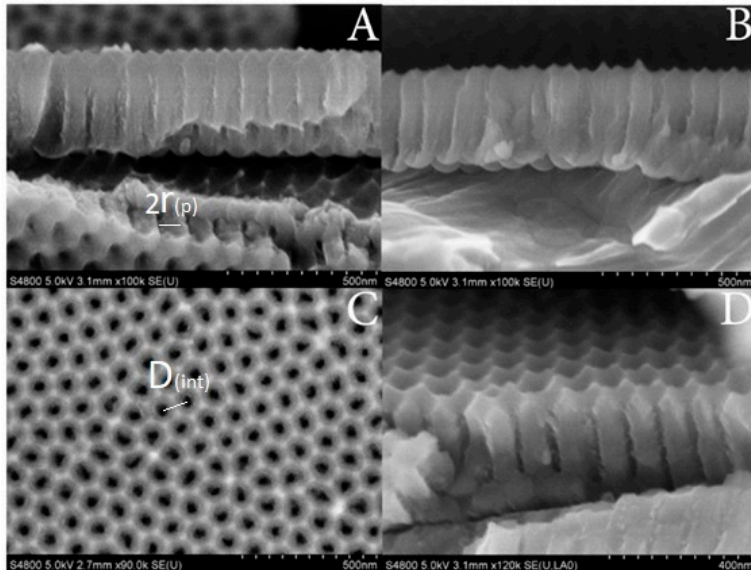**Figure 1.** SEM micrographs of porous anodic aluminium oxide (pAAO): (**A**,**B**)—cross sections; (**C**)—top view; (**D**)—tilted view.

3.2. Simulation of Non-Structured Al_2O_3 Optical Properties

A comparison of the optical properties for the two different samples, pAAO and Al_2O_3, was performed. Values of ellipsometric parameters vs. wavelength were measured for the pAAO substrate before and after immersion into PBS with 1 mg/mL of HSA in order to determine the wavelength shift of the ellipsometric parameters when a higher amount of proteins adsorbs to the nanopores. For the same reason, simulation of the Al_2O_3 ellipsometric parameters spectra before and after the formation of the HSA layer was performed. As was noticed in the introduction part, the ellipsometric parameter Δ is more sensitive when it is used for the analysis of non-homogeneous samples. Due to this, in this research, only ellipsometric parameter Δ vs. λ is presented. These data are zoomed to a spectral range from 300 to 400 nm because in this range, the spectral shift was clearly noticeable. The simulated structure consisted of aluminium substrate, an intermix layer of 13.5 nm, and a 322.75 nm Al_2O_3 layer (Figure 2, curve 1). Then, an additional HSA layer with the thickness of 8 nm (the average dimension of a HSA molecule [24,25]) was simulated on top of Al_2O_3 (Figure 2, curve 2 A_2O_3/HSA). The simulation of ellipsometric parameter $\Delta(\lambda)$ of the Al_2O_3 layer and Al_2O_3/HSA is presented in Figure 2 in order to reveal the effect of the nanopores on proteins adsorption. Thus, such simulated substrate was considered as a closely packed and planar Al_2O_3 layer. As can be seen from Figure 2, the Al_2O_3 peak of the ellipsometric parameter Δ is located at $\lambda = 353$ nm. In the case of HSA adsorption on the Al_2O_3 layer, there was a shift of 3 nm towards longer wavelengths and a peak was observed at $\lambda = 356$ nm. During the simulations, aluminium and Al_2O_3 refractive index values were taken from the database of the software. In this case, the HSA layer was simulated as a Cauchy function, which is typically used in ellipsometry for dielectric materials as proteins:

$$n(\lambda) = A + \frac{B}{\lambda^2} + \frac{C}{\lambda^4} + \dots \tag{2}$$

where Cauchy coefficients were applied as $A = 1.575$; $B = 0.01$; $C = 9.8 \times 10^{-5}$; $n(\lambda)$ refractive index dependence on wavelength.
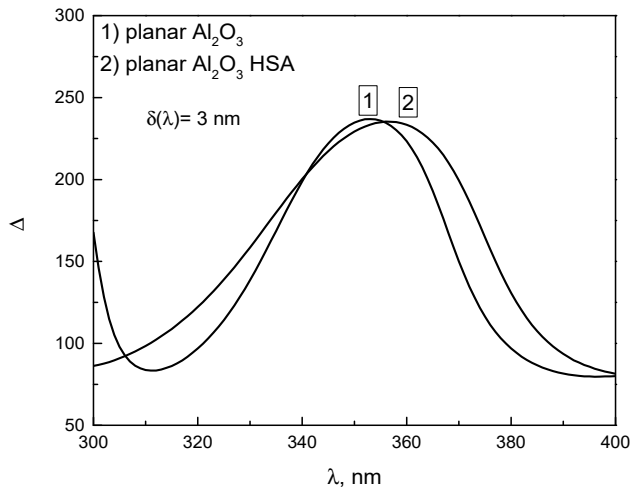

Figure 2. Simulated data of ellipsometric parameter Δ for: (1) Al_2O_3 (1st peak) at 353 nm and (2) Al_2O_3/HSA (2nd peak) at 356 nm.

3.3. Optical Properties of pAAO

A schematic representation of pAAO formed on aluminium substrate is presented in Figure 3. pAAO layer thickness calculated using the optical model applied for the analysis of ellipsometric measurements was estimated to be of 322.75 ± 0.12 nm and surface roughness was 39.4 ± 3 nm. Bruggeman effective media approximation (EMA) was used in order to calculate the porosity of pAAO, as was described by other authors [26]. The effective media layer (EMA) of pAAO was modelled as a layer consisting of two materials: Al_2O_3 and air (52% and 48%, respectively). EMA was used in order to include the porosity of pAAO. Starting values of thickness and surface roughness, which were applied for fitting, were taken from SEM images. During the regression analysis, thickness and surface roughness were treated as free fitting values and the refractive index of Al_2O_3 as a fixed value.
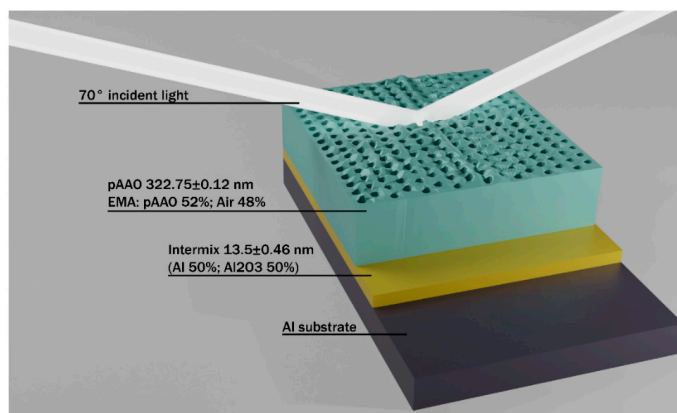

Figure 3. Schematic representation of pAAO formed on aluminium substrate.

The intermix layer of 13.5 ± 0.46 nm in the optical model was applied to simplify the approximation of the intermediate layer between aluminium and pAAO, and this includes the Al_2O_3 "barrier layer", which is formed on aluminium substrate. In the optical model, it was estimated that this "barrier layer" consisted of 50% Al_2O_3 and 50% aluminium. The presence of this "barrier layer" in the design of the optical model significantly improved the calculation quality and reduced the mean square error (MSE) of the calculated values. MSE in this case was in the range of 31–34. Optical models were designed to calculate the refractive index dispersion of the pAAO sample before and after the incubation of the pAAO substrate in the HSA-containing solution. The same pAAO substrate was investigated in the following way: firstly, the optical properties of the pAAO coating in air were registered. Then, the sample was immersed into 1 mg/mL of HSA-containing solution in PBS, pH 7.4, for 1 h. After that, the spectra of both ellipsometric parameters (Δ and Ψ) were recorded; then, the same sample again was immersed into the HSA solution for 2 h and again, the spectra of ellipsometric parameters were recorded. The same procedure was performed after 3 h immersion followed by 15 min washing in PBS solution. It was determined that when pAAO layer nanopores were filled with air, the determined ratio of pAAO layer composition according to calculations using the EMA-based optical model was 52% pAAO and 48% air.

3.4. HSA Adsorption to pAAO

HSA adsorption to pAAO was evaluated by assessment of "Δ spectral shift" and regression analysis, which are presented in Figures 4 and 5. Here, we present only the spectra of ellipsometric parameter Δ zoomed from $\lambda = 300$ to $\lambda = 370$ nm, because in this range, a clear shift of the Δ peak is observed. The determined shift of peaks' wavelength is compared to shifts of the peaks in simulated spectra for the Al_2O_3 layer, presented in Figure 2. Starting with pAAO/air, the peak of ellipsometric parameter Δ is observed at $\lambda = 330$ nm (Figure 4, curve 1). After 1 h of incubation in solution containing 1 mg/mL of HSA, ellipsometric parameter Δ shifted towards longer wavelengths, resulting in the appearance of the peak at $\lambda = 335$ nm (Figure 4, curve 2); after 2 h of incubation in solution containing 1 mg/mL of HSA, the peak shifted even more significantly and appeared at $\lambda = 341$ nm (Figure 4, curve 3). After 3 h incubation in HSA solution and 15 min washing with PBS solution, a shift of ellipsometric parameter Δ to a shorter wavelength was observed at $\lambda = 336$ nm and it indicated that part of the HSA molecules had desorbed from the pAAO surface (Figure 4, curve 4). Finally, after washing with deionised water lasting 30 min, the peak position shifted even more to shorter wavelengths and appeared at $\lambda = 333$ nm (Figure 4, curve 5).
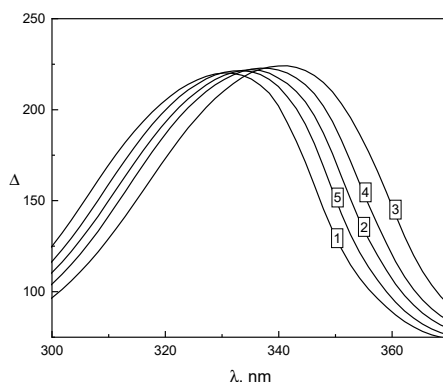

Figure 4. Ellipsometric parameter Δ vs. λ peak position at different time instances: (1) pAAO/air at $\lambda = 330$ nm; (2) pAAO/HSA$_{(1\,h\,incub.)}$ at $\lambda = 335$ nm; (3) pAAO/HSA$_{(2\,h\,incub.)}$ at $\lambda = 341$ nm; (4) pAAO/HSA$_{(3\,h\,incub.\,+\,15\,min\,wash)}$ at $\lambda = 336$ nm; (5) pAAO after washing with deionised water at $\lambda = 333$ nm.
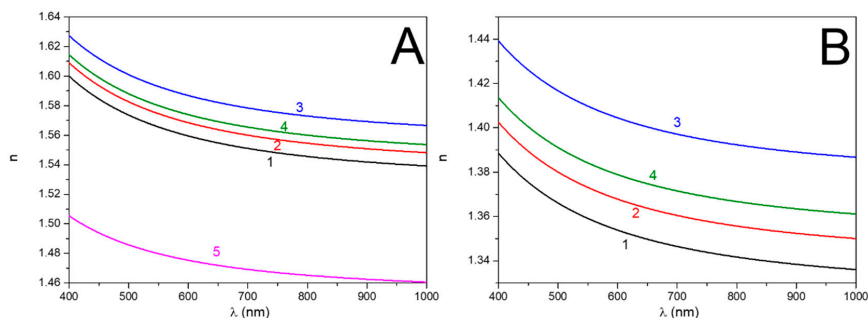
Figure 5. Refractive index dispersion of pAAO/X (**A**): (1) pAAO/PBS, (2) pAAO/HSA$_{(1\,h\,incub.)}$, (3) pAAO/HSA$_{(2\,h\,incub.)}$, (4) pAAO/HSA$_{(3\,h\,incub.\,+\,15\,min\,wash)}$, and (5) pAAO/air; (**B**) Refractive index dispersion inside nanoporous layer filled with: (1) PBS, (2) HSA after one 1 h incubation, (3) HSA after 2 h incubation, and (4) HSA after 3 h incubation followed by 15 min wash.

Results obtained after the washing of HSA-modified pAAO substrate with PBS and deionised water show that the interaction of HSA protein with pAAO substrate is reversible. Additionally, this process depends on the composition of the selected washing solution. It was determined that pAAO/HSA structure more sensitive to deionized water because more HSA molecules were removed from the substrate by washing using deionized water, than by 0.01 M PBS, pH 7.4. Despite that, the desorption of HSA proteins from the surface of pAAO takes a long time due to the inclusion of proteins within nanopores in the Al$_2$O$_3$ layer.

In order to assess changes in refractive index for the measured sample when using the EMA-based optical model for the pAAO layer, regression analysis was performed after all modification steps, namely after the formation of pAAO/air, pAAO/HSA$_{(1\,h\,incub.)}$, pAAO/HSA$_{(2\,h\,incub.)}$, and pAAO/HSA$_{(3\,h\,incub.\,+\,15\,min\,wash)}$ structures. During the regression analysis, such parameters as thickness, roughness, and intermix layer thickness, which were applied in the EMA-based optical layer, were fixed values, which were calculated by modelling of the pAAO/air structure. Cauchy function parameters A, B, and the ratio of HSA and Al$_2$O$_3$ in the EMA-based optical model were applied as free fitting parameters. Regression analysis resulted in a dispersion of refractive index, which is presented in Figure 5A,B for all evaluated structures: pAAO/air, pAAO/HSA$_{(1\,h\,incub.)}$, pAAO/HSA$_{(2\,h\,incub.)}$, pAAO/HSA$_{(3\,h\,incub.\,+\,15\,min\,wash)}$, and pAAO/PBS. Figure 5A shows the dispersion of effective refractive index for the pAAO layer, when this layer was modelled using the EMA-based optical model for the structures mentioned here: (i) pAAO in PBS while estimating that pAAO pores are filled with PBS (Figure 5A, curve 1); (ii) pAAO incubated in PBS containing HSA for 1 h (HSA$_{(1\,h\,incub.)}$) (Figure 5A, curve 2); (iii) pAAO incubated in PBS containing HSA for 2 h (HSA$_{(2\,h\,incub.)}$) (Figure 5A, curve 3); (iv) pAAO incubated in air (Figure 5A, curve 4); (v) pAAO incubated in PBS containing HSA for 3 h followed by an additional 15 min washing procedure (HSA$_{(3\,h\,incub.\,+\,15\,min\,wash)}$) (Figure 5A, curve 5). Figure 5B shows refractive index dispersion inside nanopores of pAAO when pores were filled with: (i) PBS (Figure 5B, curve 1), (ii) HSA after the incubation of pAAO in PBS containing HSA for 1 h (Figure 5B, curve 2), (iii) after the incubation of pAAO in PBS containing HSA for 2 h, (iv) after the incubation of pAAO in PBS containing HSA for 3 h and followed by a 15 min wash with PBS. In order to visualise differences between refractive indexes, the values at λ = 600 nm wavelength, which were taken for calculations, are presented in Table 1. Refractive indexes values at λ = 600 nm wavelength were taken in order to simplify the evaluation; these values are at the end of the abrupt part of dependence of the refractive index vs. wavelength.

Table 1. Values of refractive indexes of pAAO layer and trapped HSA concentration calculated inside nanopores.

Incubation Time (t_{ex}, h)	0	1	2	3	0.25 Washing	24 Washing
Effective refractive index n_{EMA}	1.486	1.5678	1.5865	1.5985	1.5733	1.5594
Refractive index of HSA solution in pores n_p	1 (void)	1.3679	1.4042	1.43	1.3788	1.3538
Concentration of HSA in pores C_{HSA} (mg/mL)	0	194	395	572	254	115

t_{ex}—pAAO substrate incubation time in 1 mg/mL HSA solution in PBS.

In order to evaluate the HSA concentration inside the pores (C_{HSA}), we used the well-known fact that the refractive index of protein in water solution is the linear function of protein concentration. For this reason, the C_{HSA} can be calculated by means of the formula obtained after a simple transformation of mathematical expression used for refractive index calculation at a known concentration [27]:

$$C_{HSA} = (n_p - n_{PBS})/I_n \tag{3}$$

Here, n_{PBS} is a refractive index of PBS, which is equal to 1.333; I_n is refractive index increment (the derivative dn/dc) according to the protein's concentration [28]. For the calculation of C_{HSA}, we used $I_n = 0.18$ mL/g that was determined at $\lambda = 632.2$ nm.

The results presented in Table 1 show the following important features of HSA adsorption on/within pAAO coating: (a) the protein concentration inside nanopores, depending on exposure time, is approximately 200–600 times higher than that in buffer solution; (b) the beginning of the absorption process is slow (3.23 mg·cm^{-3}·min^{-1}) in comparison with the desorption of proteins (21.2 mg·cm^{-3}·min^{-1}) during the washing of the pAAO/HSA structure; (c) the conventional washing procedure does not enable the desorption of all adsorbed HSA molecules.

4. Conclusions

A standard anodization protocol was successfully applied for the formation of pAAO coating of 322.75 ± 0.12 nm thickness. SEM images illustrate that the pores of pAAO are displaced in a regular hexagonal structure. The radius of the nanopores estimated using SEM micrographs was 39 ± 5 nm and the distance between nanopores was 107 ± 6 nm. These dimensions fit well the size of the HSA proteins molecules, as the average diameter of HSA is in the range of 8 nm. In this research, the evaluation of non-specific and reversible adsorption of HSA onto the pAAO layer was performed. Ellipsometric measurements showed that a part of HSA remained inside of the pAAO pores after washing with PBS solution and deionised water. Therefore, during the application of pAAO-based optical sensors, it should be taken into account that some of the HSA, which is rather fast adsorbed on/within pAAO, might desorb during washing of the sensor. However, it was determined that conventional washing with PBS solution does not fully desorb all the HSA molecules from pAAO pores and even after washing with deionised water lasting 16 h, HSA concentration inside nanopores still remains approximately 100 times higher than that in PBS solution. Hence, pores of pAAO operate as "traps" for HSA proteins, cumulating molecules of this material. However, HSA should be carefully used for the blocking of the remaining free surface of signal transducers based on pAAO when significant reduction in non-specific binding is expected.

Author Contributions: Conceptualization, I.P., V.M., A.R. (Almira Ramanaviciene), and S.B.; methodology, I.P. and V.M.; software, I.P. and V.M.; validation, V.M., U.M., and I.P.; formal analysis, V.M., U.M., and I.P.; investigation, V.M., U.M., I.P., and S.J.; resources, A.R. (Almira Ramanaviciene) and D.E.; data curation V.M., U.M., and I.P.; writing—original draft preparation, V.M., I.P., A.R. (Almira Ramanaviciene), and A.R. (Arunas Ramanavicius); writing—review and editing, V.M., I.P., U.M., A.R. (Almira Ramanaviciene), and A.R. (Arunas Ramanavicius); visualization, V.M., I.P., and S.J.; supervision, A.R. (Almira Ramanaviciene), A.R. (Arunas Ramanavicius), D.E., and S.B.; project administration, A.R. (Almira Ramanaviciene) and D.E.; funding acquisition, A.R. (Almira Ramanaviciene) and D.E. All authors have read and agreed to the published version of the manuscript.

Conflicts of Interest: The authors declare no conflict of interest.

References

1. Puziy, A.M.; Poddubnaya, O.I.; Derylo-Marczewska, A.; Marczewski, A.W.; Blachnio, M.; Tsyba, M.M.; Sapsay, V.I.; Klymchuk, D.O. Kinetics of protein adsorption by nanoporous carbons with different pore size. *Adsorption* **2016**, *22*, 541–552. [CrossRef]

2. Vinu, A.; Miyahara, M.; Ariga, K. Biomaterial immobilization in nanoporous carbon molecular sieves: Influence of solution pH, pore volume, and pore diameter. *J. Phys. Chem. B* **2005**, *109*, 6436–6441. [CrossRef] [PubMed]

3. Vinu, A.; Miyahara, M.; Sivamurugan, V.; Mori, T.; Ariga, K. Large pore cage type mesoporous carbon, carbon nanocage: A superior adsorbent for biomaterials. *J. Mater. Chem.* **2005**, *15*, 5122–5127. [CrossRef]

4. Vinu, A.; Miyahara, M.; Mori, T.; Ariga, K. Carbon nanocage: A large-pore cage-type mesoporous carbon material as an adsorbent for biomolecules. *J. Porous Mater.* **2006**, *13*, 379–383. [CrossRef]

5. Yushin, G.; Hoffman, E.N.; Barsoum, M.W.; Gogotsi, Y.; Howell, C.A.; Sandeman, S.R.; Phillips, G.J.; Lloyd, A.W.; Mikhalovsky, S.V. Mesoporous carbide-derived carbon with porosity tuned for efficient adsorption of cytokines. *Biomaterials* **2006**, *27*, 5755–5762. [CrossRef]

6. Katiyar, A.; Ji, L.; Smirniotis, P.; Pinto, N.G. Protein adsorption on the mesoporous molecular sieve silicate SBA-15: Effects of pH and pore size. *J. Chromatogr. A* **2005**, *1069*, 119–126. [CrossRef]

7. Santos, A.; Kumeria, T.; Losic, D. Nanoporous anodic aluminum oxide for chemical sensing and biosensors. *TrAC Trends Anal. Chem.* **2013**, *44*, 25–38. [CrossRef]

8. Dai, Z.; Ju, H. Bioanalysis based on nanoporous materials. *TrAC Trends Anal. Chem.* **2012**, *39*, 149–162. [CrossRef]

9. Md Jani, A.M.; Losic, D.; Voelcker, N.H. Nanoporous anodic aluminium oxide: Advances in surface engineering and emerging applications. *Prog. Mater. Sci.* **2013**, *58*, 636–704. [CrossRef]

10. Rajeev, G.; Prieto Simon, B.; Marsal, L.F.; Voelcker, N.H. Advances in nanoporous anodic alumina-based biosensors to detect biomarkers of clinical significance: A Review. *Adv. Healthc. Mater.* **2018**, *7*, 1–18. [CrossRef]

11. Reta, N.; Saint, C.P.; Michelmore, A.; Prieto-Simon, B.; Voelcker, N.H. Nanostructured electrochemical biosensors for label-free detection of water- and food-borne pathogens. *ACS Appl. Mater. Interfaces* **2018**, *10*, 6055–6072. [CrossRef] [PubMed]

12. Rajeev, G.; Melville, E.; Cowin, A.J.; Prieto-Simon, B.; Voelcker, N.H. Porous alumina membrane-based electrochemical biosensor for protein biomarker detection in chronic wounds. *Front. Chem.* **2020**, *8*, 1–11. [CrossRef] [PubMed]

13. Krismastuti, F.S.H.; Bayat, H.; Voelcker, N.H.; Schönherr, H. Real time monitoring of layer-by-layer polyelectrolyte deposition and bacterial enzyme detection in nanoporous anodized aluminum oxide. *Anal. Chem.* **2015**, *87*, 3856–3863. [CrossRef] [PubMed]

14. Pacioni, N.L.; Poblete, H. Human serum albumin as protecting agent of silver nanoparticles: Role of the protein conformation and amine groups in the nanoparticle stabilization. *J. Nanoparticle Res.* **2013**, *15*. [CrossRef]

15. Vogt, R.V.; Phillips, D.L.; Omar Henderson, L.; Whitfield, W.; Spierto, F.W. Quantitative differences among various proteins as blocking agents for ELISA microtiter plates. *J. Immunol. Methods* **1987**, *101*, 43–50. [CrossRef]

16. Amouzadeh Tabrizi, M.; Ferré-Borrull, J.; Marsal, L.F. An optical biosensor for the determination of cathepsin B as a cancer-associated enzyme using nanoporous anodic alumina modified with human serum albumin-thionine. *Microchim. Acta* **2020**, *187*. [CrossRef]

17. Tikhonravov, A.V.; Trubetskov, M.K.; Masetti, E.; Krasilnikova, A.V.; Kochikov, I.V. Sensitivity of the ellipsometric angles Psi and Delta to the surface inhomogeneity. *Adv. Opt. Interf. Coat.* **1999**, *3738*, 173–182. [CrossRef]

18. Pan, S.; Rothberg, L.J. Interferometric sensing of biomolecular binding using nanoporous aluminum oxide templates. *Nano Lett.* **2003**, *3*, 811–814. [CrossRef]

19. Hans, A. Ellipsometry on thin organic layers of biological interest: Characterization and applications. *Thin Solid Films* **2000**, *377–378*, 48–56. [CrossRef]

20. Masuda, H.; Satoh, M. Fabrication of gold nanodot array using anodic porous alumina as an evaporation mask. *Jpn. J. Appl. Phys. Part 2 Lett.* **1996**, *35*. [CrossRef]

21. Malinovskis, U.; Poplausks, R.; Apsite, I.; Meija, R.; Prikulis, J.; Lombardi, F.; Erts, D. Ultrathin anodic aluminum oxide membranes for production of dense sub-20 nm nanoparticle arrays. *J. Phys. Chem. C* **2014**, *118*, 8685–8690. [CrossRef]

22. Kunakova, G.; Meija, R.; Andzane, J.; Malinovskis, U.; Petersons, G.; Baitimirova, M.; Bechelany, M.; Bauch, T.; Lombardi, F.; Erts, D. Surface structure promoted high-yield growth and magnetotransport properties of Bi_2Se_3 nanoribbons. *Sci. Rep.* **2019**, *9*. [CrossRef] [PubMed]

23. Nielsch, K.; Choi, J.; Schwirn, K.; Wehrspohn, R.B. Self-ordering regimes of porous alumina: The 10% porosity rule. *Nano Lett.* **2002**, *2*, 677–680. [CrossRef]

24. Min He, X.; Carter, D.C. Atomic structure and chemistry of human serum albumin. *Nature* **1992**, *358*, 209–215. [CrossRef]

25. Sugio, S.; Kashima, A.; Mochizuki, S.; Noda, M. Crystal structure of human serum albumin at 2.5 Å resolution. *Protein Eng.* **1999**, *12*, 439–446. [CrossRef]

26. Thompson, D.W.; Snyder, P.G.; Castro, L.; Yan, L.; Kaipa, P.; Woollam, J.A. Optical characterization of porous alumina from vacuum ultraviolet to midinfrared. *J. Appl. Phys.* **2005**, *97*. [CrossRef]

27. Ball, V.; Ramsden, J.J. Buffer dependence of refractive index increments. *Biopolymers* **1998**, *46*, 489–492. [CrossRef]

28. Vörös, J. The density and refractive index of adsorbing protein layers. *Biophys. J.* **2004**, *87*, 553–561. [CrossRef]

Paper 2

Total internal reflection ellipsometry for kinetics-based assessment of bovine serum albumin immobilization on ZnO nanowires

Ieva Plikusiene, **Vincentas Maciulis**, Octavio Graniel, Mikhael Bechelany, Saulius Balevicius, Vilius Vertelis, Zigmas Balevicius, Anton Popov, Arunas Ramanavicius, Almira Ramanaviciene

ROYAL SOCIETY
OF CHEMISTRY

PAPER

Check for updates

Total internal reflection ellipsometry for kinetics-based assessment of bovine serum albumin immobilization on ZnO nanowires

Ieva Plikusiene, [ID] [a] Vincentas Maciulis, [b] Octavio Graniel, [ID] [c] Mikhael Bechelany, [ID] [c] Saulius Balevicius, [b] Vilius Vertelis, [bd] Zigmas Balevicius, [b] Anton Popov, [ID] [a] Arunas Ramanavicius [ID] [ab] and Almira Ramanaviciene [ID] *[a]

ZnO materials exhibit a rich family of nanostructures, which show great potential for the sensitivity improvement of optical detection systems. In this work, ~ 350 nm ZnO nanowires (ZnO-NWs) were electrochemically deposited on ZnO and an indium tin oxide coated glass (ZnO-NWs/ZnO/ITO/glass) substrate. ZnO-NWs were modified with *N*-(3-aminopropyl)triethoxysilane (APTES) for covalent bovine serum albumin (BSA) immobilization. The studies were performed using a spectroscopic total internal reflection ellipsometry (TIRE) setup based on the Kretschmann configuration. The refractive index dispersion of ZnO-NWs in the air was obtained from the optical model applying a Bruggeman effective medium approach. It was determined that the ZnO-NWs effective layer consists of 30% ZnO and 70% void. Reflectance difference before and after ZnO-NWs modification with BSA was 6.6 times higher than in the case of the plain ZnO layer. The Δ kinetics of covalent BSA immobilization on the APTES/ZnO-NWs/ZnO/glass substrate contains two phases. Evaluation of the diffusion coefficient for BSA in PBS filled APTES/ZnO-NWs/ZnO/ITO/glass was performed using numerical calculation, and the obtained diffusion coefficient was 2.4×10^{-17} m^2 s^{-1}. Simulation of BSA immobilization on a flat ZnO layer and on a ZnO-NWs modified surface showed that 13 times higher sensitivity was observed for the substrate with ZnO-NWs.

1 Introduction

Recently, metal oxides have been applied to different analytical systems thanks to their facile preparation and their nontoxicity.[1] Zinc oxide (ZnO) is an n-type semiconductor with a wide band gap (3.37 eV), a large exciton binding energy (60 meV), and a high isoelectric point (pH 9.0–9.5). It is nontoxic, biocompatible and has a number of specific advanced features such as thermal stability, enhanced electron mobility, high mechanical strength, and environmental stability for oxidation.[2] ZnO and various nanostructures formed from this metal oxide attract high interest for their application in transparent electronics, photocatalysis, solar cells, supercapacitors, sensors, and optical biosensors.[3–9] ZnO nanowires (ZnO-NWs) are typical 1D ZnO nanostructures and

due to their large surface area, direct electron pathway in the *c*-axis direction, good biocompatibility and chemical stability they were used in the development of nanosize electrodes.[10,11] The surface of ZnO-NWs is relevant for functionalization, providing an effective immobilization of biomolecules with appropriate loading capacity, high biological activity, and good stability.[12] The diameters of ZnO nanostructures are close to the sizes of biological and chemical molecules this is why such 1D nanostructures can be excellent transducers.

Nowadays, optical analytical systems play an important role in the detection of a wide range biological and chemical substances. The main advantages of optical sensing include the non-destructive nature of analytical signal registration, real-time, label-free or label-based detection of analytes with a high sensitivity, selectivity, and reliability, and a cost-effective manner. Optical biosensors based on measurements of absorbance, reflectance, photoluminescence, scattering, polarisation, or refractive index of the biological medium are the next generation of sensing devices for everyday use.[13,14,15,16] The value of optical response (which is related to sensitivity) strongly depends on the amount of biomaterial immobilized on the sensor surface. To increase the sensitivity, it is necessary to

a NanoTechnas – Center of Nanotechnology and Materials Science,
Faculty of Chemistry and Geosciences, Vilnius University, Naugarduko str. 24,
Vilnius 03225, Lithuania. E-mail: almira.ramanaviciene@chf.vu.lt
b State Research Institute Center for Physical and Technological Sciences,
Sauletekio Ave. 3, Vilnius, Lithuania
c Institut Europeen des Membranes, IEM, UMR 5635, Univ Montpellier, ENSCM,
CNRS, Place Eugene Bataillon, Montpellier 34095, Cedex 5, France
d French–German Research Institute of Saint-Louis, Saint-Louis, 68300, France

accrue an optimal surface density of biomolecules and proper orientation on the surface of the sensor. This can be realized using nanostructures, such as nanowires grown on the substrate, which increase the effective surface area of the sensor. However, the nanowires usually exhibit a strong diffuse scattering effect, which aggravates the optical signal registration due to very low specular reflectance intensity.[17,18] This effect would be a drawback if conventional optical measurements like absorbance, reflectance, or transmittance are used. In this case, the ellipsometry method, which measures relative values of p- and s-polarized light amplitude ratio Ψ and the phase differences Δ between them is less influenced by a weak reflectance intensity. Unfortunately, this advantage of the conventional ellipsometry method is weakened by the light depolarization effect appearing in the case of highly diffuse scattered surfaces.[19] For this reason, a better solution would be the application of spectroscopic ellipsometry combined with the surface plasmon resonance method, which is usually used for real-time monitoring of protein interactions at the solid–liquid interface, and is called total internal reflection ellipsometry (TIRE).[20,21,22] The TIRE configuration minimize the depolarization effect because light does not pass directly through the highly scattered surface, but enters into the structure of nanowires as an evanescent surface wave generated due to the total internal reflection phenomenon.[13] It was shown that the higher sensitivity of this method in the case of multilayered ZnO structures has been achieved because of multiple reflections of the light occurring in a total internal reflection mode. It was particularly noticeable for the ellipsometric parameter Δ, which under the total internal reflection condition depends on the angle of incidence.[23,24,25]

The aim of this study was to investigate the properties of the ZnO-NWs surface by utilizing spectroscopic ellipsometry under TIRE configuration during covalent BSA immobilization on ZnO-NWs. The capabilities of surface structures containing ZnO-NWs for the optical signal enhancement under total internal reflection mode and real-time measurement of covalent BSA binding were discussed from the sensitivity point of view. Additionally, the evaluation of diffusion coefficient based on one dimensional diffusion equation was performed.

2 Materials and methods

2.1 Materials

N-(3-Aminopropyl)triethoxysilane (APTES, 99%) and 1-(ethyl-3-(3-diaminopropyl)carbodiimide)hydrochloride (EDC) were obtained from Sigma-Aldrich (Germany). N-Hydroxysuccinimide (NHS) was obtained from Merck (Germany). Diethylzinc, $ZnCl_2$ (CAS: 7646-85-7, purity >98%) and potassium chloride (KCl, CAS: 7447-40-7, purity >99%) were purchased from Fluka (Germany). Bovine serum albumin (BSA, fraction V) was obtained from Carl Roth GmbH & Co. (Karlsruhe, Germany). Phosphate buffered saline (PBS) tablets (0.14 M NaCl, 0.0027 M KCl, 0.01 M phosphate buffer pH 7.4) were purchased from AB Medicago (Sweden). All chemicals were of analytical grade or better. All aqueous solutions were prepared in UHQ water (conductivity less than 1 μS cm^{-1}) and purified by

DEMIWA rosa 5 (WATEK, Czech Republic). Glass plates covered with a 120 nm ITO layer were obtained from Kintec (Hong Kong).

2.2 Preparation of ZnO-NWs

The ZnO-NWs were prepared as follows. Firstly, a 20 nm ZnO layer was deposited on the ITO/glass substrate (1×2 cm^2) by an atomic layer deposition method in a home-made system with diethylzinc (DEZ) and deionized water as precursors.[26,27] The deposition of ZnO was achieved by exposing the ITO/glass substrates to sequential pulses of DEZ and deionized water separated by a purge of argon at a constant temperature of 100 °C. A typical cycle consisted of a 0.2 s pulse of DEZ, 40 s exposure, and a 60 s purge with argon, followed by a 2 s pulse of deionized water, 40 s exposure, and a 60 s purge with argon. Afterward, ZnO-NWs were grown on the ZnO/ITO/glass substrate by electrodeposition in a three-electrode configuration following a previously reported procedure.[23] Briefly, a solution of 0.05 mM of $ZnCl_2$ (zinc precursor) and 0.1 M of KCl (supporting electrolyte) was prepared and used as the electrolyte with the ZnO/ITO/glass as the working electrode, a Pt plate as the counter electrode, and Ag/AgCl as the reference electrode. The electrodeposition was performed at 80 °C with a constant electric potential of −1.0 V for 30 min in a VersaSTAT 3 potentiostat, while O_2 was constantly bubbled in the electrolyte solution. Once the electrodeposition was completed, the ZnO-NWs/ZnO/ITO/glass substrates were thoroughly rinsed with deionized water.

2.3 Silanization of ZnO-NWs/ZnO/ITO/glass substrates by APTES

Silane-derivation of ZnO-NWs deposited on ZnO/ITO/glass substrates was performed by a vapor-phase deposition process according to the procedure described earlier.[24] To minimize the influence of humidity, silanization was performed in a glovebox in an inert atmosphere. A few drops of APTES were deposited in a small vial, which was then placed next to the sample located in a glass Petri dish. The heat resistant insulation tape was used for the covering of the Petri dish and isolation of the surface from the contact with air. The covered Petri dish was then placed in an oven and kept overnight at 90 °C. Afterwards, the APTES modified ZnO-NWs were washed with toluene, ethanol, and distilled water and then dried in an oven at 110 °C. In this way, the surface of ZnO-NWs was functionalized with amino groups (APTES/ZnO-NWs/ZnO/ITO/glass), which are necessary for covalent immobilization of BSA.

2.4 Covalent immobilization of BSA on the APTES/ZnO-NWs/ZnO/ITO/glass surface

To immobilize BSA covalently on the salinized surfaces of the ZnO-NWs, the carboxyl groups present on BSA were activated for 15 min by a mixture of EDC and NHS aqueous solutions. In detail, a 1.0 mg ml^{-1} concentration solution of BSA in PBS was mixed with EDC and NHS, and the final concentrations of EDC, NHS, and BSA were 400 mM, 100 mM and 0.1 mg ml^{-1}, respectively. The activated carboxyl groups of BSA were exposed to the amino groups present on the APTES/ZnO-NWs/ZnO/ITO/glass surface.

2.5 TIRE measurements

The ellipsometric experiments were conducted using a rotating compensator based ellipsometer J. A. Woollam M2000X (Lincoln, USA). The TIRE experiments were carried out at a 70° angle of incidence with the illumination being at wavelengths in the 200–1000 nm spectral range. This was conducted using a BK7 glass 70° angle prism connected *via* a refractive index matching fluid to the ZnO-NWs/ZnO/ITO/glass substrate. In the TIRE experiment, a liquid handling system with a custom-built Teflon chamber was used. In this chamber, the sensing surfaces were placed. The connecting valve was then opened, allowing the PBS to be injected into the chamber, which was needed for the performance of covalent BSA immobilization on the modified surface. TIRE measurements before and after ZnO-NWs covalent modification with BSA were performed and registered signals were compared.

3 Results and discussion

3.1 Characterization of ZnO-NWs by SEM

ZnO-NWs were successfully formed on a 20 nm ZnO layer by an electrodeposition method. The cross-section view of the ZnO-NWs array on the ZnO/ITO/glass substrate obtained by scanning electron microscopy (SEM) is presented in Fig. 1. As it can be seen from this figure, the ZnO-NWs mainly consist of ≈ 40 nm width and ≈ 350 nm length wires oriented at two angles ($\approx 60°$ and $120°$) to the substrate plane.

Additionally, it has to be noted that the density of the nanowires slightly fluctuated at different places on the substrate. The fluctuations in the density are related to the different angles of orientation and unequal distance between nanowires. As shown in Fig. 1, some parts of the formed surface nanowires are crowded or unevenly distributed. For estimation of the ratio (fill factor $f = V_{\text{ZnO-NWs}}/V_t$) between the volume occupied by ZnO-NWs ($V_{\text{ZnO-NWs}}$) and the total space of ZnO-NWs cover (V_t), we calculated the linear density of ZnO-NWs ($\rho_l = l_{\text{ZnO-NWs}}/l_t$) using the cut plane of the SEM picture presented in Fig. 1. Here, $l_{\text{ZnO-NWs}}$ is the sum of the diameters ($D_{\text{ZnO-NWs}}$) of ZnO-NWs displaced near the cut plane and l_t is the total length of this cut. It was found that

Fig. 1 SEM imagine of ZnO-NWs deposited on the ZnO/ITO/glass substrate.

$\rho_l \approx 0.536$. Assuming that the cross section of single ZnO-NWs is $D_{\text{ZnO-NW}}^2$ and taking into consideration that $f = V_{\text{ZnO-NW}}/V_t = S_{\text{ZnO-NW}}/S_t$, here $S_{\text{ZnO-NW}}$ is the square occupied by ZnO-NWs and S_t is the total cover area, and the fill factor in percentages can be obtained by the simple formula $f = \rho_l^2 \times 100\%$. Thus, in our case, $f \approx 28.7\%$. This value corresponds to the ZnO-NWs occupied volume.

3.2 Optical properties of ZnO-NWs deposited on ZnO/ITO/glass substrate

To analyze the contribution of ZnO-NWs to the optical response, the simulation of a multilayer system with a plain ZnO layer was conducted. This simulation has been done in TIRE configuration for reflectance intensity and ellipsometric parameters for the structures: 1 – ZnO/ITO/glass, 2 – APTES/ZnO/ITO/glass, and 3 – BSA/APTES/ZnO/ITO/glass. Simulated data are shown in Fig. 2A.

The experimentally obtained results for ellipsometric parameter Δ dependence on the wavelength λ for 1 – ZnO-NWs/ZnO/ITO/glass, 2 – APTES/ZnO-NWs/ZnO/ITO/glass, and 3 – BSA/APTES/ZnO-NWs/ZnO/ITO/glass are presented in Fig. 2B. Here, we present only spectra for the ellipsometric parameter Δ as it was proved to have higher sensitivity.[25] In the case of the non-modified structure ZnO-NWs/ZnO/ITO/glass ellipsometric parameter Δ (λ) peak was observed at 377 nm, such structure effective refractive index was estimated to be $n_{\text{ZnO-NWs}} = 1.355$ at 580 nm, using the Bruggeman's effective media approximation (EMA). Meanwhile, after ZnO-NWs modification with APTES, effective refractive index was modeled to be $n_{\text{APTES}} = 1.521$ at 580 nm, and the Δ (λ) peak was redshifted to the 401 nm value. As shown in Fig. 2B, the redshift observed between the two curves before modification of ZnO-NWs (Fig. 2, curve 1) and after modification of ZnO-NWs by APTES (Fig. 2, curve 2) was equal to 23 nm when the difference between refractive indexes was $n_{\text{APTES}} - n_{\text{ZnO-NWs}} = 0.166$. After further covalent immobilization of BSA on APTES/ZnO-NWs/ZnO/ITO/glass a redshift of the ellipsometric parameter Δ for 28 nm was registered, and the refractive index of this structure (BSA/APTES/ZnO-NWs/ZnO/ITO/glass) was $n_{\text{BSA}} = 1.691$ (at 580 nm). The calculated difference was $n_{\text{BSA}} - n_{\text{APTES}} = 0.17$. The total change in refractive index before and after modification of ZnO-NWs/ZnO/ITO/glass using BSA was $n_{\text{BSA}} - n_{\text{ZnO-NWs}} = 0.366$ and the total shift between peaks of 1 – ZnO-NWs/ZnO/ITO/glass and 3 – BSA/APTES/ZnO-NWs/ZnO/ITO/glass was 51 nm. The calculated sensitivity of the BSA/APTES/ZnO-NWs/ZnO/ITO/glass structure was 151.8 nm per RIU.

In the case of flat-type ZnO structure (ZnO/ITO/glass) simulation before and after modification by APTES and BSA (Fig. 2A, curves 1–3), the observed redshift was only 4 nm when the difference between refractive indexes was $n_{\text{BSA}} - n_{\text{ZnO}} = 0.366$. The clear difference before and after modification of ZnO/ITO/glass with APTES was not observed, the curves 1 and 2 in Fig. 2A overlap each other. The sensitivity of such structure was estimated to be 11.9 nm per RIU. In the case of ZnO-NWs as a sensing substrate (ZnO-NWs/ZnO/ITO/glass) for covalent BSA immobilization, the sensitivity of spectral shift to refractive index was ~ 13 times higher in comparison to flat type ZnO.
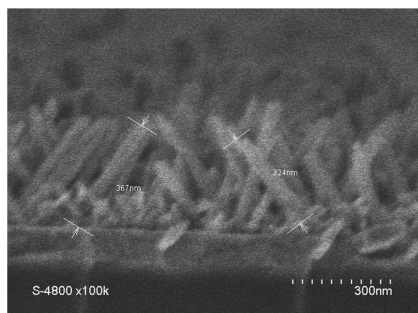
This journal is © The Royal Society of Chemistry 2021

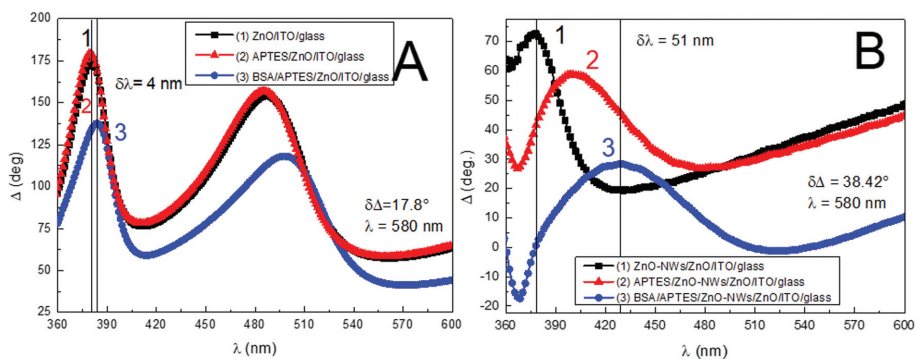*J. Mater. Chem. C*, 2021, **9**, 1345–1352 | **1347**

Fig. 2 Simulation of ellipsometric parameter Δ *vs.* wavelength during flat ZnO modification. (A) Experimental curves of ellipsometric parameter Δ *vs.* wavelength for 1 – ZnO/ITO/glass, 2 – APTES/ZnO/ITO/glass; 3 – BSA/APTES/ZnO/ITO/glass. (B) Experimental curves of ellipsometric parameter Δ *vs.* wavelength for 1 – ZnO-NWs/ZnO/ITO/glass, 2 – APTES/ZnO-NWs/ZnO/ITO/glass and 3 – BSA/APTES/ZnO-NWs/ZnO/ITO/glass.

The ellipsometric parameter Δ amplitude change at 580 nm in the case of the 350 nm flat-type ZnO/ITO/glass structure before and after modification with APTES and BSA (Fig. 2A) was 17.8 degrees. Calculated sensitivity to refractive index change in this case was 53 degrees per RIU. For structures ZnO-NWs/ZnO/ITO/glass and BSA/APTES/ZnO-NWs/ZnO/ITO/glass (Fig. 2B) Δ amplitude change at 580 nm was 38.42 degrees, the calculated sensitivity was 114.3 degrees per RIU, $\sim$2.24 times higher than in case of ZnO/ITO/glass and BSA/APTES/ZnO/ITO/glass. Such high sensitivity can be explained by the multiple reflections that occur in the ZnO-NWs matrix when this structure is used as a sensing layer in the TIRE mode. Furthermore, these findings demonstrate that a significantly higher amount of BSA molecules (or other proteins) can be covalently immobilized on ZnO-NWs modified substrates in comparison to the flat-type ZnO layer due to the higher surface area. These results allow us to suggest that ZnO-NWs based optical analytical systems exhibit higher sensitivity and can be successfully used for the development of enzymatic and affinity biosensors.

Reflectance intensity (R) spectra presented in Fig. 3 show an optical response for 1 – ZnO-NWs/ZnO/ITO/glass, 2 – APTES/ZnO-NWs/ZnO/ITO/glass, 3 – BSA/APTES/ZnO-NWs/ZnO/ITO/glass, 4 – ZnO/ITO/glass and 5 – BSA/APTES/ZnO/ITO/glass. The reflectance of ZnO/ITO/glass before (Fig. 3, curve 4) and after covalent immobilization of BSA (Fig. 3, curve 5) values were between 0.8 and 1. These results indicate that almost all light was reflected in both cases and no clear difference between these curves was observed. Reflectance difference before and after modification of simulated flat ZnO/ITO/glass with APTES and BSA was only 0.021 a.u. at 650 nm. In the case of flat-type ZnO/ITO/glass, BSA in PBS was modeled as infinite media using Cauchy dispersion which the refractive index was 1.51.[24] The BSA/APTES/ZnO-NWs/ZnO/ITO/glass BSA/APTES structure was modeled as an effective media substrate, with 30% ZnO and 70% Cauchy material, and a refractive index of 1.691 at 580 nm.

It is reasonable to assume that ZnO-NWs contribute a noticeable scattering effect from the surface, however the simulation of the optical response of the light scattered structure is rather complicated and limited due to software. Thus, the optical
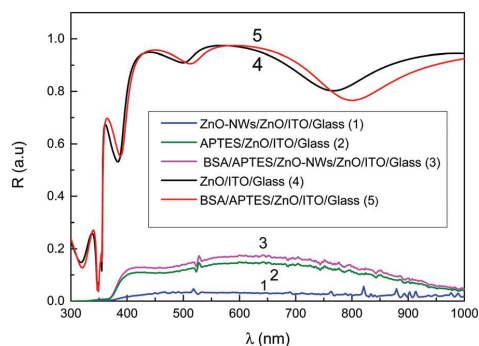

Fig. 3 Reflectance intensity (R) spectra of 1 – ZnO-NWs/ZnO/ITO/glass, 2 – APTES/ZnO-NWs/ZnO/ITO/glass, 3 – BSA/APTES/ZnO-NWs/ZnO/ITO/glass, 4 – ZnO/ITO/glass, 5 – BSA/APTES/ZnO/ITO/glass.

properties of ZnO-NWs formed on a glass substrate covered with 120 nm ITO and 20 nm ZnO layers were measured by TIRE. Ellipsometric spectra were recorded using TIRE configuration at a 70 degree angle of incidence using a 70 degree BK7 glass prism for measurements in liquids. The reflectance intensity and ellipsometric spectra for ZnO-NWs/ZnO/ITO/glass and BSA/APTES/ZnO-NWs/ZnO/ITO/glass are presented in Fig. 3. In contrast to the simulated structures with ZnO/ITO/glass, the ZnO-NWs had very weak reflectance intensity (Fig. 3, curve 1) due to the strong light scattering effect, meanwhile the ellipsometric spectra were less affected due to the relative values of ellipsometric parameters. However, the differences in reflectance intensity spectra were clearly distinguished (Fig. 3, curves 1 and 3). In the case of ZnO-NWs/ZnO/ITO/glass, the reflectance intensity value at 650 nm was observed to be 0.03 a.u., while after modification to BSA/APTES/ZnO-NWs/ZnO/ITO/glass it became 0.17 a.u. Thus, the R difference for the surface with ZnO-NWs before and after modification with BSA (Fig. 3, curves 1 and 3)

1348 | *J. Mater. Chem. C*, 2021, **9**, 1345–1352

This journal is © The Royal Society of Chemistry 2021

was 0.14 a.u., and it was about 6.6 times higher in comparison to the flat ZnO layer (Fig. 3, curves 4 and 5).

The differences of R spectra between ZnO/ITO/glass and ZnO-NWs/ZnO/ITO/glass after modification with APTES and covalent BSA immobilization can be explained by the diminishing of diffuse scattering of ZnO-NWs due to BSA protein binding. When such nanowires are modified with BSA, the surface structures become more "smooth" and as a result, the reflectance increases with the higher refractive index of the layer. This phenomenon is observed as increased reflectance (Fig. 3, curve 3). However, such a low specular reflectance from the ZnO-NWs/ZnO/ITO/glass structure is rather complicated to reliably detect using R measurements. Meanwhile, ellipsometry offers more stable optical detection at a low intensity level due to relative value measurements through the ellipsometric parameters Ψ and Δ. Moreover, as noted above, the special behavior of the ellipsometric parameter Δ increases sensitivity under conditions of total internal reflection because the phase of p- and s-polarizations starts to vary with the angle of incidence. Such behaviour of ellipsometric parameter Δ is caused by the difference of phase shifts between Fresnel reflection coefficients r_p and r_s for p- and s-polarizations, respectively.[25]

To obtain the ZnO-NWs matrix density, which has to be known for further presented diffusion evaluation, the effective refractive index dependence on wavelength was modeled using Complete EASE software. An optical model for the characterization of the ZnO-NWs layer deposited on the ZnO/ITO/glass substrate was constructed using a Bruggemen effective media approach in which the ZnO material layer was characterized using one PSemi-M0 and two Gaussian oscillators.[26] The effective ZnO-NWs layer thickness evaluated from the SEM picture presented in Fig. 1 was ≈350 nm and it was a fixed parameter during the regression analysis. The obtained effective refractive index dispersion is presented in Fig. 4. The effective refractive index obtained from regression analysis showed that this ZnO-NWs layer consists of 30% ZnO and 70% air. Taking into
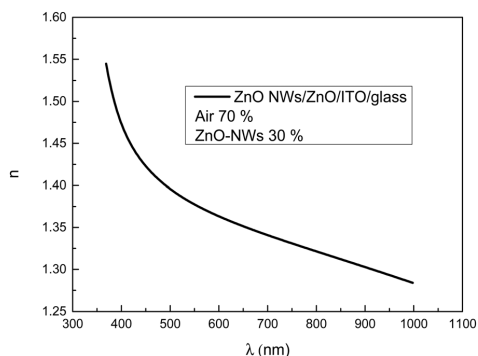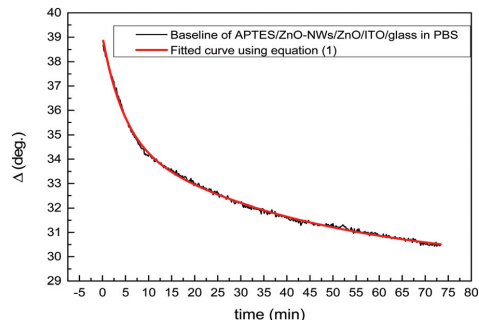

Fig. 5 Stabilization of the APTES modified ZnO-NWs/ZnO/ITO/glass substrate in PBS and establishment of a baseline.

consideration that the average width of ZnO-NWs is ≈40 nm, the width of void channels is from 40 to 90 nm.

Such evaluation of ZnO-NWs density, which is obtained from the modeling of ellipsometry measurements data is required for further analysis of BSA covalent immobilization in order to calculate the diffusion coefficient. We used modeled values that correspond to 30% ZnO-NWs and 70% air. This value coincides with that obtained from Fig. 1.

3.3 Kinetics of covalent BSA immobilization on APTES/ZnO-NWs/ZnO/ITO/glass substrate

The BSA immobilization kinetics was studied using a 390.8 nm wavelength. The selection of this wavelength was made because at this point of the spectra, the ellipsometric parameter Δ showed the highest sensitivity to refractive index changes.

For covalent BSA immobilization on the APTES/ZnO-NWs/ZnO/ITO/glass substrate, the surface was treated with PBS to establish the baseline. Fig. 5 shows the variation of the ellipsometric parameter Δ during surface stabilization with PBS. The analysis of this variation has demonstrated that the experimental curve can be well fitted by the following formula:

$$\Delta(t) = \Delta_0 + \Delta_1 \exp(-t/t_1) + \Delta_2 \exp(-t/t_2) \qquad (1)$$

here t is the time, and Δ_0, Δ_1 and Δ_2 are constants. The characteristic times t_1 and t_2 are 4.5 min and 42 min, correspondingly. The shorter time t_1 is most probably related to a lower density region of the nanowire matrix, meanwhile the longer one corresponds to higher density regions.

After the establishment of steady state conditions and a baseline in PBS, 0.1 mg ml^{-1} concentration BSA solution in PBS was injected into the chamber with the APTES/ZnO-NWs/ZnO/ITO/glass substrate. The Δ kinetics of covalent BSA immobilization on ZnO-NWs was recorded for 121 min. The kinetics of ellipsometric parameter Δ during the BSA immobilization process show changes in the total ellipsometric parameter Δ of about 6.11 degrees. As can be seen from Fig. 6, the immobilization process after the steady state conditions in PBS were reached (PBS 1) contains two phases. Phase I of the kinetics occurs during a relatively short time, i.e. about 5 s and
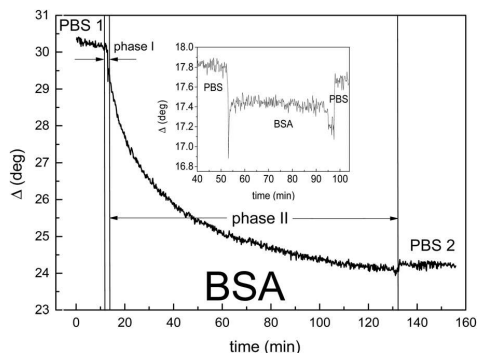

Fig. 4 Effective refractive index (n) vs. wavelength (λ) obtained from the optical model using the Bruggeman effective media approach for the ZnO-NWs/ZnO/ITO/glass structure in air.

This journal is © The Royal Society of Chemistry 2021

J. Mater. Chem. C, 2021, **9**, 1345–1352 | **1349**

Fig. 6 Kinetics of BSA covalent immobilization on the APTES/ZnO-NWs/ZnO/ITO/glass substrate.

the total change of Δ in this phase is only 0.5 degrees. The inset in Fig. 6 demonstrates the experimentally obtained BSA immobilization kinetics on flat-type ZnO (ZnO/ITO/glass). As can be seen, the amplitude and rise time of this process fully coincides with phase I, showing that this phase is a result of BSA immobilization at the top of ZnO-NWs. The change of ellipsometric parameter Δ in the case of the flat-type ZnO structure is 0.4 degree, meanwhile for ZnO-NWs (phase II) this change is about 5.2 degrees. Thus, the ratio of these values in the comparison of sensitivity between flat-type and ZnO-NWs platforms is about 13 times, which is in good agreement with the simulations presented in Section 3.2.

During phase II, the change in Δ was 5.61 degrees. Thus, the biggest amount of injected BSA was covalently immobilized on the APTES/ZnO-NWs/ZnO/ITO/glass substrate during phase II of this process, which lasted more than 100 min. The average characteristic time of this phase, assuming that the Δ parameter changing in time can be described approximately by exponential decay, was about 20 min. After covalent immobilization of BSA molecules on ZnO-NWs and washing with PBS, nonspecifically bound molecules were removed from the surface. In this case, the total ellipsometric parameter Δ signal changed only by 0.17 degrees, thus nonspecific adsorption of BSA on this surface was negligible (Fig. 6, PBS 2). This means that BSA was successfully covalently immobilized on APTES/ZnO-NWs/ZnO/ITO/glass and the layer of BSA is stable during the surface washing process.

Immobilization of BSA during phase II demonstrates a time-dependent and irreversible bonding process. For this reason, we assumed that this phase appears due to the diffusion of BSA molecules in PBS solution through the narrow channels existing between nanowires (see Fig. 1). To verify this assumption, the following modelling of ellipsometric parameter Δ kinetics during the immobilization of BSA molecules was performed.

The ellipsometric parameter Δ_{m} measured using the TIRE method is proportional to the effective refractive index (n_{e}) of the heterogenic matrix consisting of APTES/ZnO-NWs formed on the ZnO/ITO/glass substrate and interwire space filled with

PBS. During the diffusion of BSA molecules into this matrix filled with PBS, BSA changes its refractive index (n_{BSA}), which induces Δ_{m} evolution in time. Using Maxwell Garnett approximation and assuming that Δ_{m} is directly proportional to the n_{e}, it is possible to obtain the following formula for Δ_{m} as a function of time (t):

$$\Delta_{\mathrm{m}}(t) = \Delta_{\mathrm{ZnO}} \left[\frac{2\delta\left(\Delta_{\mathrm{BSA}}{}^2 - \Delta_{\mathrm{ZnO}}{}^2\right) + \Delta_{\mathrm{BSA}}{}^2 + 2\Delta_{\mathrm{ZnO}}{}^2}{2\Delta_{\mathrm{ZnO}}{}^2 + \Delta_{\mathrm{BSA}}{}^2 - \delta(\Delta_{\mathrm{BSA}}{}^2 - \Delta_{\mathrm{ZnO}}{}^2)} \right]^{1/2} \quad (2)$$

here Δ_{ZnO} and $\Delta_{\mathrm{BSA}}(t)$ are the ellipsometric parameters of APTES/ZnO-NWs and BSA solution in PBS respectively, δ is the ratio of volume between ZnO-NWs and interwire space. The normalized measured ellipsometric parameter $\Delta_{\mathrm{nm}} = [\Delta_{\mathrm{m}}(t) - \Delta_{\mathrm{m}}(0)]/[\Delta_{\mathrm{m}}(\infty) - \Delta_{\mathrm{m}}(0)]$ vs. time dependence is presented in Fig. 7. Here: $\Delta_{\mathrm{m}}(t)$, $\Delta_{\mathrm{m}}(0)$ and $\Delta_{\mathrm{m}}(\infty)$ are the ellipsometric parameters Δ at different time instances, at the beginning, during phase I and at phase II of BSA covalent immobilization.

Taking into consideration the optical properties, i.e., the refractive index (n) of the solution, depending on the concentration of BSA molecules, we assume a direct proportionality between Δ_{BSA} and C. The distribution of this concentration in the channel directed along the nanowires as a function of time can be obtained by numerically solving a one-dimensional diffusion equation:

$$D \frac{\partial^2 C(x,t)}{\partial x^2} = \frac{\partial C(x,t)}{\partial t} \quad (3)$$

Here $C(x,t)$ is the concentration of BSA molecules, x is the coordinate along the nanowires, t is time, and D is the diffusion coefficient. The boundary conditions for this equation are the following $C(0,0) = C(d,\infty) = C_0$, which is the concentration of BSA in PBS outside the nanowire matrix and $\partial C(d,t)/\partial t = 0$; here d is the length of the channel filled only by PBS. The average concentration of BSA inside the channel (C_{a}) is:

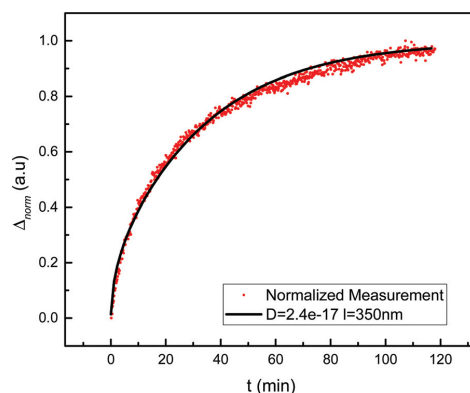$$C_{\mathrm{a}}(t) = \frac{\int_0^d C(x,t)\mathrm{d}x}{d} \quad (4)$$

Fig. 7 Dependence of the normalized signal Δ_{norm} of ellipsometric parameter vs. time during BSA covalent immobilization on the APTES/ZnO-NWs/ZnO/ITO/glass substrate.

1350 | J. Mater. Chem. C, 2021, 9, 1345–1352

This journal is © The Royal Society of Chemistry 2021

the results of numerical calculation of Δ_{norm} *vs.* time dependence, obtained using eqn (2)–(4) show the solid black curve presented in Fig. 7. For δ = 0.43 (30% ZnO and 70% air) and d = 350 nm well-fitting of experimental data was at $D = 2.4 \times 10^{-17}$ m^2 s^{-1}, which is about 6 orders lower than conventional BSA diffusion in PBS solution.[28] Taking into consideration such a low D value, BSA molecule dimensions (14 nm $\times$ 4 nm $\times$ 4 nm) and diffusion channel width (40–90 nm), it is possible to assume that during covalent BSA immobilization on APTES/ZnO-NWs/ZnO/ITO/glass substrate BSA molecule diffusion plays a significant role. This process is not conventional Brownian diffusion, because during the movement of BSA molecules along the channel filled by PBS, the interaction with ZnO-NWs is essential. For this reason, the value of diffusion coefficient has to be strongly correlated with the density of ZnO-NWs and dimensions of biomolecules. In this case, the diffusion coefficient obtained from the measurement and analysis of biomolecule immobilization kinetics could be used for the evaluation of the sizes of these molecules. Studies of D *vs.* size dependence for various ZnO-NWs dimensions and surface densities would be an interesting object of further research.

4 Conclusions

It was demonstrated that ZnO-NWs produced by a simple and cost-effective electrodeposition method on commercially available ITO/glass substrate coated with a ZnO layer can be successfully applied for the BSA immobilization. This substrate is able to accumulate a significantly higher amount of BSA molecules covalently immobilized on the ZnO-NWs coated substrate in comparison to the simulated flat-type ZnO layer. The TIRE method has shown that surfaces based on ZnO-NWs overtake the sensitivity of flat-type ZnO for wavelength to refractive index change by 13 times. Moreover, the surfaces with ZnO-NWs showed larger changes in ellipsometric parameters Ψ and Δ during the BSA binding to the ZnO-NWs surface. Particularly, the changes of ellipsometric parameter Δ was 2.24 times more sensitive compared to the flat-type ZnO sensor. The TIRE method allows us to achieve higher sensitivity because Δ measured during the BSA immobilization phase for ZnO-NWs was larger than that for the flat-type case. These differences in the phase were related to the distinct changes of the refractive index of the ZnO-NWs and flat-type ZnO surfaces.

It was found that the time of signal saturation in PBS buffer could be related to the different density of ZnO-NWs regions on the substrate. The shorter time of stabilization is related to the lower density of ZnO-NWs, while a longer time is related to the higher density of these nanostructures. The diffusion of proteins along the ZnO-NWs plays a significant role in this process, for this reason the diffusion coefficient is significantly lower than that of proteins in free liquid space.

Conflicts of interest

The authors declare that they have no known competing financial interests or personal relationships that could have appeared to influence the work reported in this paper.

Acknowledgements

References

1 O. Graniel, M. Weber, S. Balme, P. Miele and M. Bechelany, *Biosens. Bioelectron.*, 2018, **122**, 147–159.

2 A. Tereshchenko, M. Bechelany, R. Viter, V. Khranovskyy, V. Smyntyna, N. Starodub and R. Yakimova, *Sens. Actuators, B*, 2016, **229**, 664–677.

3 D.-Y. Son, J.-H. Im, H.-S. Kim and N.-G. Park, *J. Phys. Chem. C*, 2014, **118**, 16567–16573.

4 K. M. Lee, C. W. Lai, K. S. Ngai and J. C. Juan, *Water Res.*, 2016, **88**, 428–448.

5 R. Viter, M. Savchuk, N. Starodub, Z. Balevicius, S. Tumenas, A. Ramanaviciene, D. Jevdokimovs, D. Erts, I. Iatsunskyi and A. Ramanavicius, *Sens. Actuators, B*, 2019, **285**, 601–606.

6 G. Chai, O. Lupan, L. Chow and H. Heinrich, *Sens. Actuators, A*, 2009, **150**, 184–187.

7 M. Mehrabian, R. Azimirad, K. Mirabbaszadeh, H. Afarideh and M. Davoudian, *Phys. E*, 2011, **43**, 1141–1145.

8 J. H. Jun, H. Seong, K. Cho, B. Moon and S. Kim, *Ceram. Int.*, 2009, **35**, 2797–2801.

9 A. Sanginario, V. Cauda, A. Bonanno, K. Bejtka, S. Sapienza and D. Demarchi, *RSC Adv.*, 2016, **6**, 891.

10 A. Kumar, S. Jung and T. Ji, *Sensors*, 2011, **11**, 5087–5111.

11 A. Usman, O. Nur, M. Willander and B. Danielsson, *Sens. Actuators, B*, 2010, **145**, 869–874.

12 N. Tripathy and D.-H. Kim, *Nano Convergence*, 2018, **5**, 27.

13 C. Chen and J. Wang, *Analyst*, 2020, **145**, 1605–1628.

14 X. Fan, I. M. White, S. I. Shopova, H. Zhu, J. D. Suter and S. Yuse, *Anal. Chim. Acta*, 2008, **620**, 8–26.

15 A. Campu, L. Susu, F. Orzan, D. Maniu, A. M. Craciun, A. Vulpoi, L. Roiban, M. Focsan and S. Astil, *Front. Chem.*, 2019, **7**, 55.

16 P. Damborsky, J. Svitel and J. Katrlík, *Essays Biochem.*, 2016, **60**, 91–100.

17 J. Elias, C. l. Clément, M. Bechelany, J. Michler, G. Y. Wang, Z. Wang and L. Philippe, *Adv. Mater.*, 2010, **22**, 1607–1612.

18 J. Elias, M. Bechelany, I. Utke, R. Erni, D. Hosseini, J. Michler and L. Philippe, *Nano Energy*, 2012, **1**, 696–705.

19 M. Treideris, I. Simkiene, A. Selskis, Z. Balevicius and G. J. Babonas, *Acta Phys. Pol., A*, 2011, **19**, 131–134.

20 Z. Balevicius, J. Talbot, L. Tamosaitis, I. Plikusiene, A. Stirke, G. Mickiene, S. Balevicius, A. Paulauskas and A. Ramanavicius, *Sens. Actuators, B*, 2019, **297**, 126770.

21 I. Baleviciute, Z. Balevicius, A. Makaraviciute, A. Ramanaviciene and A. Ramanavicius, *Biosens. Bioelectron.*, 2013, **39**, 170–176.

22 S. Zeng, D. Baillargeat, H. P. Ho and K. Yong, *Chem. Soc. Rev.*, 2014, **43**, 3426–3452.

23 O. Graniel, I. Iatsunskyi, E. Coy, C. Humbert, G. Barbillon, T. Michel, D. Maurin, S. Balme, P. Miele and M. Bechelany, *J. Mater. Chem. C*, 2019, **7**, 15066–15073.

24 Z. Balevicius, A. Paulauskas, I. Plikusiene, L. Mikoliunaite, M. Bechelany, A. Popov, A. Ramanavicius and A. Ramanaviciene, *J. Mater. Chem. C*, 2018, **6**, 8778–8783.

25 H. Arwin, M. Poksinski and K. Johansen, *Appl. Opt.*, 2004, **43**, 15.

26 A. A. Chaaya, R. Viter, I. Baleviciute, M. Bechelany, A. Ramanavicius, Z. Gertnere, D. Erts, V. Smyntyna and P. Miele, *J. Phys. Chem. C*, 2014, **118**, 3811–3819.

27 M. Baitimirova, R. Viter, J. Andzane, A. Van Der Lee, D. Voiry, I. Iatsunskyi, E. Coy, L. Mikoliunaite, S. Tumenas, K. Zaleski, Z. Balevicius, I. Baleviciute, A. Ramanaviciene, A. Ramanavicius, S. Jurga, D. Erts and M. Bechelany, *J. Phys. Chem. C*, 2016, **120**, 23716–23725.

28 S. Koutsopoulos, L. D. Unswortha, Y. Nagaia and S. Zhanga, *Proc. Natl. Acad. Sci. U. S. A.*, 2009, **106**, 4623–4628.

1352 | *J. Mater. Chem. C*, 2021, **9**, 1345–1352

This journal is © The Royal Society of Chemistry 2021

Paper 3

Investigation and Comparison of Specific Antibodies' Affinity Interaction with SARS-CoV-2 Wild-Type, B. 1.1. 7, and B. 1.351 Spike Protein by Total Internal Reflection Ellipsometry

Ieva Plikusiene, **Vincentas Maciulis**, Silvija Juciute, Ruta Maciuleviciene, Saulius Balevicius, Arunas Ramanavicius, Almira Ramanaviciene,

MDPI

Article

Investigation and Comparison of Specific Antibodies' Affinity Interaction with SARS-CoV-2 Wild-Type, B.1.1.7, and B.1.351 Spike Protein by Total Internal Reflection Ellipsometry

Ieva Plikusiene [1] , Vincentas Maciulis [1,2], Silvija Juciute [1], Ruta Maciuleviciene [1], Saulius Balevicius [1,2], Arunas Ramanavicius [1] and Almira Ramanaviciene [1,*]

[1] NanoTechnas—Center of Nanotechnology and Materials Science, Faculty of Chemistry and Geosciences, Vilnius University, Naugarduko Str. 24, 03225 Vilnius, Lithuania; ieva.plikusiene@chgf.vu.lt (I.P.); vincentas.maciulis@ftmc.lt (V.M.); silvija.juciute@chgf.stud.vu.lt (S.J.); ruta.maciuleviciene@gmail.com (R.M.); saulius.balevicius@ftmc.lt (S.B.); arunas.ramanavicius@chf.vu.lt (A.R.)

[2] State Research Institute Center for Physical and Technological Sciences, Sauletekio Ave. 3, 03225 Vilnius, Lithuania

[*] Correspondence: almira.ramanaviciene@chf.vu.lt

Abstract: SARS-CoV-2 vaccines provide strong protection against COVID-19. However, the emergence of SARS-CoV-2 variants has raised concerns about the efficacy of vaccines. In this study, we investigated the interactions of specific polyclonal human antibodies (pAb-SCoV2-S) produced after vaccination with the Vaxzevria vaccine with the spike proteins of three SARS-CoV-2 variants of concern: wild-type, B.1.1.7, and B.1.351. Highly sensitive, label-free, and real-time monitoring of these interactions was accomplished using the total internal reflection ellipsometry method. Thermodynamic parameters such as association and dissociation rate constants, the stable immune complex formation rate constant (k_r), the equilibrium association and dissociation (K_D) constants and steric factors (P_s) were calculated using a two-step irreversible binding mathematical model. The results obtained show that the K_D values for the specific antibody interactions with all three types of spike protein are in the same nanomolar range. The K_D values for B.1.1.7 and B.1.351 suggest that the antibody produced after vaccination can successfully protect the population from the alpha (B.1.1.7) and beta (B.1.351) SARS-CoV-2 mutations. The steric factors (P_s) obtained for all three types of spike proteins showed a 100-fold lower requirement for the formation of an immune complex when compared with nucleocapsid protein.

Keywords: total internal reflection ellipsometry; SARS-CoV-2; immune complex; antibody–antigen interaction

1. Introduction

One of the key factors in preventing the spread of coronavirus disease 2019 (COVID-19), caused by severe acute respiratory syndrome coronavirus 2 (SARS-CoV-2), is the ability of the human immune system to produce neutralizing antibodies that could successfully block the SARS-CoV-2 spike (S) protein (in specific regions) and prevent its binding to the angiotensin-converting enzyme 2 (ACE2) receptor. However, the changes in SARS-CoV-2 over time, specifically in the S protein and some occurring mutations, are associated with viral survival capability, the rate of virus spread, and the severity of the disease. Additionally, these mutations in SARS-CoV-2 could affect the effectiveness of vaccines, therapeutic drugs, and diagnostic tools, as well as posing an increased risk to global public health. The World Health Organization (WHO), in collaboration with partners, has been monitoring and evaluating the evolution of the wild-type SARS-CoV-2, identified in Wuhan, China, since January 2020. Since then, an emergence of mutations has been recorded and compared to the reference SARS-CoV-2 genome. The WHO-convened expert group recommended the use of letters of the Greek alphabet (i.e., alpha, beta, gamma, delta, etc.) to name the SARS-CoV-2 variants [1].

The S protein is a large transmembrane homotrimer located on the surface of the virus. Each monomer is composed of two subunits, namely S1—with the receptor-binding domain (RBD) being responsible for binding with the ACE2 receptor present on the cell surface, and S2—responsible for the fusion of viral and host membranes [2,3]. Alpha SARS-CoV-2 (B.1.1.7) was first detected in the UK in autumn 2020. This variant is characterized by a large number of mutations, particularly within the S protein, as well as its being easier and faster to spread than other variants, mainly due to a single amino acid change (N501Y) in the RBD of the S protein [4]. The N501Y mutation improved the affinity of RBD for the human ACE2 receptor [5,6]. Almost all currently available vaccines aim to increase immunity specifically against the spike protein or just parts of it, mainly the RBD [7]. Several vaccine-producing companies, including Pfizer–BioNTech, Moderna, Astra Zeneca–Oxford, and others, confirmed the efficacy of their vaccines against alpha SARS-CoV-2. Beta SARS-CoV-2 (B.1.351) was first detected in South Africa (the genome of a variant strain was published in December 2020) and can also be characterized by specific mutations in the RBD of its S protein (N501Y, K417N, and E484K). These mutations enhance the affinity of the RBD for ACE2, while the E484K mutation could lead to an evasion of the immune system's response [8]. It is of paramount importance to understand the impact of SARS-CoV-2 mutations on the changes in viral infectivity and transmission. It is also relevant to clarify the role of mutations in the S protein, in terms of its interactions with antibodies produced in healthy (i.e., without natural exposure to SARS-CoV-2) and vaccinated individuals. The spread of the SARS-CoV-2 variants of concern is a challenge for the scientific community, who seek to be able to predict the effects of different mutations on both the virus's binding to the receptor and the antibody's binding to the virus [9]. It is well known that antibodies produced by the humoral response of the immune system after vaccination are one of the key factors in overcoming SARS-CoV-2, and their affinity for viral antigens is of high importance. However, there is still a lack of information on the antibodies' protection against new emerging variants of SARS-CoV-2, such as the alpha (B.1.1.7) and beta (B.1.351) variants that arose from the United Kingdom and South Africa, respectively. It was reported that B.1.1.7 still remains sensitive to neutralization with antibodies [10]. The results of neutralizing activity induced by a vectored vaccine against the B.1.1.7 and B.1.351 strains demonstrated that widespread immune escape was not observed in B.1.1.7, but greater resistance to B.1.351 was indicated in both the pseudo-virus and the live-virus neutralization assays [11]. Additionally, serological assays are mainly based on the wild-type SARS-CoV-2 S protein. However, the sensitive and specific assays used to monitor the antibody's immune response profile against four viral antigens (typically the RBD, the nucleocapsid, and the S1 and S2 proteins) were developed by Bio-Rad Laboratories, Inc. [12]. Thus, the spectrum of humoral responses can be assessed after COVID-19 infection or over time after vaccination.

The affinity of a specific antibody to viral antigens shows how effectively the immune complex is formed. Furthermore, the association and dissociation rate constants can give us important information about the thermodynamic parameters of this process. It was demonstrated that thermodynamic parameters enable a quantitative evaluation of an antibody's specific ability to inhibit the binding of the viral spike protein for the ACE2 receptor located in the host cell [13]. The affinity of a specific antibody for the SARS-CoV-2 S protein or for the ACE2 receptor can be measured using a sensitive, label-free, and real-time monitoring optical surface plasmon resonance (SPR) method [14–16]. Despite the fact that SPR is common in many laboratories, the other optical method, spectroscopic ellipsometry in total internal reflection mode (TIRE), recently attracted a high level of interest for its application in antibody–antigen interaction measurements, due to its higher sensitivity than SPR [17–22]. During an experiment using TIRE, the light wave polarization state's change upon the reflection from the surface is measured [19]. The TIRE method is capable of detecting even small changes in the ambient refractive index caused by the immobilization of antigens or antibodies and the interaction between them on the surface [23–25]. During

TIRE measurements, two ellipsometric parameters are determined: Ψ corresponds to the light wave amplitude and Δ to the light wave phase shift after the light reflection from the surface. The change in the ellipsometric parameter Ψ is sensitive to the large concentration range of biomolecules during the formation of the layer. However, the sensitivity of the parameter Δ decreases significantly due to the shift in surface plasmon resonance if the concentration of biomolecules is high [18]. Therefore, the measurement and assessment of both ellipsometric parameters Δ and Ψ enable a more detailed evaluation of interacting biomolecules' affinity and association/dissociation rate constants.

In this study, we performed a highly sensitive, label-free, and real-time TIRE monitoring of the interaction kinetics between the specific polyclonal human antibody (pAb-SCoV2-S) produced after vaccination and the covalently immobilized spike proteins of the three SARS-CoV-2 variants of concern—wild-type (SCoV2-S), B.1.1.7 or so-called alpha (SCoV2-αS), and B.1.351 or so-called beta (SCoV2-βS). Here, we reported the comparison of the thermodynamic parameters, such as the association rate constant (k_a), the dissociation rate constant (k_d), the stable immune complex formation rate constant (k_r), the equilibrium association and dissociation constants (K_A, K_D), and steric factors (P_s), calculated using a two-step irreversible binding mathematical model.

2. Materials and Methods

2.1. Materials

N-(3-dimethylaminopropyl)-N′-ethyl-carbodiimide hydrochloride (EDC) and N-hydroxysuccinimide (NHS) were purchased from Merck Millipore (USA). Ethanolamine, sodium dodecyl sulphate, sodium hydroxide, and 11-Mercaptoundecanoic acid (11-MUA) were purchased from Sigma Aldrich. The SPR sensors' disc, coated with a 46 nm gold layer, was received from XanTech bioanalytics (Duesseldorf, Germany). The three types of SARS-CoV-2 recombinant S proteins—the wild-type (SCoV2-S), the alpha variant (SCoV2-αS: contains nine mutations compared to the reference SARS-CoV-2 S protein), and the beta variant (SCoV2-βS: contains ten mutations compared to the reference SARS-CoV-2 S protein)—expressed in yeast Saccharomyces cerevisiae (purity > 85%), were purchased from Baltymas (Vilnius, Lithuania).

Human blood serum was collected from two volunteers. One serum was obtained from the volunteer vaccinated using 1 dose of the Vaxzevria vaccine 3 weeks before the experiment, whilst the other (control serum) was obtained from a healthy volunteer before the pandemic. Whole blood was collected in a vacutainer test tube containing 3.5 mL of CAT serum separator clot activator (Greiner Bio-One GmbH, Kremsmünster, Austria), in the laboratory of Tavo Klinika, LtD (Vilnius, Lithuania). Serum was obtained after centrifugation at $5000 \times g$ for 15 min. The titer of the antibody against the S protein of SARS-CoV-2 (pAb-SCoV2-S) was obtained using a chemiluminescent microparticle immunoassay. The titer was then recalculated to a molar concentration, and the primary blood serum pAb-SCoV2-S concentration was obtained at 33.96 nM [26]. Blood serum dilutions with a phosphate-buffered saline (PBS) solution at pH 7.4 (Carl Roth, Karlsruhe, Germany) and at 1:4, 1:10, 1:20, 1:30, and 1:40 ratios were used for the kinetics measurements of the pAb-SCoV2-S interaction with the three types of S protein. The serum sample was stored at − 20 °C until analysis. The sample was collected in accordance with the Lithuania ethics law. This study did not need the approval of the ethics committee (confirmed by the Vilnius Regional Biomedical Research Ethics Committee).

2.2. Modification of the Gold-Coated SPR Sensor Disc with SCoV2-S, SCoV2-αS, or SCoV2-βS

The covalent immobilization of SCoV2-S, SCoV2-αS, or SCoV2-βS on the gold-coated SPR sensor disc's surface was performed under standard protocol using an 11-MUA self-assembled monolayer (SAM) [21,22,27–29]. Briefly, the gold-coated SPR sensor disc was rinsed with hexane and methanol and then immersed in methanol for 3 min for ultrasound treatment. Once dried, the SPR sensor disc was immersed in a 1 mM solution of 11-MUA in methanol for 18 h to form an 11-MUA SAM. Then, the activation

of the 11-MUA SAM carboxyl groups required for the covalent immobilization of SCoV2-S, SCoV2-αS, or SCoV2-βS was accomplished by injecting the solution consisting of 0.1 M NHS and 0.4 M of EDC, mixed in equal parts, into a TIRE measurement chamber for 15 min. After the activation of the carboxyl groups, the TIRE chamber was rinsed with a PBS solution at a pH level of 7.4. Then, 333 nM SCoV2-S diluted in the PBS was injected into the TIRE chamber and incubated for 60 min. After rinsing with the PBS solution, the surface was exposed to 1 M ethanolamine at a pH level of 8.5 for 10 min to deactivate any active carboxyl groups present in the 11-MUA SAM. The schematic representation of all the steps in the surface modification is presented in Figure 1A. The same immobilization protocol was applied for SCoV2-αS and SCoV2-βS using the same 333 nM concentration in PBS (Figure 1C).
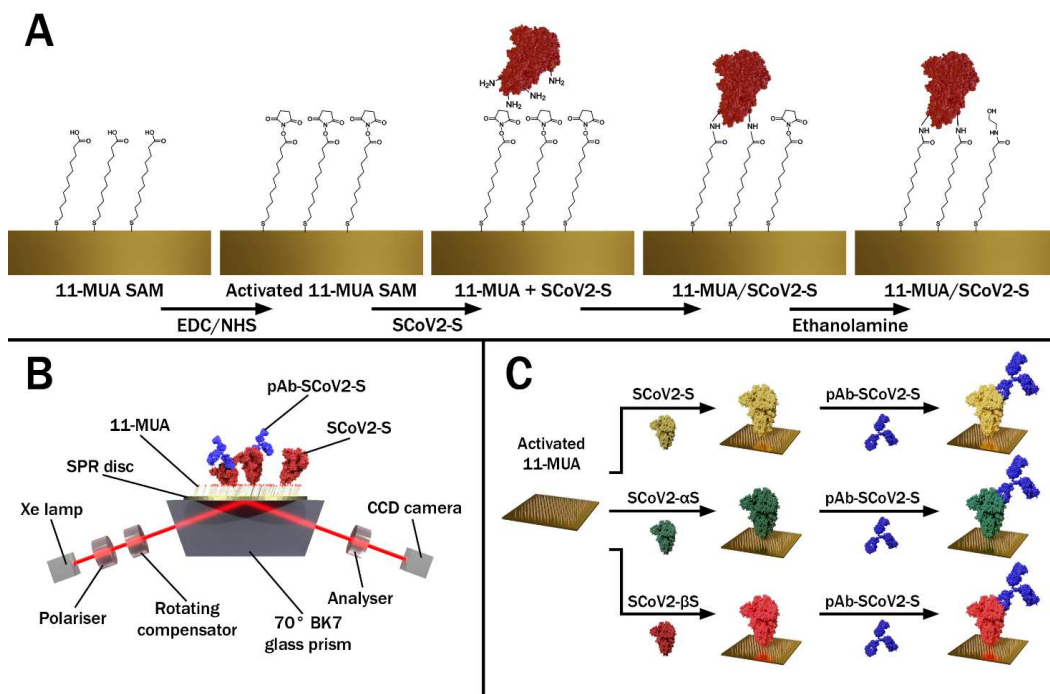
Figure 1. (**A**) Schematic representation of SARS-CoV-2 S protein (SCoV2-S, SCoV2-αS, or SCoV2-βS) covalent immobilization on the gold-coated SPR sensor disc pre-modified with 11-MUA SAM. (**B**) The principle scheme representing total internal reflection ellipsometry measurements. (**C**) Schematic representation of SCoV2-S, SCoV2-αS, and SCoV2-βS covalent immobilization and interaction with specific polyclonal antibodies (pAb-SCoV2-S).

2.3. TIRE Measurements

The ellipsometric measurements were conducted using a rotating compensator ellipsometer J. A. Woollam M2000X (Lincoln, NE, USA). All TIRE experiments were carried out at a 70° angle of incident in the spectral range of 200–1000 nm. A BK7 glass prism (set at 70°) was connected to the commercial SPR sensor disc via a refractive index matching fluid and mounted on the TIRE chamber with a 5 mm diameter. In the TIRE experimental setup, a liquid handling system with a custom-built Teflon chamber was used for measurements in liquids, and this schematic measurement setup is presented in Figure 1B. After each step in the surface modification, the spectra of the ellipsometric parameters Ψ and Δ vs. λ were recorded and compared with those obtained previously. Here, we present only the

evolution in time of parameter Ψ, as this ellipsometric parameter sensitivity remains the same throughout a wide concentration range.

3. Results and Discussion

3.1. Covalent Immobilization of SCoV2-S, SCoV2-αS, or SCoV2-βS on 11-MUA SAM

The TIRE method was used to study the covalent immobilization of three different mutations, or so-called variants of concern (VOCs), of the SARS-CoV-2 S protein and for the evaluation of interaction kinetics with diluted human blood serum containing specific pAb-SCoV2-S antibodies. The 333 nM of SCoV2-S, SCoV2-αS, and SCoV2-βS in the PBS solution were covalently immobilized on the activated 11-MUA SAM according to the protocol described in the Materials and Methods part. All three injected solutions of the S protein were kept in the chamber for about 55–60 min, and then washed with PBS. Covalent immobilization kinetics were analyzed at 661 nm for SCoV2-S, 656 nm for SCoV2-αS, and 670 nm for SCoV2-βS, close to the SPR dip. As can be seen in Figure 2A, Figure 3A, and Figure 4A, the ellipsometric parameter ΔΨ change was 13.5° for SCoV2-S, 14.0° for SCoV2-αS, and 11.0° for SCoV2-βS after immobilization, respectively.
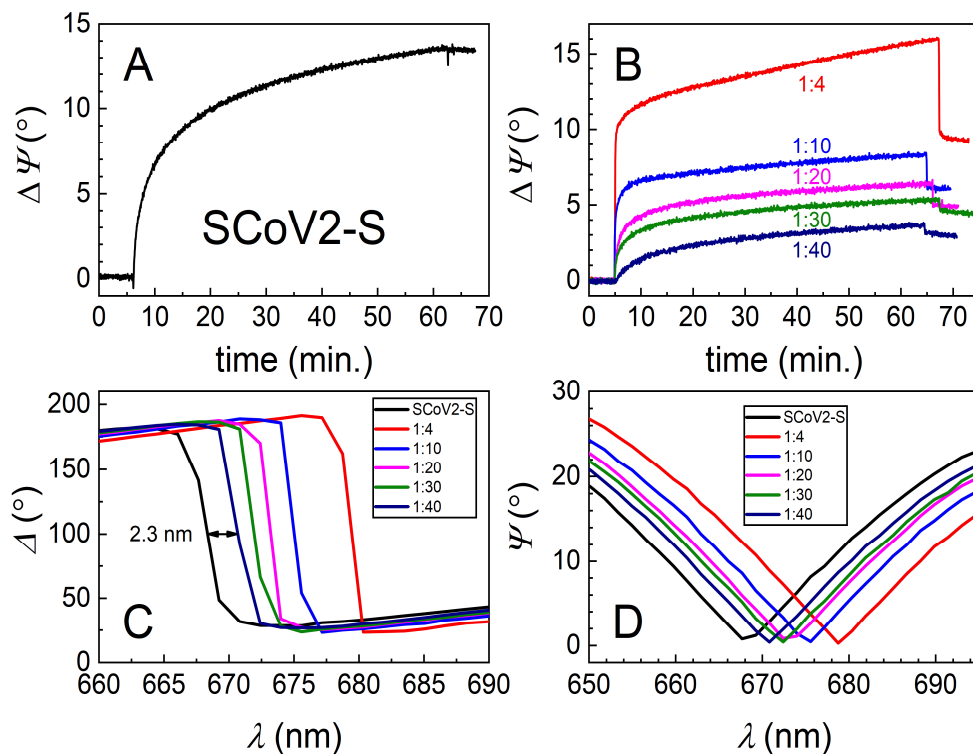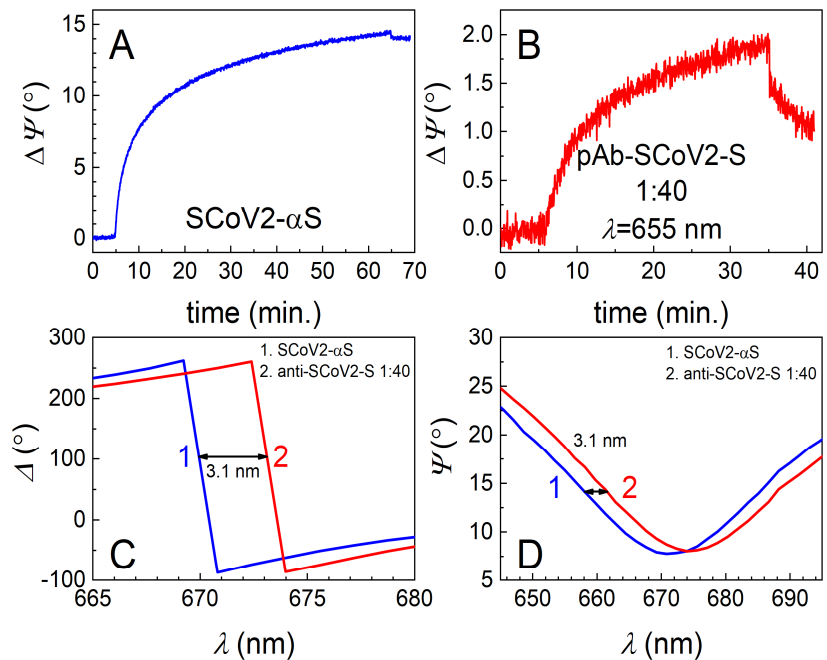

Figure 2. Time-resolved TIRE kinetics and ellipsometric parameters of SCoV2-S immobilization and interaction with specific polyclonal antibodies. (**A**) Kinetics of covalent SCoV2-S immobilization on 11-MUA SAM modified gold-coated SPR sensor disc; (**B**) kinetics of polyclonal antibody interaction with covalently immobilized ScoV2-S at different serum dilutions (1:4, 1:10, 1:20, 1:30, and 1:40); (**C**) Δ and (**D**) Ψ spectral shift after immune complex formation using the same dilutions of polyclonal antibodies.

Figure 3. Time-resolved TIRE kinetics and ellipsometric parameters of SCoV2-αS immobilization and interaction with specific polyclonal antibodies. (**A**) Kinetics of covalent SCoV2α-S immobilization on 11-MUA SAM modified gold-coated SPR sensor disc; (**B**) kinetics of polyclonal antibody interaction with covalently immobilized SCoV2-αS at 1:40 dilution of serum; (**C**) Δ and (**D**) Ψ spectral shift after immune complex formation using the same dilutions of polyclonal antibodies.

3.2. Immune Complex Formation between Covalently Immobilized SCoV2-S, SCoV2-αS, or SCoV2-βS and Specific Polyclonal Antibodies

For the evaluation of the affinity interaction and the formation of immune complexes between immobilized SCoV2-S, SCoV2-αS, or SCoV2-βS and pAb-SCoV2-S antibodies, human blood serum was diluted with PBS at 1:4, 1:10, 1:20, 1:30, and 1:40 ratios. First, the solution containing 1:40 diluted human blood serum with the 0.849 nM concentration of pAb-SCoV2-S was injected into the TIRE chamber. After 60 min, the chamber was washed with PBS. In the next step of the experiment, the surface was washed with the regeneration solution consisting of 17.34 mM SDS and 10 mM NaOH for 1 min, to remove the affinity-bound antibodies from the surface. Then, an additional rinsing with PBS was performed. The same experiments were performed with all previously mentioned blood serum dilutions at 1:30, 1:20, 1:10 and 1:4 ratios. The blood serum collected before the start of the COVID-19 pandemic and diluted at a 1:40 ratio with PBS was used to evaluate the non-specific interaction of blood serum with the covalently immobilized S protein VOCs. The time-resolved TIRE kinetics and the ellipsometric parameters of the covalently immobilized SCoV2-S interaction with specific pAb-SCoV2-S are presented in Figure 2B.
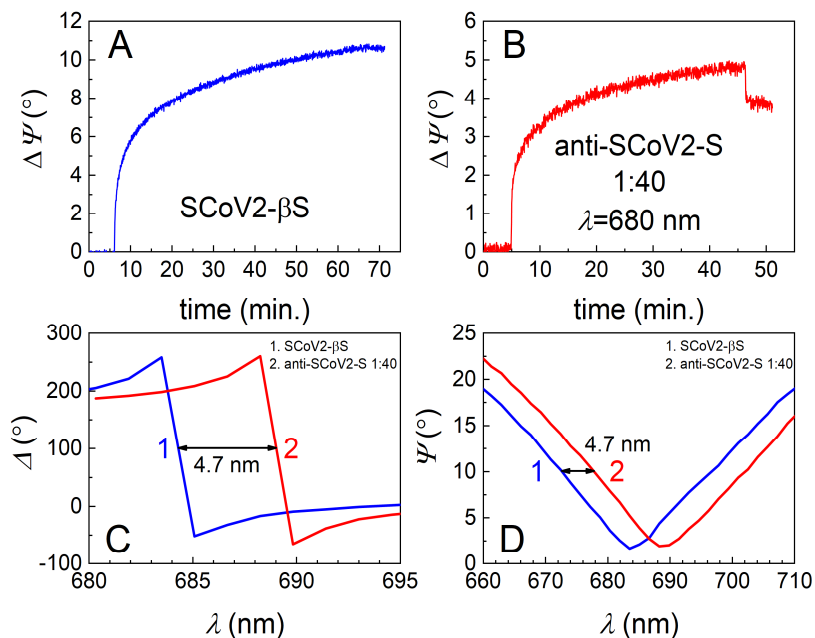
Figure 4. Time-resolved TIRE kinetics and ellipsometric parameters of SCoV2-βS immobilization and interaction with specific polyclonal antibodies. (**A**) Kinetics of covalent SCoV2β-S immobilization on 11-MUA SAM modified gold-coated SPR sensor disc; (**B**) kinetics of polyclonal antibody interaction with covalently immobilized SCoV2-βS at 1:40 dilution of serum; (**C**) Δ and (**D**) Ψ spectral shift after the formation of immune complexes using the same dilutions of polyclonal antibodies.

The highest concentration of the pAb-SCoV2-S antibody in the serum sample (with a dilution ratio at 1:4 or with an 8.49 nM concentration) showed a 16° change in the ellipsometric parameter Ψ after 60 min, while after interaction with the sample of the lowest concentration of the pAb-SCoV2-S antibody (with a dilution ratio at 1:40 or with a 0.849 nM), it was 3.8° (Figure 2B). The Ψ changes obtained using SCoV2-S, SCoV2-αS, and SCoV2-βS are presented (Figures 2B, 3B and 4B) as eliminating the signal ($\Delta\Psi = 2.5°$) that results after a non-specific interaction of serum without antibodies against the SARS-CoV-2 S protein with the immobilized S protein VOC. As can be seen, the TIRE method is able to detect a small concentration (0.849 nM) of the pAb-SCoV2-S antibody in blood serum and is also able to monitor such interaction kinetics (Figure 2B, at a 1:40 ratio). The spectral shift of the ellipsometric parameters Δ and Ψ vs. λ was 2.3 nm after the formation of the SCoV2-S/pAb-SCoV2-S immune complex, using blood serum diluted at a 1:40 ratio (Figure 2C,D). For analogous experiments with covalently immobilized SCoV2-αS or SCoV2-βS proteins, we chose to use the same 0.849 nM concentration (with a dilution ratio at 1:40) of the pAb-SCoV2-S antibody. After 60, 35, and 45 min, the change in the ellipsometric parameter ΔΨ was still significant, and washing with PBS showed only a small signal drop (Figures 2B, 3B and 4B).

For the investigation into the immune complex formation between SCoV2-αS and pAb-SCoV2-S, SCoV2-αS was covalently immobilized on the 11-MUA SAM, and this immobilization kinetics was recorded using TIRE (Figure 3A). During the interaction between the covalently immobilized SCoV2-αS with a 0.849 nM concentration of pAb-SCoV2-S antibodies (the formation of the SCoV2-αS/pAb-SCoV2-S immune complex), the change in the ellipsometric parameter ΔΨ was 2.01°, and the spectral shift of Δ and Ψ vs. λ was 3.1 nm to longer wavelengths. Furthermore, the covalent immobilization of

SCoV2-βS on the 11-MUA SAM was performed, and immobilization kinetics was recorded using TIRE (Figure 4A). The immune complex formation kinetics, using the same pAb-SCoV2-S antibody concentration (0.849 nM), and the covalently immobilized SCoV2-βS was recorded. After the immune complex formation, the change in $\Delta\Psi$ was 4.96° (Figure 4B), and a 4.7 nm spectral shift in Δ and Ψ vs. λ (Figure 4C,D) was observed.

As can be seen from the covalent SCoV2-S, SCoV2-αS, and SCoV2-βS immobilization experiments using TIRE (Figures 2A, 3A and 4A), changes in the ellipsometric parameter Ψ after 60 min were similar. These results indicate that the three types of SARS-CoV-2 S protein VOCs can be covalently immobilized on the sensing surface successfully, using the 11-MUA SAM. The SCoV2-S, SCoV2-αS, and SCoV2-βS interactions with pAb-SCoV2-S and the immune complexes formation kinetics were analyzed by two-step irreversible binding mathematical modeling [21]. Understanding the mechanism of specific antibody interaction with the whole SARS-CoV-2 S protein is critical for the development of effective therapeutics, vaccines, and detection tools [30]. Therefore, it is very important to obtain as much information as possible on the formation of immune complexes between the S protein variants of SCoV2-S, SCoV2-αS, or SCoV2-βS and the specific antibodies formed during the humoral response of the immune system. The antibodies that bind outside of the RBD region stimulate the antiviral activity of the immune system and can provide protection against COVID-19, effectively turning this serious illness into a milder form, such as the common cold [31]. Other authors reported their structural analysis of neutralizing antibodies that were RBD-directed and N-terminal (NTD)-directed. It was shown that in opposit to RBD-directed antibodies that recognize multiple non-overlapping epitopes, NTD-directed antibodies target a single supersite of an S protein with high affinity, in the range of 2–70 nM [32]. In addition to our experimental results, we used a two-step irreversible binding mathematical model [21,27] for the evaluation of interaction kinetics between covalently immobilized SCoV2-S, SCoV2-αS, SCoV2-βS, and a specific polyclonal antibody obtained from a volunteer's blood serum, who was vaccinated with one dose of the Vaxzevria vaccine, which eliminated non-specific interactions. The two-step irreversible binding mathematical model, which describes the formation of an immune complex, was applied in our previous work on the interaction of a nucleocapsid protein with a polyclonal antibody [33]. In the fitting of experimentally obtained kinetics, a normalized surface concentration allowed us to calculate the association rate constant (k_a), the dissociation rate constant (k_d), the stable immune complex formation rate constant (k_r), equilibrium association and dissociation constants (K_A, K_D), and steric factors (P_s). The fitting results obtained via this mathematical model of irreversible two-step antibody binding to covalently immobilized SCoV2-S, SCoV2-αS, or SCoV2-βS are presented in Figure 5.
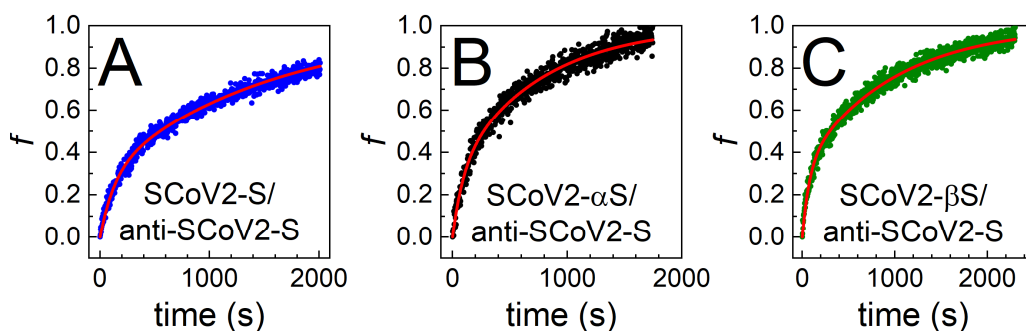

Figure 5. Normalized pAb-SCoV2-S antibody surface concentration (*f*) evolution in time obtained using 1:40 diluted blood serum during the formation of the immune complex with (**A**) SCoV2-S, (**B**) SCoV2-αS, (**C**) SCoV2-βS. Points correspond to experimentally obtained results, while lines for fitting are derived by using two-step irreversible binding immune complex formation mathematical modeling.

The calculated thermodynamic parameters of immune complex formation can provide a deeper understanding on how a specific antibody from human blood serum can interact with the wild-type (SCoV2-S) and the mutated (SCoV2-αS and SCoV2-βS) SARS-CoV-2 S proteins. The calculated values for the pAb-SCoV2-S immune complex formation with the three types of investigated S protein are presented in Table 1.

Table 1. Thermodynamic parameters of specific antibody interaction with variants of concern.

	SCoV2-S	SCoV2-αS	SCoV2-βS
k_a (M^{-1}s^{-1})	3.19×10^6	5.01×10^6	5.92×10^6
k_d (s^{-1})	1.03×10^{-5}	1.97×10^{-5}	3.27×10^{-5}
K_A (M^{-1})	3.09×10^{11}	2.54×10^{11}	1.81×10^{11}
K_D (M)	3.22×10^{-10}	$3.93 \cdot 10^{-10}$	5.47×10^{-10}
k_r (s^{-1})	5.05×10^{-6}	1.48×10^{-5}	1.33×10^{-5}
P_s	1.51×10^{-2}	1.88×10^{-2}	2.01×10^{-2}

Association rate constant (k_a), dissociation rate constant (k_d), stable immune complex rate constant (k_r), equilibrium association constant (K_A), equilibrium dissociation constant (K_D), and steric factors (P_s).

The results obtained show that the K_D for the specific antibody interaction with the mutated spike protein SCoV2-αS and SCoV2-βS are in the same range of nM, and also demonstrate the high antibody affinity against these mutations. Moreover, the K_D value for the antibodies produced against the target protein SCoV2-S is lowest ($K_D = 3.22 \times 10^{-10}$ M). However, the nM range of the K_D value for SCoV2-αS and SCoV2-βS suggests that the antibody produced after vaccination can successfully protect the population from the SARS-CoV-2 alpha (B.1.1.7) and beta (B.1.351) mutations. Other authors also reported that high affinity was observed of monoclonal anti-RBD neutralizing antibodies for RBD [34]. As it was shown by the group of authors, mutations in the RBD of the alpha (B.1.1.7) and beta (B.1.351) increased the affinity to the ACE2 receptor [6,15,35]. It was reported that affinity values varied from K_D 6 to 133 nM [15].

The obtained stable immune complex formation rate constants k_r are in the same range for SARS-CoV-2 alpha (B.1.1.7) and beta (B.1.351). In the present study, we calculated steric factors P_s for all three types of immune complexes studied: SCoV2-S/pAb-SCoV2-S, SCoV2-αS/pAb-SCoV2-S, and SCoV2-βS/pAb-SCoV2-S. The P_s provides information about the steric requirements for an antibody and antigen to form a stable complex successfully and can be calculated from the encounter theory [36,37]. We calculated P_s in our previous work on the covalently immobilized SARS-CoV-2 nucleocapsid protein and the specific antibody immune complex formation, and the obtained value was 5.49×10^{-4}. When comparing the P_s values obtained for nucleocapsid and SCoV2-S, SCoV2-αS, and SCoV2-βS, it is evident that specifically pAb-SCoV2-S has a 100-fold lower requirement for the formation of an immune complex. This can be explained by the fact of immune complexes being able to form more easily with larger antigens. In this case, the mass of the S protein (trimer) is higher (monomer is 114.11 kDa) compared to the nucleocapsid (49 kDa).

4. Conclusions

In the present investigation, we demonstrated how the highly sensitive TIRE method can be applied for the evaluation of interaction kinetics between the covalently immobilized SARS-CoV-2 S protein variants of concern and the specific polyclonal antibody from diluted voluntary blood serum. The calculated equilibrium dissociation constants K_D for the pAb-SCoV2-S immune complex formation with the covalently immobilized SCoV2-S, SCoV2-αS, and SCoV2-βS showed that these antibodies, developed by the humoral response of the immune system after vaccination, are able to bind to all three types of the mutated S protein with high affinity. The calculations of the steric factors showed that pAb-SCoV2-S can form an immune complex easily enough in comparison to the immune complex formation with a nucleocapsid protein. These results show

the ability of the antibody produced after vaccination with Vaxzevria to protect the population from the SARS-CoV-2 mutation alpha (B.1.1.7) and beta (B.1.351).

Author Contributions: Conceptualization, I.P. and A.R.; methodology, I.P., A.R. (Almira Ramanaviciene), S.B., V.M. and S.J., formal analysis I.P., V.M. and A.R. (Almira Ramanaviciene); investigation, I.P., A.R. (Almira Ramanaviciene), S.B., V.M., S.J., R.M. and A.R. (Arunas Ramanavicius); writing—I.P., A.R. (Almira Ramanaviciene), S.B., V.M., S.J. and A.R. (Arunas Ramanavicius); writing—review and editing, I.P., A.R. (Almira Ramanaviciene), S.B., V.M., S.J. and A.R. (Arunas Ramanavicius); visualization, V.M, S.J., and R.M.; supervision, I.P. and A.R. (Almira Ramanaviciene); project administration, A.R. (Almira Ramanaviciene); funding acquisition, A.R. (Almira Ramanaviciene). All authors have read and agreed to the published version of the manuscript.

Institutional Review Board Statement: Not applicable.

Informed Consent Statement: Not applicable.

Data Availability Statement: The data presented in this study are available on request from the first author.

Conflicts of Interest: The authors declare no conflict of interest.

References

1. World Health Organization. World Health Organization Tracking SARS-CoV-2 variants. Available online: https://www.who.int/en/activities/tracking-SARS-CoV-2-variants/ (accessed on 14 January 2022).
2. Walls, A.C.; Park, Y.J.; Tortorici, M.A.; Wall, A.; McGuire, A.T.; Veesler, D. Structure, Function, and Antigenicity of the SARS-CoV-2 Spike Glycoprotein. *Cell* **2020**, *181*, 281–292.e6. [CrossRef]
3. Li, Q.; Wu, J.; Nie, J.; Zhang, L.; Hao, H.; Liu, S.; Zhao, C.; Zhang, Q.; Liu, H.; Nie, L.; et al. The Impact of Mutations in SARS-CoV-2 Spike on Viral Infectivity and Antigenicity. *Cell* **2020**, *182*, 1284–1294.e9. [CrossRef] [PubMed]
4. Global Virus Network Alpha (B.1.1.7)-GVN. Available online: https://gvn.org/covid-19/alpha-b-1-1-7/ (accessed on 14 January 2022).
5. Bayarri-Olmos, R.; Johnsen, L.B.; Idorn, M.; Reinert, L.S.; Rosbjerg, A.; Vang, S.; Hansen, C.B.; Helgstrand, C.; Bjelke, J.R.; Bak-Thomsen, T.; et al. The alpha/b.1.1.7 sars-cov-2 variant exhibits significantly higher affinity for ace-2 and requires lower inoculation doses to cause disease in k18-hace2 mice. *elife* **2021**, *10*, 1–14. [CrossRef]
6. Liu, H.; Wei, P.; Kappler, J.W.; Marrack, P. SARS-CoV-2 Variants of Concern and Variants of Interest Receptor Binding Domain Mutations and Virus Infectivity. *Front. Immunol.* **2022**, *13*, 1–9. [CrossRef]
7. Krammer, F. SARS-CoV-2 vaccines in development. *Nature* **2020**, *586*, 516–527. [CrossRef]
8. Global Virus Network Beta (B.1.351)-GVN. Available online: https://gvn.org/covid-19/beta-b-1-351/ (accessed on 14 January 2022).
9. Bai, C.; Wang, J.; Chen, G.; Zhang, H.; An, K.; Xu, P.; Du, Y.; Ye, R.D.; Saha, A.; Zhang, A.; et al. Predicting Mutational E ff ects on Receptor Binding of the Spike Protein of SARS-CoV-2 Variants. *J. Am. Chem. Soc.* **2021**, *143*, 17646–17654. [CrossRef] [PubMed]
10. Shen, X.; Tang, H.; Mcdanal, C.; Glenn, G.M.; Korber, B.; Montefiori, D.C.; Shen, X.; Tang, H.; Mcdanal, C.; Wagh, K.; et al. Short Article neutralizing antibodies elicited by ancestral spike vaccines ll ll to neutralizing antibodies elicited by ancestral spike vaccines. *Cell Host Microbe* **2021**, *29*, 529–539.e3. [CrossRef] [PubMed]
11. Lou, F.; Li, M.; Pang, Z.; Jiang, L.; Guan, L.; Tian, L.; Hu, J.; Fan, J.; Fan, H. Understanding the Secret of SARS-CoV-2 Variants of Concern/Interest and Immune Escape. *Front. Immunol.* **2021**, *12*, 1–19. [CrossRef]
12. Bio-Rad Bio-Plex Multiplex SARS-CoV-2 Serology and Neutralization Assays | Bio-Rad Laboratories. Available online: https://www.bio-rad.com/en-lt/category/bio-plex-multiplex-sars-cov-2-serology-neutralization-assays?ID=QIZX4YSCUMB7 (accessed on 14 January 2022).

13. Fiedler, S.; Piziorska, M.A.; Denninger, V.; Morgunov, A.S.; Ilsley, A.; Malik, A.Y.; Schneider, M.M.; Devenish, S.R.A.; Meisl, G.; Kosmoliaptsis, V.; et al. Antibody Affinity Governs the Inhibition of SARS-CoV-2 Spike/ACE2 Binding in Patient Serum. *ACS Infect. Dis.* **2021**, *7*, 2362–2369. [CrossRef]

14. Shang, J.; Ye, G.; Shi, K.; Wan, Y.; Luo, C.; Aihara, H.; Geng, Q.; Auerbach, A.; Li, F. Structural basis of receptor recognition by SARS-CoV-2. *Nature* **2020**, *581*, 221–224. [CrossRef]

15. Barton, M.I.; Macgowan, S.; Kutuzov, M.; Dushek, O.; Barton, G.J.; Anton Van Der Merwe, P. Effects of common mutations in the sars-cov-2 spike rbd and its ligand the human ace2 receptor on binding affinity and kinetics. *elife* **2021**, *10*, 1–19. [CrossRef] [PubMed]

16. Day, C.J.; Bailly, B.; Guillon, P.; Dirr, L.; Jen, F.E.C.; Spillings, B.L.; Mak, J.; von Itzstein, M.; Haselhorst, T.; Jennings, M.P. Multidisciplinary approaches identify compounds that bind to human ACE2 or SARS-CoV-2 spike protein as candidates to block SARS-CoV-2–ACE2 receptor interactions. *mBio* **2021**, *12*, 1–14. [CrossRef] [PubMed]

17. Nabok, A.V.; Tsargorodskaya, A.; Hassan, A.K.; Starodub, N.F. Total internal reflection ellipsometry and SPR detection of low molecular weight environmental toxins. *Appl. Surf. Sci.* **2005**, *246*, 381–386. [CrossRef]

18. Baleviciute, I.; Balevicius, Z.; Makaraviciute, A.; Ramanaviene, A.; Ramanavicius, A. Study of antibody/antigen binding kinetics by total internal reflection ellipsometry. *Biosens. Bioelectron.* **2013**, *39*, 170–176. [CrossRef] [PubMed]

19. Arwin, H.; Poksinski, M.; Johansen, K. Total internal reflection ellipsometry: Principles and applications. *Appl. Opt.* **2004**, *43*, 3028–3036. [CrossRef]

20. Plikusiene, I.; Maciulis, V.; Graniel, O.; Bechelany, M.; Balevicius, S.; Vertelis, V.; Balevicius, Z.; Popov, A.; Ramanavicius, A.; Ramanaviene, A. Total internal reflection ellipsometry for kinetics-based assessment of bovine serum albumin immobilization on ZnO nanowires. *J. Mater. Chem. C* **2021**, *9*, 1345–1352. [CrossRef]

21. Balevicius, Z.; Talbot, J.; Tamosaitis, L.; Plikusiene, I.; Stirke, A.; Mickiene, G.; Balevicius, S.; Paulauskas, A.; Ramanavicius, A. Modelling of immunosensor response: The evaluation of binding kinetics between an immobilized receptor and structurally-different genetically engineered ligands. *Sens. Actuators B Chem.* **2019**, *297*, 126770. [CrossRef]

22. Buzavaite-Verteliene, E.; Plikusiene, I.; Tolenis, T.; Valavicius, A.; Anulyte, J.; Ramanavicius, A.; Balevicius, Z. Hybrid tamm-surface plasmon polariton mode for highly sensitive detection of protein interactions. *Opt. Express* **2020**, *28*, 29033–29043. [CrossRef]

23. Balevicius, Z.; Ramanaviene, A.; Baleviciute, I.; Makaraviciute, A.; Mikoliunaite, L.; Ramanavicius, A. Evaluation of intact- and fragmented-antibody based immunosensors by total internal reflection ellipsometry. *Sens. Actuators B Chem.* **2011**, *160*, 555–562. [CrossRef]

24. Maartensson, J.; Arwin, H. Interpretation of Spectroscopic Ellipsometry Data on Protein Layers on Gold Including Substrate-Layer Interactions. *Langmuir* **1995**, *11*, 963–968. [CrossRef]

25. Arwin, H. Spectroscopic ellipsometry and biology: Recent developments and challenges. *Thin Solid Film.* **1998**, *313*, 764–774. [CrossRef]

26. Amarasekera, M. Immunoglobulin E in health and disease. *Asia Pac. Allergy* **2011**, *1*, 12. [CrossRef] [PubMed]

27. Balevicius, Z.; Baleviciute, I.; Tumenas, S.; Tamosaitis, L.; Stirke, A.; Makaraviciute, A.; Ramanaviene, A.; Ramanavicius, A. In situ study of ligand-receptor interaction by total internal reflection ellipsometry. *Thin Solid Film.* **2014**, *571*, 744–748. [CrossRef]

28. Plikusiene, I.; Balevicius, Z.; Ramanaviene, A.; Talbot, J.; Mickiene, G.; Balevicius, S.; Stirke, A.; Tereshchenko, A.; Tamosaitis, L.; Zvirblis, G.; et al. Evaluation of affinity sensor response kinetics towards dimeric ligands linked with spacers of different rigidity: Immobilized recombinant granulocyte colony-stimulating factor based synthetic receptor binding with genetically engineered dimeric analyte d. *Biosens. Bioelectron.* **2020**, *156*, 112112. [CrossRef]

29. Ramanaviciene, A.; German, N.; Kausaite-Minkstimiene, A.; Voronovic, J.; Kirlyte, J.; Ramanavicius, A. Comparative study of surface plasmon resonance, electrochemical and electroassisted chemiluminescence methods based immunosensor for the determination of antibodies against human growth hormone. *Biosens. Bioelectron.* **2012**, *1*, 48–55. [CrossRef]

30. Ge, J.; Wang, R.; Ju, B.; Zhang, Q.; Sun, J.; Chen, P.; Zhang, S.; Tian, Y.; Shan, S.; Cheng, L.; et al. Antibody neutralization of SARS-CoV-2 through ACE2 receptor mimicry. *Nat. Commun.* **2021**, *12*, 1–10. [CrossRef]

31. Kaplonek, P.; Fischinger, S.; Cizmeci, D.; Bartsch, Y.C.; Kang, J.; Burke, J.S.; Shin, S.A.; Dayal, D.; Martin, P.; Mann, C.; et al. mRNA-1273 vaccine-induced antibodies maintain Fc-effector functions across SARS-CoV-2 Variants of Concern. *Immunity* **2022**, *55*, 355–365.e4. [CrossRef]

32. Cerutti, G.; Guo, Y.; Zhou, T.; Gorman, J.; Lee, M.; Rapp, M.; Reddem, E.R.; Yu, J.; Bahna, F.; Bimela, J.; et al. Potent SARS-CoV-2 neutralizing antibodies directed against spike N-terminal domain target a single supersite. *Cell Host Microbe* **2021**, *29*, 819–833.e7. [CrossRef]

33. Plikusiene, I.; Maciulis, V.; Ramanaviciene, A.; Balevicius, Z.; Buzavaite-verteliene, E.; Ciplys, E.; Slibinskas, R.; Simanavicius, M.; Zvirbliene, A.; Ramanavicius, A. Evaluation of Kinetics and Thermodynamics of Interaction between Immobilized SARS-CoV-2 Nucleoprotein and Specific Antibodies by Total Internal Reflection Ellipsometry. *J. Colloid Interface Sci.* **2021**, *594*, 195–203. [CrossRef]

34. Schardt, J.S.; Pornnoppadol, G.; Desai, A.A.; Park, K.S.; Zupancic, J.M.; Makowski, E.K.; Smith, M.D.; Chen, H.; Garcia de Mattos Barbosa, M.; Cascalho, M.; et al. Discovery and characterization of high-affinity, potent SARS-CoV-2 neutralizing antibodies via single B cell screening. *Sci. Rep.* **2021**, *11*, 1–16. [CrossRef]
35. Laffeber, C.; de Koning, K.; Kanaar, R.; Lebbink, J.H.G. Experimental Evidence for Enhanced Receptor Binding by Rapidly Spreading SARS-CoV-2 Variants. *J. Mol. Biol.* **2021**, *433*, 167058. [CrossRef] [PubMed]
36. Doktorov, A.B. Encounter Theory of Chemical Reactions in Solution: Approximate Methods of Calculating Rate Constants. In *Chemical Kinetics*; World Scientific: New Jersey, NJ, USA, 2018; pp. 35–64. ISBN 978-1-78634-700-8.
37. Berdnikov, V.M.; Doktorov, A.B. Steric factor in diffusion-controlled chemical reactions. *Chem. Phys.* **1982**, *69*, 205–212. [CrossRef]

Paper 4

Investigation of SARS-CoV-2 nucleocapsid protein interaction with a specific antibody by combined spectroscopic ellipsometry and quartz crystal microbalance with dissipation

Ieva Plikusiene, **Vincentas Maciulis**, Silvija Juciute, Arunas Ramanavicius, Zigmas Balevicius, Rimantas Slibinskas, Indre Kucinskaite-Kodze, Martynas Simanavicius, Saulius Balevicius, Almira Ramanaviciene

Investigation of SARS-CoV-2 nucleocapsid protein interaction with a specific antibody by combined spectroscopic ellipsometry and quartz crystal microbalance with dissipation

Ieva Plikusiene [a], Vincentas Maciulis [a,b], Silvija Juciute [a], Arunas Ramanavicius [a], Zigmas Balevicius [b], Rimantas Slibinskas [c], Indre Kucinskaite-Kodze [c], Martynas Simanavicius [c], Saulius Balevicius [a,b], Almira Ramanaviciene [a,*]

[a] NanoTechnas – Center of Nanotechnology and Materials Science, Faculty of Chemistry and Geosciences, Vilnius University, Naugarduko str. 24, 03225 Vilnius, Lithuania
[b] State Research Institute Center for Physical Sciences and Technology, Sauletekio ave. 3, Vilnius, Lithuania
[c] Institute of Biotechnology, Life Sciences Center, Vilnius University, Sauletekio ave. 7, LT-10257 Vilnius, Lithuania

GRAPHICAL ABSTRACT
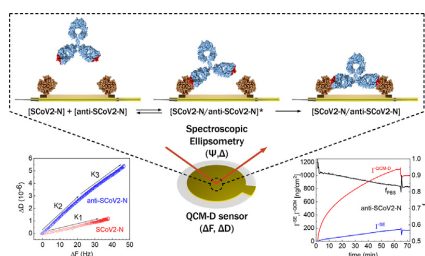
ARTICLE INFO

ABSTRACT

Detailed evaluations of the antigen and antibody interaction rate and strength of the immune complex formed are very important for medical and bioanalytical applications. These data are crucial for the development of sensitive and fast immunosensors suitable for continuous measurements. Therefore, combined spectroscopic ellipsometry (SE) and quartz crystal microbalance with dissipation (QCM-D) technique (SE/QCM-D) was used for the evaluation: (i) of covalent immobilization of SARS-CoV-2 nucleocapsid protein (SCoV2-N) on QCM-D sensor disc modified by self-assembled monolayer based on 11-mercaptoundecanoic acid and (ii) interaction of immobilized SCoV2-N with specific polyclonal anti-SCoV2-N antibodies followed by immune complex formation process. The results show that the SCoV2-N monolayer is rigid due to the low energy dissipation registered during the QCM-D measurement. In contrast, the anti-SCoV2-N layer produced after interaction with the immobilized SCoV2-N formed a soft and viscous layer. It was determined, that the sparse distribution of SCoV2-N on the surface affected the spatial arrangement of the antibody during the formation of immune complexes. The hinge-mediated flexibility of the antibody Fab fragments allows them to reach the more distantly located SCoV2-N and establish a bivalent binding between proteins in the formed SCoV2-N/anti-SCoV2-N complex. It was noted that the SE/QCM-D method can provide more precise quantitative information about the flexibility and conformational changes of antibody during the formation of the immune complex on the surface over time.

© 2022 Elsevier Inc. All rights reserved.

* Corresponding author.
E-mail address: almira.ramanaviciene@chf.vu.lt (A. Ramanaviciene).

1. Introduction

The health challenges associated with the rapid spread of Severe Acute Respiratory Syndrome Coronavirus 2 (SARS-CoV-2) have recently led to intensive studies of the SARS-CoV-2 nucleocapsid protein (SCoV2-N) and specific polyclonal antibodies (anti-SCoV2-N). Although the main focus of research has been on the SARS-CoV-2 spike protein, the investigations of the nucleocapsid protein are also important due to their critical impact on the coronavirus genomic RNR packing and viral replication [1]. Immunoglobulin G (IgG) antibodies against the SARS-CoV-2 nucleocapsid protein are detectable in infected patients. A higher titer of these antibodies was determined to be a prognostic factor of the clinical course of disease [2]. Therefore, more information on such antibody interaction with the SARS-CoV-2 nucleocapsid protein is needed. During the pandemic, different methods were developed for the detection of SARS-CoV-2 and the diagnosis of COVID-19 infection, including different serological tests to record antibody (Ab) and antigen (Ag) interactions [3,4]. Usually, as a result of the test, Abs against the most immunogenic SARS-CoV-2 spike protein and/or nucleocapsid protein are detected [5,6]. Furthermore, it was determined that Abs to the nucleocapsid protein are more sensitive to the diagnosis of early infection than Abs specific to the spike protein [7]. For this reason, the research that helps to understand how SARS-CoV-2 nucleocapsid protein interact with specific anti-SCoV2-N Abs is very expected for the industry involved in the production of viral proteins, Ab-Ag tests, and vaccines.

It is well known that Abs are large globular Y-shaped glycoproteins consisting of two heavy and two light chains. Two pairs of light and heavy chains are connected by disulfide bonds, and two heavy chains are connected by disulfide bonds located in the hinge region. This region is a flexible tether present in the IgG, IgA and IgD class Abs, and responsible for the movement of two Ab Fab fragments (antibody regions corresponding to antigen-binding fragments and consisting of both the variable and constant regions of heavy and light chains) and changes in Fab-Fab angles. IgG class Abs are the most abundant class of Abs in the blood produced by the organism after contact with the antigen. The impact of different human IgG subclass hinge-mediated flexibility on the type and sizes of soluble immune complexes was analyzed by electron microscopy. The IgG subclasses, depending on their flexibility, were ranked in such an order (most to least flexible): IgG3 > IgG1 > IgG4 > IgG2; accordingly, the mean angles between Fab-Fab were determined as 136°, 128°, 127°, and 117° [8]. The hinge-mediated flexibility of Abs, the wagging and rotational movements of the Fab fragments, the steric interactions of two Fab fragments with each other and with crystallizable fragment (Fc) of Ab are significant for the binding of Ab to Ag of different size, from small haptens to relatively large viruses [9]. The Ab affinity is defined as the combined strength of a single Ab antigen-binding site interaction with a single epitope present in the Ag structure. The Ab avidity (IgG class) is defined as the total strength of all noncovalent bivalent (Fab-Fab) affinity interactions with two epitopes. It was determined that the bivalent binding of monoclonal Abs to human immunodeficiency virus type 1 envelope glycoprotein trimer 2F5 epitopes results in greatly enhanced neutralization efficiency through an increase in binding avidity [10]. Additionally, the impact of CD20 epitopes surface density on the recognition and bivalent interaction with monoclonal Abs (rituximab) was analyzed using quartz crystal microbalance with dissipation (QCM-D) and surface plasmon resonance (SPR) technique [11]. To study the affinity and avidity features of the anti-SCoV2-N, the noncontact, real time and sensitive methods are required. Among them very promising is the polarization sensitive optical method named as spectroscopic ellipsometry (SE) and surface mass sensitive QCM-D technique method, which is based on the assessment of surface acoustic wave dissipation.

The SE is a nondestructive, label-free and highly sensitive optical technique that allows to determine the refractive index n or the thicknesses d of the formed protein layers [12–15]. These values can be used to calculate the dry surface mass of the protein layer [16–18]. During the ellipsometric measurement, two ellipsometric parameters are determined – Ψ that corresponds to the light wave amplitude and Δ that gives the information of the light phase shift after reflection from the sample. To enhance the sensitivity of the SE method, it is applied in the total internal reflection mode (TIRE) [16,19–23]. However, the SE method is not able to measure n and d values separately. Therefore, regression analysis is used to calculate the n and d values, which requires specific information about the geometry and refractive index of the proteins. The certain inaccuracy of the n and d determination from the regression analysis depends on the knowledge about these parameters.

QCM-D measures the shifts in frequency (ΔF) and energy dissipation (ΔD) of vibrational resonance overtones. It enables to determine the surface mass coupled to a pre-modified quartz crystal sensor and viscoelastic properties of the layer [12,24,25]. The mass obtained from QCM-D measurements refers to the wet mass when it is obtained for the layer of proteins coupled to the surface together with the buffer. In the case of very strong coupling (low ΔD values) between antibodies and immobilized proteins, the shifts in frequency (ΔF) of the QCM-D method give unambiguous information about the mass on the sensing surface. However, this assumption is usually not fully satisfied. Thus, for the determination of immobilized proteins layer mass and viscoelastic properties it is necessary to make several assumptions concerning models of continuum mechanics [26].

In both SE and QCM-D methods, the response signal depends on the immobilized protein mass; however, SE gives additional information about the dielectric properties of proteins layers, while QCM-D provides information about the viscoelastic properties. Thus by combining SE and QCM-D, it is possible to derive the solvent content of thin protein layers formed on the surface [24,27] and using regression analysis to obtain more precise information about antibody avidity properties. That leads to better understanding of protein–protein interaction mechanism and changes of protein conformation after specific interaction. The hybrid SE/QCM-D method could reveal additional new possibilities for antigen–antibody interaction and analysis of immune complex formation, providing quantitative information that cannot be obtained when the SE and QCM-D methods are used separately [28].

The affinity properties of the SARS-CoV-2 nucleocapsid protein (SCoV2-N) and specific anti-SCoV2-N antibodies were analyzed using the SE method in our previous work [29]. Now, we have used the hybrid SE/QCM-D technique to investigate (i) the covalent immobilization of SCoV2-N on the 11-mercaptoundecanoic acid (11-MUA) self-assembled monolayer (SAM) modified QCM-D gold sensor and (ii) the interaction with specific antibodies followed by an immune complex formation process to evaluate the structural and viscoelastic properties of the layers formed.

2. Materials and methods

2.1. Materials

11-Mercaptoundecanoic acid (11-MUA, 98%), N-(3-diemethylaminopropyl)-N'-ethylcarbodiimide hydrochloride (≥98%) (EDC), N-Hydroxysuccinimide (98%) (NHS), sodium hydroxide (≥97%), ethanolamine (ETA) (≥99%), sodium dodecyl sulfate (≥99%) (SDS) and phosphate buffered saline (PBS) tablets were purchased from Sigma Aldrich. Methanol (99.9%), ammonium sulfate (≥99%), and

hexane (99%) were purchased from Carl Roth GmbH & Co (Karlsruhe, Germany). SARS-CoV-2 recombinant nucleoprotein (SCoV2-N) (≥97%) was received from Baltymas (Vilnius, Lithuania) [29]. QCM-D gold sensors were purchased from Biolin Scientific (Gothenburg, Sweden). Specific polyclonal antibodies (anti-SCoV2-N) obtained from immunized mice and nonspecific polyclonal antibodies obtained from non-immunized mice used in this work were developed under the procedure in detail described in our previous work [29]. Anti-SCoV2-N antibodies were purified from blood serum by ammonium sulfate precipitation, which results in 90% purity. All experiments using laboratory mice were performed under controlled laboratory conditions according to European and Lithuanian legislation (permission no. G2-117 issued by the State Food and Veterinary Service, Vilnius, Lithuania).

2.2. The combined SE/QCM-D measurement setup

A combined SE/QCM-D measurement setup consists of SE and QCM-D techniques. QCM-D QSense Explorer, operating at frequency range 5 MHz, that allows the measurement of 7 harmonics and full viscoelastic modelling (Biolin Scientific, Sweden, with proprietary software QSoft401) was connected with a spectroscopic ellipsometry module, mounted on a rotating compensator spectroscopic ellipsometer M-2000X, operating in a spectral range from 200 nm to 1000 nm wavelength (J. A. Woolam, USA, with proprietary software for data analysis Complete EASE). Ellipsometric measurements were performed at a fixed 65° angle of incident light in a 200–1000 nm wavelength range. For the evaluation of the SCoV2-N and anti-SCoV2-N layers formed during the immobilization of SCoV2-N followed by the interaction with anti-SCoV2-N, the simulation of Δ and Ψ vs λ curves was performed using the Complete EASE software (Woollam, USA). Liquid flow was regulated with a peristaltic pump (Cole-Parmer GmbH, Germany) connected to a liquid intake through a flow chamber with PTFE tubing. The measurements were performed by injecting the liquids at a rate of 1.35 mL/min. During the measurements, the temperature inside the SE/QCM-D module was kept at 20 °C. The volume of the QSense Explorer chamber above the QCM-D gold sensor was 100 μl. QSoft401 software was used for the analysis of the frequency change (ΔF) and energy dissipation (ΔD) kinetics during covalent immobilization of SCoV2-N and affinity interaction with anti-SCoV2-N. The modelled values that can be obtained from such kinetics analysis are: the mass, thickness, and viscoelasticity of the formed protein layers.

2.3. Surface modification with 11-MUA

The QCM-D gold-coated sensor disc surface was prepared for modification with 11-MUA by cleaning in an ultrasonic bath, first in hexane and later in methanol for 2 min, respectively. The sensor surface was rinsed with methanol. A self-assembled monolayer (SAM) of 11-MUA was formed by immersing the QCM-D sensor disc into a solution of 1 mM of 11-MUA in methanol for 22 h. After-

wards, it was rinsed with methanol and dried with compressed air. A modified QCM-D sensor disc was placed and fixed in an SE/QCM-D module. Then the module chamber was filled with deionized water to establish a baseline for 30 min. For the activation of carboxyl groups of 11-MUA SAM, the solution of 0.1 M NHS and 0.4 M EDC mixed in equal parts was injected into the chamber for 15 min. Subsequently, deionized water was injected for the establishment of the baseline for 10 min.

2.4. Immobilization of SCoV2-N and deactivation of the activated carboxyl groups

In the next step of the experiment, SCoV2-N was covalently immobilized on the surface of the 11-MUA SAM modified QCM-D sensor disc. The PBS solution was injected into the chamber for 60 s and left stagnant for 10 min to establish a baseline. Subsequently, a 1.02 μM concentration SCoV2-N solution in PBS was pumped to the premodified QCM-D sensor disc and left to incubate for about 60 min. until a steady state conditions in both SE and QCM-D simultaneous measurements were achieved. Then, washing with PBS was performed for 10 min. Subsequently, the surface was treated with 1 M ethanolamine hydrochloride, pH 8.5, for 10 min to deactivate the remaining activated carboxyl groups. Then PBS was injected into the SE/QCM-D chamber for 20 min until steady state conditions were reached.

2.5. Formation of SCoV2-N/anti-SCoV2-N complex and regeneration of the surface for multiple detection of anti-SCoV2-N

The solution of 170 nM polyclonal anti-SCoV2-N antibody in PBS was injected into the chamber for 65 min for SCoV2-N/anti-SCoV2-N complex formation. The association phase was followed by the dissociation phase using PBS for 20 min. Afterwards, a regeneration solution consisting of 50 mM NaOH and 17.34 mM SDS was injected for 5 min, and the removal of anti-SCoV2-N from the surface was registered. Following, PBS solution was injected for 20 min to ensure that the remaining SCoV2-N layer is stable and not affected by the regeneration solution. Subsequently, the solution containing the same concentration (170 nM) of nonspecific antibodies was injected into the chamber for 30 min and washed with PBS. The schematic representation of the formation of the SCoV2-N/anti-SCoV2-N complex is presented in Fig. 1.

3. Results and discussion

Covalent SCoV2-N immobilization on 11-MUA SAM, and interaction with the anti-SCoV2-N kinetics were registered simultaneously using a combined setup of SE with QCM-D.
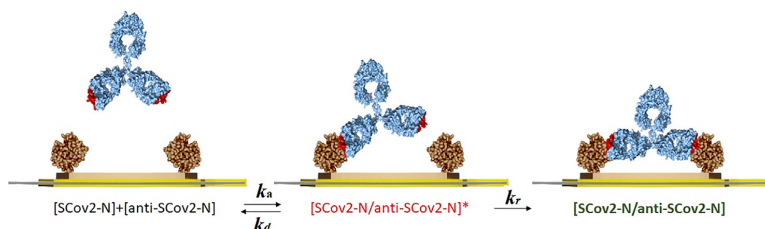

Fig. 1. Schematic representation of the anti-SCoV2-N interaction with covalently immobilized SCoV2-N. The formation of the immune complex takes two steps.

3.1. QCM-D-based assessment of SCoV2-N covalent immobilization and affinity interaction with anti-SCoV2-N

The changes in ΔF and ΔD by all overtones mastered by QCM-D were registered. The dependences of ΔF and ΔD vs. time for the third, fifth and seventh overtones are presented in Fig. 2. The information provided by the changes in ΔD corresponds to the viscoelastic properties of the formed SCoV2-N monolayer and SCoV2-N/anti-SCoV2-N complexes. As shown in Fig. 2, ΔD after covalent SCoV2-N immobilization is $1.09 \cdot 10^{-6}$ while after interaction with anti-SCoV2-N ΔD changed to $4.33 \cdot 10^{-6}$. The value of ΔD obtained after SCoV2-N immobilization on 11-MUA is small, therefore SCoV2-N layer can be considered as rigid and its properties can be described using the Sauerbrey equation [30,31].

ΔD measured for the anti-SCoV2-N interaction with SCoV2-N was 3.9 times higher than in the case of covalent SCoV2-N immobilization on 11-MUA self-assembled monolayer formed on the sensor disc. Anti-SCoV2-N monolayer viscoelastic properties were described using the Smart fit viscoelastic model from DFind software (Biolin). The decrease in frequency indicated an increase of surface mass density after covalent SCoV2-N immobilization and affinity interaction with anti-SCoV2-N. For SCoV2-N immobilization, ΔF was 37.63 Hz, while after interaction with anti-SCoV2-N during the same time interval, it was 47.57 Hz. Such changes of ΔF after SCoV2-N/anti-SCoV2-N complex formation confirmed the specific affinity interaction between SCoV2-N and anti-SCoV2-N antibodies. For the regeneration of SCoV2-N/anti-SCoV2-N complex the solution containing 50 mM NaOH and 17.34 mM SDS was injected into the chamber for 5 min. After that, the chamber was filled with PBS pH 7.4 and the baseline was established. The effectiveness of regeneration was evaluated by comparing the PBS baselines after a certain period of time from the start of experiment. As shown in Fig. 2, the baselines of PBS after SCoV2-N covalent immobilization (at 160 min) and after the regeneration of the surface (at 270 min) are at the same level. After regeneration of SCoV2-N/anti-SCoV2-N (anti-SCoV2-N was removed from the surface modified with SCoV2-N), the control solution containing the same concentration (170 nM) of nonspecific antibodies from non-immunized mice were injected for 30 min. In this case, no distinguishable change in SE or QCM-D signals was observed (Fig. 2, part 3). Finally, the chamber was washed with PBS. In this case, ΔF was 1.68 Hz and ΔD was $1.05 \cdot 10^{-6}$. Such a small ΔF showed that the interaction between SCoV2-N and the control solution containing non-specific antibodies was not established and the frequency change can be associated with non-specific adsorption of some proteins.

$\Delta D / \Delta F$ plots of QCM-D data were obtained by plotting ΔF (representing the increase in mass on the surface) on the x axis and ΔD (representing the changes in viscoelastic properties of the layer) on the y axis and eliminating time as an explicit parameter [32,33]. The $\Delta D / \Delta F$ plot is a complementary method of data presentation and it highlights the viscoelastic processes that occur during the protein monolayer formation [33]. The $\Delta D / \Delta F$ plots presented in Fig. 3 show how the viscoelastic properties change during the formation of the SCoV2-N monolayer and the subsequent interaction with anti-SCoV2-N, i.e. the formation of immune complexes.

During the covalent immobilization of SCoV2-N on the 11-MUA SAM, the increase in ΔD was gradual from the initial stage and consistent with the frequency change. The density of the points indicated the fast and slow steps of the SCoV2-N immobilization kinetics. As can be seen from curve 1 in Fig. 3, the points are more distantly placed when ΔF is from 0 to 25 Hz. This feature indicates
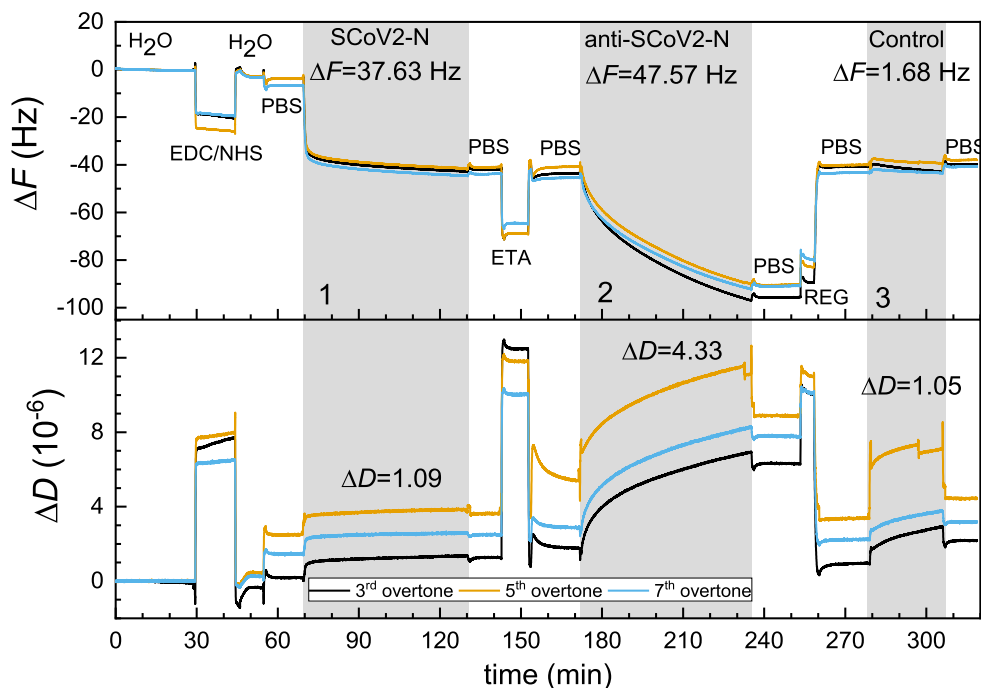

Fig. 2. Real-time frequency (ΔF) and energy dissipation (D) change for: (1) covalent SCoV2-N immobilization, (2) affinity interaction with anti-SCoV2-N, and (3) nonspecific interaction with polyclonal antibodies from mice non-immunized with SCoV2-N.
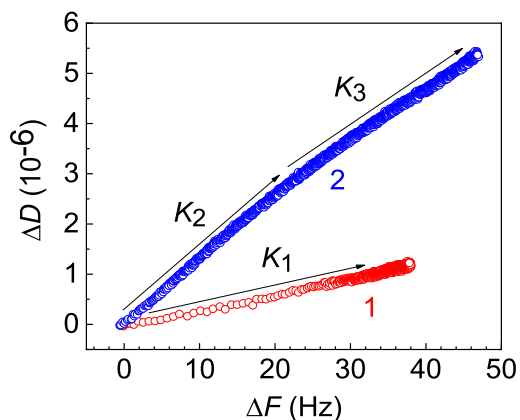
Fig. 3. $\Delta D/\Delta F$ plots for: SCoV2-N covalent immobilization on 11-MUA SAM (curve 1), and affinity interaction with anti-SCoV2-N (curve 2). The arrows K_1, K_2, and K_3 indicate the slopes to curves 1 and 2.

that in this particular ΔF range the kinetics of SCoV2-N covalent immobilization on 11-MUA SAM is faster than in the range from 25 to 38 Hz. The range from 0 to 25 Hz is obtained during the beginning of SCoV2-N monolayer formation. The slope of K_1 calculated for SCoV2-N covalent immobilization on 11-MUA SAM was equal to 0.031. Such a small value of K_1 also indicated that the formed SCoV2-N monolayer is rigid and, therefore, Sauerbrey equation can be very accurately applied for the calculation of surface mass density [34]. For the formation of the SCoV2-N/anti-SCoV2-N complex, the increase in ΔD was gradual from the beginning, with a slight change of direction in the $\Delta D/\Delta F$ plot at 22 Hz, thus curve 2 had two distinct tangents – K_2 and K_3 (Fig. 3, curve 2). This small change of SCoV2-N and anti-SCoV2-N interaction can be associated with conformational changes and rearrangements of anti-SCoV2-N antibodies during the formation of the SCoV2-N/anti-SCoV2-N complex [34]. The $\Delta D/\Delta F$ plot (Fig. 3, curve 2) shows that the formation of SCoV2-N/anti-SCoV2-N complex is slow because the points are distributed close to each other from the beginning of the interaction with SCoV2-N. The calculated slopes K_2 and K_3 for the formation of the SCoV2-N/anti-SCoV2-N complex were 0.134 and 0.121, respectively. These values are close to those obtained by other authors for cysteine peptidase and specific polyclonal antibody complex formation [34]. However, higher values of ΔD registered during anti-SCoV2-N affinity interaction with immobilized SCoV2-N show that the formation of the SCoV2-N/anti-SCoV2-N complex creates a soft and viscoelastic layer of anti-SCoV2-N antibodies. As it was reported in our previous publication [29], the equilibrium dissociation constant K_D of SCoV2-N/anti-SCoV2-N complex obtained from spectroscopic ellipsometry measurements in the total internal reflection mode was $9.3 \cdot 10^{-7}$ M (Table 1).

Most antibodies have K_D values are in the range of 10^{-6} to 10^{-9}. Antibody affinity can be measured using different methods such as label-free optical scanner for microarray detection based on polarization-modulated oblique-incidence reflectivity difference,

SPR, and ellipsometry-based (label-free) optical scanner [11,35–38]. K_D calculated from the experimental results obtained after polyclonal anti-SCoV2-N interaction with covalently immobilized SCoV2-N falls in this range of K_D values.

3.2. Analysis of SCoV2-N monolayer and SCoV2-N/anti-SCoV2-N complex formation by SE

For the evaluation of SCoV2-N covalent immobilization on 11-MUA SAM and SCoV2-N/anti-SCoV2-N complex formation on the gold-coated sensor disk, measurements of ellipsometric parameters (Δ and Ψ) were performed simultaneously with QCM-D signals registration (ΔF and ΔD). Here we present only the kinetics of the ellipsometric parameter Δ due to its higher sensitivity [16,22,39]. The simulation of ellipsometric parameters Ψ and Δ vs λ has been conducted to determine the difference between the optical properties in case of full coverage by SCoV2-N and anti-SCoV2-N versus partial coverage by the same proteins. Then the evaluation of fully formed SCoV2-N and anti-SCoV2-N monolayers was performed by the simulation of Δ and Ψ vs λ curves according to Cauchy dispersion function using Complete EASE software for ellipsometric data analysis.

The refractive index n of such fully formed monolayers in both cases (SCoV2-N and anti-SCoV2-N) was 1.6 at 600 nm wavelength. Measured and simulated Δ vs λ dispersion curves are presented for comparison in Fig. 4A for SCoV2-N, and Fig. 4B for anti-SCoV2-N, respectively. Curves 1 and 1′ presented in Fig. 4 A, and B correspond to the pure PBS ($n = 1.333$) before injection of SCoV2-N and before the SCoV2-N/anti-SCoV2-N complex formation. Curves 2 and 2′ were obtained experimentally when monolayers of SCoV2-N and anti-SCoV2-N antibodies were formed, respectively. The $\delta\Delta$ differences calculated at 601 nm between curves 1 and 2, 1′ and 2′ (Fig. 4A, and B) were 1.11° after SCoV2-N monolayer formation and 0.81° after anti-SCoV2-N affinity interaction with immobilized SCoV2-N, respectively. This difference was compared to that between curves 1 and 3, 1′ and 3′ that corresponded to simulated fully formed monolayers ($n = 1.6$) of SCoV2-N and anti-SCoV2-N. Simulated data (Fig. 4A, curves 1–3) for the formed SCoV2-N monolayer showed the $\delta\Delta$ between PBS and the fully formed SCoV2-N layer would be 8.01°. For the fully formed anti-SCoV2-N monolayer, $\delta\Delta$ would be 6.78° (Fig. 4B curves 1–3). The kinetics of SCoV2-N covalent immobilization and affinity interaction with anti-SCoV2-N are presented in Fig. 4 C and D, respectively. The $\delta\Delta$ presented in Fig. 4 C, and D for SCoV2-N and anti-SCoV2-N meets the difference between curves 1 and 2, 1′ and 2′ in Fig. 4 A, and B. As can be seen from these Figures, the SCoV2-N covers only small part on the surface. Consequently, only a small amount of anti-SCoV2-N forms a complex with covalently immobilized SCoV2-N.

3.3. Wet and dry SCoV2-N and anti-SCoV2-N layers' surface mass density calculation from SE and QCM-D data

For the calculation of SCoV2-N monolayer thickness and index of refraction (n), modelling of the experimentally obtained ellipsometric parameters Ψ and Δ vs λ was done by designing an optical model. The experimental results obtained were fitted with optical model using Complete EASE software for ellipsometric data analy-

Table 1
Association, dissociation, residence time rate constants (k_a, k_d, k_r), equilibrium association and dissociation constants (K_A, K_D) for SCoV2-N/anti-SCoV2-N immune complex formation . adopted from [29]

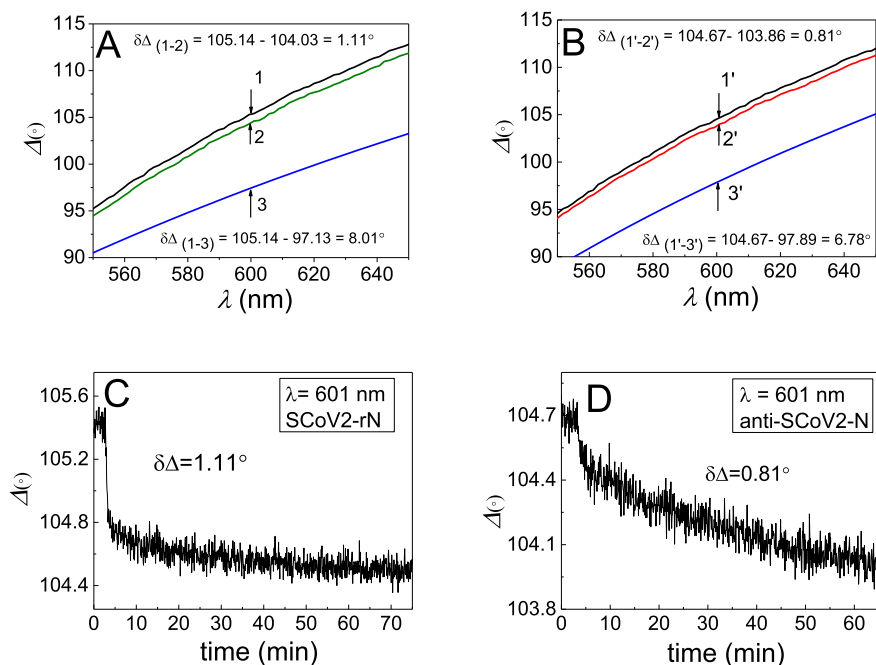|	k_a (M^{-1} s^{-1})	k_d (s^{-1})	K_A (M^{-1})	K_D (M)	k_r (s^{-1})
anti-SCoV2-N	$3.6 \cdot 10^4 \pm 0.002$	$3.35 \cdot 10^{-2} \pm 0.047$	$1.07 \cdot 10^6$	$9.3 \cdot 10^{-7}$	$4.8 \cdot 10^{-3} \pm 0.026$

Fig. 4. Spectra of ellipsometric parameter Δ vs. λ (**A, B**) and time (**C, D**) for covalent SCoV2-N immobilization and formation of immune complexes with specific anti-SCoV2-N antibodies. **A** - the ellipsometric parameter Δ vs. λ for covalent SCoV2-N immobilization on 11-MUA SAM: 1- PBS, 2- SCoV2-N partially covered monolayer, 3- simulated monolayer fully covered by SCoV2-N; **B** - the ellipsometric parameter Δ vs. λ for SCoV2-N interaction with anti-SCoV2-N and monolayer formation: 1'- PBS, 2'- anti-SCoV2-N monolayer, 3'- simulated fully covered by anti-SCoV2-N; **C** - evolution of Δ in time for SCoV2-N covalent immobilization, and **D** – for anti-SCoV2-N monolayer formation.

sis. This model consisted of a thick QCM-D gold substrate, thickness $d_{(gold)}$ = 200 nm, covered by 11-MUA SAM, $d_{(SAM)}$ = 0.8 nm and $d_{(SCoV2-N)}$ = 5.9 nm SCoV2-N layers. The refractive index dispersion of the QCM-D gold-coated sensor substrate was modelled using B-Spline function [24], 11-MUA SAM was modelled by Cauchy dispersion (n = 1.450) and the SCoV2-N monolayer was described using the Bruggeman effective media approach (EMA) [22,39–41].

The monolayer of SCoV2-N described as EMA consisted of 66% PBS (n = 1.333) and of 34% SCoV2-N (n = 1.610). During the regression analysis for the calculation of the refractive index, the thickness of the monolayer $d_{(SCoV2-N)}$ was a fixed parameter and the volume fraction of PBS was a free fitting value in the EMA. The anti-SCoV2-N monolayer was fitted using the same Bruggeman EMA layer on top of SCoV2-N under the similar procedure. Anti-SCoV2-N monolayer consisted of 81% PBS and 19% of antibody, the thickness of this monolayer $d_{(anti-SCoV2-N)}$ = 8 nm was a fixed value during regression analysis for modelling of n evolution in time. After that the thickness $d_{(SCoV2-N)}$ and $d_{(anti-SCoV2-N)}$ evolution in time was performed fixing the refractive index values of fully formed SCoV2-N and anti-SCoV2-N monolayers (Fig. 5A, B). Anti-SCoV2-N $d_{(anti-SCoV2-N)}$ obtained from regression analysis of SE data was further fitted to be 8.1 nm and this value is close to one of the IgG antibody dimensions, when the antigen-binding sites are in about 13.7 nm distance [42]. This means that the conformation of anti-SCoV2-N antibodies on the surface of the formed SCoV2-N layer is T shape [43]. As the Ab is a flexible molecule and the mean angle between antibody Fab-Fab arms can differ, the T shape position makes it possible to reach small antigens located on the surface far from each other [44] and to establish a tightly bound

complex [45]. The calculated Δn, $d_{(SCoV2-N)}$ and $d_{(anti-SCoV2-N)}$ evolution in time for the formation of SCoV2-N and anti-SCoV2-N monolayers are presented in Fig. 5C, D. Calculation of dry layers thickness d and refractive index changes Δn from the results obtained by SE allowed us to evaluate the dry surface mass density for SCoV2-N and anti-SCoV2-N monolayers.

As shown in Fig. 5C, after 70 min, when the SCoV2-N monolayer was formed, the difference in refractive indexes Δn = ($n_{SCoV2-N}$ - n_{PBS}) = 0.08. For anti-SCoV2-N, Δn = 0.38 after 70 min (Fig. 5D). Surface mass densities calculated using SE data (Γ^{SE}) of SCoV2-N or anti-SCoV2-N monolayers ($\Gamma^{SE}_{SCoV2-N}$ and $\Gamma^{SE}_{anti-SCoV2-N}$) presented in Fig. 5E, F were calculated using de Feijter approach:

$$\Gamma^{SE} = \frac{d(n_{layer} - n_{PBS})}{dn/dc} \cdot 100 \qquad (1)$$

Here d is the thickness of the formed antigen or antibody monolayer (SCoV2-N or anti-SCoV2-N), dn/dc is the refractive index increment for proteins (0.18) [24,40,46]. The evolution of $\Gamma^{SE}_{SCoV2-N}$ and $\Gamma^{SE}_{anti-SCoV2-N}$ in time during monolayer formation is presented in Fig. 5E, and F. Γ^{SE} for the SCoV2-N and anti-SCoV2-N layers corresponds to the dry mass, without PBS between the proteins. Calculated dry mass Γ^{SE} for the SCoV2-N monolayer was 200 ng/cm² after 70 min and for anti-SCoV2-N (the initial concentration of specific antibodies was 170 nM) is 167 ng/cm².

When the SCoV2-N monolayer was formed (after 70 min), the wet surface mass density calculated using QCM-D data obtained simultaneously with SE was C = 672 ng/cm² (Fig. 5E). The Γ^{QCM-D} was calculated using Voinova-Voight model in the QSoft401 software (Biolin Scientific) [47,48]. After anti-SCoV2-N interaction
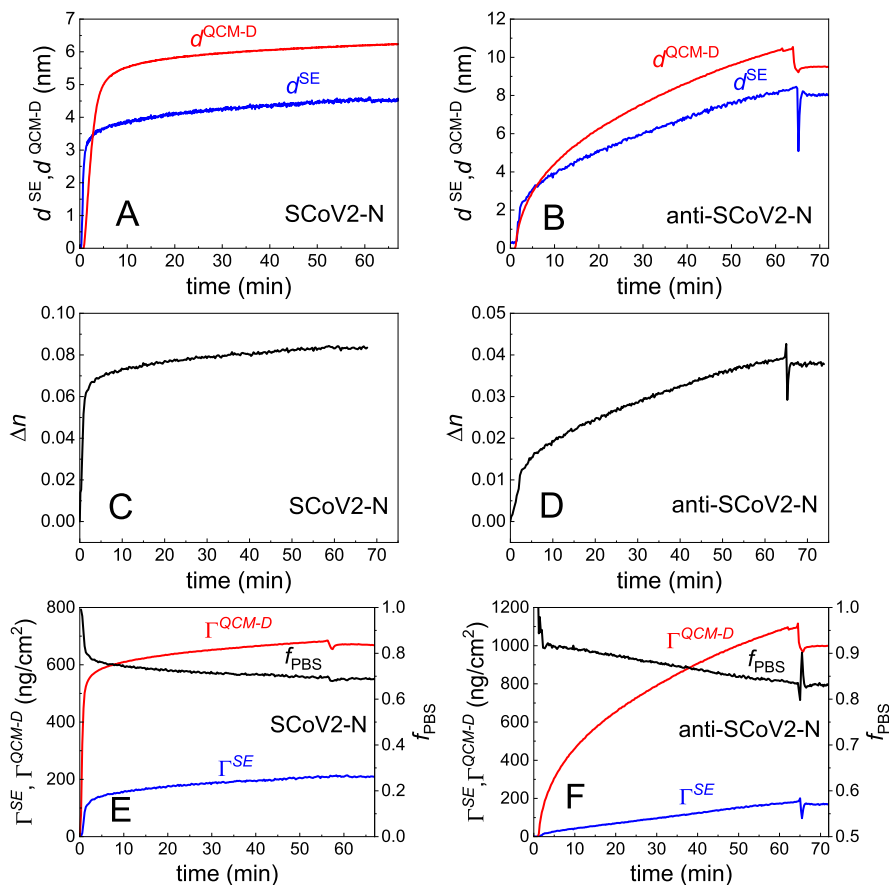
Fig. 5. Evolution of the formation of SCoV2-N and anti-SCoV2-N monolayers in time: dry (d^{SE}) and wet (d^{QCM-D}) monolayer thickness versus time for SCoV2-N (**A**) and anti-SCoV2-N (**B**), change of refractive index versus time for SCoV2-N (**C**) and anti-SCoV2-N (**D**), and dry (Γ^{SE}) and wet (Γ^{QCM-D}) surface mass density for SCoV2-N (**E**) and anti-SCoV2-N (**F**).

with immobilized SCoV2-N and anti-SCoV2-N monolayer formation (70 min), wet Γ^{QCM-D} = 995 ng/cm^2 (Fig. 5F). The Γ^{QCM-D} corresponds to the wet mass and presents the surface mass density for the monolayer containing SCoV2-N or anti-SCoV2-N molecules, and PBS. The thicknesses of the SCoV2-N and anti-SCoV2-N wet layers calculated from QCM-D data modelling were 6.24 nm and 9.55 nm, respectively. Calculated hydration (f_{PBS}) of the protein layers is presented in Fig. 5E and 5F as the amount of PBS trapped between the molecules of the SCoV2-N or anti-SCoV2-N.

Using SE in combination with QCM-D, changes in the amount of PBS between SCoV2-N and anti-SCoV2-N were evaluated simultaneously. The hydration was calculated using the following formula (2) [49]:

$$f_{PBS} = 1 - \frac{\Gamma^{SE}}{\Gamma^{QCM-D}} \qquad (2)$$

Here f_{PBS} is the amount of PBS between protein SCoV2-N or anti-SCoV2-N monolayers, Γ^{SE} - dry mass of SCoV2-N or anti-SCoV2-N, Γ^{QCM-D} – wet mass of SCoV2-N or anti-SCoV2-N + PBS. In this case, the amount of PBS in the SCoV2-N monolayer was close to 0.7 and for the anti-SCoV2-N monolayer the amount of PBS was 0.83

(Fig. 5E and F). These values of hydration (amount of PBS) for the SCoV2-N and anti-SCoV2-N monolayers are in good agreement with the results obtained from SE data modeling, where the amount of PBS in the SCoV2-N monolayer was 66% and for anti-SCoV2-N monolayer it was 81%, respectively.

Assuming that SCoV2-N monolayer is formed as a square shape site lattice and using simple geometrical considerations, it is possible to estimate the minimal distance between the SCoV2-N immobilized on the surface (lattice constant d_l) using the calculated hydration (f_{PBS}). Using such a geometrical model, d_l can be obtained from the formula $d_l = r \cdot (2\pi/3f)^{1/2}$, where r is the radius of the SCoV2-N molecule of ball-like shape. At r = 3 nm and f_{PBS} = 0.325, the d_l calculated using this formula was about 7.6 nm. Another way to estimate the d_l is to calculate the surface density of SCoV2-N molecules immobilized on the square unit (cm^2) of the substrate. It can be done by dividing the total mass (m_{pt}) of these molecules by the mass (m_{ps} = 48 kDa) of a single SCoV2-N molecule ("mass" model). It should be noted that m_{pt} value depends on f_{PBS} and protein's density (ρ_p), which can be in the range of 1.22–1.34 g/cm^3. For this reason, the surface density of the square-shaped site lattice changes from 3.0 10^{12} cm^{-2} to 3.3 10^{12} cm^{-2} and d_l ranged from 6.0 to 5.5 nm correspondingly, which is of the same order as obtained
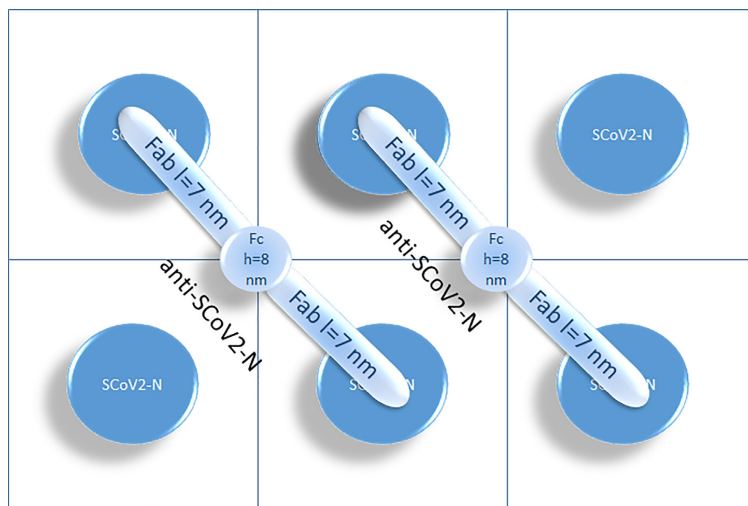
Fig. 6. Schematic representation (the relative sizes of SCoV2-N and anti-SCoV2-N are not in scale) of the displacement of SCoV2-N approximated by a square lattice. The lattice constant is the average distance between SCoV2-N molecules of the real monolayer.

from the geometrical model. The difference in about 20% of d_l value estimated using both "mass" and geometrical models can be easy explained taking into consideration that "mass" model assume hard packaging of protein material into one SCoV2-N molecule, meanwhile the geometrical model, which is more close to reality, is based on soft larger size molecule approach.

Assuming that SCoV2-N monolayer is formed as a square shape site lattice and using simple geometrical considerations, it is possible to estimate the minimal distance between the SCoV2-N immobilized on the surface (lattice constant d_l) using the calculated f_{PBS}. The d_l can be obtained from the formula $d_l = r \cdot (2\pi/3f)^{1/2}$, where r is the radius of the ball-shaped SCoV2-N molecule. At $r = 3$ nm and $f = 0.3$, the d_l calculated using this formula was 7.9 nm. The other important parameter of such a lattice is the diagonal distance (d_d) between the middle of each SCoV2-N molecules, that is, $d_d = d_l \cdot 2^{1/2} = 11.2$ nm. Thus, there are two possible ways to attach anti-SCoV2-N to the SCoV2-N using d_l and d_d distances. It is evident that d_d is preferable because in this case the anti-SCoV2-N present in T shape and a distance between the middle of each SCoV2-N molecules is close to 14 nm distance between paratopes. To evaluate the maximal hydration of the formed monolayer after affinity interaction of SCoV2-N with anti-SCoV2-N, we used the approximated square lattice presented in Fig. 6.

As can be seen, the lattice unit is occupied by one SCoV2-N molecule, one anti-SCoV2-N Fab fragment, and half of the anti-SCoV2-N Fc unit (two quarters of Fc fragments from two anti-SCoV2-N). Taking into account that the radius of SCoV2-N is 3 nm and the density of both proteins, i.e. SCoV2-N and anti-SCoV2-N is the same, we estimated that the diameter of the average anti-SCoV2-N cross section is about 2 nm. Thus, the total volume occupied by the proteins in one lattice unit (V_{pr}) consisting of SCoV2-N, an anti-SCoV2-N Fab fragment, and half of anti-SCoV2-N Fc fragment is approximately $V_{pr} = 434$ nm³. The volume of a lattice unit (V_l) 7.9 × 7.9 × 14 nm³ is approximately $V_l = 874$-nm³. The height of this lattice unit, i.e., 14 nm, was estimated as a sum of SCoV2-N monolayer thickness (6 nm) and anti-SCoV2-N monolayer thickness (8 nm). Thus, the maximal hydration of the formed SCoV2-N/anti-SCoV2-N complex $f_{comp} = V_{pr}/V_l \approx 0.5$. This value is close to $f_{comp} = 0.47$ obtained from hydration calculations

for SCoV2-N/anti-SCoV2-N (for SCoV2-N $f_{comp} = 0.3$ (Fig. 5E) and for anti-SCoV2-N $f_{comp} = 0.17$ (Fig. 5F), respectively).

4. Conclusions

SARS-CoV-2 nucleocapsid protein is one of the diagnostic markers that can be detected earlier than the clinical symptoms appears in infected patients [50]. Conversely, the detection of specific antibodies against nucleocapsid protein can increase the diagnostic capacity [51,52]. Based on our results we showed that the monolayer formed on the solid–liquid interface as a result of covalent immobilization of SCoV2-N can be described as a rigid due to low energy dissipation registered during QCM-D measurement. In contrary, anti-SCoV2-N monolayer after the interaction with the covalently immobilized SCoV2-N formed a soft, flexible, and viscous layer with 3.9 times higher energy dissipation. The flexibility of the antibody Fab arms allows them to reach the more distantly located SCoV2-N and to establish a bivalent interaction between proteins in formed SCoV2-N/anti-SCoV2-N complex. Different methods, such as electron microscopy [8], cryo-electron tomography [53], small-angle X-ray scattering [49], and other techniques were used to evaluate the flexibility of antibodies and conformational variability of the antigen-binding fragments. In this research we showed that SE/QCM-D can be applied for the evaluation of antibody flexibility and for the selection of antibodies with the desired properties since this factor limits the assembly of antibodies on the surface with immobilized antigens. The antibody flexibility can be taken into account for the design of sensitive immunoassays of different formats whereas distinct types of immune complexes (closed sandwich-like or the extended linear complexes of antibodies and antigens) can be formed. It was showed that in the direct sandwich enzyme-linked immunosorbent assay, the rigid enzyme-labeled antibody with dominating linear arrangement increased the sensitivity of the analytical system while more labeled antibody was bound to the same surface concentration of antigen in comparison to the flexible enzyme-labeled antibodies [50].

All in all, we have applied and adapted the combination of two highly surface-sensitive and label-free methods, that enables

simultaneously to study interaction between novel coronavirus SARS-CoV-2 nucleocapsid protein and specific antibody at the solid–liquid interface in real time and to evaluate viscoelastic properties of formed layers. The obtained results showed that anti-SCoV2-N flexibility was important factor for the bivalent interaction with small nucleocapsid protein distantly located from each other on the solid–liquid interface.

CRediT authorship contribution statement

Ieva Plikusiene: Conceptualization, Methodology, Visualization, Investigation, Writing – review & editing, Formal analysis, Writing – original draft. **Vincentas Maciulis:** Methodology, Formal analysis, Investigation, Writing – original draft. **Silvija Juciute:** Methodology, Investigation. **Arunas Ramanavicius:** Conceptualization, Methodology, Writing – review & editing. **Zigmas Balevicius:** Methodology, Conceptualization, Writing – review & editing. **Rimantas Slibinskas:** Methodology, Writing – original draft, Resources. **Indre Kucinskaite-Kodze:** Methodology, Resources. **Martynas Simanavicius:** Methodology, Resources. **Saulius Balevicius:** Methodology, Writing – review & editing, Formal analysis, Writing – original draft. **Almira Ramanaviciene:** Conceptualization, Visualization, Writing – original draft, Writing – review & editing, Funding acquisition, Supervision.

Declaration of Competing Interest

The authors declare that they have no known competing financial interests or personal relationships that could have appeared to influence the work reported in this paper.

Acknowledgment

References

[1] P.S. Masters, Coronavirus genomic RNA packaging, Virology 537 (2019) 198–207, https://doi.org/10.1016/j.virol.2019.08.031.

[2] M. Batra, R. Tian, C. Zhang, E. Clarence, C.S. Sacher, J.N. Miranda, J.R.O. De La Fuente, M. Mathew, D. Green, S. Patel, M.V.P. Bastidas, S. Haddadi, M. Murthi, M.S. Gonzalez, S. Kambali, K.H.M. Santos, H. Asif, F. Modarresi, M. Faghihi, M. Mirsaeidi, Role of IgG against N-protein of SARS-CoV2 in COVID19 clinical outcomes, Sci. Rep. 11 (2021) 1–9, https://doi.org/10.1038/s41598-021-83108-0.

[3] G. Guglielmi, Fast coronavirus tests: what they can and can't do, Nature 585 (2020) 496–498, https://doi.org/10.1038/d41586-020-02661-2.

[4] M. Drobysh, A. Ramanaviciene, R. Viter, A. Ramanavicius, Affinity sensors for the diagnosis of covid-19, Micromachines 12 (2021) 1–19, https://doi.org/10.3390/mi12040390.

[5] K. Guevara-Hoyer, J. Fuentes-Antrás, E. De la Fuente-Muñoz, A.R. de la Peña, M. Viñuela, N. Cabello-Clotet, V. Estrada, E. Culebras, A. Delgado-Iribarren, M. Martínez-Novillo, M.J. Torrejón, R.P. de Diego, M. Fernández-Arquero, A. Ocaña, P. Pérez-Segura, S. Sánchez-Ramón, Serological tests in the detection of SARS-CoV-2 antibodies, Diagnostics. 11 (2021) 1–10, https://doi.org/10.3390/diagnostics11040678.

[6] C. Dobaño, R. Santano, A. Jiménez, M. Vidal, J. Chi, N. Rodrigo Melero, M. Popovic, R. López-Aladid, L. Fernández-Barat, M. Tortajada, F. Carmona-Torre, G. Reina, A. Torres, A. Mayor, C. Carolis, A.L. García-Basteiro, R. Aguilar, G. Moncunill, L. Izquierdo, Immunogenicity and crossreactivity of antibodies to the nucleocapsid protein of SARS-CoV-2: utility and limitations in seroprevalence and immunity studies, Transl. Res. 232 (2021) 60–74. https://doi.org/10.1016/j.trsl.2021.02.006.

[7] P.D. Burbelo, F.X. Riedo, C. Morishima, S. Rawlings, D. Smith, S. Das, J.R. Strich, D.S. Chertow, R.T. Davey, J.I. Cohen, Sensitivity in detection of antibodies to nucleocapsid and spike proteins of severe acute respiratory syndrome

[8] K.H. Roux, L. Strelets, T.E. Michaelsen, Flexibility of human IgG subclasses, J. Immunol. 159 (1997) 3372–3382. http://www.ncbi.nlm.nih.gov/pubmed/9317136.

[9] I.S. Mian, A.R. Bradwell, A.J. Olson, Structure, function and properties of antibody binding sites, J. Mol. Biol. 217 (1991) 133–151, https://doi.org/10.1016/0022-2836(91)90617-F.

[10] P. Wang, X. Yang, Neutralization Efficiency Is Greatly Enhanced by Bivalent Binding of an Antibody to Epitopes in the V4 Region and the Membrane-Proximal External Region within One Trimer of Human Immunodeficiency Virus Type 1 Glycoproteins, J. Virol. 84 (2010) 7114–7123, https://doi.org/10.1128/jvi.00545-10.

[11] L. Bar, J. Dejeu, R. Lartia, F. Bano, R.P. Richter, L. Coche-Guerente, D. Boturyn, Impact of Antigen Density on Recognition by Monoclonal Antibodies, Anal. Chem. 92 (2020) 5396–5403, https://doi.org/10.1021/acs.analchem.0c00092.

[12] K.B. Rodenhausen, B.A. Duensing, T. Kasputis, A.K. Pannier, T. Hofmann, M. Schubert, T.E. Tiwald, M. Solinsky, M. Wagner, In-situ monitoring of alkanethiol self-assembled monolayer chemisorption with combined spectroscopic ellipsometry and quartz crystal microbalance techniques, Thin Solid Films 519 (2011) 2817–2820, https://doi.org/10.1016/j.tsf.2010.11.081.

[13] J. Martensson, H. Arwin, Interpretation of Spectroscopic Ellipsometry Data on Protein Layers on Gold Including Substrate-Layer Interactions, Langmuir. 11 (1995) 963–968, https://doi.org/10.1021/la00003a045.

[14] H. Arwin, D.E. Aspnes, Unambiguous determination of thickness and dielectric function of thin films by spectroscopic ellipsometry, Thin Solid Films 113 (1984) 101–113, https://doi.org/10.1016/0040-6090(84)90019-1.

[15] H. Arwin, Spectroscopic ellipsometry and biology: Recent developments and challenges, Thin Solid Films 313–314 (1998) 764–774, https://doi.org/10.1016/S0040-6090(97)00993-0.

[16] H. Arwin, M. Poksinski, K. Johansen, Total internal reflection ellipsometry: Principles and applications, Appl. Opt. 43 (2004) 3028–3036, https://doi.org/10.1364/AO.43.003028.

[17] A.V. Nabok, A. Tsargorodskaya, A.K. Hassan, N.F. Starodub, Total internal reflection ellipsometry and SPR detection of low molecular weight environmental toxins, Appl. Surf. Sci. 246 (2005) 381–386, https://doi.org/10.1016/j.apsusc.2004.11.084.

[18] Z. Balevicius, A. Ramanaviciene, I. Baleviciute, A. Makaraviciute, L. Mikoliunaite, A. Ramanavicius, Evaluation of intact- and fragmented-antibody based immunosensors by total internal reflection ellipsometry, Sensors Actuat. B Chem. 160 (2011) 555–562, https://doi.org/10.1016/j.snb.2011.08.029.

[19] I. Baleviciute, Z. Balevicius, A. Makaraviciute, A. Ramanaviciene, A. Ramanavicius, Study of antibody/antigen binding kinetics by total internal reflection ellipsometry, Biosens. Bioelectron. 39 (2013) 170–176, https://doi.org/10.1016/j.bios.2012.07.017.

[20] Z. Balevicius, I. Baleviciute, S. Tumenas, L. Tamosaitis, A. Stirke, A. Makaraviciute, A. Ramanaviciene, A. Ramanavicius, In situ study of ligand-receptor interaction by total internal reflection ellipsometry, Thin Solid Films 571 (2014) 744–748, https://doi.org/10.1016/j.tsf.2013.10.090.

[21] Z. Balevicius, J. Talbot, L. Tamosaitis, I. Plikusiene, A. Stirke, G. Mickiene, S. Balevicius, A. Paulauskas, A. Ramanavicius, Modelling of immunosensor response: the evaluation of binding kinetics between an immobilized receptor and structurally-different genetically engineered ligands, Sensors Actuat. B Chem. 297 (2019), https://doi.org/10.1016/j.snb.2019.126770 126770.

[22] I. Plikusiene, Z. Balevicius, A. Ramanaviciene, J. Talbot, G. Mickiene, S. Balevicius, A. Stirke, A. Tereshchenko, L. Tamosaitis, G. Zvirblis, A. Ramanavicius, Evaluation of affinity sensor response kinetics towards dimeric ligands linked with spacers of different rigidity: Immobilized recombinant granulocyte colony-stimulating factor based receptor binding with genetically engineered dimeric analyte d, Biosens. Bioelectron. 156 (2020), https://doi.org/10.1016/j.bios.2020.112112 112112.

[23] I. Plikusiene, V. Maciulis, S. Juciute, R. Maciuleviciene, S. Balevicius, A. Ramanavicius, A. Ramanaviciene, Investigation and Comparison of Specific Antibodies' Affinity Interaction with SARS-CoV-2 Wild-Type, B.1.1.7, and B.1.351 Spike Protein by Total Internal Reflection Ellipsometry, Biosensors. 12 (2022) 351, https://doi.org/10.3390/bios12050351.

[24] E. Bittrich, K.B. Rodenhausen, K.-J. Eichhorn, T. Hofmann, M. Schubert, M. Stamm, P. Uhlmann, Protein adsorption on and swelling of polyelectrolyte brushes: A simultaneous ellipsometry-quartz crystal microbalance study, Biointerphases. 5 (2010) 159–167, https://doi.org/10.1116/1.3530841.

[25] H.T.M. Phan, S. Bartelt-Hunt, K.B. Rodenhausen, M. Schubert, J.C. Bartz, D. Hinderberger, Investigation of bovine serum albumin (BSA) attachment onto self-assembled monolayers (SAMs) using combinatorial quartz crystal microbalance with dissipation (QCM-D) and spectroscopic ellipsometry (SE), PLoS One 10 (10) (2015) e0141282.

[26] M.V. Voinova, M. Rodahl, M. Jonson, B. Kasemo, Viscoelastic acoustic response of layered polymer films at fluid-solid interfaces: continuum mechanics approach, Phys. Scr. 59 (1999) 391–396, https://doi.org/10.1238/physica.regular.059a00391.

[27] M.B. Hovgaard, K. Rechendorff, J. Chevallier, M. Foss, F. Besenbacher, Fibronectin adsorption on tantalum: The influence of nanoroughness, J. Phys. Chem. B 112 (2008) 8241–8249, https://doi.org/10.1021/jp801103n.

[28] S. Adam, M. Koenig, K.B. Rodenhausen, K.J. Eichhorn, U. Oertel, M. Schubert, M. Stamm, P. Uhlmann, Quartz crystal microbalance with coupled spectroscopic

ellipsometry-study of temperature-responsive polymer brush systems, Appl. Surf. Sci. 421 (2017) 843–851, https://doi.org/10.1016/j.apsusc.2017.02.078.

[29] I. Plikusiene, V. Maciulis, A. Ramanaviciene, Z. Balevicius, E. Buzavaite-Verteliene, E. Ciplys, R. Slibinskas, M. Simanavicius, A. Zvirbliene, A. Ramanavicius, Evaluation of kinetics and thermodynamics of interaction between immobilized SARS-CoV-2 nucleoprotein and specific antibodies by total internal reflection ellipsometry, J. Colloid Interface Sci. 594 (2021) 195–203, https://doi.org/10.1016/j.jcis.2021.02.100.

[30] P. Hampitak, D. Melendrez, M. Iliut, M. Fresquet, N. Parsons, B. Spencer, T.A. Jowitt, A. Vijayaraghavan, Protein interactions and conformations on graphene-based materials mapped using quartz-crystal microbalance with dissipation monitoring (QCM-D), Carbon N. Y. 165 (2020) 317–327, https://doi.org/10.1016/j.carbon.2020.04.093.

[31] G. Sauerbrey, Verwendung von Schwingquarzen zur Wägung dünner Schichten und zur Mikrowägung, Zeitschrift Für Phys. 155 (1959) 206–222, https://doi.org/10.1007/BF01337937.

[32] F. Höök, M. Rodahl, B. Kasemo, P. Brzezinski, Structural changes in hemoglobin during adsorption to solid surfaces: Effects of pH, ionic strength, and ligand binding, Proc. Natl. Acad. Sci. USA 95 (1998) 12271–12276, https://doi.org/10.1073/pnas.95.21.12271.

[33] A. Makaraviciute, T. Ruzgas, A. Ramanavicius, A. Ramanaviciene, Antibody fragment immobilization on planar gold and gold nanoparticle modified quartz crystal microbalance with dissipation sensor surfaces for immunosensor applications, Anal. Methods 6 (2014) 2134–2140, https://doi.org/10.1039/c4ay00070f.

[34] A.S. Afonso, B.F. Zanetti, A.C. Santiago, F. Henrique-Silva, L.H.C. Mattoso, R.C. Faria, QCM immunoassay for recombinant cysteine peptidase: A potential protein biomarker for diagnosis of citrus canker, Talanta 104 (2013) 193–197, https://doi.org/10.1016/j.talanta.2012.11.003.

[35] J.P. Landry, Y. Fei, X. Zhu, Simultaneous measurement of 10,000 protein-ligand affinity constants using microarray-based kinetic constant assays, Assay Drug Dev. Technol. 10 (2012) 250–259, https://doi.org/10.1089/adt.2011.0406.

[36] Y. Fei, Y.S. Sun, Y. Li, K. Lau, H. Yu, H.A. Chokhawala, S. Huang, J.P. Landry, X. Chen, X. Zhu, Fluorescent labeling agents change binding profiles of glycan-binding proteins, Mol. Biosyst. 7 (2011) 3343–3352, https://doi.org/10.1039/c1mb05332a.

[37] Y.S. Sun, J.P. Landry, Y.Y. Fei, X.D. Zhu, J.T. Luo, X.B. Wang, K.S. Lam, Effect of fluorescently labeling protein probes on kinetics of protein-ligand reactions, Langmuir. 24 (2008) 13399–13405, https://doi.org/10.1021/la802097z.

[38] D.G. Myszka, M.D. Jonsen, B.J. Graves, Equilibrium analysis of high affinity interactions using BIACORE, Anal. Biochem. 265 (1998) 326–330, https://doi.org/10.1006/abio.1998.2937.

[39] I. Plikusiene, V. Maciulis, O. Graniel, M. Bechelany, S. Balevicius, V. Vertelis, Z. Balevicius, A. Popov, A. Ramanavicius, A. Ramanaviciene, Total internal reflection ellipsometry for kinetics-based assessment of bovine serum albumin immobilization on ZnO nanowires, J. Mater. Chem. C 9 (2021) 1345–1352, https://doi.org/10.1039/d0tc05193d.

[40] Z. Balevicius, A. Paulauskas, I. Plikusiene, L. Mikoliunaite, M. Bechelany, A. Popov, A. Ramanavicius, A. Ramanaviciene, Towards the application of Al2O3/ZnO nanolaminates in immunosensors: total internal reflection spectroscopic ellipsometry based evaluation of BSA immobilization, J. Mater. Chem. C 6 (2018) 8778–8783, https://doi.org/10.1039/c8tc03091j.

[41] V. Maciulis, U. Malinovskis, D. Erts, A. Ramanavicius, A. Ramanaviciene, S. Balevicius, S. Juciute, I. Plikusiene, Porous aluminium oxide coating for the development of spectroscopic ellipsometry based biosensor: Evaluation of human serum albumin adsorption, Coatings 10 (2020) 1–10, https://doi.org/10.3390/coatings10111018.

[42] Y.H. Tan, M. Liu, B. Nolting, J.G. Go, J. Gervay-hague, G. Liu, ARTICLE A nanoengineering approach for immobilization, ACS Nano 2 (2008) 2374–2384.

[43] H.R. Maun, R. Vij, B.T. Walters, A. Morando, J.K. Jackman, P. Wu, A. Estevez, X. Chen, Y. Franke, M.T. Lipari, M.S. Dennis, D. Kirchhofer, C. Ciferri, K.M. Loyet, T. Yi, C. Eigenbrot, R.A. Lazarus, J.T. Koerber, Bivalent antibody pliers inhibit β-tryptase by an allosteric mechanism dependent on the IgG hinge, Nat. Commun. 11 (2020) 1–12, https://doi.org/10.1038/s41467-020-20143-x.

[44] S. Sandin, L.G. Öfverstedt, A.C. Wikström, Ö. Wrange, U. Skoglund, Structure and flexibility of individual immunoglobulin G molecules in solution, Structure. 12 (2004) 409–415, https://doi.org/10.1016/j.str.2004.02.011.

[45] I. Correia, J. Sung, R. Burton, C.G. Jakob, B. Carragher, T. Ghayur, C. Radziejewski, The structure of dual-variable-domain immunoglobulin molecules alone and bound to antigen, MAbs. 5 (2013) 364–372, https://doi.org/10.4161/mabs.24258.

[46] H. Zhao, P.H. Brown, P. Schuck, On the distribution of protein refractive index increments, Biophys. J. 100 (2011) 2309–2317, https://doi.org/10.1016/j.bpj.2011.03.004.

[47] M.V. Voinova, M. Jonson, B. Kasemo, Dynamics of viscous amphiphilic films supported by elastic solid substrates, J. Phys. Condens. Matter. 9 (1997) 7799–7808, https://doi.org/10.1088/0953-8984/9/37/011.

[48] M.V. Voinova, M. Jonson, B. Kasemo, "Missing mass" effect in biosensor's QCM applications, Biosens. Bioelectron. 17 (2002) 835–841, https://doi.org/10.1016/S0956-5663(02)00050-7.

[49] K.B. Rodenhausen, M. Schubert, Virtual separation approach to study porous ultra-thin films by combined spectroscopic ellipsometry and quartz crystal microbalance methods, Thin Solid Films 519 (2011) 2772–2776, https://doi.org/10.1016/j.tsf.2010.11.079.

[50] C.D. Hodge, D.J. Rosenberg, P. Grob, M. Wilamowski, A. Joachimiak, G.L. Hura, M. Hammel, C.D. Hodge, D.J. Rosenberg, P. Grob, M. Wilamowski, A. Joachimiak, G.L. Hura, M. Hammel, Rigid monoclonal antibodies improve detection of SARS-CoV-2 nucleocapsid protein ABSTRACT, MAbs 13 (2021), https://doi.org/10.1080/19420862.2021.1905978.

[51] D.L. Ng, G.M. Goldgof, B.R. Shy, A.G. Levine, J. Balcerek, S.P. Bapat, J. Prostko, M. Rodgers, K. Coller, S. Pearce, S. Franz, L. Du, M. Stone, S.K. Pillai, A. Sotomayor-Gonzalez, V. Servellita, C.S.S. Martin, A. Granados, D.R. Glasner, L.M. Han, K. Truong, N. Akagi, D.N. Nguyen, N.M. Neumann, D. Qazi, E. Hsu, W. Gu, Y.A. Santos, B. Custer, V. Green, P. Williamson, N.K. Hills, C.M. Lu, J.D. Whitman, S.L. Stramer, C. Wang, K. Reyes, J.M.C. Hakim, K. Sujishi, F. Alazzeh, L. Pham, E. Thornborrow, C.-Y. Oon, S. Miller, T. Kurtz, G. Simmons, J. Hackett, M.P. Busch, C.Y. Chiu, SARS-CoV-2 seroprevalence and neutralizing activity in donor and patient blood, Nat. Commun. 11 (2020) 4698, https://doi.org/10.1038/s41467-020-18468-8.

[52] L. Wanbing, L. Lei, K. Guomei, Z. Yaqiong, D. Yinjuan, N. Wenxu, W. Qiongshu, T. Li, W. Wanlei, T. Shi, X. Zhou, Z. Shangen, M.a. j.,, Evaluation of Nucleocapsid and Spike Protein-Based Enzyme-Linked Immunosorbent Assays for Detecting Antibodies against SARS-CoV-2, J. Clin. Microbiol. 58 (2022) e00461–e520, https://doi.org/10.1128/JCM.00461-20.

[53] L. Bongini, D. Fanelli, F. Piazza, P.D.L. Rios, S. Sandin, U. Skoglund, Dynamics of antibodies from cryo-electron tomography, 115 (2005) 235–240. https://doi.org/10.1016/j.bpc.2004.12.037.

Paper 5

Recent Advances in Synthesis and Application of Metal Oxide Nanostructures in Chemical Sensors and Biosensors

Vincentas Maciulis, Almira Ramanaviciene, Ieva Plikusiene

Review

Recent Advances in Synthesis and Application of Metal Oxide Nanostructures in Chemical Sensors and Biosensors

Vincentas Maciulis [1,2] , Almira Ramanaviciene [2,*] and Ieva Plikusiene [1,2,*]

1   State Research Institute Centre for Physical Sciences and Technology, Sauletekio Ave. 3,
    LT-10257 Vilnius, Lithuania
2   Nanotechnas–Center of Nanotechnology and Materials Science, Faculty of Chemistry and Geosciences,
    Vilnius University, Naugarduko Str. 24, LT-03225 Vilnius, Lithuania
*   Correspondence: almira.ramanaviciene@chf.vu.lt (A.R.); ieva.plikusiene@chgf.vu.lt (I.P.)

Abstract: Nanostructured materials formed from metal oxides offer a number of advantages, such as large surface area, improved mechanical and other physical properties, as well as adjustable electronic properties that are important in the development and application of chemical sensors and biosensor design. Nanostructures are classified using the dimensions of the nanostructure itself and their components. In this review, various types of nanostructures classified as 0D, 1D, 2D, and 3D that were successfully applied in chemical sensors and biosensors, and formed from metal oxides using different synthesis methods, are discussed. In particular, significant attention is paid to detailed analysis and future prospects of the synthesis methods of metal oxide nanostructures and their integration in chemical sensors and biosensor design.

Keywords: nanostructures; biosensors; chemosensors; metal oxides

1. Introduction

Nanostructured materials offer a number of advantages, such as large surface area, improved mechanical and other physical properties, as well as adjustable electronic properties that are important in the development of various sensors [1–8]. Properties of nanostructures differ greatly when compared to bulk materials. New material properties appear at nanometer dimensions, and a greater amount of atoms are found on the surface of the nanoparticle compared to higher volume particles. Therefore, the size is inversely proportional to the surface area and its surface-to-volume ratio [9]. Nanostructures are classified using the dimensions of the nanostructure itself and their components. Nanostructure classes were built using the comprising elementary units, namely, 0D nanoclusters and nanoparticles, 1D nanotubes and nanowires, and 2D nanoplates and nanolayers [10]. Nanostructures where the particles are smaller than 100 nm in all relevant directions can be referred to as '0D nanostructures'. These nanostructures include nanoclusters, nanospheres and fluorescent semiconductor nanocrystals—quantum dots [11–13]. For example, ZnO nanospheres can be prepared from zinc acetate in an alcoholic solution under basic conditions; however, the shape of the particles is very sensitive to the concentration of precursor materials [14]. Therefore, to allow some nanoparticle size control and protection from aggregation, 0D nanostructures must be synthesized from micelles or within hard templates. One avenue for the formation of 0D nanostructures is the use of soft templates, surfactants, or polymers of well-defined structure, dendrimers. Alternatively, surface masking or patterning can also be used, applying different lithographic approaches [15]. One-dimensional nanostructures are structures that have lateral dimensions greater than 100 nm, which can be formed using different metals and metal oxides and obtain desirable morphology, such as nanowires, nanorods, nanotubes, nanobelts, and nanoribbons [16–19]. Because of their unique properties and potential in application for many fields such as batteries, solar cells, gas sensors and biosensing, these materials are being studied in great detail [20–22]. Various

synthesis approaches are available for the formation of 1D nanostructures, electrospinning, electrochemical deposition/anodization, chemical/physical vapor deposition, and chemical bath deposition [23]. Two-dimensional nanostructures are two-dimensional structures, such as nanofilms, nanocoatings, nanolayers, and nanowalls. All of these structures have a large surface-to-volume ratio and confined thickness, which is highly desirable in applications such as catalysis, photovoltaics, and sensing [24–27]. Example methods to synthesize 2D materials include: liquid exfoliation, chemical vapor deposition (CVD), and atomic layer deposition (ALD) [28]. The nanostructures named '3D nanostructures' are made of lower dimensional structures (0D, 1D, 2D); thus, the 3D nanostructures have the most varied morphology out of all classes of nanostructures, and the morphology includes structures containing rods, cubes, spheres, etc. [29–31]. Although 3D nanostructures are not bound to the nanoscale, just as bulk materials, they still have the effect of being made of nanostructures (quantum confinement effect, high surface-to-volume ratio) [32]. Chemical synthesis is the most straightforward way of forming 3D nanostructures applying methods of CVD, vapor liquid solid (VLS), electrode-position, and electrochemical etching [33–37]. Nanostructures of a wide variety of materials are applied for sensing technologies due to increased surface area and tuneable properties for sensor signal enhancement.

Hence, the present review deals with various types of metal oxide nanostructured synthesis methods. In particular, the review presents detailed analysis and future prospects on the synthesis methods of 0D, 1D, 2D, and 3D nanostructures and their integration in sensors and biosensor design.

2. Nanostructure Synthesis Methods

In this review, we present selected synthesis methods most commonly used to form metal oxide nanostructures applied for chemical sensing and biosensing. In the last decade, a large number of publications were dedicated to the presented synthesis methods and for the development of desirable properties from 0D to 3D metal oxide nanostructures. Metal oxide nanostructures can be made as a result of a simple precipitation chemical reaction. These syntheses can be referred to as 'wet chemical' methods. However, it can be difficult to achieve precise dimensions and novel morphology of nanostructures using wet chemical methods alone. Therefore, the application of templates, external energy (thermal or electrical), and pressure can lead to more control and more variation in the morphology of the formed metal oxide nanostructures. The presented methods are suitable for the fabrication of metal oxide nanostructures of different sizes and morphologies, which can be used for various target analytes in the development of sensors.

2.1. Reverse Microemulsion Method for the Synthesis of Nanostructures

Synthesis in reverse microemulsions is an avenue for the formation of 0D nanostructures. Microemulsion is an isotropic and thermodynamically stable system of two non-miscible liquids and a surfactant [38]. Depending on the polar/nonpolar fluid ratio, surfactants can be thermodynamically driven to self-assembly generating micelles (in polar surroundings) or reverse micelles (in non-polar surroundings). Usually, 0D nanostructure synthesis is undertaken in reverse micelles, sometimes described as 'nanoreactors' [39,40]. This allows the polar and ionic compounds to be separated into isolation from nonpolar surroundings, inside the hydrophilic centers of the reverse micelles. Micelles can, and frequently do, interact with each other, colliding, breaking apart, and exchanging trapped compounds; this is what drives nucleation and growth [41]. The methods for nanostructure synthesis are presented in Figure 1.
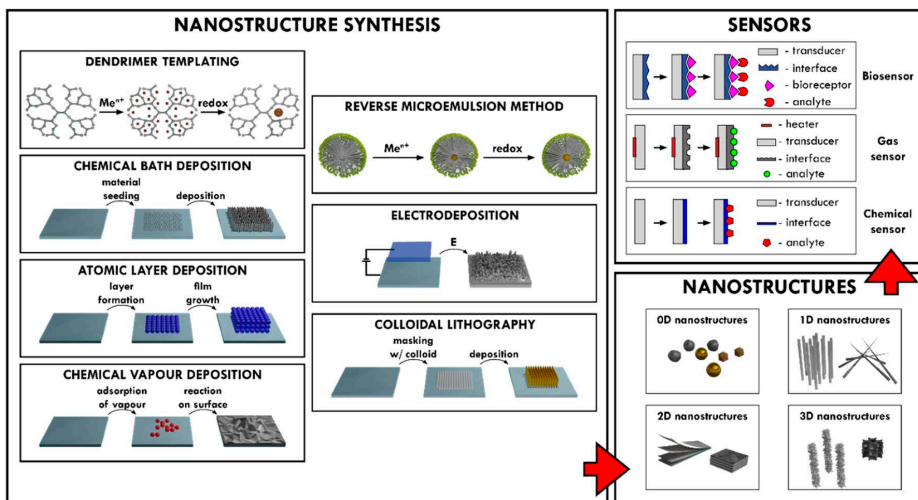
Figure 1. Synthesis methods of various nanostructures and their application in different sensors design.

In a work by Du et al., 2012, NiO nanoparticles were synthesized in reverse micelles by reducing $NiCl_2$ with aqueous NH_3 and calcinated in a furnace. Microemulsion consisted of oil (cyclohexane)/surfactant (Triton X-100)/cosurfactant (n-hexanol)/water ($NiCl_2$ + NH_3). By varying the proportions of microemulsion constituent parts, mixing method and calcination temperature, the particle size of NiO was controlled from 11.5 to 31.5 nm. The smallest NiO nanoparticles were synthesized in 44% cyclohexane: 33% Triton X-100: 16% n-hexanol: 7% water solution (inorganic precursors), mixing the microemulsions in a dropwise manner, calcinating in 450 °C for 2 h. Controlling particle size is crucial for sensing application, as lowering the diameter of the NiO particles increased the sensitivity to H_2S gas when measured at 150 °C [42]. However, not all syntheses methods require mixing two separate microemulsions to form nanoparticles. Liang et al., 2017, synthesized ultrafine α-Fe_2O_3 nanoparticles using the microemulsion method. The solution consisted of $Fe(NO_3)_3$, NaCl, deionised water, CTAB, benzene, and was stirred at 70 °C for 6 h. The temperature was then increased to 90 °C for azeotrope distillation to remove the water. The dried sample was calcinated for 5 h at 500 °C. The resultant particles have a narrow distribution, spanning from 2.3 to 3.9 nm [43]. Ali et al., 2019, produced well defined V-doped ZnO nanoparticles by microemulsion, with a tunable band gap based on incorporated vanadium amount [44].

2.2. Dendrimer Templating for Nanostructure Formation

Dendrimers are monodisperse macromolecular structures with extending branches from the center, highly symmetrical and exhibit 3D or 0D morphology, which is essential for not only the formation but the stabilization of 0D nanostructures [45,46]. Generally, for metal nanocluster synthesis, metal ions are incorporated inside the dendrimer structure by coordinative interaction with functional groups of dendrimer interior. Then, trapped ions are chemically reduced to form nanoclusters with a defined number of atoms. The number of atoms in a cluster can be controlled by changing the encapsulating dendrimer [47].

Dendrimers are used not only for 0D metal oxide nanostructure synthesis but also as stabilizers. In the study by Nakanishi and Imae, 2005, TiO_2 nanoparticles were formed by hydrolysis of $TiCl_4$ in water with and without dendrimers. Liquid $TiCl_4$ (-20 °C) was added to a solution at pH 10 in the presence and absence of G4.5-COONa dendrimer under stirring and maintained 0 °C. TiO_2 nanoparticles were evaluated and their diame-

ters compared. The TiO$_2$ nanoparticles synthesized without the use of dendrimers were larger and dependent on the pH of the solution, while the average size of the particles formed inside the dendrimers was smaller (7.5 nm for non-dendrimers and 4.4 to 6.7 nm for dendrimer-protected) and the particle size depended on the dendrimer terminal groups. Additionally, suspensions of dendrimer-protected nanoparticles were stable over several months, as the dendrimer coating prevents TiO$_2$ NPs from aggregating [48]. A comparative study was conducted by Vijayalakshmi et al., 2020, on stabilizing agents of polyvinylpyrrolidone (PVP), glycodendrimer, and chalcone dendrimer for Ag@SnO$_2$ nanoparticle synthesis. Ag core-SnO$_2$ shell nanoparticles were synthesized by the redox-transmetalation method, using stabilizing agents that result in nanoparticles of 30–40 nm diameter with similar structural parameters and indirect band gap energy of 3.84–4.0 eV. Photoluminescence studies identified that Ag@SnO$_2$ nanoparticles emitted photons in UV. The antibacterial and antifungal properties were tested with mixed results [49]. Dendrimer templating can also be used as a part in multi-step synthesis. The following development of microporous SiO$_2$ nanoparticles was published by Rosenberg et al., 2019: microporous SiO$_2$ nanoparticles were synthesized by silanization in the reverse microemulsion of Zn^{2+}- and Cu^{2+}-loaded dendrimers. A scheme for total synthesis is depicted in Figure 2. The composition of the reverse microemulsion system, in addition to varying the dendrimer generation, allowed for the control of microporous SiO$_2$ nanoparticle generation with a particle size of 20–50 nm and a micropore size of 2–15 nm. Dendrimers loaded with Cu^{2+} produced larger micropores than Zn^{2+}, while empty dendrimers did not provide micropore formation.
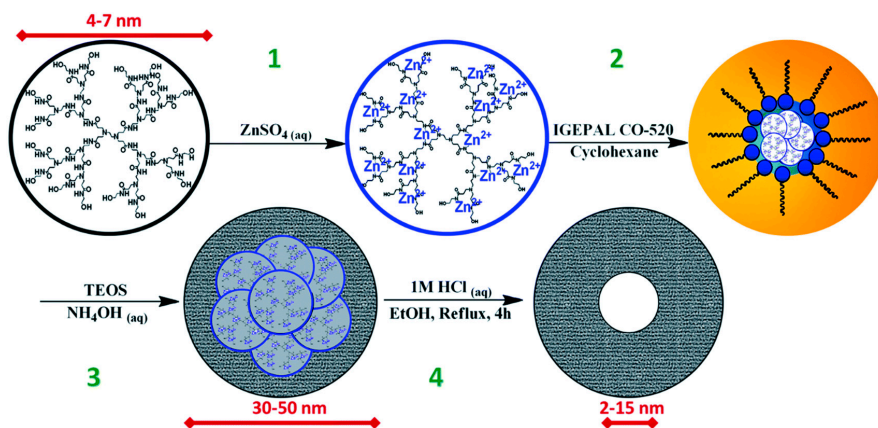

Figure 2. Scheme for total synthesis of dendrimer encapsulated mesoporous silica NPs. Step (1) inoculation of dendrimer with metal ions, (2) formation of reverse microemulsion with disperse phase (blue) and continuous phase (orange), (3) base catalyzed silica formation, and (4) acid catalyzed etching of metal encapsulated dendrimers. Adapted from [45].

2.3. Chemical Bath Deposition (CBD) for Nanostructure Synthesis

CBD can be considered to be the simplest method for depositing films of semiconductors or metal oxides. The procedure is generally performed from aqueous solutions where the material is generated and deposited on the substrate in the same bath. The method requires minimal substrate preparation and can be used to deposit films on any substrate as long as it is chemically stable while in deposition solution. Glass is a common choice when transparency is necessary [50]. Plastics can also be used as a substrates; however, their adhesive properties to deposited material can vary, meaning surface treatment before deposition may be required [51,52]. Monolayers (for example, silanes) with specific functional groups can be used to coat the substrate and direct the deposition toward (with hydrophilic groups) or away from (with hydrophobic groups) specific areas in an attempt to create patterned surface depositions [53–55]. ZnO nanostructures, named microflowers

(MFs), have been formed by a chemical bath deposition method by Strano et al. The formed nanostructures are presented in Figure 3 [56].
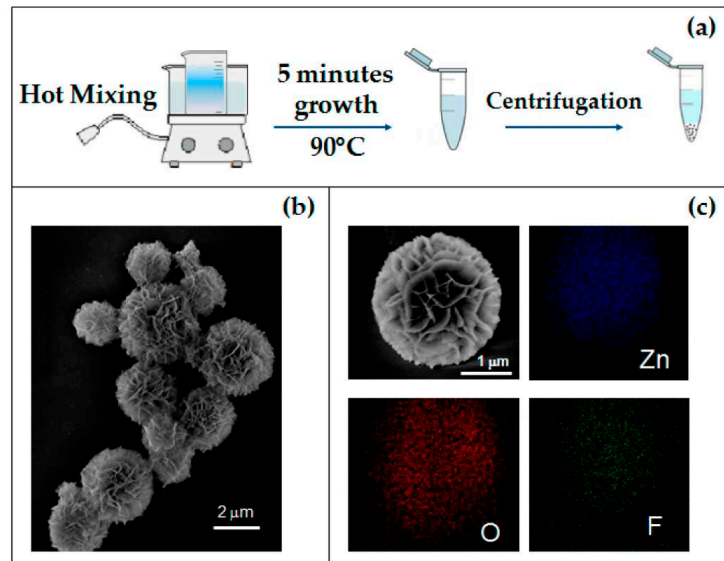

Figure 3. (**a**) Schematic synthesis diagram of the 3D flower-like hierarchical ZnO microstructures; (**b**) SEM image of as-grown MFs; (**c**) SEM image of a single MF and corresponding EDX elemental maps. Adapted from [56].

CBD can be utilized to form films on substrates of any shape. In the work by Chua et al., 2021, MoO_3 nanorods were deposited on tapered optical fiber for room temperature ammonia sensors. The deposition was carried out in an aqueous solution mixture of 0.1 M Na_2MoO_4 and 0.65 M HNO_3 solution at 85 °C, in a two-step synthesis. First, the optical fibers were immersed in synthesis solution for 20 min to form MoO_3 nucleates, rinsed with deionized water and placed back in synthesis solution for 10 min to grow MoO_3 nanorods. Optic fiber with MoO_3 deposition was then annealed. Few annealing temperatures were chosen, with 150 °C having the best results for optical ammonia sensor [57]. Nanostructures of ZnO are widely deposited using the chemical bath deposition method. In this work by Vessalli et al., 2017, ZnO nanorods (ZnO NRs) were grown with graphene oxide (GO) to form a composite material. The ZnO NRs were deposited in $Zn(NO_3)_2$ HMTA solution: (1) on ZnO seed layer, (2) on GO layer, and (3) with added GO in solution. This resulted in three different sensors to volatile organic compounds (VOCs) of varied selectivity. This change in selectivity is explained by the sensor's change in resistance when GO is deposited under ZnO NRs. When the sensor was modified with GO deposition under and on ZnO NRs, better sensor selectivity was achieved [58]. Husham et al., 2017, introduced a synthesis of ZnO NRs from $Zn(NO_3)_2$ and HMTA solution using microwave-assisted CBD to form a metal-semiconductor-metal-based UV sensor. The ZnO seeding layer was deposited by RF sputtering on clean Si substrate and annealed at 400 °C for 1 h. ZnO NRs were grown in $Zn(NO_3)_2$, HMTA solution at 90 °C for 2 h, heated by microwave heating. Aluminum and palladium contacts were deposited to utilize ZnO NRs for UV sensing. Grown ZnO NRs show vertical alignment and low defect density. A device based on ZnO NRs show remarkable potential for low-/self-powered sensor [59]. Gas sensing properties of CBD-formed ZnO nanostructures are also studied widely [60–62].

2.4. Electrodeposition for the Formation of Nanostructures

As a deposition method, electrodeposition has many advantages compared to other methods, such as catalyst-free process, a short deposition time, a low deposition temperature and the ability to make homogeneous large-area depositions [63,64]. The flexibility of the electrodeposition method for the formation of ZnO nanostructures was fully shown in a study by Chen et al., 2013. The ZnO nanostructure deposition from the $Zn(NO_3)_2$ electrolyte with KCl was analyzed by looking at the effects of $Zn(NO_3)_2$, KCl concentrations, deposition temperature and deposition voltage. An increase in KCl supporting electrolyte concentration from 0 to 1 M created ZnO depositions of varied structures from microspheres (0.03 M KCl) to nanosheets (0.1–1 M KCl). Running an electrodeposition with high KCl concentrations also forms zinc hydroxyl compounds alongside ZnO, with the decomposition of the former in high temperatures potentially leading to the formation of porous ZnO nanosheets. An increase in the concentration from 0.005 to 0.5 M creates ZnO depositions from nanospikes (0.005–0.02 M) to nanosheets (0.1–0.5 M). Deposition temperature also has an effect on electrodeposited nanostructures, with deposited structures changing from nanowires to nanosheets with increasing temperature. Increasing the deposition potential seems to increase the density of nanostructures; it also promotes the formation of zinc hydroxyl compounds along with ZnO [65]. Mollarasouli et al., 2020, used the two-step electrodeposition method to form $NiWO_4$ nanostructures for non-enzymatic glucose sensor. The first step was the deposition of Ni-W metal alloy under –1.4 V for 60 s using 0.67 mM $NiSO_4$, 0.3 mM Na_3WO_4, 0.26 mM citric acid, and 31 mM Na_2SO_3. The pH was adjusted to 8.0, for the citrate to form complex with Ni and W. The second step involved formation of $NiWO_4$ from deposited Ni-W alloy by cyclic voltammetry in 1 M NaOH for 15 cycles at 50 mV s^{-1}. CV treatment under basic conditions with low scan rate is required for the diffusion of OH$^-$ anions to the Ni-W alloy [66]. Patella et al., 2022, developed an immunosensor based on ZnO NRs fabricated by electrodeposition. Indium tin oxide on polyethylene terephthalate (ITO-PET) was used as a flexible substrate and ZnO NRs were deposited with optimized conditions of -0.95 V vs. Ag/AgCl, for 60 min in 10 mM $ZnCl_2$ and 10 mM $NaNO_3$ at pH 4.5, resulting in hexagonal ZnO NRs with 800 nm mean length. The schematic representation of ZnO nanorods formed using the electrodeposition method and application in sandwich format immunosensor designed for human immunoglobulin G detection is presented in Figure 4 [67].
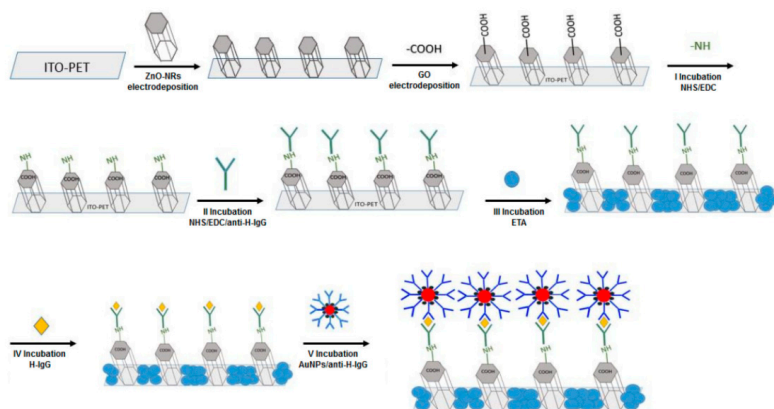

Figure 4. Scheme of the fabrication of immunosensor with a sandwich configuration based on ZnO nanorods. Adapted from [67].

2.5. Chemical Vapor Deposition (CVD) for Synthesis of Nanostructures

It is a well-known and widely applied technique for solid phase material formation [68–71]. Unlike physical vapor deposition, which requires sputtering or evaporation, CVD is a method in which the precursor material is thermally decomposed or chemically reacts on

the substrate and is allowed to grow, producing a thin film. The growth of thin films is regulated by temperature, concentration of reactants, and pressure [72]. There are modified CVD procedures, for example: plasma-enhanced chemical vapor deposition (PECVD), where plasma is created of the reacting gases and deposition occurs, low-pressure chemical vapor deposition (LPCVD) and atmospheric pressure chemical vapor deposition (APCVD) [73–75]. Deposition using CVD on substrates with 3D morphology has been tested and offered promising applications. A process for metal-organic-framework growth on carbon cloth was tested. ZnO and cobalt carbonate hydroxide ($Co(CO_3)0.5(OH)\cdot0.11H_2O$) were deposited on carbon cloth. Using CVD, the ZnO layer was converted into ZnO@ZIF-8 using 2-methylimidazole (2-Melm) vapor at 100 °C, while ($Co(CO_3)_{0.5}(OH)\cdot0.11H_2O$) was converted into $Co(CO_3)_{0.5}(OH)\cdot0.11H_2O$@ZIF-67. Subsequent heat treatment for the $Co(CO3)_{0.5}(OH) < 0.11H_2O$ sample resulted in the formation of CoO_3 and nanoporous carbon (CoO_3/NC), creating an electrode exhibiting excellent electrochemical performance (Figure 5).
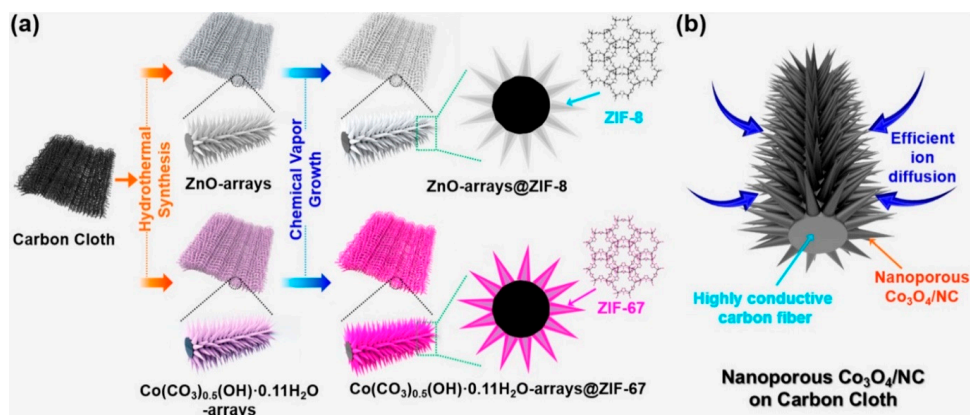

Figure 5. Scheme showing the synthetic process to generate (**a**) ZnO@ZIF-8-x-y and $Co(CO_3)_{0.5}(OH)\cdot$ $0.11H_2O$@ZIF-67-x-y using 2-Melm vapor, where x and y are the synthesis temperature and synthesis time, respectively. (**b**) Advantages of Co_3O_4/NC hybrid materials. Adapted from [34], 2018, American Chemical Society.

In a work by Barreca et al., 2010, 1D ZnO nanostructures of high aspect ratio were grown on alumina substrates at 300 °C by PECVD for the application of CO, H_2 and CH_4 gas sensors. CVD precursors were obtained by reaction of diethyl zinc with neutral ketoiminate in hexane. For CO and CH_4, best sensing temperature was 200 and 300 °C, respectively. For H_2 gases, the sensing ability increased with increasing temperature, with the best response to H_2 gases at a maximum measured temperature of 400 °C [76]. Zhang et al., 2012, produced a gas sensor for NO_2, CH_4 and CO based on 1D SnO_2 nanobelts formed from high-purity Sn powder modified with gold (Au). SnO_2 nanobelts were formed using the water-assisted CVD method at 850 and 1000 °C. Au modification plays a crucial role in the formation of the SnO_2 nanobelts as a structure directing agent [77]. A modification of quartz crystal microbalance (QCM) sensor was published by Wu et al., 2020, Mg-ZnO nanostructures were directly grown by MOCVD at 500 °C using diethyl zinc, bis-methyl-cyclopentadienyl magnesium, and oxygen, resulting in uniform NRs of 405 nm in average height. Formation of 1D nanostructures greatly increased the surface area of the sensor, and Mg inclusion to the nanostructure stabilizes the ZnO denying the release of toxic Zn^{2+} ions, thus minimizing the toxicity to microorganisms [78]. A gas sensor for ethanol and acetone was formed on fluorine-doped and undoped Co_3O_4 nanodeposits grown on alumina substrates by Barreca et al., 2011. Two precursors enabled the synthesis using PECVD of fluorine-doped and undoped Co_3O_4. This resulted in a favorable influence of fluorine on

the Co_3O_4 system. The introduction of fluorine into deposition created a more responsive gas sensor and lowered its working temperature, both features are highly regarded in technological application [79].

2.6. Atomic Layer Deposition (ALD) Method for the Formation of Nanostructures

ALD is a subclass of CVD in which the process is self-limiting and requires the separation of precursor materials and the introduction to the substrate in sequence [80]. Deposition happens in cycles with a given amount of material deposited per cycle, from less than 0.2 to 12 nm per cycle [81]. ALD can be applied to form thin 2D metal oxide nanostructures that usually are amorphous due to low deposition temperatures, and require post deposition treatment or deposition at a higher temperatures [82]. ALD can be applied for deposition on more complex substrates (2D, 3D nanostructures) and on variety of materials: metals, glasses, oxides, graphene, and polymers [83–88]. Water-soluble polymers can be coated with ALD and used as sacrificial layers to form free-floating 2D structures [89]. ALD is considered to be the main method of choice for conformal deposition of thin film/monolayer metal oxide, sulphide, and nitride formation on complex nanostructures, despite the wasteful usage of energy and reagents [80,90].

As mentioned above, ALD-based nanostructures and nanolayer depositions can be used on complex nanostructures for the uniform deposition of functional material. Recently, ZnO nanostructure application in biosensor design became a hot topic. ZnO has high isoelectric point and this feature makes it a good candidate for biosensor applications. Moreover, it can be mass produced due to its cost-effectiveness, it is nontoxic, it is chemically stable and different nanostructures can be formed. The different dimensions of the ZnO nanostructures with their advantages are presented in Figure 6 [27].
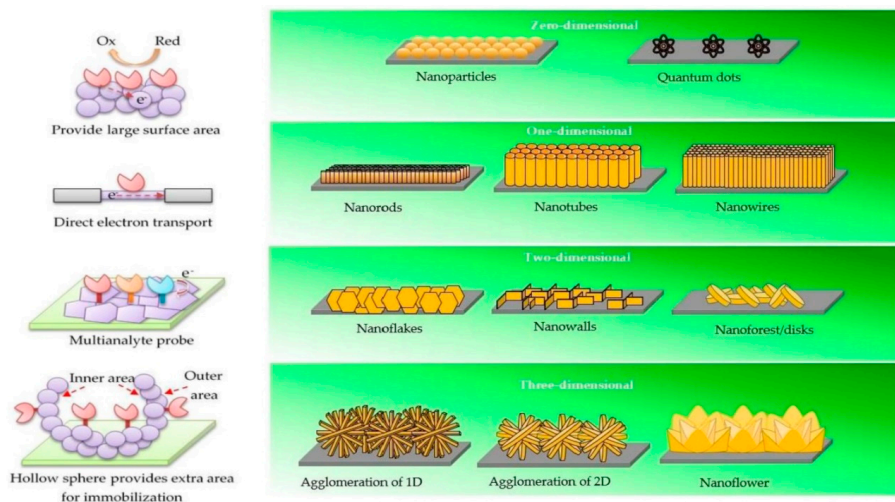

Figure 6. Four different dimensions of ZnO nanostructures with their advantages. Zero-dimensional nanostructures provide a large surface area. One-dimensional nanostructures possess stable and direct electron transport. Two-dimensional nanostructures give specific planes for immobilization process for the simultaneous detection of different analytes. Three-dimensional nanostructures have extra surface area (outer and inner area) to provide more sites for immobilization. Adopted from [27].

Chaaya et al., 2014, proposed the deposition of ZnO thin films by ALD on electrospun poly(acrylonitrile) (PAN) fibers, to enhance the UV detection capabilities. Diethyl zinc (DEZ) and H_2O were used as precursors for the deposition of ZnO ALD. The effects on the sensitivity of the UV sensor of the deposition cycle number, temperature, and electrospinning increased the photoresponsive current of UV by a factor of 250 compared to a flat electrode. This in-

crease in sensitivity comes from an increase in surface area, with smaller grain sizes having a more positive UV photoresponse [16]. The ALD technique has advantages in comparison to other chemical deposition methods, namely, the deposited material is conformal, pinhole-free, has good adhesion to the substrate and is suitable for periodic nanostructures, such as nanolaminates, and periodic coating of multiple materials of thickness in the nanoscale formations [16,91–94]. In the article by Balevicius et al., 2018, Al_2O_3/ZnO nanolaminates were formed by ALD and tested for optical biosensor application using total internal reflection ellipsometry (TIRE). Nanolaminates were formed on glass substrates from DEZ and H_2O for ZnO and trimethylaluminium (TMA) and H_2O for Al_2O_3, and deposition was performed at fixed 100 °C. The samples had a total thickness of 200 nm, consisting of (i) four alternating Al_2O_3 and ZnO layers of 50 nm thickness and (ii) two Al_2O_3 and ZnO layers of 100 nm thickness. When comparing the two nanolaminate structures, a higher sensitivity was achieved using 50 nm layers of Al_2O_3 and ZnO. This increased sensitivity was explained by multiple reflections from the layer boundaries [1].

Lou et al., 2021, proposed the use of ALD for the formation and application of formaldehyde detection. Hydrothermally synthesized powdered SnO_2 nanospheres were coated with ZnO using ALD at 180 °C using DEZ and H_2O, and they were annealed at 400 °C for 2 h. SnO_2/ZnO heterojunction formation using ALD created a superior nanosphere gas sensor compared to SnO_2 nanospheres, the optimal working temperature was lowered by 40 °C and reached 200 °C, and sensor response was increased by a factor of 7 [95].

3. Application of Metal Oxide Nanostructures for Chemical Sensing and Biosensing

In 1962, Clark and Lyons presented the idea of the biosensor and suggested that enzymes may be immobilized on electrical detectors to create enzyme electrodes. Using glucose oxidase (GOx), the first enzyme electrode was developed to track blood glucose levels [96]. A biosensor is an analytical system consisting of a biological sensing component connected to a transducer that transforms biochemical reactions into an electrical or optical signal that is proportional to the concentration of the targeted analyte.

Biosensor technology has received interest in the last decade and has been applied in many areas: food, environment, and healthcare [97,98]. Biosensors have a very broad definition; they can be classified by bioreceptor type (enzyme, antibody, DNA, cells, biomimetic) and by signal transduction (optical, calorimetric, piezoelectric, electrochemical) [99]. There is plenty of application for nanostructures to be utilized in signal transducing as signal enhancers. The nanostructure formation methods and application in biosensor design are summarized in Table 1.

Faria and Mazon, 2019, fabricated electrochemical immunosensors based on ZnO nanowires (NWs) to diagnose early-stage Zika virus infection from patient urine. ZnO NWs were deposited using the CBD method on a graphene-modified Au printed circuit board. Such modification has potential in lowering the limit of detection (LOD) by increasing the surface area of the electrode, as well as providing a surface with high chemical stability, thus having a suitable surface for antibody immobilization. Monoclonal Zika virus antibodies (ZIKV-NS1) were immobilized on the ZnO NW using cystamine (Cys) and glutaraldehyde (GA), and a diluted solution of antibodies was dropped on the surface and left to incubate for 12 h. Calibration of the sensor was performed, achieving good linearity in the 0.1–100 ng/mL range of ZIKV-NS1 and a low LOD of 1 pg/mL, showing potential in application as a rapid point-of-care test [100].

Table 1. Nanostructure formation methods, detected analyte and reported biosensing properties.

Nanostructure	Method of Synthesis	Application	Reported Sensing Properties	Ref.
ZnO nanostructures	Chemical bath deposition	Electrochemical immunosensor for ZIKV-NS1 antigen	LOD: 1.00 pg/mL LDR: 0.1–100 ng/mL	[100]
MoS_2/Cu_2O	Chemical vapour deposition, electrodeposition	GSH, GSSG biosensor for indirect cancer cell detection	LDR: 0–50,000 cells	[101]
$Au(Fe_3O_4)$ MNPs	Co-precipitation, wet chemical	Colorimetric hGH sensor	LOD: 0.082 nM LDR: 0.1–5.0 nM	[102]
$Au(Fe_3O_4)$ MNPs	Co-precipitation, wet chemical	SPR CD5 immunosensor	LOD: 8.31 fM	[103]
ZnO NRs-rGO	Electrodeposition	Electrochemical IgG detection	LOD: 1.25 ng/mL LDR: 10–1000 ng/mL	[67]
ZnO NWLs	Electrodeposition	Electrochemical enzymatic H_2O_2 sensor for cancer cell detection	LOD: 0.8 μM LDR: 1–1000 μM	[104]
$Au/(TiO_2/SiO_2)$ Photonic crystal	Ion beam sputtering	TIRE signal enhancement	6.4 times more sensitive than SPR	[105]
$Au/(TiO_2/SiO_2)/Au$	Ion beam sputtering	SE/QCM-D signal enhancement	23 and 49 times increased SE signal	[106]
$Ag/ZnO-NRs/Au$	Thermal evaporation; hydrothermal; sputtering	SERS sensing platform	LOD (λ-DNA): 10 ng/μL LOD (Rh6G): 10^{-16} M	[107]
Au/PAA	Two-step anodization; thermal evaporation	Interferometric aptamer based bacterial cell sensor	LOD: 20 CFU/mL LDR: 10^3–10^9 CFU/mL	[108]

Abbreviations: ZIKV-NS1—Zika virus NS1 antigen, LOD—limit of detection, LDR—linear dynamic range, GSH—glutathione, GSSG—glutathione disulphide, MNP—magnetic nanoparticle, hGH—human growth hormone, SPR—surface plasmon resonance, CD5—lymphocyte antigen T1, NRs—nanorods, rGO—reduced graphene, IgG—Immunoglobulin G, NWLs—nanowalls, TIRE—total internal reflection ellipsometry, SE—spectroscopic ellipsometry, QCM-D—quartz crystal microbalance with dissipation, SERS—surface enhanced Raman spectroscopy, Rh6G—Rhodamine—6 G, PAA—porous anodic alumina, CFU—colony forming unit.

In the work by Buzavaite-Verteliene et al., 2020, the TIRE method was used for the study of the excitation and sensitivity properties of the hybrid Tamm plasmon polariton-surface plasmon polariton (TPP-SPP) and single surface plasmon resonance (SPR) modes of immobilization of bovine serum albumin (BSA) and the granulocyte colony stimulating factor receptor (GCSF-R) on the surface. The plasmonic photonic nanostructure was formed from high (TiO_2) and low (SiO_2) refractive index bilayers covered by a thin (40 nm) Au layer. The SPP component ($\delta\Delta_{h-SPP}/\delta\lambda = 53.9°/nm$) of the hybrid TPP-SPP mode showed 6.4 times higher sensitivity than the single SPR ($\delta\Delta_{SPR}/\delta\lambda = 8.4°/nm$) during the formation of the bovine serum albumin (BSA) layer on the Au film. The sensitivity using the hybrid plasmonic mode was found to be controlled by using the strong coupling effect between the components of TPP and SPP. Two optical sensor geometries are presented in Figure 7 [105].
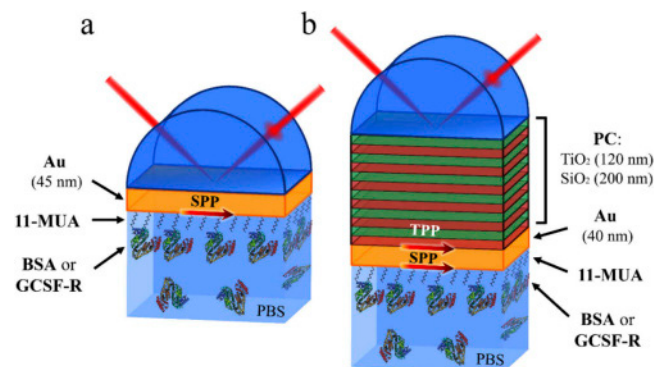

Figure 7. Total internal reflection geometry schematic of the Au (a) and PC/Au (b) samples with a self-assembled monolayer of 11-mercaptoundecanoic acid (11-MUA) and the GCSF-R or BSA protein in phosphate-buffered saline solution. Adopted from [105].

In the work by Plikusiene et al., 2021, the formation of 1D plasmonic photonic structures from TiO_2 and SiO_2 nanolayers on the commercially available quartz crystal microbalance with dissipation (QCM-D) sensors chip was reported. This thin Au film is able to generate Tamm plasmon polaritons and cavity modes that can enhance the optical signal of spectroscopic ellipsometry (SE) without using a coupler, as is usually necessary for the excitation of surface waves applied for biosensing [109–112]. The scanning electron microscope (SEM) micrograph of the nanostructures used for Tamm plasmons and cavity mode (CM) excitation, formed on the QCM-D sensor disc, is presented in Figure 8.
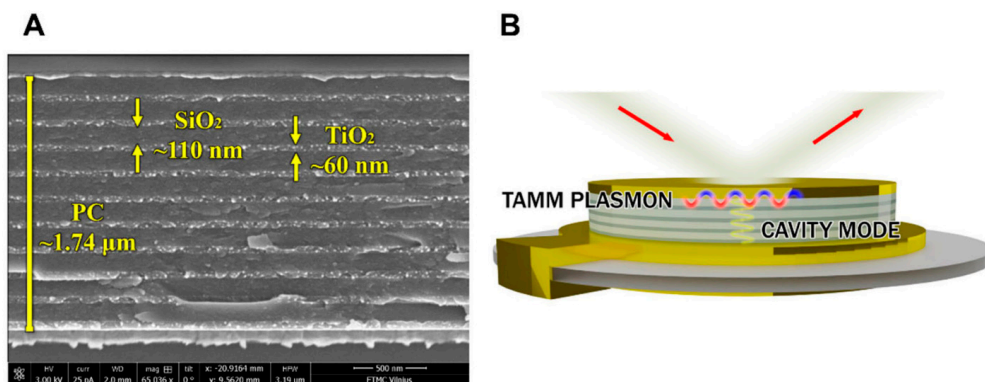

Figure 8. SEM micrograph of the plasmonic photonic structure modified QCM-D sensor chip (**A**) and Tamm plasmons and cavity mode excitation using nanometer structures of formed photonic crystal (**B**). Adopted from [106].

The Tamm plasmon optical state and CM for the modified QCM-D sensor disc showed sensitivity of ellipsometric parameters to refractive index unit (RIU) as follows: $\Psi_{TPP} = 126.78\ RIU^{-1}$ and $\Delta_{TPP} = 325\ RIU^{-1}$, and $\Psi_{CM} = 264\ RIU^{-1}$ and $\Delta_{CM} = 645\ RIU^{-1}$, respectively. This study shows that Tamm plasmon and CM have 23 and 49 times better performance of ellipsometric parameters, respectively, for refractive index sensing than standard SE signal on a QCM-D sensor chip [106].

A chemical sensor is a system that produces a useful signal as a result of a chemical interaction, both qualitative and quantitative. This system contains a transducer domain and a chemical interface layer. At a chemical interface, an analyte chemically reacts with a surface and creates a change in chemical or physical properties; this change is then measured by the transducer and generates an electrical signal proportional to the analyte concentration. Chemical sensors are classified by their transduction method (optical (refractometric, ellipsometric), electrical (conductometry, amperometry), and mechanical (QCM-D)) as well as their structure/composition of the chemical interface layer (metal, metal oxide, and metal semiconductor) [113]. The summary on nanostructures used for chemical sensing is presented in Table 2.

Table 2. Nanostructure formation methods, detected analyte, and reported chemical sensing properties.

Nanostructure	Method of Synthesis	Application	Reported Sensing Properties	Ref.
Ni(OH)$_2$ HRs	Chemical bath deposition	Electrochemical glucose sensor	LOD: 0.6 µM LDR: 0.002–3.8 mM	[114]
ZnO NSs	Chemical bath deposition	Electrochemical aqueous formaldehyde sensor	LOD: 210 nM	[115]
ZnO NRs	Hydrothermal	Fluorescence thiabendazole sensor	LOD: 304 nM LDR: 10–80 µM	[116]
SiO$_2$/GSCDs	Hydrothermal, reverse microemulsion	Fluorescence phenobarbital sensor	LOD: 0.1 nM LDR: 0.4–34.5 nM	[117]
Ag-TiO$_2$ NPs/MWCNTs	Hydrothermal, powder blending	Electrochemical cetirizine sensor	LOD: 8.76 nM LDR: 0.3–3 µM	[118]
TiO$_2$@SiO$_2$ NSs	Sol-gel	Electrochemical ascorbic acid sensor	LOD: 383.3 µM LDR: 50–2500 µM	[119]
Lucigenin doped SiO$_2$ NPs	Reverse microemulsion	Fibre optic Cl$^-$ sensor	LDR: 0.02–0.06 M	[120]
ZnO/NiO/Al$_2$O$_3$ NPs	Wet chemical	Electrochemical L-glutamic acid sensor	LOD: 95.35 pM LDR: 0.1 nM–0.01 mM	[121]
Ni-ZnO NPs	Wet chemical	Electrochemical hydrazine sensor	LOD: 1.7 pM LDR: 0.2 nM–0.02 M	[122]

Abbreviations: HRs—hollow rods, LOD—limit of detection, LDR—linear dynamic range, NS—nanosheets, GSCDs—green source carbon dots, NPs—nanoparticles, MWCNTs—multi-walled carbon nanotubes.

Rahman et al., 2020, published work on modifying a glassy carbon electrode (GCE) with nickel-doped ZnO (Ni-ZnO) nanostructures in Nafion solution to form an electro-chemical hydrazine sensor. A three-electrode system was used for electrochemical analysis, and Ag/AgCl, Ni-ZnO/Nafion/GCE, and Pt were used as reference, working, and counter electrodes, respectively. The Ni-ZnO/Nafion/GCE sensor for hydrazine detection was employed in the phosphate buffer system in room-temperature conditions. The sensor exhibited excellent sensitivity with a linear response from 0.2 nM to 0.02 M with an LOD of 1.7 pM. This sensitivity can be explained by the hydrazine detection mechanism. When the Ni-ZnO surface is exposed to hydrazine, surface-mediated hydrazine oxidation takes place, producing N$_2$H$_4$ decomposition and delivery of electrons onto Ni-ZnO; at the same time, OH$^-$ removal lowers the conduction band of Ni-ZnO, yielding a shift of the current during electrochemical investigation. This shift effect, along with an injection from hydrazine oxidation, produces an increased number of electrons, enhancing the conductance of the electrode. A real sample analysis of industrial effluent water and wastewater showed ~100% recovery of hydrazine from sample solutions, thus concluding its suitability to determine hydrazine in real aqueous samples [122].

In a study by Shetti et al., 2019, an electrochemical sensor was manufactured using Ag-doped TiO$_2$ nanoparticles (Ag-TiO$_2$ NPs) mixed with multi-walled carbon nanotubes (MWCNTs) for the detection of cetirizine, an anti-inflammatory drug. The electrochemical sensor is based on the modified carbon paste electrode, by blending MWCNTs and Ag-TiO$_2$ NPs together with graphite powder and homogenizing with paraffin oil. This results in a sensor that exhibits a higher peak current with a less positive potential for cetirizine oxida-tion than for an unmodified electrode; however, the oxidation of cetirizine was found to be irreversible. Both Ag-TiO$_2$ and MWCNT have a positive effect on enrichment in cetirizine oxidation, playing significant roles in the fast electron transfer process. This enables the sensor to detect cetirizine in very low amounts with LDR from 0.3 to 3 µM and an LOD of 8.76 nM [118].

4. Conclusions

Recently, progress and advances in the synthesis methods and application area of various metal oxide nanostructures illustrate the great relevance and necessity of such structures in the design of different types of sensors. The present review summarizes progress and advances in the synthesis methods of various 0D, 1D, 2D, and 3D metal oxide

nanostructures and their application in chemical sensors and biosensors for different target analytes' detection.

The 0D nanostructures, formed by microemulsion or co-precipitation/reduction methods, can be successfully applied in highly sensitive chemical sensors and biosensor design. Efficient synthesis of 0D nanostructures lies in the control of the nanoparticle formation process. However, these methods usually require expensive, complex or wasteful protocols; thus, more simple methods with less size control tend to be preferred. Simple, time-saving and convenient methods of synthesis, such as chemical bath deposition, can be used to form 1D metal oxide nanostructures. Biosensors in which such structures were applied exhibit enhanced sensitivity due to the high surface area, especially in hollow 1D nanostructures. The development of optical biosensors requires one to form nanostructures that can tune and enhance optical signal for the detection of target biological substances. In this case, 2D nanostructures or thin films that can be formed by the ALD method are frequently applied. Novel structures, a high surface-to-volume ratio, and the porosity of 3D nanostructures formed by the wet chemical method allowed to achieve an extremely low LOD and opened a new way of forming 3D nanostructures in electrochemistry-based chemical sensors and biosensors. Flower-like MoO_3/In_2O_3 microstructures formed by the hydrothermal method and composed of numerous nanosheets are promising for the development of gas sensors [123].

However, there is still room for improvement and challenges related to different synthesis methods. Improvements and more research are required to form nanostructures without side effects and with the desired properties for the development of sensitive, reproducible, easy to use, and fast biosensors with minimal pollution of the living nature. The achievement of high stability and nontoxicity in various nanostructures formed from metal oxides, such as ZnO, TiO_2 or SiO_2, which are applied in vivo biosensing and are exposed by different liquid ambient, is still an issue. Therefore, we expect significant experimental and theoretical research activity regarding the synthesis methods for metal oxide nanostructures of different properties and application for sensing.

Author Contributions: Conceptualization, V.M. and I.P.; methodology, V.M., I.P., and A.R.; writing—original draft preparation, V.M., I.P. and A.R.; writing—review and editing, V.M., I.P. and A.R.; visualization, V.M.; supervision, I.P. and A.R.; project administration, A.R.; funding acquisition, A.R. All authors have read and agreed to the published version of the manuscript.

Institutional Review Board Statement: Not applicable.

Informed Consent Statement: Not applicable.

Data Availability Statement: Not applicable.

References

1. Balevicius, Z.; Paulauskas, A.; Plikusiene, I.; Mikoliunaite, L.; Bechelany, M.; Popov, A.; Ramanavicius, A.; Ramanaviciene, A. Towards the application of Al_2O_3/ZnO nanolaminates in immunosensors: Total internal reflection spectroscopic ellipsometry based evaluation of BSA immobilization. *J. Mater. Chem. C* **2018**, *6*, 8778–8783. [CrossRef]
2. Maciulis, V.; Malinovskis, U.; Erts, D.; Ramanavicius, A.; Ramanaviciene, A.; Balevicius, S.; Juciute, S.; Plikusiene, I. Porous aluminium oxide coating for the development of spectroscopic ellipsometry based biosensor: Evaluation of human serum albumin adsorption. *Coatings* **2020**, *10*, 1018. [CrossRef]
3. Plikusiene, I.; Maciulis, V.; Graniel, O.; Bechelany, M.; Balevicius, S.; Vertelis, V.; Balevicius, Z.; Popov, A.; Ramanavicius, A.; Ramanaviciene, A. Total internal reflection ellipsometry for kinetics-based assessment of bovine serum albumin immobilization on ZnO nanowires. *J. Mater. Chem. C* **2021**, *9*, 1345–1352. [CrossRef]
4. Filipovic, L.; Selberherr, S. Application of Two-Dimensional Materials towards CMOS-Integrated Gas Sensors. *Nanomaterials* **2022**, *12*, 3651. [CrossRef] [PubMed]
5. Tyagi, D.; Wang, H.; Huang, W.; Hu, L.; Tang, Y.; Guo, Z.; Ouyang, Z.; Zhang, H. Recent advances in two-dimensional-material-based sensing technology toward health and environmental monitoring applications. *Nanoscale* **2020**, *12*, 3535–3559. [CrossRef]

6. Ponzoni, A.; Baratto, C.; Cattabiani, N.; Falasconi, M.; Galstyan, V.; Nunez-Carmona, E.; Rigoni, F.; Sberveglieri, V.; Zambotti, G.; Zappa, D. Metal oxide gas sensors, a survey of selectivity issues addressed at the SENSOR lab, Brescia (Italy). *Sensors* **2017**, *17*, 714. [CrossRef]

7. Zhao, Z.; Zhang, J.; Wang, W.; Sun, Y.; Li, P.; Hu, J.; Chen, L.; Gong, W. Synthesis and electrochemical properties of Co_3O_4-rGO/CNTs composites towards highly sensitive nitrite detection. *Appl. Surf. Sci.* **2019**, *485*, 274–282. [CrossRef]

8. Popov, A.; Lisyte, V.; Kausaite-Minkstimiene, A.; Bernotiene, E.; Ramanaviciene, A. Experimental Evaluation of Quantum Dots and Antibodies Conjugation by Surface Plasmon Resonance Spectroscopy. *Int. J. Mol. Sci.* **2022**, *23*, 12626. [CrossRef]

9. Oberdörster, G.; Oberdörster, E.; Oberdörster, J. Nanotoxicology: An emerging discipline evolving from studies of ultrafine particles. *Environ. Health Perspect.* **2005**, *113*, 823–839. [CrossRef]

10. Pokropivny, V.V.; Skorokhod, V.V. Classification of nanostructures by dimensionality and concept of surface forms engineering in nanomaterial science. *Mater. Sci. Eng. C* **2007**, *27*, 990–993. [CrossRef]

11. Cook, A.W.; Hayton, T.W. Case Studies in Nanocluster Synthesis and Characterization: Challenges and Opportunities. *Acc. Chem. Res.* **2018**, *51*, 2456–2464. [CrossRef]

12. Li, Z.; Wang, W.; Yin, Y. Colloidal Assembly and Active Tuning of Coupled Plasmonic Nanospheres. *Trends Chem.* **2020**, *2*, 593–608. [CrossRef]

13. García de Arquer, F.P.; Talapin, D.V.; Klimov, V.I.; Arakawa, Y.; Bayer, M.; Sargent, E.H. Semiconductor quantum dots: Technological progress and future challenges. *Science* **2021**, *373*, eaaz8541. [CrossRef]

14. Pacholski, C.; Kornowski, A.; Weller, H. Self-assembly of ZnO: From nanodots to nanorods. *Angew. Chem.—Int. Ed.* **2002**, *41*, 1188–1191. [CrossRef]

15. Xu, S.; Lei, Y. Template-Assisted Fabrication of Nanostructured Arrays for Sensing Applications. *Chempluschem* **2018**, *83*, 741–755. [CrossRef]

16. Chaaya, A.A.; Bechelany, M.; Balme, S.; Miele, P. ZnO 1D nanostructures designed by combining atomic layer deposition and electrospinning for UV sensor applications. *J. Mater. Chem. A* **2014**, *2*, 20650–20658. [CrossRef]

17. Wu, C.C.; Pan, T.M.; Wu, C.S.; Yen, L.C.; Chuang, C.K.; Pang, S.T.; Yang, Y.S.; Ko, F.H. Label-free detection of prostate specific antigen using a silicon nanobelt field-effect transistor. *Int. J. Electrochem. Sci.* **2012**, *7*, 4432–4442.

18. Ackermann, J.; Metternich, J.T.; Herbertz, S.; Kruss, S. Biosensing with Fluorescent Carbon Nanotubes. *Angew. Chem.—Int. Ed.* **2022**, *61*, e202112372. [CrossRef]

19. Aykaç, A.; Gergeroglu, H.; Beşli, B.; Akkaş, E.Ö.; Yavaş, A.; Güler, S.; Güneş, F.; Erol, M. An Overview on Recent Progress of Metal Oxide/Graphene/CNTs-Based Nanobiosensors. *Nanoscale Res. Lett.* **2021**, *16*, 65. [CrossRef]

20. Huo, D.; Kim, M.J.; Lyu, Z.; Shi, Y.; Wiley, B.J.; Xia, Y. One-Dimensional Metal Nanostructures: From Colloidal Syntheses to Applications. *Chem. Rev.* **2019**, *119*, 8972–9073. [CrossRef]

21. Javed, M.S.; Khan, A.J.; Asim, S.; Shah, S.S.A.; Najam, T.; Siyal, S.H.; Tahir, M.F.; Zhao, Z.; Mai, W. Insights to pseudocapacitive charge storage of binary metal-oxide nanobelts decorated activated carbon cloth for highly-flexible hybrid-supercapacitors. *J. Energy Storage* **2020**, *31*, 101602. [CrossRef]

22. Kwak, D.; Wang, M.; Koski, K.J.; Zhang, L.; Sokol, H.; Maric, R.; Lei, Y. Molybdenum Trioxide (α-MoO3) Nanoribbons for Ultrasensitive Ammonia (NH3) Gas Detection: Integrated Experimental and Density Functional Theory Simulation Studies. *ACS Appl. Mater. Interfaces* **2019**, *11*, 10697–10706. [CrossRef] [PubMed]

23. Samykano, M. Progress in one-dimensional nanostructures. *Mater. Charact.* **2021**, *179*, 111373. [CrossRef]

24. Heard, C.J.; Čejka, J.; Opanasenko, M.; Nachtigall, P.; Centi, G.; Perathoner, S. 2D Oxide Nanomaterials to Address the Energy Transition and Catalysis. *Adv. Mater.* **2019**, *31*, e1801712. [CrossRef] [PubMed]

25. Wang, L.; Huang, L.; Tan, W.C.; Feng, X.; Chen, L.; Huang, X.; Ang, K.W. 2D Photovoltaic Devices: Progress and Prospects. *Small Methods* **2018**, *2*, 1700294. [CrossRef]

26. Kumar, S.; Pavelyev, V.; Mishra, P.; Tripathi, N.; Sharma, P.; Calle, F. A review on 2D transition metal di-chalcogenides and metal oxide nanostructures based NO_2 gas sensors. *Mater. Sci. Semicond. Process.* **2020**, *107*, 104865. [CrossRef]

27. Napi, M.L.M.; Sultan, S.M.; Ismail, R.; How, K.W.; Ahmad, M.K. Electrochemical-Based Biosensors on Different Zinc Oxide Nanostructures: A Review. *Materials* **2019**, *12*, 2985. [CrossRef]

28. Li, Z.; Zhang, X.; Cheng, H.; Liu, J.; Shao, M.; Wei, M.; Evans, D.G.; Zhang, H.; Duan, X. Confined Synthesis of 2D Nanostructured Materials toward Electrocatalysis. *Adv. Energy Mater.* **2020**, *10*, 1900486. [CrossRef]

29. Jang, J.M.; Kim, S.D.; Choi, H.M.; Kim, J.Y.; Jung, W.G. Morphology change of self-assembled ZnO 3D nanostructures with different pH in the simple hydrothermal process. *Mater. Chem. Phys.* **2009**, *113*, 389–394. [CrossRef]

30. Chiu, H.Y.; Wi-Afedzi, T.; Liu, Y.T.; Ghanbari, F.; Lin, K.Y.A. Cobalt Oxides with Various 3D Nanostructured Morphologies for Catalytic Reduction of 4-Nitrophenol: A Comparative Study. *J. Water Process Eng.* **2020**, *37*, 101379. [CrossRef]

31. Yang, Z.; Lin, Y.; Jiao, F.; Li, J.; Wang, W.; Gong, Y.; Jing, X. Morphology engineering of 3D nanostructure MMNS as bifunctional electrocatalysts towards high-efficient overall water splitting. *Appl. Surf. Sci.* **2020**, *502*, 144147. [CrossRef]

32. Tiwari, J.N.; Tiwari, R.N.; Kim, K.S. Zero-dimensional, one-dimensional, two-dimensional and three-dimensional nanostructured materials for advanced electrochemical energy devices. *Prog. Mater. Sci.* **2012**, *57*, 724–803. [CrossRef]

33. Joshi, R.K.; Schneider, J.J. Assembly of one dimensional inorganic nanostructures into functional 2D and 3D architectures. Synthesis, arrangement and functionality. *Chem. Soc. Rev.* **2012**, *41*, 5285–5312. [CrossRef]

34. Young, C.; Wang, J.; Kim, J.; Sugahara, Y.; Henzie, J.; Yamauchi, Y. Controlled Chemical Vapor Deposition for Synthesis of Nanowire Arrays of Metal-Organic Frameworks and Their Thermal Conversion to Carbon/Metal Oxide Hybrid Materials. *Chem. Mater.* **2018**, *30*, 3379–3386. [CrossRef]

35. Altintas Yildirim, O. Efficient vapor-liquid-solid synthesis of copper doped zinc oxide (Cu:ZnO) nanonails with highly homogeneous dopant distribution. *Mater. Sci. Semicond. Process.* **2019**, *101*, 238–246. [CrossRef]

36. Pei, Y.; Hu, M.; Xia, Y.; Huang, W.; Li, Z.; Chen, S. Electrochemical preparation of Pt nanoparticles modified nanoporous gold electrode with highly rough surface for efficient determination of hydrazine. *Sens. Actuators B Chem.* **2020**, *304*, 127416. [CrossRef]

37. Dondapati, J.S.; Govindhan, M.; Chen, A. Direct growth of three-dimensional nanoflower-like structures from flat metal surfaces. *Chem. Commun.* **2022**, *1*, 11127–11130. [CrossRef]

38. Slomkowski, S.; Alemán, J.V.; Gilbert, R.G.; Hess, M.; Horie, K.; Jones, R.G.; Kubisa, P.; Meisel, I.; Mormann, W.; Penczek, S.; et al. Terminology of polymers and polymerization processes in dispersed systems (IUPAC recommendations 2011). *Pure Appl. Chem.* **2011**, *83*, 2229–2259. [CrossRef]

39. Ye, Z.; Tan, M.; Wang, G.; Yuan, J. Preparation, characterization and application of fluorescent terbium complex-doped zirconia nanoparticles. *J. Fluoresc.* **2005**, *15*, 499–505. [CrossRef]

40. Shlapa, Y.; Sarnatskaya, V.; Timashkov, I.; Yushko, L.; Antal, I.; Gerashchenko, B.; Nychyporenko, I.; Belous, A.; Nikolaev, V.; Timko, M. Synthesis of CeO$_2$ nanoparticles by precipitation in reversal microemulsions and their physical–chemical and biological properties. *Appl. Phys. A Mater. Sci. Process.* **2019**, *125*, 1–10. [CrossRef]

41. Malik, M.A.; Wani, M.Y.; Hashim, M.A. Microemulsion method: A novel route to synthesize organic and inorganic nanomaterials. 1st Nano Update. *Arab. J. Chem.* **2012**, *5*, 397–417. [CrossRef]

42. Du, Y.; Wang, W.; Li, X.; Zhao, J.; Ma, J.; Liu, Y.; Lu, G. Preparation of NiO nanoparticles in microemulsion and its gas sensing performance. *Mater. Lett.* **2012**, *68*, 168–170. [CrossRef]

43. Liang, S.; Li, J.; Wang, F.; Qin, J.; Lai, X.; Jiang, X. Highly sensitive acetone gas sensor based on ultrafine α-Fe$_2$O$_3$ nanoparticles. *Sens. Actuators B Chem.* **2017**, *238*, 923–927. [CrossRef]

44. Ali, H.S.; Alghamdi, A.S.; Murtaza, G.; Arif, H.S.; Naeem, W.; Farid, G.; Sharif, S.; Ashiq, M.G.B.; Shabbir, S.A. Facile microemulsion synthesis of vanadium-doped ZnO nanoparticles to analyze the compositional, optical, and electronic properties. *Materials* **2019**, *12*, 821. [CrossRef] [PubMed]

45. Rosenberg, D.J.; Alayoglu, S.; Kostecki, R.; Ahmed, M. Synthesis of microporous silica nanoparticles to study water phase transitions by vibrational spectroscopy. *Nanoscale Adv.* **2019**, *1*, 4878–4887. [CrossRef]

46. Li, B.; You, N.; Liang, Y.; Zhang, Q.; Zhang, W.; Chen, M.; Pang, X. Organic Templates for Inorganic Nanocrystal Growth. *Energy Environ. Mater.* **2019**, *2*, 38–54. [CrossRef]

47. Yamamoto, K.; Imaoka, T.; Tanabe, M.; Kambe, T. New Horizon of Nanoparticle and Cluster Catalysis with Dendrimers. *Chem. Rev.* **2020**, *120*, 1397–1437. [CrossRef]

48. Nakanishi, Y.; Imae, T. Synthesis of dendrimer-protected TiO$_2$ nanoparticles and photodegradation of organic molecules in an aqueous nanoparticle suspension. *J. Colloid Interface Sci.* **2005**, *285*, 158–162. [CrossRef]

49. Vijayalakshmi, R.V.; Kuppan, R.; Kumar, P.P. Investigation on the impact of different stabilizing agents on structural, optical properties of Ag@SnO$_2$ core-shell nanoparticles and its biological applications. *J. Mol. Liq.* **2020**, *307*, 112951. [CrossRef]

50. Hodes, G. Semiconductor and ceramic nanoparticle films deposited by chemical bath deposition. *Phys. Chem. Chem. Phys.* **2007**, *9*, 2181–2196. [CrossRef]

51. Thamaraiselvan, C.; Carmiel, Y.; Eliad, G.; Sukenik, C.N.; Semiat, R.; Dosoretz, C.G. Modification of a polypropylene feed spacer with metal oxide-thin film by chemical bath deposition for biofouling control in membrane filtration. *J. Memb. Sci.* **2019**, *573*, 511–519. [CrossRef]

52. Breen, M.L.; Woodward IV, J.T.; Schwartz, D.K.; Apblett, A.W. Direct Evidence for an Ion-by-Ion Deposition Mechanism in Solution Growth of CdS Thin Films. *Chem. Mater.* **1998**, *10*, 710–717. [CrossRef]

53. Lu, Y.; Meng, X.; Yi, G.; Jia, J. In situ growth of CuS thin films on functionalized self-assembled monolayers using chemical bath deposition. *J. Colloid Interface Sci.* **2011**, *356*, 726–733. [CrossRef]

54. Collins, R.J.; Shin, H.; DeGuire, M.R.; Heuer, A.H.; Sukenik, C.N. Low temperature deposition of patterned TiO$_2$ thin films using photopatterned self-assembled monolayers. *Appl. Phys. Lett.* **1996**, *69*, 860–862. [CrossRef]

55. Masuda, Y.; Saito, N.; Hoffmann, R.; De Guire, M.R.; Koumoto, K. Nano/micro-patterning of anatase TiO$_2$ thin film from an aqueous solution by site-selective elimination method. *Sci. Technol. Adv. Mater.* **2003**, *4*, 461–467. [CrossRef]

56. Strano, V.; Greco, M.G.; Ciliberto, E.; Mirabella, S. Zno microflowers grown by chemical bath deposition: A low-cost approach for massive production of functional nanostructures. *Chemosensors* **2019**, *7*, 62. [CrossRef]

57. Chua, W.H.; Yaacob, M.H.; Tan, C.Y.; Ong, B.H. Chemical bath deposition of h-MoO$_3$ on optical fibre as room-temperature ammonia gas sensor. *Ceram. Int.* **2021**, *47*, 32828–32836. [CrossRef]

58. Vessalli, B.A.; Zito, C.A.; Perfecto, T.M.; Volanti, D.P.; Mazon, T. ZnO nanorods/graphene oxide sheets prepared by chemical bath deposition for volatile organic compounds detection. *J. Alloys Compd.* **2017**, *696*, 996–1003. [CrossRef]

59. Husham, M.; Hamidon, M.N.; Paiman, S.; Abuelsamen, A.A.; Farhat, O.F.; Al-Dulaimi, A.A. Synthesis of ZnO nanorods by microwave-assisted chemical-bath deposition for highly sensitive self-powered UV detection application. *Sens. Actuators A Phys.* **2017**, *263*, 166–173. [CrossRef]

60. Wu, T.; Wang, Z.; Tian, M.; Miao, J.; Zhang, H.; Sun, J. UV excitation NO_2 gas sensor sensitized by ZnO quantum dots at room temperature. *Sens. Actuators B Chem.* **2018**, *259*, 526–531. [CrossRef]

61. Wang, H.; Dai, M.; Li, Y.; Bai, J.; Liu, Y.; Li, Y.; Wang, C.; Liu, F.; Lu, G. The influence of different ZnO nanostructures on NO_2 sensing performance. *Sens. Actuators B Chem.* **2021**, *329*, 129145. [CrossRef]

62. Yuliarto, B.; Ramadhani, M.F.; Septiani, N.L.W.; Hamam, K.A. Enhancement of SO_2 gas sensing performance using ZnO nanorod thin films: The role of deposition time. *J. Mater. Sci.* **2017**, *52*, 4543–4554. [CrossRef]

63. Ananthoju, B.; Biroju, R.K.; Theis, W.; Dryfe, R.A.W. Controlled Electrodeposition of Gold on Graphene: Maximization of the Defect-Enhanced Raman Scattering Response. *Small* **2019**, *15*, 1901555. [CrossRef] [PubMed]

64. Ojo, A.A.; Dharmadasa, I.M. Electroplating of semiconductor materials for applications in large area electronics: A review. *Coatings* **2018**, *8*, 262. [CrossRef]

65. Chen, H.; Zhu, L.; Liu, H.; Li, W. Effects of preparing conditions on the nanostructures electrodeposited from the Zn(NO3)2 electrolyte containing KCl. *Thin Solid Films* **2013**, *534*, 205–213. [CrossRef]

66. Mollarasouli, F.; Majidi, M.R.; Asadpour-Zeynali, K. Enhanced activity for non-enzymatic glucose biosensor by facile electro-deposition of cauliflower-like NiWO4 nanostructures. *J. Taiwan Inst. Chem. Eng.* **2021**, *118*, 301–308. [CrossRef]

67. Patella, B.; Moukri, N.; Regalbuto, G.; Cipollina, C.; Pace, E.; Di Vincenzo, S.; Aiello, G.; O'Riordan, A.; Inguanta, R. Electrochemical Synthesis of Zinc Oxide Nanostructures on Flexible Substrate and Application as an Electrochemical Immunoglobulin-G Immunosensor. *Materials* **2022**, *15*, 713. [CrossRef]

68. Sun, L.; Yuan, G.; Gao, L.; Yang, J.; Chhowalla, M.; Gharahcheshmeh, M.H.; Gleason, K.K.; Choi, Y.S.; Hong, B.H.; Liu, Z. Chemical vapour deposition. *Nat. Rev. Methods Prim.* **2021**, *1*, 5. [CrossRef]

69. Chen, K.; Shi, L.; Zhang, Y.; Liu, Z. Scalable chemical-vapour-deposition growth of three-dimensional graphene materials towards energy-related applications. *Chem. Soc. Rev.* **2018**, *47*, 3018–3036. [CrossRef]

70. Gleason, K.K. Nanoscale control by chemically vapour-deposited polymers. *Nat. Rev. Phys.* **2020**, *2*, 347–364. [CrossRef]

71. Saeed, M.; Alshammari, Y.; Majeed, S.A.; Al-Nasrallah, E. Chemical Vapour Deposition of Graphene—Synthesis, Characterisation, and Applications: A Review. *Molecules* **2020**, *25*, 3856. [CrossRef]

72. Choy, K.L. Chemical vapour deposition of coatings. *Prog. Mater. Sci.* **2003**, *48*, 57–170. [CrossRef]

73. Wu, C.; Guo, D.Y.; Zhang, L.Y.; Li, P.G.; Zhang, F.B.; Tan, C.K.; Wang, S.L.; Liu, A.P.; Wu, F.M.; Tang, W.H. Systematic investigation of the growth kinetics of β-Ga_2O_3 epilayer by plasma enhanced chemical vapor deposition. *Appl. Phys. Lett.* **2020**, *116*, 072102. [CrossRef]

74. Hulkko, J.G.; Böőr, K.; Qiu, R.; Bäcke, O.; Boman, M.; Halvarsson, M.; Lindahl, E. Kinetics of the low-pressure chemical vapor deposited tungsten nitride process using tungsten hexafluoride and ammonia precursors. *J. Vac. Sci. Technol. A* **2021**, *39*, 063403. [CrossRef]

75. Xu, W.; Li, S.; Zhou, S.; Lee, J.K.; Wang, S.; Sarwat, S.G.; Wang, X.; Bhaskaran, H.; Pasta, M.; Warner, J.H. Large Dendritic Monolayer MoS2 Grown by Atmospheric Pressure Chemical Vapor Deposition for Electrocatalysis. *ACS Appl. Mater. Interfaces* **2018**, *10*, 4630–4639. [CrossRef]

76. Barreca, D.; Bekermann, D.; Comini, E.; Devi, A.; Fischer, R.A.; Gasparotto, A.; MacCato, C.; Sberveglieri, G.; Tondello, E. 1D ZnO nano-assemblies by Plasma-CVD as chemical sensors for flammable and toxic gases. *Sens. Actuators B Chem.* **2010**, *149*, 1–7. [CrossRef]

77. Zhang, J.B.; Li, X.N.; Bai, S.L.; Luo, R.X.; Chen, A.F.; Lin, Y. High-yield synthesis of SnO_2 nanobelts by water-assisted chemical vapor deposition for sensor applications. *Mater. Res. Bull.* **2012**, *47*, 3277–3282. [CrossRef]

78. Wu, Y.; Li, G.; Hong, Y.; Zhao, X.; Reyes, P.I.; Lu, Y. Rapid and dynamic detection of antimicrobial treatment response using spectral amplitude modulation in MZO nanostructure-modified quartz crystal microbalance. *J. Microbiol. Methods* **2020**, *178*, 106071. [CrossRef]

79. Barreca, D.; Bekermann, D.; Comini, E.; Devi, A.; Fischer, R.A.; Gasparotto, A.; Gavagnin, M.; MacCato, C.; Sada, C.; Sberveglieri, G.; et al. Plasma enhanced-CVD of undoped and fluorine-doped Co_3O_4 nanosystems for novel gas sensors. *Sens. Actuators B Chem.* **2011**, *160*, 79–86. [CrossRef]

80. Oviroh, P.O.; Akbarzadeh, R.; Pan, D.; Coetzee, R.A.M.; Jen, T.C. New development of atomic layer deposition: Processes, methods and applications. *Sci. Technol. Adv. Mater.* **2019**, *20*, 465–496. [CrossRef]

81. Hausmann, D.; Becker, J.; Wang, S.; Gordon, R.G. Rapid vapor deposition of highly conformal silica nanolaminates. *Science (80-.)* **2002**, *298*, 402–406. [CrossRef] [PubMed]

82. Hao, W.; Marichy, C.; Journet, C. Atomic layer deposition of stable 2D materials. *2D Mater.* **2019**, *6*, 012001. [CrossRef]

83. Makhlouf, H.; Karam, C.; Lamouchi, A.; Tingry, S.; Miele, P.; Habchi, R.; Chtourou, R.; Bechelany, M. Analysis of ultraviolet photo-response of ZnO nanostructures prepared by electrodeposition and atomic layer deposition. *Appl. Surf. Sci.* **2018**, *444*, 253–259. [CrossRef]

84. Song, G.-T.; Wang, Y.; Qi, Y.; Li, W.-M.; Zhang, L.-X. Fabrication of titanium nitride nanoparticles onto carbon nanotubes by atomic layer deposition for utilization as Pt electrocatalyst supports. *Rare Met.* **2020**, *39*, 784–791. [CrossRef]

85. Cho, S.; Ahn, C.; Park, J.; Jeon, S. 3D nanostructured N-doped TiO_2 photocatalysts with enhanced visible absorption. *Nanoscale* **2018**, *10*, 9747–9751. [CrossRef]

86. Hazarika, A.; Fedin, I.; Hong, L.; Guo, J.; Srivastava, V.; Cho, W.; Coropceanu, I.; Portner, J.; Diroll, B.T.; Philbin, J.P.; et al. Colloidal Atomic Layer Deposition with Stationary Reactant Phases Enables Precise Synthesis of "digital" II-VI Nano-heterostructures with Exquisite Control of Confinement and Strain. *J. Am. Chem. Soc.* **2019**, *141*, 13487–13496. [CrossRef]

87. Xu, X.; Wang, G.; Wan, G.; Shi, S.; Hao, C.; Tang, Y.; Wang, G. Magnetic Ni/graphene connected with conductive carbon nano-onions or nanotubes by atomic layer deposition for lightweight and low-frequency microwave absorption. *Chem. Eng. J.* **2020**, *382*, 122980. [CrossRef]

88. Singh, J.A.; Thissen, N.F.W.; Kim, W.H.; Johnson, H.; Kessels, W.M.M.; Bol, A.A.; Bent, S.F.; MacKus, A.J.M. Area-Selective Atomic Layer Deposition of Metal Oxides on Noble Metals through Catalytic Oxygen Activation. *Chem. Mater.* **2018**, *30*, 663–670. [CrossRef]

89. Lee, K.; Losego, M.D.; Kim, D.H.; Parsons, G.N. High performance photocatalytic metal oxide synthetic bi-component nanosheets formed by atomic layer deposition. *Mater. Horizons* **2014**, *1*, 419–423. [CrossRef]

90. Cremers, V.; Puurunen, R.L.; Dendooven, J. Conformality in atomic layer deposition: Current status overview of analysis and modelling. *Appl. Phys. Rev.* **2019**, *6*, 021302. [CrossRef]

91. Chaaya, A.A.; Viter, R.; Baleviciute, I.; Bechelany, M.; Ramanavicius, A.; Gertnere, Z.; Erts, D.; Smyntyna, V.; Miele, P. Tuning optical properties of Al_2O_3/ZnO nanolaminates synthesized by atomic layer deposition. *J. Phys. Chem. C* **2014**, *118*, 3811–3819. [CrossRef]

92. Baitimirova, M.; Viter, R.; Andzane, J.; Van Der Lee, A.; Voiry, D.; Iatsunskyi, I.; Coy, E.; Mikoliunaite, L.; Tumenas, S.; Zaleski, K.; et al. Tuning of Structural and Optical Properties of Graphene/ZnO Nanolaminates. *J. Phys. Chem. C* **2016**, *120*, 23716–23725. [CrossRef]

93. Iatsunskyi, I.; Coy, E.; Viter, R.; Nowaczyk, G.; Jancelewicz, M.; Baleviciute, I.; Załeski, K.; Jurga, S. Study on Structural, Mechanical, and Optical Properties of Al_2O_3-TiO_2 Nanolaminates Prepared by Atomic Layer Deposition. *J. Phys. Chem. C* **2015**, *119*, 20591–20599. [CrossRef]

94. Iatsunskyi, I.; Pavlenko, M.; Viter, R.; Jancelewicz, M.; Nowaczyk, G.; Baleviciute, I.; Załęski, K.; Jurga, S.; Ramanavicius, A.; Smyntyna, V. Tailoring the Structural, Optical, and Photoluminescence Properties of Porous Silicon/TiO_2 Nanostructures. *J. Phys. Chem. C* **2015**, *119*, 7164–7171. [CrossRef]

95. Lou, C.; Yang, C.; Zheng, W.; Liu, X.; Zhang, J. Atomic layer deposition of ZnO on SnO_2 nanospheres for enhanced formaldehyde detection. *Sens. Actuators B Chem.* **2021**, *329*, 129218. [CrossRef]

96. Clark, L.C.; Lyons, C. Electrode systems for continuous monitoring in cardiovascular surgery. *Ann. N. Y. Acad. Sci.* **1962**, *102*, 29–45. [CrossRef]

97. Şerban, I.; Enesca, A. Metal Oxides-Based Semiconductors for Biosensors Applications. *Front. Chem.* **2020**, *8*, 1–8. [CrossRef]

98. Zhou, X.; Pu, H.; Sun, D.-W. DNA functionalized metal and metal oxide nanoparticles: Principles and recent advances in food safety detection. *Crit. Rev. Food Sci. Nutr.* **2021**, *61*, 2277–2296. [CrossRef]

99. Perumal, V.; Hashim, U. Advances in biosensors: Principle, architecture and applications. *J. Appl. Biomed.* **2014**, *12*, 1–15. [CrossRef]

100. Faria, A.M.; Mazon, T. Early diagnosis of Zika infection using a ZnO nanostructures-based rapid electrochemical biosensor. *Talanta* **2019**, *203*, 153–160. [CrossRef]

101. Mukundan, A.; Feng, S.W.; Weng, Y.H.; Tsao, Y.M.; Artemkina, S.B.; Fedorov, V.E.; Lin, Y.S.; Huang, Y.C.; Wang, H.C. Optical and Material Characteristics of MoS_2/Cu_2O Sensor for Detection of Lung Cancer Cell Types in Hydroplegia. *Int. J. Mol. Sci.* **2022**, *23*, 4745. [CrossRef] [PubMed]

102. Ramanaviciene, A.; Popov, A.; Baliunaite, E.; Brasiunas, B.; Kausaite-Minkstimiene, A.; Tamer, U.; Kirdaite, G.; Bernotiene, E.; Mobasheri, A. Magneto-Immunoassay for the Detection and Quantification of Human Growth Hormone. *Biosensors* **2022**, *12*, 65. [CrossRef] [PubMed]

103. Kausaite-Minkstimiene, A.; Popov, A.; Ramanaviciene, A. Surface Plasmon Resonance Immunosensor with Antibody-Functionalized Magnetoplasmonic Nanoparticles for Ultrasensitive Quantification of the CD5 Biomarker. *ACS Appl. Mater. Interfaces* **2022**, *14*, 20720–20728. [CrossRef] [PubMed]

104. Rui, Q.; Komori, K.; Tian, Y.; Liu, H.; Luo, Y.; Sakai, Y. Electrochemical biosensor for the detection of H_2O_2 from living cancer cells based on ZnO nanosheets. *Anal. Chim. Acta* **2010**, *670*, 57–62. [CrossRef] [PubMed]

105. Buzavaite-Verteliene, E.; Plikusiene, I.; Tolenis, T.; Valavicius, A.; Anulyte, J.; Ramanavicius, A.; Balevicius, Z. Hybrid Tamm-surface plasmon polariton mode for highly sensitive detection of protein interactions. *Opt. Express* **2020**, *28*, 29033. [CrossRef]

106. Plikusienė, I.; Bužavaitė-Vertelienė, E.; Mačiulis, V.; Valavičius, A.; Ramanavičienė, A.; Balevičius, Z. Application of tamm plasmon polaritons and cavity modes for biosensing in the combined spectroscopic ellipsometry and quartz crystal microbalance method. *Biosensors* **2021**, *11*, 501. [CrossRef]

107. Pal, A.K.; Pagal, S.; Prashanth, K.; Chandra, G.K.; Umapathy, S.; Mohan, D.B. Ag/ZnO/Au 3D hybrid structured reusable SERS substrate as highly sensitive platform for DNA detection. *Sens. Actuators B Chem.* **2019**, *279*, 157–169. [CrossRef]

108. Kim, D.-K.; Kim, D.M.; Yoo, S.M.; Lee, S.Y. Controllable gold-capped nanoporous anodic alumina chip for label-free, specific detection of bacterial cells. *RSC Adv.* **2017**, *7*, 18815–18820. [CrossRef]

109. Plikusiene, I.; Balevicius, Z.; Ramanaviciene, A.; Talbot, J.; Mickiene, G.; Balevicius, S.; Stirke, A.; Tereshchenko, A.; Tamosaitis, L.; Zvirblis, G.; et al. Evaluation of affinity sensor response kinetics towards dimeric ligands linked with spacers of different rigidity: Immobilized recombinant granulocyte colony-stimulating factor based synthetic receptor binding with genetically engineered dimeric analyte d. *Biosens. Bioelectron.* **2020**, *156*, 112112. [CrossRef]

110. Balevicius, Z.; Talbot, J.; Tamosaitis, L.; Plikusiene, I.; Stirke, A.; Mickiene, G.; Balevicius, S.; Paulauskas, A.; Ramanavicius, A. Modelling of immunosensor response: The evaluation of binding kinetics between an immobilized receptor and structurally-different genetically engineered ligands. *Sens. Actuators B Chem.* **2019**, *297*, 126770. [CrossRef]

111. Plikusiene, I.; Maciulis, V.; Ramanaviciene, A.; Balevicius, Z.; Buzavaite-Verteliene, E.; Ciplys, E.; Slibinskas, R.; Simanavicius, M.; Zvirbliene, A.; Ramanavicius, A. Evaluation of kinetics and thermodynamics of interaction between immobilized SARS-CoV-2 nucleoprotein and specific antibodies by total internal reflection ellipsometry. *J. Colloid Interface Sci.* **2021**, *594*, 195–203. [CrossRef]

112. Plikusiene, I.; Maciulis, V.; Juciute, S.; Maciuleviciene, R.; Balevicius, S.; Ramanavicius, A.; Ramanaviciene, A. Investigation and Comparison of Specific Antibodies' Affinity Interaction with SARS-CoV-2 Wild-Type, B.1.1.7, and B.1.351 Spike Protein by Total Internal Reflection Ellipsometry. *Biosensors* **2022**, *12*, 351. [CrossRef]

113. Stetter, J.R.; Penrose, W.R. Understanding Chemical Sensors and Chemical Sensor Arrays (Electronic Noses): Past, Present, and Future. *Sens. Update* **2002**, *10*, 189–229. [CrossRef]

114. Yang, J.; Cho, M.; Lee, Y. Synthesis of hierarchical $Ni(OH)_2$ hollow nanorod via chemical bath deposition and its glucose sensing performance. *Sens. Actuators B Chem.* **2016**, *222*, 674–681. [CrossRef]

115. Kim, E.B.; Seo, H.K. Highly sensitive formaldehyde detection using well-aligned zinc oxide nanosheets synthesized by chemical bath deposition technique. *Materials* **2019**, *12*, 250. [CrossRef]

116. Kaur, N.; Raj, P.; Singh, A.; Singh, N.; Kim, D.Y. A facile route to ionic liquids-functionalized ZnO nanorods for the fluorometric sensing of thiabendazole drug. *J. Mol. Liq.* **2018**, *261*, 137–145. [CrossRef]

117. Shariati, R.; Rezaei, B.; Jamei, H.R.; Ensafi, A.A. Application of coated green source carbon dots with silica molecularly imprinted polymers as a fluorescence probe for selective and sensitive determination of phenobarbital. *Talanta* **2019**, *194*, 143–149. [CrossRef]

118. Shetti, N.P.; Malode, S.J.; Nayak, D.S.; Aminabhavi, T.M.; Reddy, K.R. Nanostructured silver doped TiO_2/CNTs hybrid as an efficient electrochemical sensor for detection of anti-inflammatory drug, cetirizine. *Microchem. J.* **2019**, *150*, 104124. [CrossRef]

119. Yadav, M.; Dhanda, M.; Arora, R.; Jagdish, R.; Singh, G.; Lata, S. Titania (TiO_2)/silica (SiO_2) nanospheres or NSs amalgamated on a pencil graphite electrode to sense l-ascorbic acid electrochemically and augmented NSs for antimicrobial behaviour. *New J. Chem.* **2022**, *46*, 12783–12796. [CrossRef]

120. Xiao, W.; Ding, L.; He, J.; Huang, J. Preparation of lucigenin-doped silica nanoparticles and their application in fiber optic chloride ion sensor. *Opt. Mater. (Amst.)* **2019**, *98*, 109467. [CrossRef]

121. Alam, M.M.; Rahman, M.M.; Uddin, M.T.; Asiri, A.M.; Chani, M.T.S.; Islam, M.A. Development of L-glutamic acid biosensor with ternary $ZnO/NiO/Al_2O_3$ nanoparticles. *J. Lumin.* **2020**, *227*, 117528. [CrossRef]

122. Rahman, M.M.; Ahmed, J.; Asiri, A.M.; Alamry, K.A. Fabrication of a hydrazine chemical sensor based on facile synthesis of doped NZO nanostructure materials. *New J. Chem.* **2020**, *44*, 13018–13029. [CrossRef]

123. Hu, J.; Zhang, M.; Wang, X.; Sun, Y.; Li, P.; Zhang, W.; Lian, K.; Chen, L.; Chen, Y. Synthesis and characterization of flower-like MoO_3/In_2O_3 microstructures for highly sensitive ethanol detection. *RSC Adv.* **2017**, *7*, 23478–23485. [CrossRef]

NOTES

NOTES